Vibration of Granular Materials

Thesis by

Carl R. Wassgren, Jr.

In Partial Fulfillment of the Requirements

for the Degree of

Doctor of Philosophy

California Insitute of Technology

Pasadena, California

1997

(Submitted July 11, 1996)

Acknowledgements

> It is not the critic who counts, not the man who points out how the strong man stumbled, or where the doer of deeds could have done them better. The credit belongs to the man who is actually in the arena; whose face is marred by dust and sweat and blood; who strives valiantly, who errs and comes short again and again; who knows the great enthusiasms, the great devotions, and spends himself in a worthy cause; who, at the best, knows in the end the triumph of high achievement; and who, at the worst, at least fails while daring greatly, so that his place shall never be with those cold and timid souls who know neither victory nor defeat. *Theodore Roosevelt*

There are many people to whom I owe my deepest gratitude for the support they have given me during my time at Caltech. I am fortunate to have had the opportunity to spend the past several years learning from them about science as well as life.

I would like to thank the people in my research group: Prof. Chris Brennen, Prof. Melany Hunt, Anna Karion, Rajan Natarajan, and Roberto Zenit. They have been excellent mentors and have given me much guidence and support throughout my stay at Caltech. A special thanks goes to Bob Behnken and Sudipto Sur, not only for their technical support, but also for their friendship. I would also like to thank my officemates, Bob Uy and Garrett Reisman, for patiently listening to my questions and explanations.

Most of all, I'd like to thank my wife, Sarah. I couldn't possibly express in words the support, help, and love she has given me throughout the past five years. I dedicate this thesis to her.

Abstract

This thesis examines the fundamental behavior of a granular material subject to external vibrations. Experiments were designed to investigate the phenomena that appear in a container filled with glass spheres subject to vertical, sinusoidal oscillations. In addition, a discrete element computer simulation code was written to supplement the experimental program.

Experiments and simulations reveal that the behavior of the particle bed can be classified into two regimes known as shallow and deep beds. For example, when a shallow bed consisting of less than six layers of glass spheres is subjected to oscillations with acceleration amplitudes greater than approximately $2.0g$ where g is the acceleration due to gravity, the particles in the container are fluidized and do not display coordinated movement. However, when more than six particle layers are used, the particles move coherently and the deep bed behaves as a single, completely inelastic mass.

In the shallow bed regime three distinct sub-states are observed that differ in the degree of coherency in the particle motions. Each appears depending upon the number of particle layers in the bed and on the acceleration amplitude of the oscillations. The transitions between the states are gradual and not well-defined.

The transition from the deep bed to the shallow bed state is characterized by a sudden expansion of the bed that occurs at a critical acceleration amplitude for a fixed bed depth and particle type. Simulations indicate that when the particle fluctuating kinetic energy is dissipated completely each oscillation cycle, the bed remains in the deep bed state. If the energy is not completely dissipated, a shallow bed state results. A simple model consisting of an inelastic ball bouncing on a sinusoidally oscillating table reproduces the sudden expansion.

In the deep bed regime, phenomena such as side wall convection, surface waves, kinks, and kink convection cells appear depending primarily on the acceleration am-

plitude of the oscillations and, to a lesser degree, the number of particle layers in the bed. Phase maps of when these behaviors occur were constructed using both experimental and simulation data.

When the acceleration amplitude is greater than approximately $1g$, side wall convection cells appear at the vertical wall boundaries of the container. Particles move down along the vertical walls of the container and up within the bulk of the bed. Simulations indicate that the convection cells are the result of the frictional contact between particles and the walls and the asymmetry of the particle/wall collision rate over an oscillation cycle. Using the simulations, the width of the boundary layer next to the walls, the height of the convection cell center from the container base, and the particle flux in the boundary layer were measured as functions of the vibration parameters and particle properties. The results from the simulation compare well with experimental measurements. The simulation indicates that the boundary layer width is proportional to the container width when the bed aspect ratio, defined as the bed depth to the bed width, is greater than approximately 0.2. For beds with aspect ratios less than 0.2, however, the boundary layer width remains constant. Simulation results also demonstrate that the convection cell height is proportional to the bed depth and that the flux of particles in the boundary layer increases with increasing particle/wall friction and decreases for coefficients of restitution near one.

At acceleration amplitudes between approximately $2.0g$ and $3.5g$, standing waves appear on the top free surface of the bed. These waves form at half the forcing oscillation frequency and are referred to as $f/2$ waves. A second set of standing waves appears when the acceleration amplitude is greater than approximately $5.0g$ and persist up to at least $7.0g$. These waves form at one-quarter the forcing frequency and are known as $f/4$ waves. Experimental measurements indicate that the wave amplitude expressed as a Froude number increases with increasing acceleration amplitude for the $f/2$ waves but remains constant for the $f/4$ waves. Additionally, measurements of the wavelength suggest that the waves have a dispersion relation similar to that for deep fluid gravity waves where the wavelength is proportional to the square of the inverse frequency.

Kinks and kink convection cells appear in the particle bed after a period doubling bifurcation occurs in the flight dynamics of the bed. The formation of kinks can be explained using a simple model consisting of a completely inelastic ball on a sinusoidally oscillating table. Experimental measurements indicate a minimum allowable distance between nodes that is a function of the bed depth and acceleration amplitude. The convection cells bracketing each kink are shown to be the result of the out-of-phase motion of the bed sections and the interaction between fluidized and solidified regions of the bed.

The effect of vertical, sinusoidal vibrations on a discharging wedge-shaped hopper was also investigated. When the hopper exit is closed, side wall convection cells appear with particles moving up at the inclined container boundaries and down at the centerline of the bed. The same mechanism that causes downward convection at vertical walls can also explain the upward motion at inclined walls. Experimental measurements also indicate that the discharge rate from the vibrating hopper scales with the oscillation velocity amplitude. At low velocity amplitudes, the discharge rate from the hopper is slightly greater than the non-vibrating hopper discharge rate. At high velocity amplitudes, however, the discharge rate decreases significantly. A simple model accounting for the change in the effective gravity acting on the particle bed throughout the oscillation cycle and the impact velocity of the bed with the hopper predicts the observed trend.

The experiments and simulations conducted in the present work suggest that the boundary conditions and the fluid- and solid-like nature of granular materials are significant factors affecting the response of a granular bed. Additionally, this work demonstrates the value of discrete element computer simulations as a tool for complementing experimental observations.

Contents

List of Figures

List of Tables

Nomenclature

g	acceleration due to gravity, $g = 9.81$ m/s^2
a	oscillation amplitude [m]
f	oscillation cyclic frequency [Hz]
ω	oscillation radian frequency [rad/s] ($\omega = 2\pi f$)
T	oscillation period [s]
Γ	dimensionless oscillation acceleration amplitude ($\Gamma = a\omega^2/g$)
W	container width [m]
h_0, H	initial particle bed depth [m]
d	particle diameter [m]
r	particle radius [m]
ρ, ρ_p	particle density [kg/m^3]
m	particle mass [kg]
I	particle moment of inertia [N·m^2]
N	number of particles
$k_{n,pp}$	normal spring constant for a particle/particle contact [N/m]
$k_{n,pw}$	normal spring constant for a particle/wall contact [N/m]
ν_{pp}	normal dashpot coefficient for a particle/particle contact [N/(m/s)]
ν_{pw}	normal dashpot coefficient for a particle/wall contact [N/(m/s)]
$k_{s,pp}$	tangential spring constant for a particle/particle contact [N/m]
$k_{s,pw}$	tangential spring constant for a particle/wall contact [N/m]
μ_{pp}	particle/particle sliding friction coefficient
μ_{pw}	particle/wall sliding friction coefficient
ϵ_{pp}	particle/particle coefficient of restitution
ϵ_{pw}	particle/wall coefficient of restitution
t	time [s]

ϕ	oscillation phase angle [rad]
Δt	simulation time step [s], flight time [s]
Δ_{ij}	overlap between particles i and j [m]
$\hat{n}_{ij}$	normal unit vector pointing from the center of particle i to the center of particle j
$\hat{s}_{ij}$	tangential unit vector for the contact between particles i and j
$\vec{x}_i$	particle i position vector [m]
θ_i	particle i rotational position [rad]
$\dot{\delta\vec{x}}_{ij}$	relative velocity of particle j with respect to particle i at the point of contact [m/s]
$\delta\vec{s}_{ij}$	the tangential displacement of particle j relative to particle i from the initial point of contact [m]
$\vec{F}_{gi}$	force acting on particle i due to gravity [N]
$\vec{F}_{ij}$	force acting on particle i due to contact with particle j [N]
$\vec{F}_{nij}$	contact normal force acting on particle i due to particle j [N]
$\vec{F}_{s,spring}$	contact spring force in the tangential direction acting on particle i due to particle j [N]
$\vec{F}_{s,friction}$	contact sliding friction force acting on particle i due to particle j in the tangential direction [N]
Δ_{max}	the maximum amount of overlap for a two particle collision [m]
$m*$	the effective mass for a two particle collision ($m* = m_i m_j/(m_i + m_j)$) [kg]
$\dot{\delta\vec{x}}_{max,ij}$	the maximum relative velocity of particle j with respect to particle i at the point of contact [m/s]

τ	collision duration time for a two particle collision [s]
τ_{trans}	translational period of oscillation [s]
τ_{rot}	rotational period of oscillation [s]
h	lid/base separation distance [m], convection cell height above the container floor [m]
Fr	Froude number
b	base vertical position [m]
p	particle vertical position [m]
Γ_1	the dimensionless acceleration amplitude at which a saddle node bifurcation occurs
Γ_1'	the dimensionless acceleration amplitude at which a change of stability bifurcation occurs
Γ_1^*	the dimensionless acceleration amplitude at which the flight time of an inelatic particle returns to a single flight time
γ	granular temperature per unit mass [m^2/s^2]
Γ_v	dimensionless vertical oscillation acceleration amplitude
Γ_h	dimensionless horizontal oscillation acceleration amplitude
w	boundary layer width [m]
j_d	downward particle flux in the boundary layer at height h [particles/(m·s)]
I_0	first-order modified Bessel function
j_e	particle flux from the downward flowing boundary layer to the upward moving flow [particles/(m·s)]
F_y	total vertical force acting on the particle bed due to a wall [N]
m_{tot}	total particle bed mass [kg]
$\dot{N}_c$	particle/wall collision rate [collisions/s]
η	wave amplitude [m]
λ	wavelength [m]
g_{eff}	effective gravity [m/s^2]
λ_0	minimum wavelength at high frequencies [m]

l	minimum separation distance between kinks [m]
W_e	hopper exit width [m]
W_{fb}	distance between the front and back walls of the hopper [m]
θ_w	hopper wall inclination from the vertical [deg]
ρ_b	bulk material density [kg/m^3]
D_h	hopper exit hydraulic diameter [m]
$\dot{D}$	vibrating hopper average mass discharge rate [kg/s]
$\dot{D}_0$	non-vibrating hopper average mass discharge rate [kg/s]
$\dot{d}$	hopper instantaneous mass discharge rate [kg/s]
Ba	Bagnold number
du/dy	shear rate [1/s]
μ_f	fluid viscosity [N·s/m]
ν	solid fraction
ν_M	maximum solid fraction
dp/dy	pressure gradient [N/m^2]
κ	bed permeability
Φ	bed porosity

Chapter 1 Introduction

1.1 Description of a Granular Material

A granular material consists of discrete, solid particles dispersed in a vacuum or an interstitial fluid. Examples of such materials include sand, stones, soil, ores, grains, pharmaceuticals, and a variety of chemicals. A distinguishing feature between flows of granular materials and other solid-fluid mixtures is that in granular flows, the direct interaction of particles plays an important role in the flow mechanics. Thus, most of the energy dissipation and momentum transfer in granular flows occurs when particles are in contact with each other or with a boundary. One parameter that has been suggested to quantify this distinction is the "Bagnold number." In shear cell experiments containing neutrally buoyant spheres immersed in a water-glycol mixture, Bagnold (1954) found three regimes of rheological behavior that depend on the ratio of the particle inertial stress to the fluid viscous stress:

$$Ba = \frac{\rho_p d^2 (du/dy)}{\mu_f ((\frac{\nu_M}{\nu})^{\frac{1}{3}} - 1)^{\frac{1}{2}}} \tag{1.1}$$

where ρ_p is the density of the particles, d the particle diameter, du/dy the shear rate, μ_f the fluid viscosity, ν_M the maximum packing solid fraction, and ν the solid fraction. Bagnold found that when $Ba < 40$ the momentum transfer is primarily through fluid-particle interactions and the mixture behaves as a viscous fluid. He referred to this as the "macro-viscous" regime. When $40 < Ba < 450$, known as the "transition" regime, both particle-particle and particle-fluid interactions contribute to the momentum transfer. For values of $Ba > 450$, the primary momentum transfer mechanism is through particle-particle interactions and the mixture behaves as if the interstitial fluid were removed. Bagnold referred to this granular flow behavior as the "grain inertia" regime. The resulting granular system can be considered as consisting

solely of solid particles and interstitial voids.

Although granular materials are commonly found both in natural and industrial settings, there is no general understanding of how these materials behave. Particulate systems are unique in that they can exhibit gas-, liquid-, and solid-like properties. There are, however, important differences with each of these phases that make the behavior of granular materials even more unusual.

Highly agitated systems of particles are often modeled in a manner similar to a rarefied gas (see, for example, Haff, 1983 and Jenkins and Savage, 1983). An important difference, though, is that, unlike collisions between gas molecules, solid particle collisions are inelastic and dissipate energy. Thus, a granular material "gas" can quickly reach a zero effective temperature.

Granular materials also have liquid-like properties. For example, a granular material can flow as in an hourglass or an avalanche. Furthermore, when particles are poured into a large container, the assembly conforms, in a bulk sense, to the shape of the container. Unlike a liquid, though, a granular material can resist shear as in the slope of a sand pile.

This solid-like behavior is limited only to compressive loads. When subjected to tensile loads, particles come apart.[1] The reason granular materials can resist shear loads is due to the discrete size of the particles. In order for a densely packed assembly of particles to flow, it must first dilate, a phenomenon known as the Reynolds' Principle of Dilatancy (Reynolds, 1885). The resulting normal strain due to an applied shear stress is a result of particles moving over one another as the assembly deforms.[2] Another unusual result of the material granularity is that load transmission is typically anisotropic. Forces are transmitted along particle contacts and form long "force chains" (an example of these is shown in Jaeger and Nagel, 1992).

[1] Assemblies of cohesive particles can resist a limited tensile load, however for simplicity, the present definition of a granular material refers to non-cohesive particles.

[2] Note that a loosely packed assembly may actually contract when sheared since, as the particles move, they can fall into neighboring voids.

1.2 Motivation for Studying Granular Materials

Since granular materials are often encountered in both natural and industrial settings, understanding how they behave can provide important design information. Natural processes such as erosion, sedimentation, dune formation, soil liquefaction, and landslides significantly affect the environment and often result in property damage as well as fatalities. FEMA (Federal Emergency Management Agency) estimates that landslides alone result in an annual loss of $1.5 billion and at least 25 fatalities in the United States (FEMA, 1996). Clearly, having knowledge of the granular state would help to prevent some the losses associated with these natural phenomena.

Many industrial processes also involve particulate materials. The types vary greatly ranging from pharmaceuticals to frozen peas. In the chemical industrial alone it is estimated that half of the products and three-quarters of the raw materials are in the form of particulates (Nedderman, 1992). The abundance of these materials implies that there are enormous costs associated with handling them. For example, a straightforward process such as crushing ores uses approximately 1.3% of the U.S. annual energy consumption (Ennis *et al.*, 1994). Even small increases in efficiency can result in tremendous savings.

Even with these incentives, a poor understanding remains of how these materials behave. Most of the knowledge of how to handle particulates is empirical and no general approach to analyzing these flows exists. Although models based on kinetic theory and soil plasticity have shown promise, they have a number of constraining assumptions that limit their use to extreme flow cases (for a review of these models, refer to Savage, 1984). As a result, much of the current granular material work focuses on several "benchmark" flows in order to examine the fundamental behavior of particle assemblies.

1.3 Vibration of Granular Materials

An example of a benchmark experiment involves a granular material in a container subject to external oscillations. Since collisions (and contacts) between particles are dissipative, kinetic energy is converted to heat in a flowing granular material. If additional energy is not added to the system, the moving material will quickly come to rest. This energy can be added by an external force field, such as gravity, by shearing the material at a boundary as in a Couette flow, or by subjecting the material to vibrations.

Vibration of granular materials is also of interest for more practical reasons. In industry, vibration is commonly used as an aid to handling and transporting particulate materials such as foodstuffs, coal, and pharmaceuticals. Examples of devices that often utilize vibration include conveyor belts, hoppers, sorting tables, packing tables, drying plates, and fluidized bed reactors. Vibration of a granular material may also play an important role in natural events such as earthquakes and avalanches. Clearly, understanding how a granular material responds when subjected to vibration can provide valuable design information.

Experiments have shown that a number of interesting phenomena appear when beds of granular materials are subjected to external, vertical oscillations. Chladni (1787) was perhaps the first to systematically study the behavior of vibrated beds of particles. He found that when sand is scattered on a vibrating membrane, the sand particles collect in heaps corresponding to the vibration anti-nodes. Faraday (1831) also examined these patterns and found that particles move in circulation patterns within the piles. Particles avalanche down the free surface of the pile, are entrained back into the bed at the base and re-circulate to the peak to repeat the cycle.

Other researchers have found equally interesting phenomena in vibrated beds of granular material. An important observation made by Bachmann (1940), and later investigated by Kroll (1954), is that the behavior of the particle bed is significantly different depending on the depth of the bed. Bachmann found that when the average depth of the particle bed is less than about six particle diameters, ($h_0/d < 6$ where

h_0 is the bed depth and d is a particle diameter), particles bounce around randomly as in a fluidized bed. However, when the depth is greater than six particle layers, the assembly of particles acts as a single, coherent, plastic body. Other researchers have investigated these two distinct regimes of behavior and have found significantly different phenomena appearing in each.

Thomas *et al.* (1989) described four discernible states of behavior when shallow beds of material are subjected to external oscillations. For the shallowest beds (for example when $h_0/d = 0.17$ - implying that there are fewer particles than is necessary to fill a single packed layer) they describe a "Newtonian-I" state in which particles bounce around so randomly that there is little variation in the vertical concentration profile over an oscillation cycle. At somewhat larger h_0/d (at 0.273 for example) the bed transitions to a "Newtonian-II" state in which a dense layer of particles accumulates on the surface during one part of each cycle. Thicker layers of particles (for example $h_0/d = 1.7$) lead to a "coherent-expanded" state in which the particles all oscillate as a coherent mass. This mass does, however, expand and contract considerably during each cycle. The last state, referred to by Thomas *et al.* as the "coherent-condensed" state is, in fact, the same deep bed regime observed by Bachmann when $h_0/d > 6$.

These shallow beds have also been studied by a number of other researchers. For example, Chlenov and Mikhailov (1965) examined heat transfer in vibrated shallow beds and Lan and Rosato (1995) performed computer simulations of shallow beds and compared the results with the kinetic theory predictions formulated by Richman and Martin (1992). The dynamics of the transition between the shallow bed and deep bed states was examined by Brennen *et al.* (1996).

Deep beds of granular materials display very different behaviors when subject to oscillations. These behaviors include heaps and convection cells similar to those described by Faraday (1831), traveling and standing surface waves, and "kinks" in the bed with corresponding convection cells.

Heaps and convection cells similar to those described by Faraday (1831) have been reproduced in a number of experimental devices. Faraday's experiment used a vi-

brating membrane with fixed boundaries giving rise to vibration amplitude gradients. Other experiments using rigid vibrating bases, and with both fixed and oscillating side wall boundaries have also produced heaps and convection cells. These experiments are described in papers by Evesque and Rajchenbach (1989), Ehrichs *et al.* (1995), Knight *et al.* (1996), Rátkai (1976), and Zik and Stavans, (1991) to name just a few. A number of experiments have also investigated how the interstitial fluid affects the formation of heaps and convection cells (see, for example, Laroche *et al.*, 1990ab, Evesque, 1990, and Pak *et al.*, 1995). In addition, both behaviors have been studied with computer simulations by Gallas *et al.* (1992), Taguchi (1992), Lee (1994), Rosato and Lan (1994), and Wassgren *et al.* (1996b) and with kinetic theory models by Savage (1988) and Goldshtein *et al.* (1995).

Despite the large number of investigations, few measurements of the heaping and convection cell behaviors have been made. The most extensive study of the convection cell phenomenon was made by Knight *et al.* (1996) in their nuclear magnetic resonance imaging (NMR) experiments of poppy seeds in containers subjected to discrete, vertical taps. Most of the remaining experimental and simulation work has focused on onset conditions for the two behaviors. A number of hypotheses have been proposed for the mechanisms that cause convection and heaps (Rajchenbach, 1991, Gallas *et al.* 1992, Taguchi 1992, and Lee 1994); however, none of these hypotheses have been supported by conclusive evidence.

Less studied are the waves that appear on the free surface of a vibrating deep bed. Pak and Behringer (1993) reported the appearance of waves on the surface of a heap traveling from the heap's base to its peak. Standing waves have also been observed on the free surface of a deep bed. Fauve *et al.* (1989) reported the appearance of parametrically forced surface waves and mentioned their similarity to Faraday instability waves which appear in vertically vibrated fluids (see, for example, Miles and Henderson, 1990). Melo *et al.* (1994, 1995), and more recently, Metcalf *et al.* (1996) and Clément *et al.* (1996), measured the dispersion relation for the standing surface waves and also studied the variety of wave patterns that appear on the surface of beds in wide-mouthed containers. Wassgren *et al.* (1996a) also studied the dispersion

relation for the surface waves as well as the wave amplitudes as a function of the vibration parameters.

Another interesting behavior that appears for vibrating deep beds are "kinks" and their associated convection cells. A kink is defined as the region of a particle bed between two sections that oscillate out-of-phase. Bracketing each kink are two convection cells where particles move down at the kink and up on either side of it. These behaviors were first examined in experiments by Douady *et al.* (1989) and have also been reported in experiments by Melo *et al.* (1995) and Wassgren *et al.* (1996a). The kink behavior is a result of a bifurcation in the flight dynamics of the bed, a point that will be discussed in detail in chapter 7. Douady *et al.* hypothesized that the convection cells associated with kinks are a result of the out-of-phase bed motion and an interaction between fluidized and solidified regions of the bed. They did not, however, provide any evidence to support this theory.

As reflected in the previous paragraphs, this simple experiment consisting of a container filled with granular material subjected to vertical oscillations produces a surprising number of complex phenomena. Unfortunately, little is understood about these behaviors. Most of the previous work has focused on showing that these various behaviors exist. However, detailed measurements of the phenomena and the mechanisms that cause them are lacking. Part of the present work details experiments and simulations designed to provide some of this information.

1.4 Vibrating Hopper Flows

One common industrial device that often utilizes vibration is the "live wall" hopper. A hopper is essentially a funnel and storage unit for granular materials. The term "live wall" refers to the fact that the walls of the hopper are sometimes subjected to vibration in order to aid in the discharge of the granular material.

Hoppers are usually classified as being either of the mass or funnel flow type. In mass flow hoppers, the first material poured into the hopper is also the first material out. When discharging, all of the material in the hopper flows simultaneously; no

stagnant regions of material exist within the hopper. Although hoppers are usually designed with mass flow in mind, various factors including geometric constraints and material-wall frictional interactions do not always permit this type of flow. Instead, stagnant regions of material form near the walls of the hopper and the first material into the hopper can be the last to leave. Flows of this type are known as a funnel flows.

Funnel flows are problematic for a number of reasons. First, the first-in, last-out flow pattern is often unacceptable when time-dependent material is passed through the hopper. Materials such as organic grains can decay in the stagnant regions while other materials, such as soda ash or cement, consolidate over time and become more difficult to handle. Another problem with funnel flows is that the flowing material often crushes the material in the stagnant regions resulting in the production of fine dust and increasing the risk of explosions. Lastly, a severe form of funnel flow, known as a "rathole," may form in the hopper. A rathole is a narrow flow channel that discharges completely while most of the material in the hopper remains. Ratholes often end in "flooding" which occurs when a rathole collapses and a sudden surge of material exits the hopper. These surges can cause structural damage to the hopper. Problems such as these make mass flow hoppers preferable to the funnel flow type.

One problem that plagues both types of hoppers is known as bridging or arching. Bridging occurs when a mechanically stable arch of material forms within the hopper (usually at the exit) and supports the material load above it. As a result, flow through the hopper is stopped. Flooding typically occurs when the bridge collapses.

One method of alleviating these problems involves vibrating the hopper walls. In its crudest form, this is accomplished by pounding the walls with a sledgehammer. A condition known as "hopper rash," where the hopper walls have a ball-peened appearance, is often observed when this method is employed. A more common method of implementing vibration involves attaching unbalanced motors to the hopper walls. Hoppers utilizing this design are typically known as "live wall" hoppers.

Few researchers have examined the effects of vibrating hopper walls. Most investigations focus on the stress and velocity fields in non-vibrating, mass flow hoppers (for

reviews, refer to Nedderman, 1982, Nedderman *et al.*, 1982, and Tüzün *et al.*, 1982). A number of experiments and simulations have also investigated non-vibrating, funnel flows (see, for example, Nguyen, *et al.*, 1980 and Langston *et al.*, 1994).

Perhaps the first work including the effects of vibration was performed by Takahashi *et al.* (1968) and Suzuki *et al.* (1968) in their experiments of vertically oscillating wedge hoppers and flat bottom bins. They examined the trajectories of particles and discharge of material through an exit orifice and found that convection cells appear near the wall boundaries and that the discharge rate from the hopper is decreased significantly at high oscillation accelerations. Evesque and Meftah (1993) studied the time of discharge for sand in a vertically vibrated hourglass and found similar results. Knight *et al.* (1993), although not investigating hopper flows, reported the appearance of convection cells in experiments using vertically oscillating conical containers. Experiments and simulations of particle flow in wedge-shaped hoppers were performed by Wassgren *et al.* (1995). They also reported the appearance of convection cells at the inclined container walls as well as standing waves on the free surface of the material. In addition, Wassgren *et al.* examined the discharge rate from the hopper as a function of the vibration parameters.

Chapter 8 describes the experiments and simulations designed to investigate vertically oscillating hopper flows. The work was designed to observe the effect of vibration on particle trajectories and examine how the discharge rate from the hopper varies due to the vibrations.

1.5 Computer Simulations of Granular Materials

A resurgence in granular materials research occurred in the early 1980s. Part of this renewed interest may be attributed to the development of computer simulations to study granular flows. Prior to the 1980s, computer processing speed and data storage capabilities were too limited to study systems of thousands of particles. However, as processor speed increased and hard drive and memory costs decreased, computer simulations became an increasingly effective tool for studying granular materials.

Simulations offer several important features for studying granular flows. Perhaps the most significant is that the state of the particulate system is known at all times in a simulation. Hence, the interior of a flow can be examined and measurements can be made that may be difficult to make in experiments. Furthermore, simulations can model environments that are not easily produced in experiments. For example, many simulations are performed with altered gravity environments or with frictionless particles. The insights that these simulations can provide are valuable for understanding how granular materials behave.

Most granular flow computer simulations are discrete element (DE) methods. The term "discrete element" refers to the fact that the simulation models the granular material as a system of individual particles. Examples of DE simulations include Monte Carlo techniques, cellular automata, and hard and soft particle methods (see Campbell, 1996 for a review of these methods).

Monte Carlo techniques are statistically based. A particle assembly state is chosen based on the energy of the configuration. For each new state, particles are given a random velocity or position within some distribution function. The configuration which gives the lowest system energy is chosen as the new state. The movement of particles is limited by physical restraints which appear in the state energy. For example, two particles occupying the same position can be assigned to have a high energy making that particular configuration improbable. Simulations using the Monte Carlo technique have been performed by Rosato *et al.* (1986) and Hopkins and Shen (1992).

Another discrete element simulation technique is the cellular automata method. This is a lattice-based, kinematic approach, where particles are constrained to move on discrete lattice points. At each time step, particles are allowed to move into neighboring empty lattice points with the constraint that only one particle may occupy a given lattice point at a time. The particle movement is also governed by a probability function which reflects the physics of the system (refer to Baxter and Behringer, 1991).

Hard particle methods evolved from molecular dynamic simulations of rarefied gases. Individual particles move in well-defined trajectories (typically ballistic trajectories in a gravity field or in straight lines when gravity is not present) until a collision

occurs with another particle or a boundary. Particle-particle and particle-wall interactions are modeled as binary, instantaneous collisions and the post-collision particle states are easily determined from classical particle dynamics (refer to Campbell, 1982 for details). Because of the assumption that collisions are binary and instantaneous, this method is most appropriate for low density, highly agitated flows.

Many flows, however, especially those occurring in a gravity field, have multiple, long duration particle contacts. Soft particle methods are best suited for these situations. In a soft particle simulation, the forces acting on each particle in the system are determined. Using Newton's second law, the acceleration of each particle is found and the resulting particle states are determined by integrating the accelerations in time to yield both velocities and positions. New forces are calculated based on the updated particle states and the procedure is repeated until some ending criteria is reached. This type of DE simulation is perhaps the most common simulation technique and was pioneered by Cundall and Strack (1979).

Several features of soft particle methods make them preferable to the previously mentioned simulation techniques. First, the soft particle technique is exact when determining forces and particle states. Monte Carlo and cellular automata approaches incorporate probabilistic functions in order to determine particle positions and velocities. Second, soft particle methods can easily model flows that have long duration, multiple particle contacts as well as particles involved in binary, near-instantaneous collisions. Hard particle models break down when long duration and multiple particle contacts occur. Soft particle techniques can also incorporate a variety of forces in a straightforward manner unlike the other methods. Lastly, inter-particle force information can be examined in soft particle simulations. None of the other methods can provide this information. The disadvantage to using the soft particle approach is that they often require more computational power than the other simulation techniques.

Discrete element simulations have often been used to examine vibrating granular beds and hopper flows. Gallas *et al.* (1992), Taguchi (1992), Lee (1994), Rosato and Lan (1994), and Luding *et al.* (1994a) have examined the side wall convection cells in vibrating beds using soft particle methods. Shallow bed behavior was examined

in hard particle simulations by Lan and Rosato (1995) and in, both, hard and soft particle simulations by Luding *et al.* (1994b). Rosato *et al.* (1986) also used a Monte Carlo approach to study particle segregation in vibrating containers. Lastly, both soft particle methods and cellular automata have been been used to simulate non-vibrating, hopper flows in work by Potapov and Campbell (1996) and Baxter and Behringer (1991) among others. It is clear that computer simulations have become an invaluable tool for studying granular flows.

In the present work, soft particle simulations were used to supplement the experimental work. Results from the simulations helped to determine the mechanisms causing the observed vibration phenomena and allowed for the examination of flow properties that were not easily studied in the experimental work.

1.6 Topics of Investigation

This thesis examines the fundamental behavior of a granular material subject to external vibrations. Chapter 2 discusses the experiments and simulations designed to better understand both the shallow and deep bed behaviors described in section 1.3. The remainder of the chapters examine each phenomenon in detail. Side wall convection is discussed in chapter 5, surface waves in chapter 6, kinks and their associated convection cells in chapter 7, and vibrating hopper flows in chapter 8. Lastly, chapter 9 summarizes the current work and discusses the implications of this work to granular material flows in general.

Chapter 2 Approach

2.1 Experiments

2.1.1 Shallow Beds

Several experiments were performed to investigate the behavior of a shallow bed of granular material subjected to vertical oscillations.[1] The granular material consisted of A-285 glass beads with a mean diameter of 2.85 mm. The particles were massive enough so that interstitial fluid and electrostatic effects could be neglected (refer to appendix I). Various quantities of these beads were placed in a rectangular box with cross-sectional dimensions of 11 cm by 13.2 cm. The box, in turn, was mounted on an Electroseis electro-mechanical shaker and subjected to vertical vibration at frequencies between 4 and 10 Hz with accelerations up to about $2.5g$. A Statham A73TC-4-350 accelerometer was used to measure the acceleration level accurately. A schematic of the apparatus is shown in figure 2.1.

The box had a thick aluminum base and back but the other three sides were made of lucite so that the behavior of the beads could be observed. In order to determine the expansion of the bed of particles, paper lids of various thickness were placed on top of the beads leaving a clearance of about 1 mm between the edge of the lid and the walls of the box. When the box was vibrated vertically the bed of beads would expand and the lid would float on the beads due to particle-lid collisions. Fortunately, the lid proved to be quite stable and under all of the conditions used in the present experiments and would remain horizontal and centralized with a roughly equal spacing all around the periphery. Because this spacing was smaller than the diameter of the beads, all of the beads would remain under the lid. A strobe lamp

[1]These experiments were first performed by a former SURF student, Supriya Ghosh, in 1984 and were later reproduced by the author.

was used to examine the motion of the lid and the beads during various parts of the oscillation cycle. By this means it was observed that the spacing, h, between the base and the lid did not vary greatly during the oscillations. The beads would bounce around below the lid but because of the resistance to the flow of air around the sides of the lid, the volume of beads and air would remain almost constant during a cycle of oscillation. Thus, using the strobe and a scale attached to the exterior of the box, it was possible to measure the expansion or height, h, for each operating condition.

Experiments were conducted by observing the evolution of the bed of beads as the vibration amplitude, a, was increased from zero to the maximum of which the shaker was capable at a fixed frequency. Such experiments were conducted over a range of frequencies ($4 \rightarrow 10$ Hz) for various quantities of beads and for lids with different weights as listed in table 2.1.

It should be noted that a single packed layer of beads resting on the base of the box would weigh approximately 62 gm. Consequently the masses of beads range from less than the mass for a single layer to about ten layers. The 45 gm of experiment 7 (table 2.1) was close to the minimum at which the lid would remain horizontal for the duration of the experiment.

2.1.2 Deep Beds

The apparatus used to study the deep bed behaviors is similar to the set-up used in the shallow bed experiments (refer to figure 2.1). Boxes of several sizes were filled with various types of glass spheres and were mounted on an electro-magnetic shaker. A Ling electro-magnetic shaker (model A-175) was used since it was capable of a much greater range of frequencies and accelerations than the Electro-Seis shaker used in the shallow bed experiments. As with the Electro-Seis shaker, both the frequency, f, and amplitude, a, of the oscillations could be controlled independently. Typically, though, the experiments were performed at a fixed frequency while the amplitude was varied to give a specified acceleration amplitude, $a\omega^2$, where $\omega = 2\pi f$. In these experiments, the frequencies ranged between 15 and 40 Hz while the amplitude varied

such that the vibration acceleration amplitude varied between zero and shaker's limit of roughly seven gs, where g is the acceleration due to gravity. The precision of the frequency control was ± 0.5 Hz while the acceleration level could be controlled to within $\pm 0.1g$. A Dytran 3126A accelerometer was attached to the mounting base of the shaker in order to monitor the acceleration level precisely.

Three lucite boxes with rectangular cross-sectional dimensions of 13.5 cm by 1.6 cm, 18.0 cm by 1.6 cm, and 18.0 cm by 4.8 cm were constructed to contain the granular material. In order to reduce electrostatic effects, the interior vertical walls of the boxes were lined with smooth window glass. The base of the containers consisted of a 2.5 cm thick steel plate while the tops remained open to the atmosphere.

Three different types of soda lime glass spheres (with a density of 2.5 g/cm^3) were used in the experiments. Most of the runs, and all of the measurements, were performed using particles with a mean diameter of 1.3 mm. A few experiments, however, were run using two different types of 3 mm diameter glass spheres. One set of the 3 mm glass spheres was much more uniformly shaped and spherical than the other. The particles are considered massive enough so that interstitial fluid effects on the bed can be considered negligible (refer to appendix I).

A typical experiment proceeded as follows. At a given frequency, f, data were obtained for acceleration amplitude levels, $\Gamma = a\omega^2/g$, between zero and the maximum limit of the shaker (roughly $\Gamma = 7.0$). Both the acceleration amplitude and frequency were determined from the accelerometer output signal. Using a strobe lamp, the motion of the particle mass was observed at various phase angles while spatial measurements were made using a grid taped to the outside of the rear wall of the box. Measurements of the bed's time of flight (the time between successive collisions with the base) were collected using the output from the accelerometer signal. The collisions between the particle bed and the steel base produced a narrow band of high frequency noise in the accelerometer output that could be isolated using a high pass filter. The time between the successive peaks in the filtered signal corresponded with the flight time of the bed.

2.2 Simulations

The soft particle method was employed to study the phenomena discussed in the previous chapter for several reasons. First, the experiments indicate that most of the particles in the system experience multiple, long duration contacts for at least part of an oscillation cycle. This point rules out the possibility of using a hard particle method. In addition, it was expected that inter-particle forces play an important role in the formation of the phenomena that are observed.

2.2.1 Issues

Although the concept of a soft particle simulation is straightforward, there are several important issues that must be considered. First, the simulation environment must be addressed. This includes whether the simulation is two- or three-dimensional, how many particles will be included in the simulations, what types of forces will be considered, and what boundary conditions are most appropriate. Next, consideration must be given as to how to model the particles and forces and what physical constants should be used. Lastly, the numerical scheme for integrating the equations of motion must be addressed.

Two and Three Dimensional Simulations

Most current simulations model flows in two instead of three dimensions because of the increased number of computations and memory storage required for three-dimensional simulations. Another reason three-dimensional simulations are not more commonly used is because it is not clear that the extra spatial degree of freedom is necessary to reproduce many of the phenomena observed experimentally. A number of two-dimensional simulations of situations such as chute flows (Campbell, 1982), Couette flows (Campbell, 1982), shaking containers (Gallas, 1992 and Taguchi, 1992), hopper flows (Tanaka, *et al.*, 1988), and particle saltation (Werner, 1987) have all produced results that have been observed in real systems.

In situations where particle packing is important, three dimensions may be necessary to obtain results consistent with real systems. Particles can pack more closely in two-dimensions (a maximum solid fraction of 0.91) than in three dimensions (a maximum solid fraction of 0.74). Furthermore, in two dimensions particles are more likely to form the maximum solid fraction packing geometry, a hexagonal close pack arrangement. This results in a higher shear stress required to dilate the material than would be expected in a real system.

Furthermore, the number of contacts a particle can have in 3D is greater than that for 2D. For example, uniform diameter spheres (3D) have a maximum of twelve contacts while uniform diameter circles (2D) can have at most only six contacts. As a result, more energy can be dissipated per particle in 3D systems than in 2D systems. Another effect of the increased number of contacts in 3D systems is that there are an increased number of paths along which forces can be transmitted. This results in an effectively stiffer assembly in 3D systems than in 2D because more force paths will be in parallel in 3D.

The present simulations are all two-dimensional. As will be discussed later, all of the phenomena observed in the experiments are also observed in the simulations. This fact demonstrates that the third spatial dimension is not fundamental to the vibrated bed behaviors despite the effects mentioned above.

Number of Particles

Since the purpose of the simulation is to provide some insight as to how a large assembly of particles behaves, using a sufficient number of particles in the simulation is important. If too few particles are used, the system will not represent a real granular system. However, it is desired to use as few particles as is necessary to model the system in order to minimize computational costs. What constitutes a sufficient number of particles, however, is not clear.

This issue was addressed in the present work by using a number of particles that reproduced the experimentally observed behaviors. This number depended on which behavior was to be studied but was typically on the order of 10^3 particles. Since

the simulations show good visual agreement with the experiments, it is assumed that enough particles are being used.

Particle Properties

For a number of reasons, the most commonly used particle shapes in discrete element simulations are two-dimensional circular disks. First, collisions, or particle overlaps, are easily detected (this is discussed in more detail later) and the location of the contact point during a collision is easily determined. In addition, circular particles are used because the kinetic theories for granular flows assume spherical or circular particles (see, for example, Jenkins and Savage, 1983). In the present work, circular particles best represent the spherical particles used in the experiments.

Other particle shapes such as ellipsoids or polygons have been used in simulations in order to represent more common materials such as sand or grains (see, for example, Ting *et al.* 1993 and Cundall, 1988). Particle asymmetries reduce the likelihood of forming a regular packing structure; however, it also introduces the possibility of particle "interlocking" (Potapov and Campbell, 1995). The result is that the irregularly shaped particles have a higher effective shear resistance than spherical particles. This effect is readily observed when considering the angle of repose of a pile of material. Typically, piles of spherical particles have lower angles of repose than piles of irregular particles.

Another effect of using irregular particles is that it is possible to have particle contacts with lines of action not passing through the centroid of the particle. The resulting moment acting on the particle causes it to rotate. The consequence is that particles orient themselves in preferential configurations resulting in anisotropic behavior of the collection of particles (see, for example, Baxter and Behringer, 1991).

An additional concern with using non-circular particles is that more complicated numerical schemes must be used to determine when contacts have occurred between particles and where the contact is located on the particle surface. A considerable amount of research has been done to produce efficient contact detection algorithms for this purpose (see, for example, Cundall, 1988).

Since the experiments described in the previous chapter use glass spheres as the granular material, the particles in the simulation are modeled as having circular cross-section. Note that instead of simulating circular disks, the simulation models particles as spheres constrained to move in two dimensions. The difference between using disks or spheres appears only in the moment of inertia of the particles. The moment of inertia for a circular disk is $\frac{1}{2}mr^2$ and for a sphere it is $\frac{2}{5}mr^2$ where m is the mass of the particle and r is the particle radius. The result is that spheres rotate more easily than disks. The mass of the particles is also based on that for a sphere, $m = \rho\frac{4}{3}\pi r^3$. As will become apparent when discussing the simulation parameters, the mass and density of the particles can be scaled and will not effect the simulation results since only inter-particle contact and body forces are considered. If forces due to other effects are considered, such as electrostatic or interstitial fluid forces for example, then the mass of the particles could potentially become important because these other forces could significantly affect the momentum of the particle.

Although all of the particles have a circular cross-section, their diameters are not uniform. Instead, the particles in the simulation have a range of diameters that are randomly chosen between a specified minimum and maximum giving a uniform distribution of diameters. By using a distribution of particle sizes, not only does the simulation reflect the variety of particle sizes in the experiments, but the likelihood of forming a hexagonal packing structure is reduced.

Forces

One particular advantage of soft particle simulations is that many types of forces can be simulated to act on a particle: a feature not possible with hard particle simulations. These forces are generally classified as either body or contact forces. Body forces typically act on all particles in the flow. Examples include forces due to gravitational and electromagnetic fields. Contact forces, however, act only when particles are in contact (or are in contact with a boundary). Examples of these forces include tractions due to contacting surfaces and cohesive forces. Interstitial fluid forces are a third type of force that can be included in the soft particle simulations.

The present simulation includes only a gravity body force and particle-particle and particle-boundary contact forces. No electromagnetic, interstitial fluid, or cohesive forces were included. This model is, in effect, simulating a dry, massive granular material in a gravity field and a vacuum.

The gravitational body force acts on all particles in the system. The force acting on particle i due to gravity, $\vec{F}_{gi}$, acts at the particle's centroid and is given by

$$\vec{F}_{gi} = m_i \vec{g} \tag{2.1}$$

where m_i is the mass of particle i and $\vec{g}$ is the gravitational acceleration vector.

Unlike the gravitational body force, the particle contact forces only occur during collisions; a condition that, in simulations, occurs when particles penetrate or overlap. For circular particles, overlap occurs when

$$\Delta_{ij} = (r_j + r_i) - |\vec{x}_j - \vec{x}_i| \geq 0 \tag{2.2}$$

where Δ_{ij} is the amount of overlap between particles i and j, r a particle radius, and $\vec{x}$ the position vector for the particle center. The amount of overlap allowed in the simulations is usually small, typically limited to 1% of the smallest particle radius. The particle overlap is kept small since excluded volume effects become important when the overlap is too large (Campbell, 1986). During a collision, particles are considered rigid and do not deform. In real collisions, however, particle deformations do occur and consist of an elastic and plastic regime (Goldsmith, 1960). For most particle contacts the size of the deformation is much smaller than the particle size and so the approximation that particles remain rigid is assumed. An important consequence of the plastic deformation is that energy is lost during the collision. This effect is explicitly accounted for in the simulation by including a dissipative mechanism in the collision model.

The particle contact force is separated into a normal and tangential component. The normal component acts along a line connecting the center of particle i to the

center of particle j with a normal unit vector, $\hat{n}_{ij}$, given by,

$$\hat{n}_{ij} = \frac{\vec{x}_j - \vec{x}_i}{|\vec{x}_j - \vec{x}_i|} \tag{2.3}$$

The tangential unit vector, $\hat{s}_{ij}$ is rotated 90 degrees from the normal component such that $\hat{n}_{ij} \times \hat{s}_{ij} = \hat{k}$ where $\hat{k}$ is the direction of the third dimension. Figure 2.2 shows these coordinates.

The normal contact between two particles is modeled as a linear spring in parallel with a dashpot element (see figure 2.3a). This model was first used in simulations by Cundall and Strack (1979) and remains the most common form of contact model. The spring provides an elastic restoration force while the dashpot dissipates energy during the contact. The result is a collision with an effective coefficient of restitution less than one. The force acting on particle i due to particle j in the normal direction, $\vec{F}_{nij}$, is given by,

$$\vec{F}_{nij} = (-k_n \Delta_{ij} + \nu_n \dot{\delta\vec{x}}_{ij} \cdot \hat{n})\hat{n} \tag{2.4}$$

where k_n and ν_n are the normal spring constant and normal dashpot coefficient and Δ_{ij} is the amount of overlap between the particles (see equation 2.2). A more in-depth discussion of the constants will be given in a following section. The relative velocity of particle j with respect to particle i at the point of contact, $\dot{\delta\vec{x}}_{ij}$, is given by

$$\dot{\delta\vec{x}}_{ij} = \dot{\vec{x}}_j - \dot{\vec{x}}_i - (\dot{\theta}_j r_j + \dot{\theta}_i r_i)\hat{s}_{ij} \tag{2.5}$$

where $\dot{\vec{x}}$ is the translational velocity of the particle center and $\dot{\theta}$ is the rotational velocity of the particle.

The tangential contact model is slightly more complicated than the normal contact model. The tangential model consists of a spring in series with a Coulombic friction sliding element (refer to figure 2.3b). The spring allows the particle to respond elastically while the sliding friction element allows particles to slide against each other. The magnitude of the tangential force is limited by the sliding element. This simple model captures important features exhibited in more complicated theories describing

the micromechanics of collisions (see, for example, Maw *et al.*, 1976). For example, when a spherical particle collides with a wall, the region of contact may be sticking, sliding, or may involve both simultaneously. Typically at low impact incidence angles the region of contact sticks throughout most of the duration of the collision until the very end when the contact transitions to sliding. For larger incidence angles the contacts starts with sliding then transitions to sticking and then back to sliding. At very large incidence angles the contact slides throughout the duration of impact. The simple model proposed above behaves in much the same way.

The interaction between the spring and the frictional slider has some subtleties. First, the tangential force due to the spring is examined. The tangential spring force acting on a particle i due to a particle j, $\vec{F}_{s,spring}$, is given by,

$$\vec{F}_{s,spring} = (k_s \delta s_{ij})\hat{s}_{ij} \tag{2.6}$$

where k_s is the tangential spring constant. The quantity δs_{ij} is a measure of the tangential displacement between the initial contact points and is given by,

$$\delta s_{ij}(t) = \int_{t_0}^{t} (\delta \dot{\vec{x}}_{ij} \cdot \hat{s}_{ij}) dt' \tag{2.7}$$

where t denotes time and t_0 is the initial value of the spring extension ($\delta s_{ij}(0) = 0$).

The contact model, however, is more complicated when the sliding friction element is considered. When the magnitude of the spring force exceeds the magnitude of the friction sliding force, $|\vec{F}_{s,friction}| = \mu |\vec{F}_{nij}| < |\vec{F}_{s,spring}|$, the sliding friction element becomes active and the force applied to the particle is

$$\vec{F}_{s,friction} = \mu |\vec{F}_{nij}| \frac{\vec{F}_{s,spring}}{|\vec{F}_{s,spring}|} \tag{2.8}$$

This force is implemented by changing the tangential spring extension (or tangential displacement), δs_{ij}, to give a spring force equal to the sliding friction force,

$$\delta s_{ij}(t) = \mu |\vec{F}_{nij}| / k_s \tag{2.9}$$

Thus the tangential force, when sliding friction is active, has a magnitude of $\mu|\vec{F}_{nij}|$ and acts in the same direction as the spring force. Furthermore, the spring extension, δs_{ij}, is changed in order to give the magnitude of the sliding friction force. If the spring element becomes active once again, $|k_s \delta s_{ij}| < \mu|\vec{F}_{nij}|$, the initial value of the tangential displacement, $\delta s_{ij}(t_0)$ will be given by equation 2.9.

Real particle contact dynamics are more complicated than what the simple models given above propose. A number of other, more detailed, contact models have been suggested in order to model real contacts more accurately (see, for example, Walton, 1992, Sadd *et al.*, 1993, and Langston *et al.*, 1994). It is not clear, however, how accurate the contact models need to be to give results similar to real systems. Certainly the level of detail included in all of the current contact models is still far from what occurs in real systems. The important aspect of modeling the contacts is to include the important physics relevant to the problem at hand. For example, if wave propagation through a system of particles is to be studied, models which include the effects of surface asperities may be required. For studying the present experiment, the important physical behaviors were expected to be the vibration dynamics, the system granularity (the discreteness of the particulate system), and the energy dissipation in the particle contacts. These features are inherent in the simple models proposed.

Equations of Motion

After the forces on the particles have been determined, the acceleration of each particle in the system is found using Newton's second law. The new particle states are then determined by integrating the particle accelerations in time to give new velocities and positions. For a particle, i, the equations of motion are given by

$$m_i \ddot{\vec{x}}_i = \vec{F}_{gi} + \sum_{j=1, j\neq i}^{N} \vec{F}_{cij} \tag{2.10}$$

$$I_i \ddot{\vec{\theta}}_i = \sum_{j=1, j\neq i}^{N} (\vec{r}_i \times \vec{F}_{cij}) \tag{2.11}$$

where $\vec{x}$ and $\vec{\theta}$ are the translational and rotational position of particle i, N the number of particles in the simulation, m_i and I_i the particle mass and rotational moment of inertia, $\vec{F}_{gi}$ the gravitational force acting on particle i, $\vec{F}_{cji}$ the contact force due to particle j ($\vec{F}_{cji} = \vec{0}$ if the particles are not in contact), and $\vec{r}_i$ a vector directed from the center of particle i to the location of the contact force.

The particle velocities and positions are determined by integrating in time,

$$\begin{aligned} \dot{\vec{x}}_i &= \int \ddot{\vec{x}}_i dt, \quad \dot{\vec{\theta}}_i = \int \ddot{\vec{\theta}}_i dt \\ \vec{x}_i &= \int \dot{\vec{x}}_i dt, \quad \vec{\theta}_i = \int \dot{\vec{\theta}}_i dt \end{aligned} \tag{2.12}$$

A center-difference (also known as a leap-frog) scheme, a method that is often used in soft-particle simulations (Cundall and Strack, 1979 and Walton, 1992), was used to numerically integrate the equations. The center-difference scheme is given by,

$$\begin{aligned} \dot{x}_{n+\frac{1}{2}} &= \dot{x}_{n-\frac{1}{2}} + \Delta t \ddot{x}_{n-1} \\ x_{n+1} &= x_{n-1} + \Delta t \dot{x}_{n+\frac{1}{2}} \end{aligned} \tag{2.13}$$

Predictor-corrector numerical integration routines are also common (Werner, 1987 and Gallas *et al.*, 1992); however, this type of scheme is better suited for very smooth differential equations instead of the discontinuous functions found in these simulations (Press, 1992).

Simulation Parameters

The parameters used in the simulation must also be addressed. These parameters can be classified into two categories according to the method in which they are chosen. The first category is for parameters that are taken directly from the experiments while the second is for parameters that are based on the force contact models.

The simulation parameters that are taken directly from the experiments include the gravitational acceleration, $\vec{g}$, vibration cyclic frequency, $f = \omega/(2\pi)$, dimensionless vibration acceleration amplitude, $\Gamma = a\omega^2/|\vec{g}|$, dimensionless container width, W/d, dimensionless bed depth, h_0/d, mean particle diameter, d, particle density, ρ,

particle/particle coefficient of restitution, ϵ_{pp}, particle/wall coefficient of restitution, ϵ_{pw}, particle/particle sliding friction coefficient, μ_{pp}, and particle/wall sliding friction coefficient, μ_{pw}.

The values for the vibration frequencies, accelerations, container widths, and bed depths are similar to what were used in the experiments. Similarly, the mean particle diameter and density are based on 1 mm diameter soda lime glass spheres ($\rho = 2500$ kg/m^3), used in the experiments. The mass, $m = \rho\frac{4}{3}\pi(\frac{d}{2})^3$, and moment of inertia, $I = \frac{2}{5}m(\frac{d}{2})^2$, of each particle are determined assuming they are spherical. Furthermore, the particles in the simulated system have a uniform distribution of particle diameters between a specified minimum and maximum value. These bounding diameters were chosen to give a maximum diameter variation of at most, 10% of the mean value, corresponding to 0.9 mm and 1.1 mm for the 1 mm particles. Measurements of the particles in the experiments indicate that the actual distribution is Gaussian; however, this discrepancy between the simulation and experiment was not expected to cause significantly different results.

The values for coefficients of restitution, ϵ_{pp} and ϵ_{pw}, and sliding friction coefficient, μ_{pp} and μ_{pw}, were also based on experimental values; however, a range of values were used. The baseline value for both ϵ_{pp} and ϵ_{pw} is 0.8. This value is lower than the experimental values for these parameters which are $\epsilon_{pp} = 0.97$ for two colliding 3 mm glass spheres and $\epsilon_{pw} = 0.83$ for a 3 mm glass sphere colliding with a thick aluminum base (Foerster *et al.*, 1994). The reason for a lower value of ϵ is because less energy is dissipated per particle in 2D systems than in 3D systems due to the decreased number of particle contacts in 2D. The sliding friction parameter, μ, also had a range of values varying from frictionless particles, $\mu = 0.0$, to highly frictional particles, $\mu = 1.0$. A typical experimental value for μ between two 3 mm glass particles is 0.01 while μ for a 3 mm glass sphere and an aluminum wall is 0.13 (Foerster *et al.*, 1994).

The set of parameters that are based on the contact model described previously include the normal particle/particle (particle/wall) spring constant, $k_{n,pp}$ ($k_{n,pw}$), normal particle/particle (particle/wall) dashpot coefficient, $\nu_{n,pp}$ ($\nu_{n,pw}$), tangential particle/particle (particle/wall) spring constant, $k_{s,pp}$, ($k_{s,pw}$), and the simulation time

step, Δt.

The normal spring constants, $k_{n,pp}$ and $k_{n,pw}$, are determined from the maximum allowable overlap between particles (or a particle and a wall), Δ_{max}, based on an assumed maximum relative impact velocity, $\dot{\delta\vec{x}}_{max,ij}$, particle mass, m, and coefficient of restitution, ϵ.

For the damped linear spring model, the maximum overlap of a two particle collision is given by

$$\Delta_{max} = (\dot{\delta\vec{x}}_{max,ij} \cdot \hat{n}_{ij})\sqrt{\frac{m^*}{k_n}}(\exp\frac{\arctan -\alpha}{\alpha}) \tag{2.14}$$

where $\alpha = \pi/\ln\epsilon$ and $m^* = m_i m_j/(m_i + m_j)$. If particle i collides with a wall, $m^* = m_i$, since $m_j \to \infty$.

Rearranging equation 2.14,

$$\frac{k_n}{m^*} = \left(\frac{(\dot{\vec{x}}_{max,ij} \cdot \hat{n}_{ij})/r}{(\Delta_{max}/r)}\right)^2 (\exp\frac{\arctan -\alpha}{\alpha})^2 \tag{2.15}$$

The value of k_n/m^* is important since the collision duration time, τ, is given by

$$\tau = \frac{\pi}{\sqrt{(\frac{k_n}{m^*})(1 + \frac{1}{\alpha^2})}} \tag{2.16}$$

If a very large k_n/m^* is used, the collision duration, τ, will be small and the time step for the simulation, Δt, which is a fraction of τ, will also be small. Thus, a smaller value of k_n/m^* is most desirable since the resulting simulation time step will be larger and the simulation will proceed more rapidly. If the spring constant is too small, however, particles can overlap significantly and affect the measured material transport properties. Walton (cited by Campbell, 1986) suggests that the maximum overlap should be less than 1% of the particle radius at high solid fractions.

The normal spring constant could also be chosen such that the collision duration is similar in magnitude to the Young's modulus of the particle material. Another option is to choose the spring constant such that the propagation of disturbances in

the system is similar to real sonic speeds. In both of these cases, the magnitude of the spring constant is large and the resulting time step for the simulation is very small, for example, on the order of $1 * 10^{-7}$ seconds. As a result, these choices for the spring constant are not commonly used except in simulations where sound propagation modeling is considered.

When a collision occurs between particles, energy is lost due to plastic deformation. The inelasticity of the collision is typically quantified by a coefficient of restitution, ϵ, defined as the ratio of the relative velocity after the collision divided by the relative velocity just prior to the collision. Analysis shows that the damped spring model gives a constant coefficient of restitution. The effective normal coefficient of restitution for a two particle collision is given by

$$\epsilon = \exp\left(\frac{\pi}{\left(\frac{4(k_n/m^*)}{(\nu_n/m^*)^2} - 1\right)^{1/2}}\right) \tag{2.17}$$

Note that the spring/dashpot system is assumed underdamped ($\frac{4m^*k}{\nu^2} > 1$) since if the system was critically damped or overdamped, ϵ would be zero and the collision would be completely inelastic.

In real collisions the coefficient of restitution decreases with increasing collision velocity (Goldsmith, 1960 and Sondergaard *et al.*, 1990). If the relative impact velocities in the system of particles have similar magnitudes, the assumption of a constant coefficient of restitution should be valid.

Rearranging equation 2.17 gives an expression for the dashpot coefficient, ν_n, based on the spring constant, k_n, and coefficient of restitution, ϵ

$$\frac{\nu_n}{m^*} = \sqrt{\frac{4\frac{k_n}{m^{*2}}}{1+\alpha^2}} \tag{2.18}$$

Thus the dashpot coefficient is determined by the choice of spring constant and coefficient of restitution.

For the tangential spring constant, Cundall and Strack (1979) recommend that

$$\frac{2}{3} \leq \frac{k_s}{k_n} \leq 1 \tag{2.19}$$

based on Mindlin and Deresiewicz's (1961) analytical models of tangential contacts. Cundall and Strack (1979) found that for small values of μ the ratio k_s/k_n did not change the behavior of the simulated system because the tangential behavior was governed almost immediately by sliding friction. However as μ is increased, the damped spring element is active for a longer duration and so the ratio k_s/k_n becomes more important. All of the present simulations use $k_s/k_n = 1$.

The simulation time step, Δt, was chosen such that the highest frequency in the system (corresponding to the smallest period), could be integrated accurately. The highest frequency in a system consisting of identical spheres constrained to move in 2D is for a particle in contact with six other particles. Assuming that the surrounding particles are fixed in space, the translational period of oscillation, τ_{trans}, for the particles is,

$$\tau_{trans} = 2\pi\sqrt{\frac{m}{3k_n + 3k_s}} \tag{2.20}$$

The rotational period for the particle, τ_{rot}, is

$$\tau_{rot} = 2\pi\sqrt{\frac{I}{6k_s r^2}} \tag{2.21}$$

When $k_s/k_n = 1$ and $I = \frac{2}{5}mr^2$, $\tau_{rot} = \sqrt{\frac{2}{5}}\tau_{trans}$. Thus, the smallest period in the system is given by τ_{rot}. The simulation time step is chosen to be approximately one-tenth this period in order to ensure integration stability and accuracy.

Boundary Conditions

In addition to modeling how particles interact with one another, the simulation must also address what types of boundaries are to be used. In the present simulation, two types of boundary conditions are implemented: wall and periodic boundaries. The wall boundaries consist of smooth, but frictional, walls (particles are not "glued" to

the walls) that have prescribed positions and velocities. This simulates the use of massive smooth walls. The boundaries move, in-phase, in the vertical direction with a sinusoidal displacement and velocity.

Lateral periodic boundaries are also used in the present simulations. These boundaries are implemented by reflecting the workspace control volume to either side of the workspace (refer to Campbell, 1982). This approach eliminates any effects which may be due to the lateral wall boundaries.

Initial Conditions

Soft particle simulations are deterministic. If the same parameters and the same initial conditions are used, the simulation will give the same results each time it is run. In order to ensure that the observations made in one particular simulation are not unique to the initial conditions, several runs were made with different initial conditions.

Particles are placed in the workspace in prescribed positions but with random initial velocities which are chosen to be between a specified minimum and maximum velocity. In all of the simulations, the behavior of the particle bed after several seconds was the same despite the initial conditions of the particles. In order to ensure the initial conditions were not influencing any of the measurements made in the simulations, measurements were made only after one second of simulation time had elapsed (on the order of 10^5 time steps).

2.2.2 Implementation

The simulation code is written in *C* and is divided into several logical subroutines. Figure 2.4 shows the flow of the simulation. First the particle and environment data is read from an input file and then the particle initial conditions are determined. After these preliminary routines are called, the main loop of the simulation is begun. First the forces acting on each particle in the system are determined based on the contact models described in the previous section. After this force subroutine is finished,

the particle equations of state are integrated using a center-difference method. Next, appropriate measurements are made and particle states are recorded to an output file. This loop repeats until an ending condition, usually based on a maximum allowable time, is achieved.

The coding for the simulation is straightforward and is not discussed in detail here (a copy of the simulation code is given in appendix III). One computational technique that is used to increase the speed of the simulation, however, is examined. Since much of the computational cost in soft particle simulations comes from checking whether particles have collided, an efficient method for determining contacts is imperative. Checking to see whether each particle has collided with every other particle is a time-consuming process. In order to reduce the number of collision checks for each particle, a neighboring-cell technique is implemented in the present simulation. This technique works as follows. The workspace is divided into an array of square cells with the length of a side being just greater than the largest particle diameter in the system. Each cell is a *C* pointer that points to a particle with its center located in that particular cell. All other particles in the cell are linked together using a double-linked list of pointers. This use of double-linked lists allows particles to be easily included and removed from cells as particles pass through them. The advantage of monitoring the cells in which the particles are located is that a given particle only needs to check for collisions with particles in the current cell and neighboring cells. Checks do not need to be made with particles located in cells far from the current cell. Although there is an increase in the computational cost of the cell book-keeping, the overall speed of the simulation is increased, especially when the simulation involves many particles. Other techniques for reducing the number of contact checks exist, however; this method is straightforward, easily implemented, and robust.

All of the simulations were run on one of the following machines: a Sun Sparcstation 20 with two 50 MHz processors, a Sun Sparcstation 5 with a single 110 MHz processor, a PC with a Pentium 90 MHz processor (using the Linux operating system), and an IBM RISC 6000. Table 2.2 shows the CPU time required for a benchmark simulation to run on each of these machines. The benchmark simulation parameters

are given in table 2.3.

Tables and Figures

Experiment No.	Bead Mass [gm.]	Lid Mass [gm.]
1	250	3.44
2	125	3.44
3	125	7.17
4	375	3.44
5	125	17.06
6	625	3.44
7	45	3.51
8	125	28.14

Table 2.1: Bead and lid masses for the various shallow bed expansion experiments.

Machine	CPU time [hrs]
Sparc 20 (50 MHz)	8.1
Sparc 5 (100 MHz)	6.6
IBM RISC 6000	8.9
Pentium (90 MHz)	8.0

Table 2.2: The CPU time for a benchmark simulation to run on various computer systems. The benchmark simulation uses the parameters given in table 2.3.

N	1000
Γ	2.0
f	20.0 Hz
number of cycles	60 cycles
W/d	100
ϵ_{pp}	0.80
$k_{n,pp}$	$5.289 * 10^3$ N/m
ν_{pp}	$8.337 * 10^{-3}$ N/(m/s)
$k_{s,pp}$	$5.289 * 10^3$ N/m
μ_{pp}	0.1
lateral boundaries	walls
$k_{n,pw}$	$1.058 * 10^4$ N/m
ν_{pw}	$1.667 * 10^{-2}$ N/(m/s)
$k_{s,pw}$	$1.058 * 10^3$ N/m
μ_{pw}	0.1
d	0.9 - 1.1 mm
ρ	2500 kg/m^3
Δt	$2.552 * 10^{-6}$ sec

Table 2.3: The simulation parameters used in the benchmark simulation.

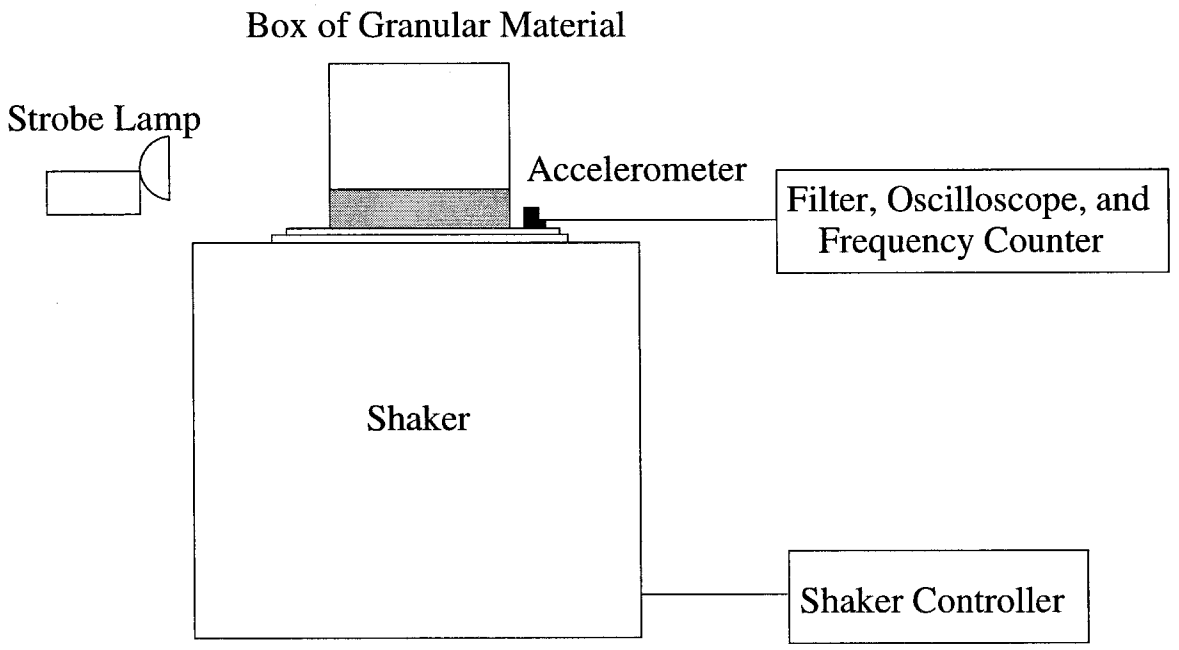

Figure 2.1: The experimental apparatus used in the deep bed experiments. Note that the precise experimental set-up differs for the shallow bed experiments but the concept remains the same.

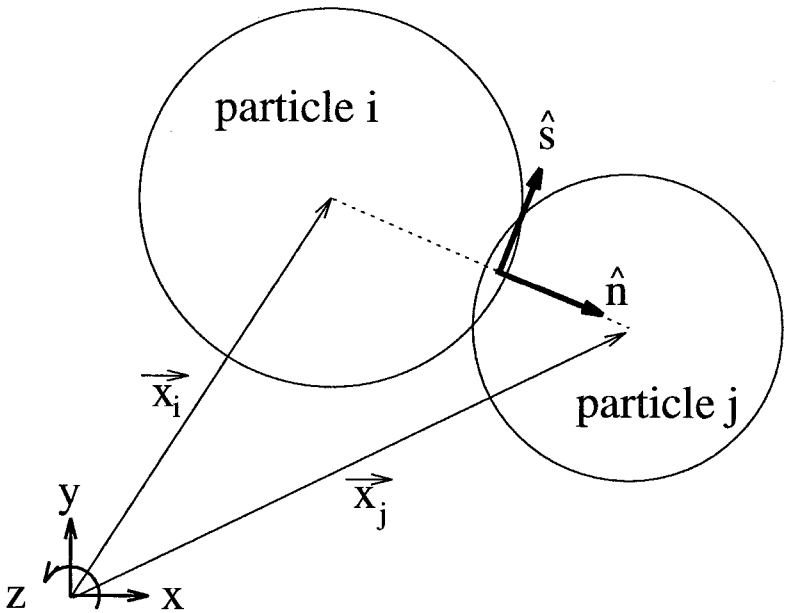

Figure 2.2: The coordinate system used in the simulations.

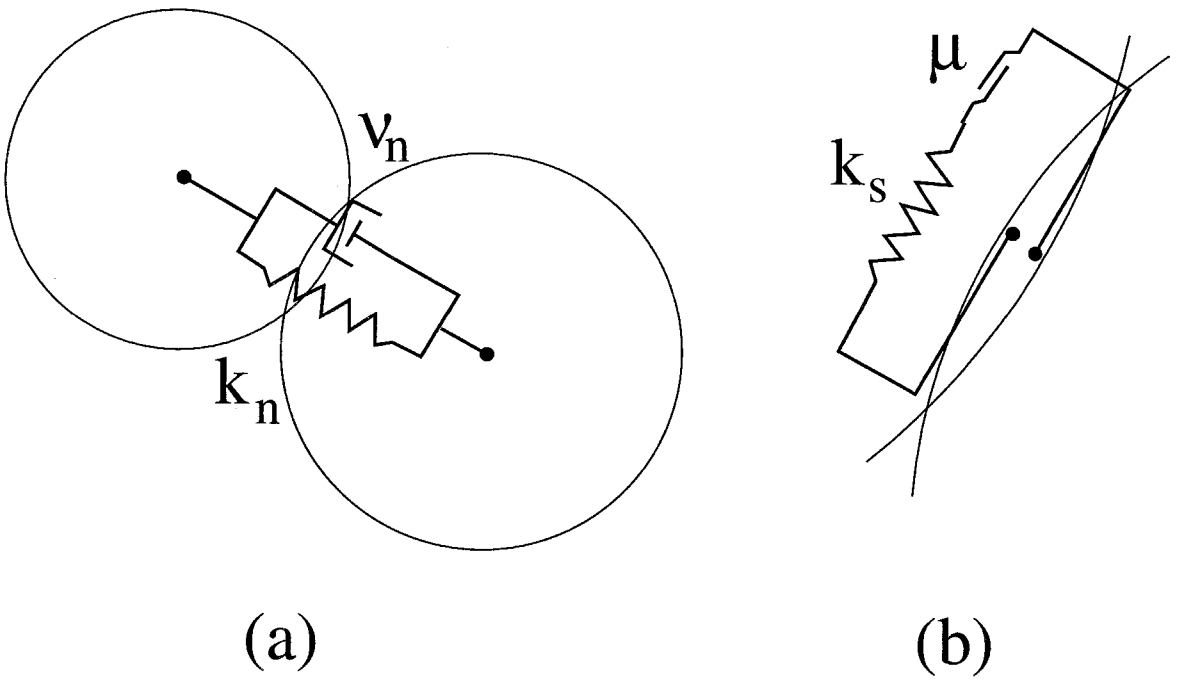

Figure 2.3: The simulation contact model in the (a) normal direction and (b) the tangential direction.

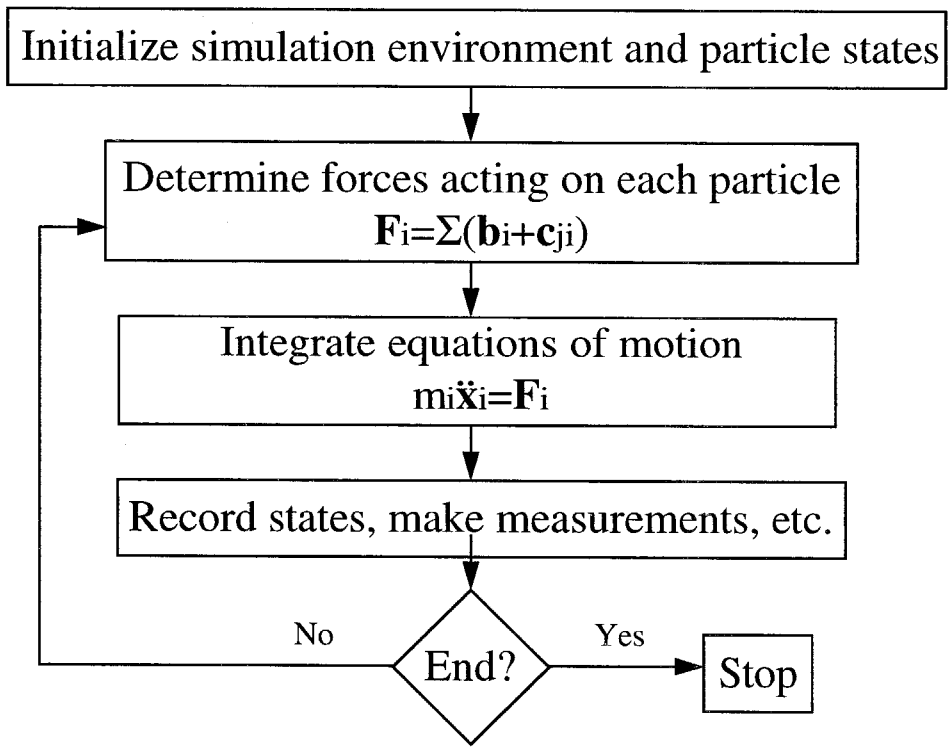

Figure 2.4: The simulation flow chart.

Chapter 3 Phase Map

3.1 Experiments

Two distinct regimes of bed behavior are observed in the experiments depending upon the dimensionless bed depth, h_0/d. For $h_0/d < 6$, particles bounce around randomly in the container and little coherent motion is observed. This fluidized regime is the shallow bed state. The deep bed state occurs when $h_0/d > 6$ and is characterized by coherent particle motion where the bed of material moves as a single, plastic mass.

In the shallow bed regime, three states, similar to those described by Thomas *et al.* (1989), were observed depending on the dimensionless acceleration amplitude of the vibrations, $\Gamma = a\omega^2/g$, where a is the vibration amplitude, ω the vibration radian frequency ($\omega = 2\pi f$), and g the gravitational acceleration, and the dimensionless bed depth, h_0/d. These states are called the "Newtonian-I," "Newtonian-II," and "coherent-expanded" regimes and are differentiated by the degree of coherency in the bed motion. The "Newtonian-I" state is characterized by energetic, random particle motions such that the vertical density of particles changes little over an oscillation cycle. Thomas *et al.* reported that this state occurs for small bed depths and large accelerations. For slightly deeper beds or at lower accelerations, a "Newtonian-II" state appears. This regime also has considerable random particle but during part of the oscillation cycle particles form a dense band near the base. At even larger h_0/d or lower Γ, a transition to a "coherent-expanded" state occurs. In this state the bed of particles oscillate en masse but the mass expands and contracts considerably throughout the vibration cycle. The transition to the deep bed regime (Thomas *et al.* refer to this as the "coherent-condensed" state), occurs at even deeper bed depths or lower accelerations. The transitions between the two Newtonian and the coherent-expanded states are gradual but the transition from the coherent-expanded state to the deep bed state is sudden and repeatable.

Thomas *et al.* (1989) reported that the transition from the coherent-expanded state to the coherent-condensed, or deep bed, state was sudden and repeatable for large particles. Bachmann (1940) reported this transition occurring at approximately $h_0/d = 6$ for glass spheres. The transition in the present experiments with all three types of particles was found to also occur when $h_0/d \approx 6$ for $\Gamma \approx 2.0$. Prior to the transition, the particle bed, expands and contracts considerably throughout an oscillation cycle. After the transition, however, the change in the bed density over an oscillation cycle is much smaller.

The response of deep particle beds is much different than what was observed for shallow beds. In the deep bed regime, phenomena such as convection cells, heaps, surface waves, and kinks are observed depending on the dimensionless acceleration amplitude of the oscillations, Γ, and the dimensionless bed depth, h_0/d. Although each of these behaviors is discussed in detail in the following chapters, a brief description of each follows as an introduction.

For acceleration amplitude levels greater than $1g$, convection cells appear in the bed. Particles move down in a boundary layer along the vertical walls of the container, re-circulate within the bulk of the granular bed to the free surface, and then avalanche toward the walls to repeat the cycle. Figure 3.1 shows an illustration of the convection cell motion for a vertical slice through a granular bed.

The heaping behavior is characterized by a mound of material that forms in the container as shown in figure 3.2. For sufficiently large particles (typically $d > 1$ mm) the mound is rounded in appearance with the lowest points occurring at the wall boundaries and the highest point located in the center of the bed. When smaller particles are used (for example, $d = 0.1$ mm), a sharp peak is reported to form in place of the rounded mound (refer to Pak *et al.*, 1995).

Another phenomena that appears in vibrated deep beds are surface waves. Two regimes of standing waves appear for different values of the acceleration amplitude, Γ, and they differ in both formation frequency and in shape. In the first regime, the waves, referred to as $f/2$ waves, form with a frequency that is one-half the forcing frequency. The waves in this regime typically have smooth, rounded peaks. The second

regime of waves, known as $f/4$ waves, appears with a frequency that is one-quarter the forcing frequency. These waves have a sharper, cusp-shaped peaks. Figures 3.3 and 3.4 are photographs of the $f/2$ and $f/4$ waves, respectively.

For acceleration amplitudes greater than $\Gamma \approx 3.6$, "kinks" are observed in the particle bed. A kink is defined as a region of the particle bed between two sections that oscillate out-of-phase with each other. The resulting bed motion appears as if arches form and collapse in time. Figure 3.5 shows a photograph of a granular bed with three kinks.

Bracketing each kink are a pair of counter-rotating convection cells. The orientation of the convection cells is such that particles move down at the kink and up to the free surface just to either side of it. An illustration of the particle streamlines for a bed with three kinks is shown in figure 3.6.

As mentioned previously, the appearance of the various phenomena depends on two parameters, the acceleration amplitude of the oscillations, Γ, and the depth of the particle bed, h_0/d. The frequency of the forcing oscillations did not significantly affect the onset of the phenomena for the range of frequencies examined here (between 15 and 40 Hz).

Using the 1.3 mm particles and operating at 20 Hz, a phase diagram was constructed showing when the various behaviors appear as a function of Γ and h_0/d (refer to figure 3.7). When using the 3 mm particles, the transitions between phenomena occurred at lower values of Γ. The general trends, however, remained the same.

The mapping procedure was performed in the following manner. The container was filled with granular material to a prescribed h_0/d and the frequency of the oscillations was set to a fixed value (here, f=20 Hz). The vibration amplitude was increased in increments corresponding to $\Gamma = 0.2$ from zero to an amplitude such that $\Gamma \approx 7$ and then back to zero. Little hysteresis is observed in the transitions from one phenomena to the other. At each value of Γ, the bed was observed both in ordinary lighting conditions and with the strobe lamp in order to observe whether waves appeared. The output signal from the accelerometer was also examined to determine

the flight time of the bed. This procedure was repeated for several values of h_0/d.

Below $1g$, there is no sustained bulk movement of particles within the bed. Particles are observed to occasionally fall into neighboring voids resulting in an increase in the bulk density of the bed (see, for example, Ben-Naim *et al.*, 1996).

When the acceleration level is greater than approximately $1.2g$ (for all h_0/d), particles move down along the vertical walls of the container in the side wall convection cell pattern described previously. For Γ close to 1.2, the particle velocity is small and it is necessary to observe the evolution of the bed over a long period in order to discern the convective motion. This convection behavior appears for all $\Gamma > 1.2$ with the particle velocities increasing as Γ increases. The heaping or mounding behavior also appears when $\Gamma > 1.2$. Unlike the convection cells, however, the mounds observed in these experiments no longer appear when $\Gamma > 2.0$.

At $\Gamma \approx 2.0$ (for all h_0/d) the first set of standing surface waves, the $f/2$ waves, appears. The onset of these waves was difficult to determine precisely since the waves have small amplitudes at low acceleration amplitudes. The wave amplitude increases with increasing Γ, however, making the observation of these waves easier at larger acceleration levels. The side wall convection behavior persists along the container walls and does not interfere significantly with the wave formation.

The $f/2$ waves continue to form as Γ increases until a period doubling bifurcation in the flight time of the bed occurs. For $\Gamma < \Gamma_1'$, where Γ_1' is the value of the acceleration amplitude when the bifurcation occurs, the particle bed collides with the container base after a flight time, Δt, that is less than the period of the forcing oscillations, T. At a fixed Γ, this flight time does not vary from cycle to cycle and so the bulk motion of the bed repeats every oscillation cycle. For $\Gamma > \Gamma_1'$, however, two flight times are observed, Δt_1 and Δt_2, where $\Delta t_1 > T$, $\Delta t_2 < T$ and $\Delta t_1 + \Delta t_2 < 2T$. As a result, the bed motion repeats every two oscillation cycles, hence the term period doubling. As Γ increases, the first flight time, Δt_1, increases while the second flight time, Δt_2 decreases until a single flight time that is greater than the forcing oscillation remains. This second transition occurs at Γ_1^*. The period doubling and flight time behavior was observed by examining the accelerometer output signal as described in

section 2.1.

The critical acceleration amplitude, Γ_1', decreases with increasing bed depth. For example, when $h_0/d = 10$, $\Gamma_1' = 4.2$, but when $h_0/d = 40$, Γ_1' is 3.0. For $\Gamma > \Gamma_1'$, waves would occasionally appear on the free surface of the bed, however, they formed aperiodically and were often "smeared" due to fluidized particle motion on the free surface.

For $\Gamma > \Gamma_1'$ to at least $\Gamma = 7.0$, kinks and their associated convection cells are observed. Although a kink may not actually form after the bifurcation, it has the potential to appear. The period doubling bifurcation is a necessary condition for the formation of kinks, however, it is not a sufficient one. This point is discussed later in chapter 7. When kinks did form, the side wall convection pattern observed for $\Gamma > 1$ disappeared in the region neighboring the kink. The convection cells associated with the kink were stronger than the side wall convection pattern and were the dominant particle motion.

The second set of standing surface waves, the $f/4$ waves, appear for Γ greater than approximately Γ_1^*, the Γ at which the flight time of the bed returns to a single flight time after the bifurcation, and persist to at least $\Gamma = 7.0$. The value of Γ_1^* decreases as h_0/d increases; similar to what was observed for Γ_1'. The difference between the two, $\Gamma_1^* - \Gamma_1'$, remains nearly constant, however.

The onset of $f/4$ waves is much easier to determine than for the $f/2$ waves since the $f/4$ waves have much larger peaks. Additionally, kinks and $f/4$ were observed to occur simultaneously in the same particle bed. The $f/4$ waves, though, only appeared in regions of the particle bed not strongly influenced by the kinks.

3.2 Simulations

A similar deep bed phase map was constructed using the simulations. In order to determine when the behaviors appeared, a fundamental property of each phenomenon was measured in the simulation. A visual observation was also made as an added check.

The downward particle movement at the vertical walls of the container is used as an indicator for side wall convection. The procedure for determining this quantity is as follows. First, the simulation workspace (the container) is divided into a grid of squares with a side length of just greater than a particle diameter. The mass-averaged particle displacement per cycle for each square, or cell, over an oscillation cycle is determined by

$$\Delta\vec{x}_{(i,j),c} = \frac{1}{M_{(i,j)}} \sum_{n=1}^{n=N_{(i,j)}} m_n(\vec{x}_{n,c} - \vec{x}_{n,c-1}) \tag{3.1}$$

where (i,j) refers to a particular cell, c is the oscillation cycle, $\Delta\vec{x}_{(i,j),c}$ the mass-averaged particle displacement for cell (i,j) from cycle $c-1$ to cycle c (at the same phase angle), $M_{(i,j)}$ the total mass of particles in cell (i,j), $N_{(i,j)}$ the number of particles with centers located in cell (i,j), m_n the mass of particle n, and $\vec{x}$ the particle's position vector. In order to determine the mean motion over several oscillation cycles, the displacements are averaged over many cycles,

$$\overline{\Delta\vec{x}_{(i,j)}} = \frac{1}{C-1} \sum_{c=2}^{c=C} \Delta\vec{x}_{(i,j),c} \tag{3.2}$$

where C is the total number of oscillation cycles. This displacement quantity can be thought of as a long term velocity.

For the side wall convection behavior, only the cells next to the walls are considered. The average vertical displacement over one cycle at the walls, Δy_w, is found by

$$\Delta y_w = \frac{1}{N_w} \sum_{n=1}^{n=N_w} (\overline{\Delta\vec{x}_n} \cdot \hat{j}) \tag{3.3}$$

where N_w is the number of cells bordering the walls, and $\hat{j}$ is the unit vector in the vertical direction. When Δy_w is less than zero there is a net flow of particles down along the walls indicating that side wall convection is present.

To determine whether the $f/2$ or $f/4$ waves occur, the frequency spectra of the average vertical and horizontal particle velocities are examined for various regions of

the bed. The average velocities are determined in a manner similar to the method described above. The workspace is divided into bins extending in the vertical direction with a horizontal width of approximately $5d$. The mass averaged particle velocity for a bin, $\overline{\dot{\vec{x}}_b(t)}$, where b refers to a particular bin and t is the time, is found by

$$\overline{\dot{\vec{x}}_b(t)} = \frac{1}{M_b} \sum_{n=1}^{n=N_b} m_n \dot{\vec{x}}_n(t) \tag{3.4}$$

where M_b is the total mass of particles in bin b, N_b the number of particles with their centers in bin b, m_n the mass of particle n, and $\dot{\vec{x}}_{n,b}(t)$ the velocity vector for particle n in bin b at time t. The average velocity is sampled twenty times per oscillation cycle for many cycles and the Fourier spectrum of the velocities is calculated for both velocity components. When $f/2$ waves appear, a large magnitude peak appears in the frequency spectra at one-half the oscillation frequency. Similarly, a peak appears at one-quarter the forcing frequency for the $f/4$ waves. These subharmonic peaks are the result of the coherent particle "swaying" motion caused by the waves.

The flight time of the bed is determined by examining the normal force acting on the floor as a function of time. When the particle bed is in flight, the force on the floor is zero since there is no contact with the base. At impact, however, the force increases suddenly. The time between these impacts is the flight time of the bed. This information is used to determine when period doubling occurs.

The baseline simulations used for determining the onset of the various phenomena have the parameters listed in table 3.1. The acceleration amplitude of the oscillations, Γ, was varied between zero and 7.0 in steps of 0.2 at an oscillation frequency of $f = 20$ Hz for a dimensionless bed depth of $h_0/d = 20$. The results of the simulations are shown in figure 3.8.

All of the phenomena appear in the simulations for values of Γ similar to those found experimentally. Side wall convection appears for all Γ greater than one and the mounding behavior is observed for $1.0 < \Gamma < 1.6$, a range slightly lower than that found in the experiments. When $1.6 < \Gamma < 3.6$, $f/2$ waves appear. At $\Gamma = \Gamma_1' \approx 3.6$ a period doubling bifurction is discernible. For $\Gamma > \Gamma_1'$, kinks appear in the bed and at

$\Gamma = \Gamma*_1 = 4.8$ the bed returns to a single flight time. Note that when $\Gamma_1' < \Gamma < \Gamma_1^*$, poorly formed $f/2$ and $f/4$ waves appear intermittently on the surface of the bed. The $f/4$ waves appear in a consistent manner for $\Gamma > \Gamma_1^* = 4.8$ up to at least $\Gamma = 7.0$.

3.3 Discussion

In the shallow bed regime, three different bed states are distinguishable. Thomas *et al.* (1989) referred to these as the Newtonian-I, II and the coherent-expanded states. In the present experiments, the appearance of the various states depends primarily upon the dimensionless bed depth, h_0/d, and the acceleration amplitude of the oscillations for $0.0 < \Gamma < 2.5$. As h_0/d increases, the degree of coherency in the particle bed motion also increases, presumably due to the increased number of particle interactions. The transitions between the various shallow bed states is gradual. The transition to deep bed behavior, however, is sudden and repeatable and occurs at $h_0/d \approx 6$ in the present experiments. Thomas *et al.* and Bachmann (1940) also report a similar result. This sudden transition is examined in further detail in chapter 4.

The behavior of the particle bed in the deep bed regime is significantly different than that observed for shallow beds. Phenomena such as side wall convection cells, mounding, surface waves, kinks, and kink convection cells are observed depending upon the acceleration amplitude of the oscillations, Γ, and the dimensionless bed depth, h_0/d.

The experiments indicate that side wall convection and mounding occur for Γ just greater than 1.2. A number of other researchers have found similar values (see, for example, Evesque and Rajchenbach, 1989, Clément *et al.*, 1992, and Fauve *et al.*, 1989). In the simulations, these behaviors appear for $\Gamma > 1.0$, a value slightly less than that found in the experiments. This discrepancy may be due to the observational difficulties associated with determining when these phenomena first occur. Since the motion of the particles is very slow at Γ near one, it is easy to mistake that no movement is occurring unless the bed is observed over a long period of time. The

simulations are able to detect these small displacements although they may be difficult to determine visually.

Taguchi (1992) also studied the onset of side wall convection in simulations. He measured the average particle displacement per cycle in the container using a method similar to the one used here to determine when convection appears. The primary difference between the two methods is that Taguchi averages the particle motion over the entire container while the method used here examines only the particle movement along the walls. Taguchi's results indicate that convection first occurs when $1.0 < \Gamma < 1.2$, similar to the present results.

The mounding behavior also appears when $\Gamma > 1.2$ in the experiments and for $\Gamma > 1.0$ in the simulations. As is discussed in chapter 5, mounding is a result of the side wall convection behavior. Note that although side wall convection persists for oscillation acceleration amplitudes greater than one, mounding is not observed for Γ greater than approximately 2.0. Two factors may contribute to this effect. First, as Γ increases, the convection speed and the magnitude of the bed/base collision impulse increase. Both act to destabilize the slope of the mound on the free surface. The formation of surface waves for $\Gamma > 2.0$ may also contribute to the disappearance of the mound.

The $f/2$ waves first appear for $\Gamma \approx 2.0$ and persists to a value of Γ_1', the acceleration amplitude at which period doubling occurs. The latter value of Γ decreases with increasing bed depth, h_0/d. Melo *et al.* (1995) and Metcalf *et al.* (1996) also examined these $f/2$ waves in experiments and, in particular, the transitions between the various wave patterns observed on the free surface of particle bed in cylindrical containers. Melo *et al.*'s experiments used beds of 0.15-0.18 mm bronze spheres with $7 \leq h_0/d \leq 12$. They found that $f/2$ waves appeared for $2.4 < \Gamma < 4.4$ and that this range did not vary with oscillation frequency. Additionally, they report the appearance of kinks, an indication that the period doubling bifurcation has occurred, for $\Gamma > 4.4$. These results are consistent with the observations made in the present experiments.

Metcalf *et al.*'s experiments used beds of 0.5 mm diameter glass spheres in an

evacuated container with h_0/d ranging from four to eight. They found that $f/2$ waves first appeared for Γ between 3.0 and 4.0 and persisted to a value of Γ between 4.5 and 6.0. The range of Γ over which the waves appeared decreased with increasing frequency and shifted to higher values of Γ for increasing bed depth. For the thinnest bed, $h_0/d = 4$, the range of Γ at which the surface waves appear is a strong function of the frequency. In fact, for frequencies greater than approximately 25 Hz, the waves cease to appear.

This frequency dependence at $h_0/d = 4$ may be due to the fact that the bed is near the boundary between the shallow bed and deep bed regimes. Metcalf *et al.* also report that the range of Γ is sensitive to moisture and other impurities on the particle surfaces. These effects become less significant as particle size increases.

The $f/2$ waves also appear in simulations for values of Γ similar to those observed in the experiments. The onset of the waves occurs for lower Γ in the simulations but the Γ at which the waves disappear, corresponding to the Γ at which period doubling occurs, is consistent with experimental observations.

The critical acceleration amplitude at which period doubling occurs, Γ_1', decreases as h_0/d increases in the experiments. For example, $\Gamma_1' = 4.2$ when $h_0/d = 10$ but at $h_0/d = 40$, $\Gamma_1' = 3.0$. This observation is contrary to what is reported by Douady *et al.* (1989). They found that Γ_1' increases with increasing h_0/d and attribute this behavior to the effects of the interstitial fluid. The reason for this discrepancy is not clear. Indeed, drag on the particle bed will cause the critical value of Γ to increase. Since Douady *et al.* used smaller particles ($d = 0.63 - 0.80$ mm) than those used in the present experiments ($d = 1$ mm), a greater sensitivity to interstitial fluid effects is expected. One effect that may also be an important factor is the dilation, or expansion, of the bed. A study of this effect was not made however.

Kinks and the convection cells associated with kinks appear for $\Gamma > \Gamma_1'$ in both the experiments and simulations. The period doubling of the flight time is critical for the formation of kinks and is discussed in detail in chapter 7. Note that a degenerate case consisting of zero kinks exists where the entire particle bed oscillates in phase.

The last behavior observed in the experiments and simulations are $f/4$ waves.

The Γ at which these waves first appear in the experiments decreases with increasing bed depth. For example, at $h_0/d = 10$, the onset value of Γ is 6.0. When $h_0/d = 40$, however, the critical Γ is 5.0. These waves persist to the maximum Γ investigated here, $\Gamma = 7.0$. Melo *et al.* (1995) also examined the onset of these waves and found that the $f/4$ waves appeared for $\Gamma > 5.8$ to at least 8.0 (note that $h_0/d \approx 7$ in their experiments).

Several important conclusions can be made regarding the phase map of the phenomena that appear in a vertically vibrating bed of granular material. First, the key parameters that determine the appearance of the behaviors are the dimensionless bed depth, h_0/d, and the dimensionless acceleration amplitude of the oscillations, $\Gamma = a\omega^2/g$. For small h_0/d, (less than six), fluidized bed behavior is observed. When h_0/d is sufficiently large, the particles in the bed move coherently and the bed moves as a single, plastic mass. In this regime, convection cells, surface waves, and kinks appear depending on both Γ and h_0/d. Another important point regards the use of simulations as a tool to study these behaviors. Not only did the simulations reproduce all of the experimentally observed phenomena, but the onset values of Γ were similar to those found experimentally.

Tables and Figures

f	20 Hz
W/d	100
h_0/d	20
N	2000
ϵ_{pp}	0.80
$k_{n,pp}$	$5.289 * 10^3$ N/m
ν_{pp}	$8.337 * 10^{-3}$ N/(m/s)
$k_{s,pp}$	$5.289 * 10^3$ N/m
μ_{pp}	0.1
lateral boundaries	walls
$k_{n,pw}$	$1.058 * 10^4$ N/m
ν_{pw}	$1.667 * 10^{-2}$ N/(m/s)
$k_{s,pw}$	$1.058 * 10^4$ N/m
μ_{pw}	0.1
d	0.9 - 1.1 mm
ρ	2500 kg/m^3
Δt	$3.504 * 10^{-6}$ sec

Table 3.1: The simulation parameters used to examine the phase space for deep beds.

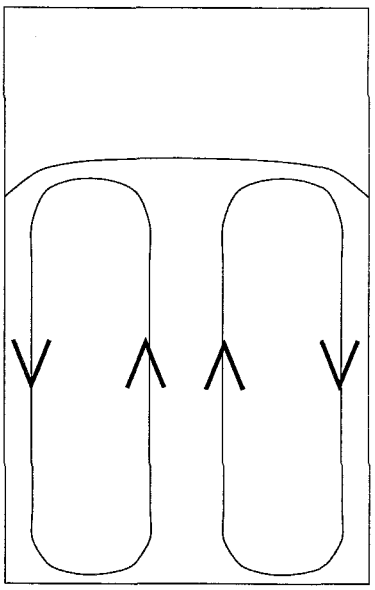

Figure 3.1: An illustration showing the particle trajectories in a bed exhibiting side wall convection cells. The drawing is for a vertical slice through the interior of the bed.

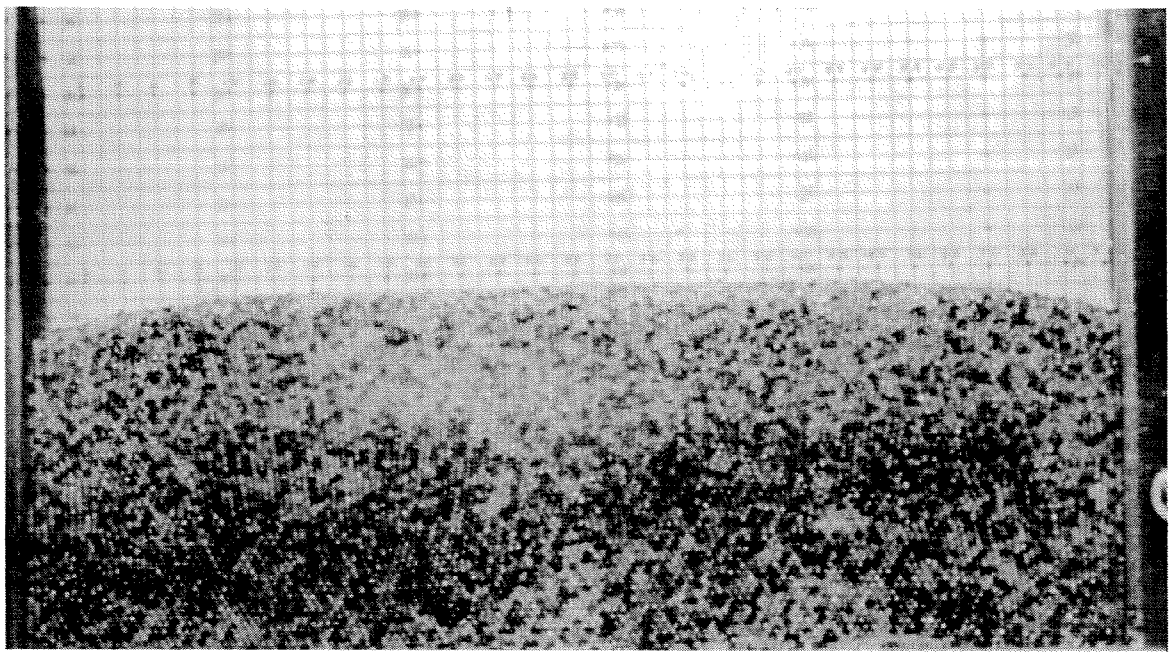

Figure 3.2: A photograph of a rounded mound using 1.3 mm glass spheres. The other experimental parameters are $\Gamma = 1.6$, $f = 20$ Hz, $h_0/d = 18$, $W/d = 104$.

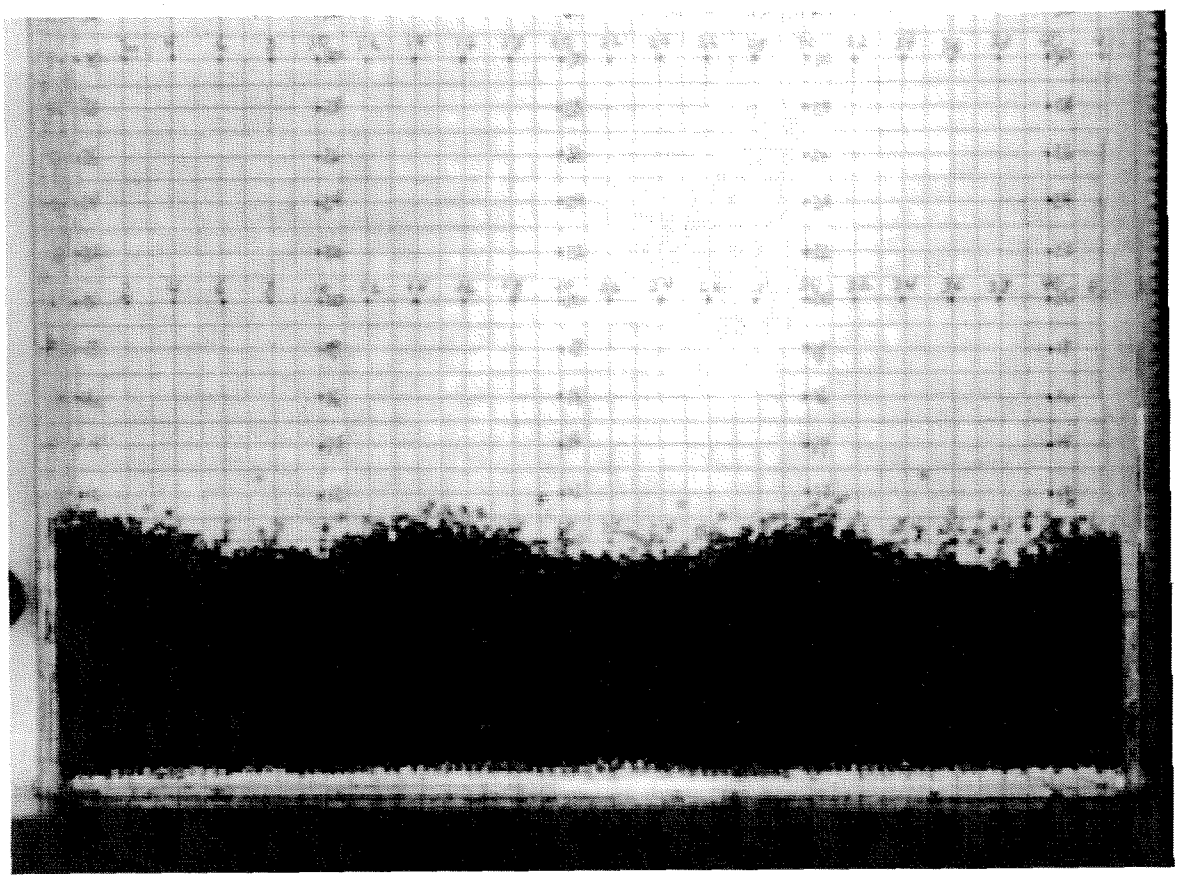

Figure 3.3: A photograph of $f/2$ standing surface waves using 1.3 mm glass spheres. The other experimental parameters are $\Gamma = 3.3$, $f = 20$ Hz, $h_0/d = 18$, $W/d = 104$.

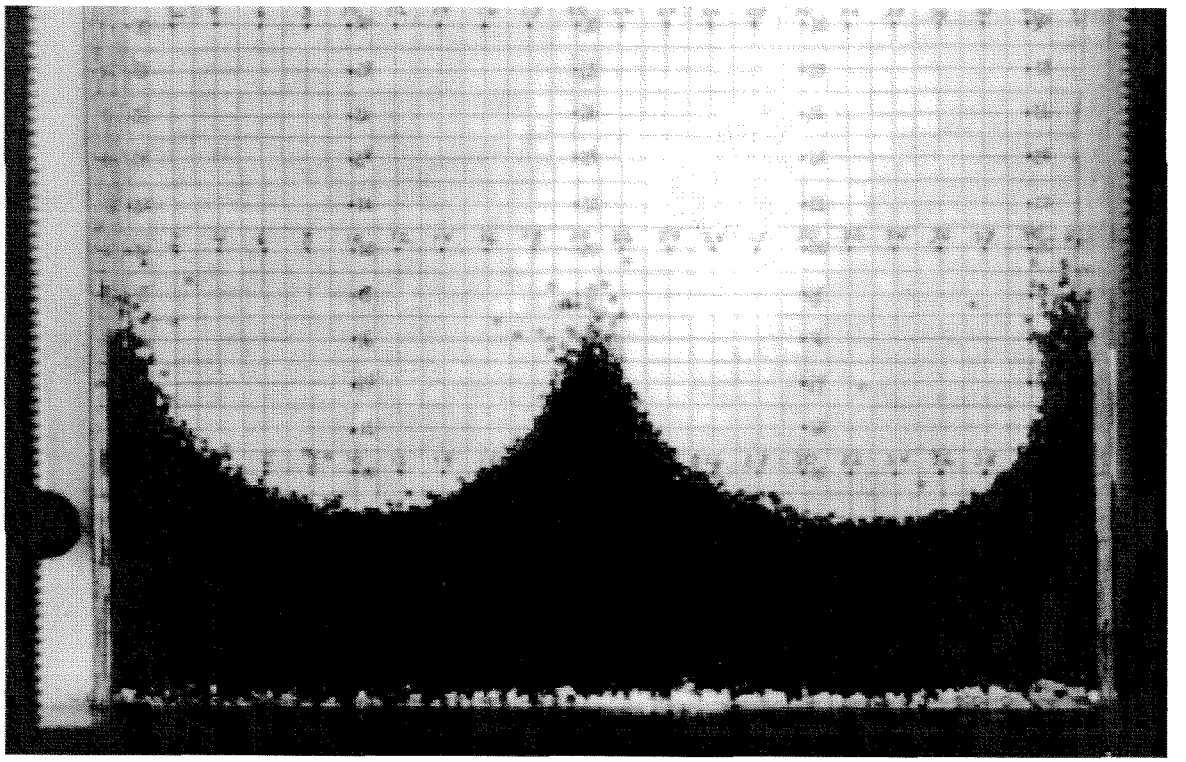

Figure 3.4: A photograph of $f/4$ standing surface waves using 1.3 mm glass spheres. The other experimental parameters are $\Gamma = 6.2$, $f = 20$ Hz, $h_0/d = 18$, $W/d = 104$.

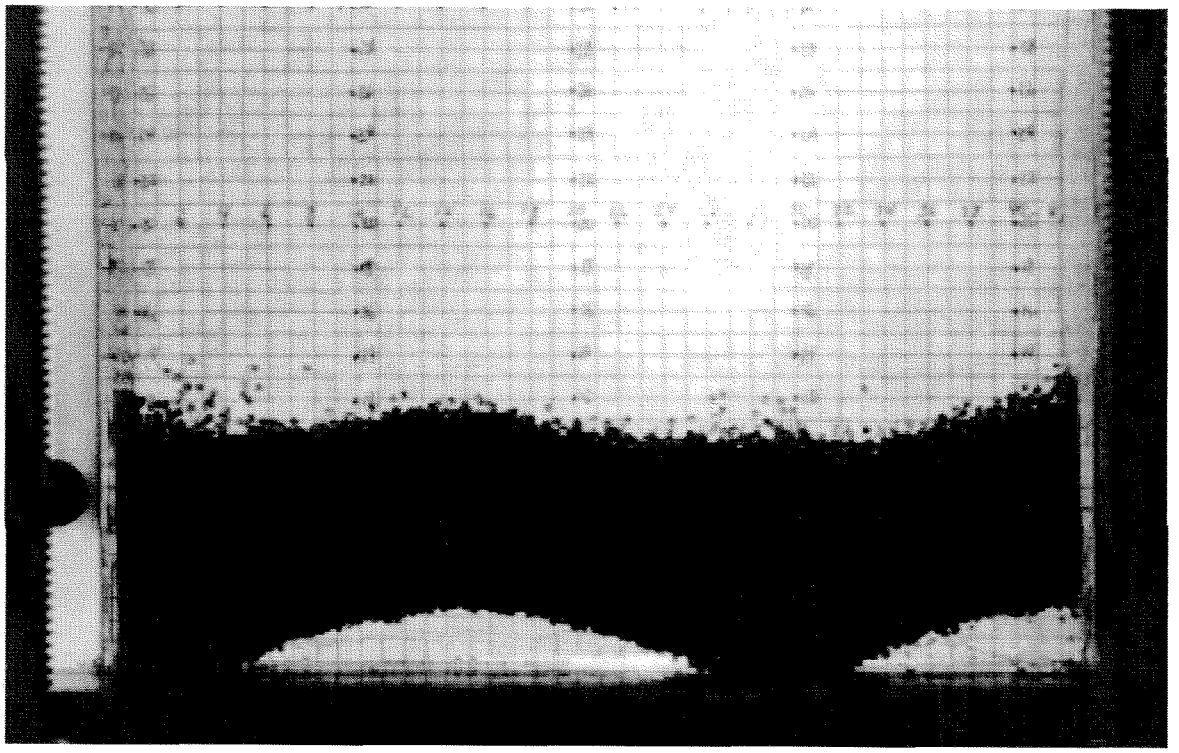

Figure 3.5: A photograph of a bed with three kinks using 1.3 mm glass spheres. The other experimental parameters are $\Gamma = 8.5$, $f = 30$ Hz, $h_0/d = 18$, $W/d = 104$.

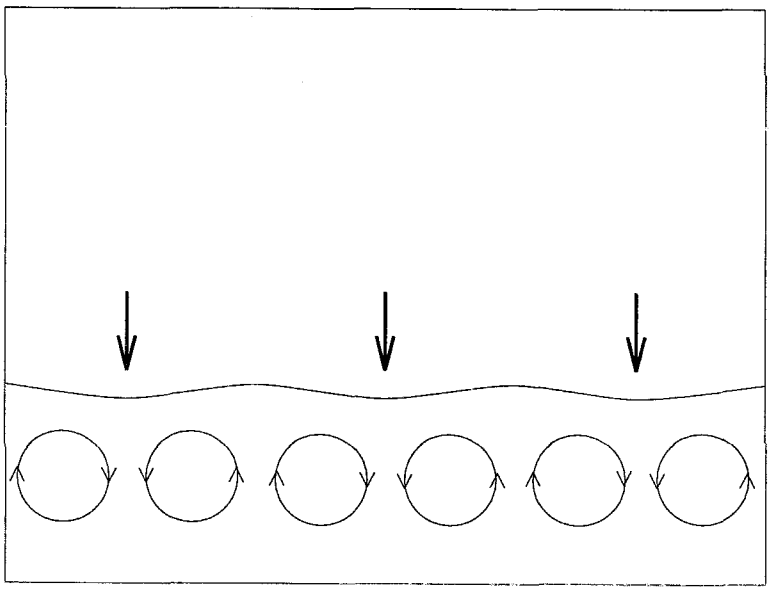

Figure 3.6: An illustration of the long duration particle streamlines for a bed with three kinks. The arrows indicate the location of the kinks.

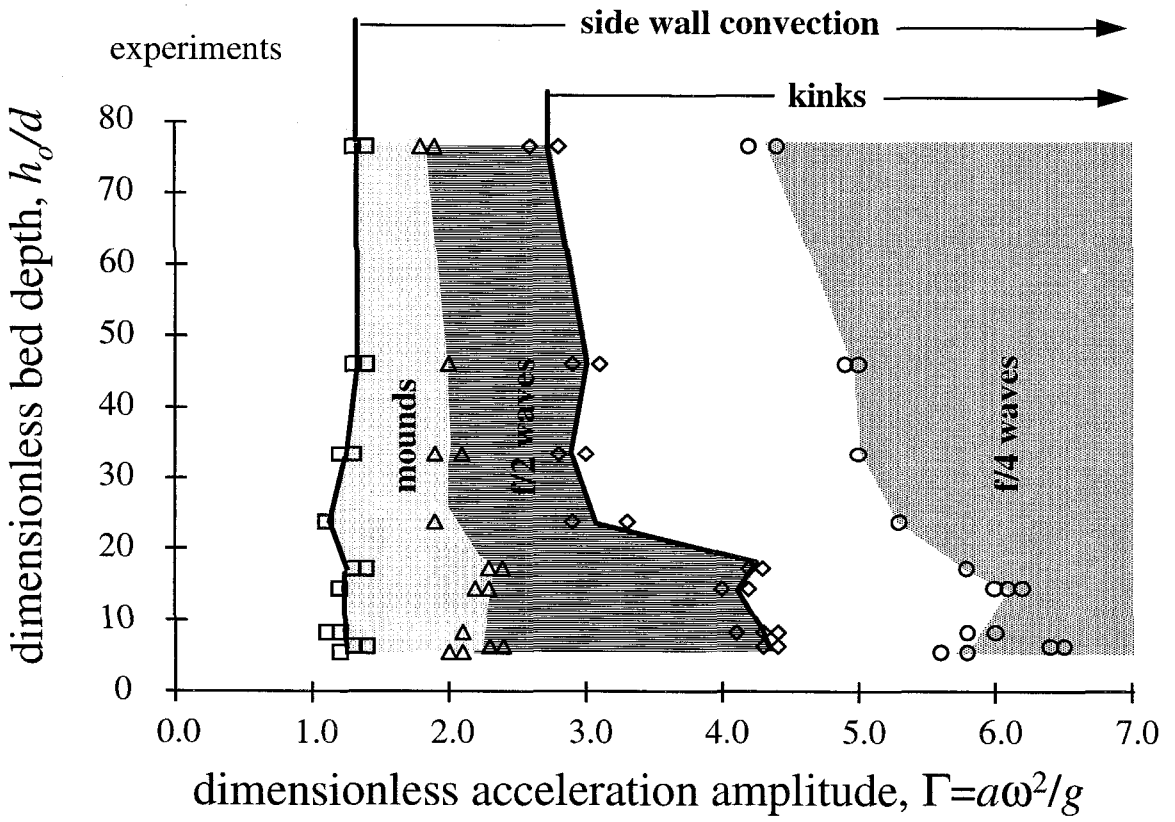

Figure 3.7: The phase space diagram of when the deep bed behaviors appear as a function of the oscillation acceleration amplitude, $\Gamma = a\omega^2/g$, and the dimensionless bed depth, h_0/d. The experiments were performed with 1.3 mm diameter glass spheres in the $W/d = 104$ container at 20 Hz.

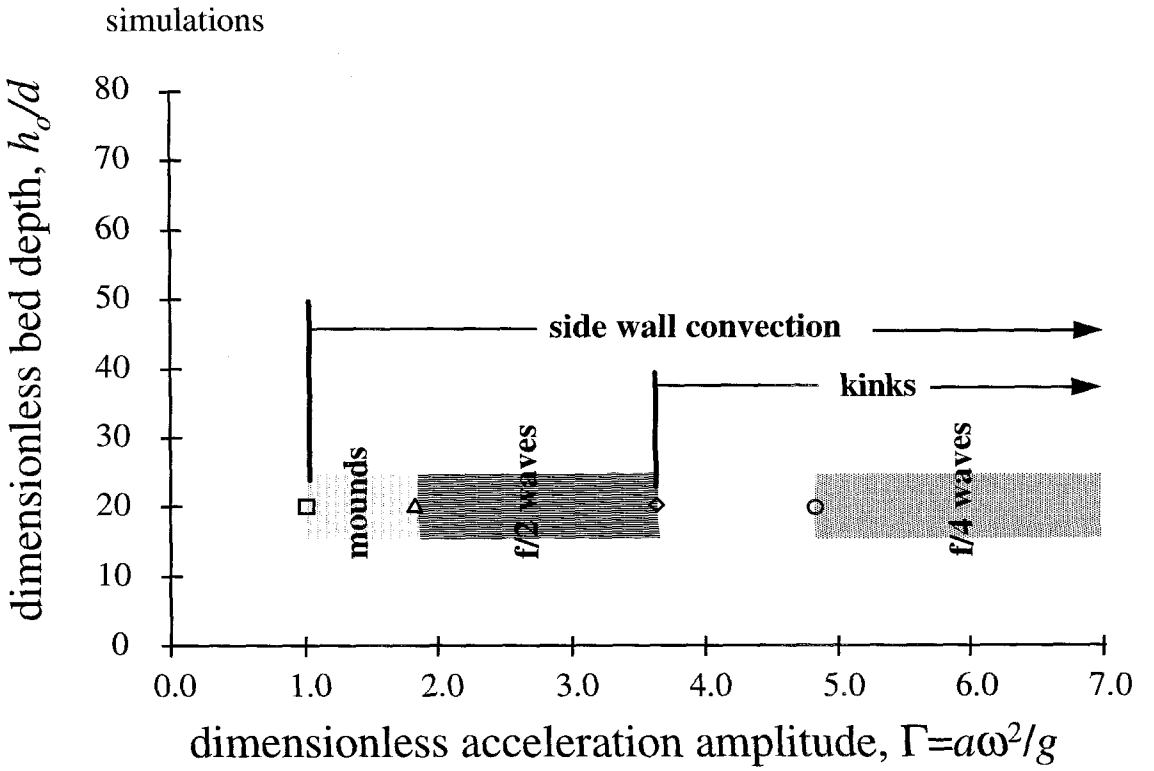

Figure 3.8: The phase space diagram of when the deep bed behaviors appear as a function of the oscillation acceleration amplitude, $\Gamma = a\omega^2/g$ for $h_0/d = 20$ and $f = 20$ Hz. The remainder of the simulation parameters are given in table 3.1.

Chapter 4 Shallow Beds

4.1 Experiments

The three shallow bed states consisting of the Newtonian-I, Newtonian-II, and coherent-expanded states were observed in the experiments but were not examined in detail. Instead, the transition to the deep bed regime from the coherent-expanded state was investigated. During the course of these experiments it was observed that the bed appeared to expand considerably beyond a critical value of Γ for values of Γ between one and two. This expansion is the transition from the deep bed state to the coherent-expanded state. In order to quantify the expansion, a lightweight paper lid was placed on the top surface of the bed as described in section 2.1.1. The difference of the spacing between the base and lid, h, and the spacing at rest, h_0, is a measure of the bed expansion, $(h - h_0)$.

For reasons which will become clear, $(h - h_0)$ is presented both as a function of the non-dimensional acceleration amplitude, Γ, and as a function of the vibration velocity amplitude, $a\omega$. The typical behavior of the bed is best illustrated by the results from experiment 7 which are presented in figure 4.1. Recall that table 2.1 lists the mass of particles and lid mass for the shallow bed experiments.

The bed expands at an acceleration amplitude of roughly $1g$ and this expansion gradually increases until a critical value of the acceleration amplitude, Γ_c, is reached. This critical value is independent of frequency but varies with both the mass of beads and the mass of the lid. At the critical acceleration amplitude the lid rises quite abruptly and then settles down at a substantially larger spacing, h. As illustrated in figure 4.1, further increase in the acceleration results in further bed expansion but this is more gradual than the expansion encountered during transition. The top graph in figure 4.1 illustrates the fact that the critical conditions appear to occur at a given dimensionless acceleration amplitude regardless of the frequency. On the other hand,

the bottom graph in figure 4.1 illustrates the fact that the supercritical conditions correlate with the velocity amplitude, $a\omega$, rather than the acceleration amplitude.

Using the strobe, it was observed that for $\Gamma < \Gamma_c$, the beads move as a mass which collides once per cycle with the base and the lid. The collision with the base seemed quite inelastic and it appeared that the mass only left the base again when the acceleration of the base exceeded some critical value. These motions are characteristic of the deep bed regime. For $\Gamma > \Gamma_c$, however, the motions of the particles are fairly uncoordinated as in the coherent-expanded state.

Experiment 7 was chosen to illustrate the transition between the two states because it does so most clearly since it used the smallest mass of beads. As the mass of beads is increased (for the same lid weight) the critical transition becomes less distinct in the sense that the expansion at the critical acceleration becomes smaller and less abrupt. The same trend is manifest as the weight of the lid is increased. Both effects are illustrated in figure 4.2 which presents data from experiments 4 and 5. The critical acceleration, Γ_c, also increases with both the mass of the beads and the mass of the lid. These trends are shown in figure 4.3.

In order to help understand the fundamental dynamics behind this expansion, the data is presented in non-dimensional form. The dimensionless expansion is given by $(h - h_0)\omega^2/g$ and is plotted as a function of the non-dimensional acceleration amplitude, $\Gamma = a\omega^2/g$. Examples from experiments 2 and 3 are shown in figure 4.4 in which the subcritical and supercritical data clearly form two distinct groups of points. Indeed the two groups of points both appear to lie close to quadratic curves implying that each group of points corresponds to a roughly constant value of the inverse Froude number based on the bed expansion and vibration velocity amplitude,

$$Fr^{-1} = \frac{[g(h - h_0)]^{1/2}}{a\omega} \tag{4.1}$$

To examine this further, the inverse Froude number is plotted versus the acceleration, Γ, in figure 4.5 for the typical data of experiments 2 and 3. It seems particularly noteworthy that the subcritical data corresponds roughly to an inverse Froude num-

ber, Fr^{-1}, of between 0.5 and 1.0 and that the supercritical values corresponds quite closely to $Fr^{-1} = 1.5$ (recall that the values of $(h - h_0)$ and a for some of the subcritical data are quite small and this may account for the larger scatter in that group of points). The specific values for Fr^{-1} decrease significantly as the mass of beads is increased and as the mass of the lid is increased. The subcritical data shows similar trends though they are less distinct due to greater scatter in the data.

4.2 Theory

This expansion behavior can be explained using a simple model consisting of a partially inelastic ball bouncing on a flat plate performing vertical, sinusoidal oscillations. Modeling the bed of particles as a single, partially inelastic mass could be considered appropriate since the agglomeration of particles moves coherently and collisions between particles (and between particles and the base) are inelastic. To first order, the resulting motion of the particle assembly would be similar to that of the single, inelastic particle.

The dynamics of the ball bouncing problem have been previously examined and are a classic example of the occurrence of bifurcations (see, for example, Holmes, 1982, Mehta and Luck, 1990, and Luck and Mehta, 1993). These bifurcations seem to be the probable explanation for the experimentally observed sudden expansion.

The model is as follows. The base moves with a sinusoidal trajectory given by

$$b(t) = a\sin(\omega t) \tag{4.2}$$

where b is the vertical position of the base, a the vibration amplitude, ω the radian vibration frequency, and t the time. The ball has a ballistic trajectory when not in contact with the base,

$$p(t) = -1/2g(t - t_{n-1})^2 + \dot{p}^{+}_{n-1}(t - t_{n-1}) + p_{n-1} \tag{4.3}$$

where p is the vertical position of the particle, g the acceleration due to gravity, t_{n-1}

the time of the last contact with the base, $\dot{p}_{n-1}^{+}$ the particle velocity immediately following the last contact with the base at time t_{n-1}, and p_{n-1} the particle position at t_{n-1}.

The interaction between the base and the particle is characterized by a coefficient of restitution, ϵ. The coefficient of restitution is defined as the ratio of the relative velocity between the particle and base after the collision to the relative velocity prior to the collision,

$$\epsilon = -\frac{\dot{p}(t_n^+) - \dot{b}(t_n^-)}{\dot{p}(t_n^-) - \dot{b}(t_n^-)} \tag{4.4}$$

Note that values for ϵ range from 0 to 1; a completely inelastic impact has a value of $\epsilon = 0$ while a totally elastic one has $\epsilon = 1$.

These equations can be written in dimensionless form using the following parameters: $B = b\omega^2/g$, $P = p\omega^2/g$, $\Gamma = a\omega^2/g$, $\dot{B} = \dot{b}\omega/g$, $\dot{P} = \dot{p}\omega/g$, and $\phi = \omega t$. After non-dimensionalizing and re-arranging, the discrete mapping becomes,

$$f : (\phi_{n-1}, \dot{P}_{n-1}) \mapsto (\phi_n, \dot{P}_n) \tag{4.5}$$

$$-\frac{1}{2}(\phi_n - \phi_{n-1})^2 + \dot{P}_{n-1}^{+}(\phi_n - \phi_{n-1}) + \Gamma \sin\phi_{n-1} - \Gamma \sin\phi_n = 0 \tag{4.6}$$

$$\dot{P}_n^{+} = -\epsilon \dot{P}_{n-1}^{+} + \epsilon(\phi_n - \phi_{n-1}) + (1+\epsilon)\Gamma \cos\phi_n \tag{4.7}$$

The fixed point trajectories for this mapping are periodic,

$$\phi_n = \phi_{n-1} + 2\pi m \tag{4.8}$$

$$\dot{P}_n^{+} = \dot{P}_{n-1}^{+} \tag{4.9}$$

where m is a positive integer. The solution $(\phi^*, \dot{P}^*)$ is given by

$$\Gamma \cos\phi^* = \frac{m\pi(1-\epsilon)}{(1+\epsilon)} \tag{4.10}$$

$$\dot{P}^* = m\pi \tag{4.11}$$

where $(\phi^*, \dot{P}^*)$ are the fixed points. Note that only those fixed points that are stable will be observed. The stability of the solutions is determined by examining the eigenvalues of the linearized Jacobian of equations (4.6) and (4.7) and is discussed in detail in Luck and Mehta (1996). Holmes (1982) does a similar analysis for an approximation to the map.

The resulting analysis gives two critical values for Γ,

$$\Gamma_m = \frac{m\pi(1-\epsilon)}{(1+\epsilon)} \tag{4.12}$$

and

$$\Gamma'_m = \{(\frac{m\pi(1-\epsilon)}{(1+\epsilon)})^2 + (\frac{2(1+\epsilon^2)}{(1+\epsilon)^2})^2\}^{1/2} \tag{4.13}$$

These Γ are bifurcation values at the first of which a pair of fixed points appears in a saddle-node bifurcation and at the second of which a change of stability occurs. At the saddle-node bifurcation, two fixed point trajectories appear, only one of which is stable. At the stability bifurcation, the stable fixed point solution becomes unstable and a period two motion appears instead (refer to Holmes, 1982). Particle and base trajectory examples are shown in figure 4.6 for three values of Γ. The trajectories were calculated using equations (4.6) and (4.7) for a coefficient of restitution, ϵ, of 0.25. For this ϵ, the first saddle node bifurcation occurs at $\Gamma_1 = 1.89$ and the first period doubling bifurcation at $\Gamma'_1 = 2.32$. This value of ϵ was chosen in order to give a value of Γ_1 that coincides with the critical Γ_c at which the sudden expansion occurs in experiment 2. The top figure is for $\Gamma = 1.8$, the middle for $\Gamma = 1.9$, and the bottom for $\Gamma = 2.5$. In the top plot, the particle collides with the base after a flight time that is less than the oscillation period and bounces several times before effectively coming to rest on the base. This same motion is repeated every oscillation cycle. In the middle plot, the periodic fixed point trajectory is apparent where the particle motion repeats after every collision. The bottom plot shows the particle motion exhibiting a period two motion.

Another result of the bifurcation is that the maximum rebound velocity of the particle off the base changes significantly at Γ_1. The result is that the maximum

separation height between the particle and the base also suddenly increases. This same effect is observed in the present experimental data. A plot of the calculated dimensionless expansion, h, using a value of $\epsilon = 0.25$ is plotted against the dimensionless acceleration amplitude, Γ, in figure 4.7 and is compared with the data from experiment 2. This analogy between the bed and an inelastic ball is qualitatively consistent with the experiments since the effective ϵ for the mass of particles may be as low as 0.25 because of the large number of collisions occurring between all of the particles.

Thus, the model is consistent with the following explanation of the observed experimental behavior. Below $1g$, the particle bed does not leave the base. Just above $1g$, however, the particles in the bed bounce around; yet, the individual particle motions settle down prior to the next oscillation cycle. The motion repeats every oscillation cycle similar to the single particle with $\epsilon = 0.25$. When the acceleration approaches the critical or bifurcation value of Γ_1' a sudden expansion of the bed occurs as the particle mass repeats the same motion every two oscillation cycles and the rebound velocity suddenly increases.

Note that the analysis predicts additional bifurcations occurring at higher values of Γ. The second period doubling bifurcation is predicted to occur at $\Gamma_2 = 3.77$ and a third occurring at $\Gamma_3 = 5.66$ when $\epsilon = 0.25$. The experiments, however, did not examine values of Γ greater than 2.5 due to shaker limitations. Thus, these other bifurcations could not be investigated experimentally.

4.3 Simulations

Several simulations were run to determine if this expansion could be reproduced in a 2D bed of particles with high coefficients of restitution, ϵ. One hundred frictionless particles were placed in a container with periodic lateral boundaries and a rigid base oscillating with the sinusoidal trajectory, $y_b = a\sin(\omega t)$, where y_b is the base vertical position, a the oscillation amplitude, ω the oscillation radian frequency, and t the time. The container width, W, was twenty-five particle diameters giving a dimensionless

bed depth of four, $h_0/d = 4$. All of the particles had the same diameter (and mass) and the coefficients of restitution for the particle-particle and particle-base collisions was $\epsilon = 0.80$. A summary of the remaining simulation parameters is given in table 4.1.

In order to determine whether the simulated bed suddenly expands at a critical acceleration amplitude, the average separation, h_{cm}, between the vertical component of the bed's center of mass, y_{cm}, and the base, y_b, was examined for various Γ. The vertical position of the center of mass is determined by

$$y_{cm}(t) = \frac{1}{N}\sum_{i=1}^{i=N} y_i(t) \tag{4.14}$$

where N is the number of particles and y_i the vertical location of particle i. The averaging process started after five seconds of vibration, a duration sufficient to eliminate any initial transients, and continued for five more seconds.

The average non-dimensional bed expansion, $\overline{(h_{cm} - h_{cm,0})}\omega^2/g$, where $h_{cm,0}$ is the vertical component of the bed's center of mass for a static bed is shown in figure 4.8 as a function of the oscillation acceleration amplitude, $\Gamma = a\omega^2/g$, for a frequency of 20 Hz. A sudden expansion clearly appears at a critical Γ between 1.7 and 1.8. Note that no other expansions appear for values of Γ up to 6.0. The experiments were only able to investigate accelerations up to $2.5g$ due to shaker limitations.

Particle motion within the bed was also examined. When $\Gamma < \Gamma_c$, particles move coherently as in the deep bed regime. However, for $\Gamma > \Gamma_c$, the bed has a structure similar to the coherent-expanded state discussed in section 3.1. The other shallow bed states were also observed in the simulations, however, a clear transition between them was not evident.

One measure of the random particle motion in the bed is the granular temperature per unit mass, γ, defined as the kinetic energy per unit mass in the bed due to the particle fluctuation velocities,

$$\gamma = \frac{1}{2M}\sum_{n=1}^{n=N} m_n((\dot{x_n}')^2 + (\dot{y_n}')^2) \tag{4.15}$$

where M is the total mass of the particles, N the number of particles, m_n the mass of particle n, and $\dot{x}'_n = \dot{x}_n - \dot{x}_{cm}$ and $\dot{y}'_n = \dot{y}_n - \dot{y}_{cm}$ are the fluctuating particle velocities where $\dot{x}_n$ and $\dot{y}_n$ are the velocity components of particle n and $\dot{x}_{cm}$ and $\dot{y}_{cm}$ are the bed's center of mass velocity components. Figure 4.9 shows the granular temperature per unit mass as a function of time for a bed with a pre-expansion Γ of 1.7 and a post-bifurcation Γ of 1.8. The sudden increase in the granular temperature once each cycle corresponds to the particle bed impacting the base. The temperature then decreases in time as collisions between particles occur and the degree of coherency in the particle motions increases. For $\Gamma = 1.7$ the fluctuating kinetic energy in the bed is completely dissipated before performing the next oscillation cycle. When $\Gamma = 1.8$, however, the granular temperature is not dissipated before the next cycle.

Several parameters, including the number of particle layers, h_0/d, the coefficient of restitution, ϵ, and the inter-particle friction, μ_{pp}, were varied in order to determine their effect on the response of the bed. The critical transition occurs for higher Γ when h_0/d and μ increase and when ϵ decreases, all of which act to increase the energy dissipation in the bed.

4.4 Discussion

The simulation results are consistent with the simple model described in section 4.2 of a single inelastic ball bouncing on a vibrating base. A ball with a low coefficient of restitution bouncing on a vibrating table at low Γ dissipates all its kinetic energy in repeated impacts with the base before repeating the next oscillation cycle. This situation occurs for $\Gamma < \Gamma_c$. When $\Gamma > \Gamma_c$, the energy in the ball is not completely dissipated in the impacts and the expansion is observed.

Lan and Rosato (1995) determined an effective coefficient of restitution for a simulated bed by dropping the bed onto a fixed base and taking the ratio of the bed's center of mass vertical velocity after the collision to the velocity prior to the collision (refer to equation (4.4)). A similar measurement for the present simulation gives $\epsilon_{\text{eff}} \approx 0.11$. This value is close to $\epsilon = 0.27$ which results from equation (4.13)

using a value of $\Gamma_1' = 1.8$, the critical Γ at which the sudden expansion occurs in the simulations.

It is interesting to note that the simple model predicts other bifurcations at higher Γ yet the simulations show that only one sudden expansion occurs. The simulations by Lan and Rosato (1995) also produced only a single expansion for accelerations up to $30g$. The reason only a single expansion occurs is not clear.

Tables and Figures

W/d	25
h_0/d	4
N	100
ϵ_{pp}	0.80
$k_{n,pp}$	$5.289 * 10^3$ N/m
ν_{pp}	$8.337 * 10^{-3}$ N/(m/s)
$k_{s,pp}$	$5.289 * 10^3$ N/m
μ_{pp}	0.0
lateral boundaries	periodic
$k_{n,pw}$	$1.058 * 10^4$ N/m
ν_{pw}	$1.667 * 10^{-2}$ N/(m/s)
$k_{s,pw}$	$1.058 * 10^4$ N/m
μ_{pw}	0.0
d	1.0 mm
ρ	2500 kg/m^3
Δt	$3.504 * 10^{-6}$ sec

Table 4.1: The parameters used in shallow bed simulations.

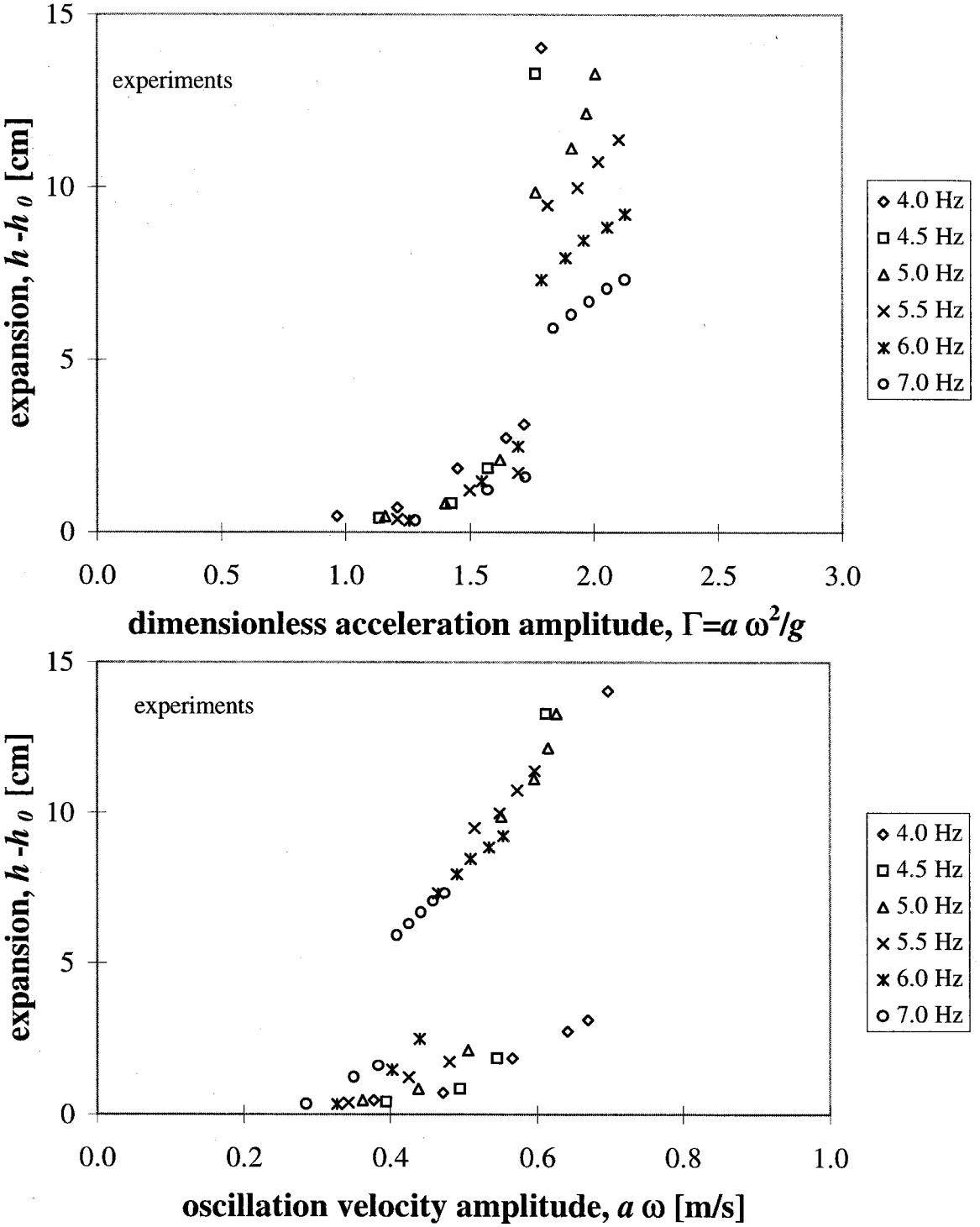

Figure 4.1: The dependence of the bed expansion, $h - h_0$, on the dimensionless acceleration amplitude, $\Gamma = a\omega^2/g$, and the velocity amplitude, $a\omega$, for experiment 7.

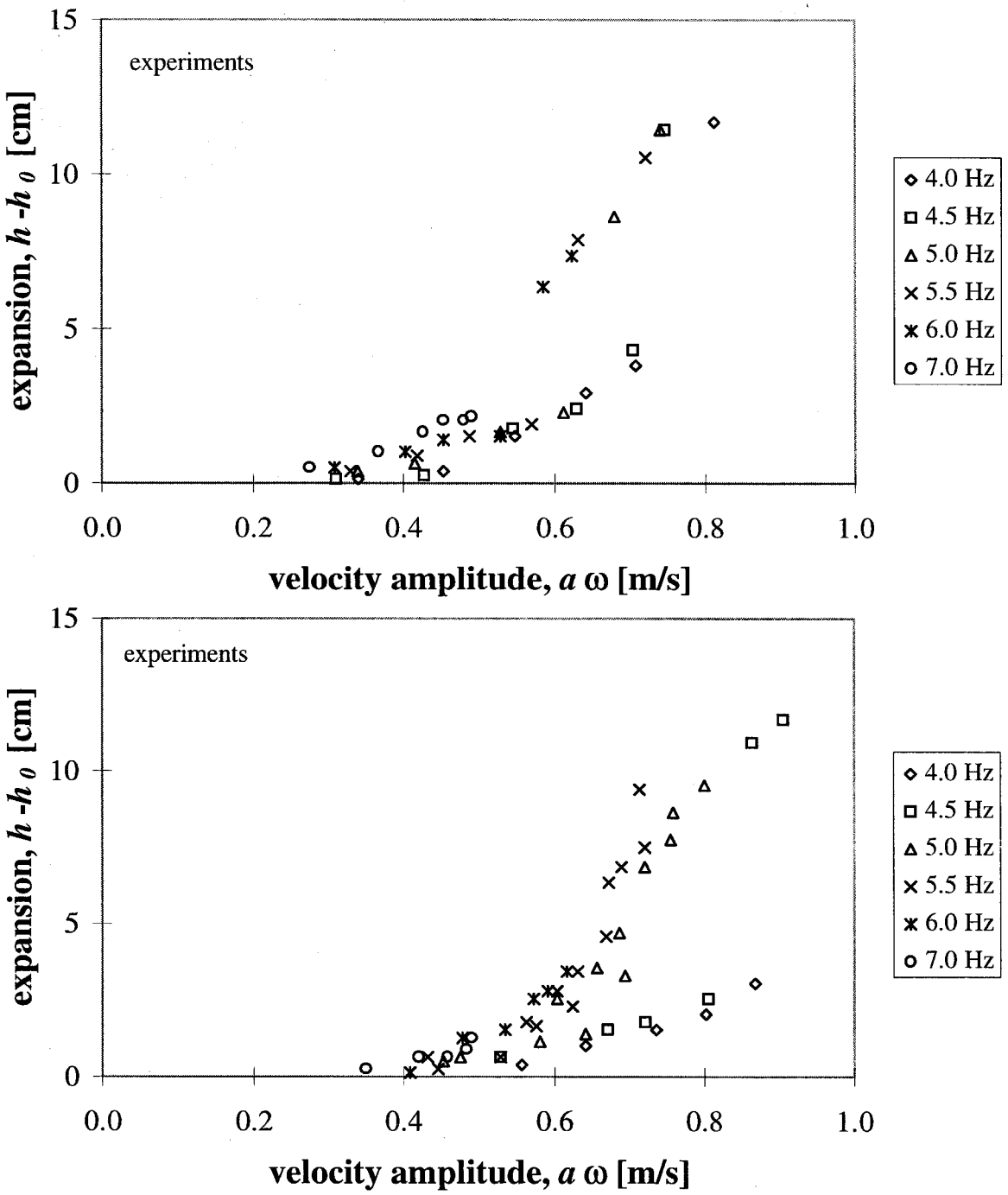

Figure 4.2: The bed expansion, $h - h_0$, from experiments 4 (top) and 5 (bottom) plotted as a function of the oscillation velocity amplitude, $a\omega$.

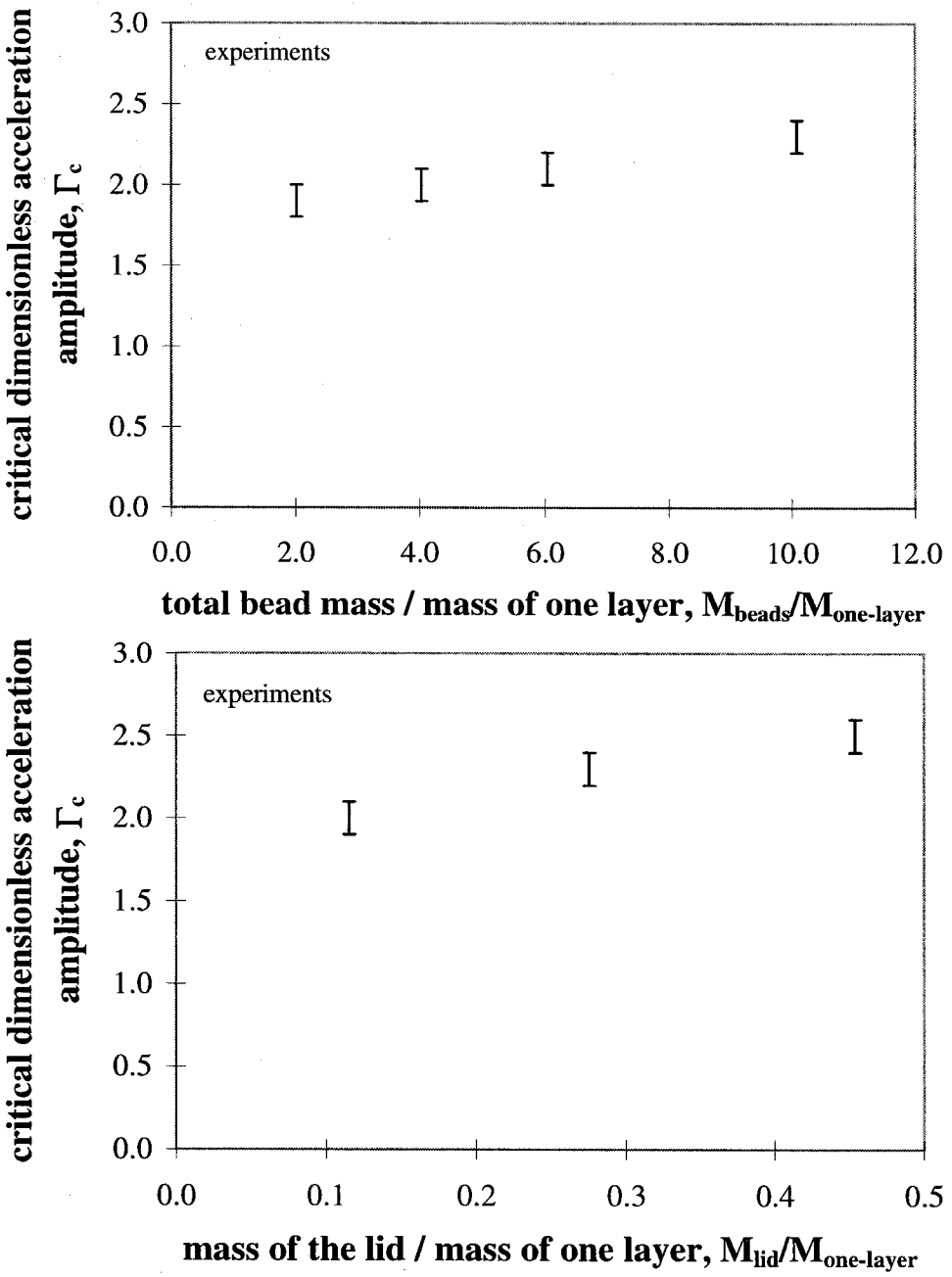

Figure 4.3: The critical acceleration amplitude, $\Gamma_c = (a\omega^2/g)_c$, as a function of the mass of beads (top graph for 3.44 gm lid) and as a function of the mass of the lid (bottom graph for 125 gm of beads).

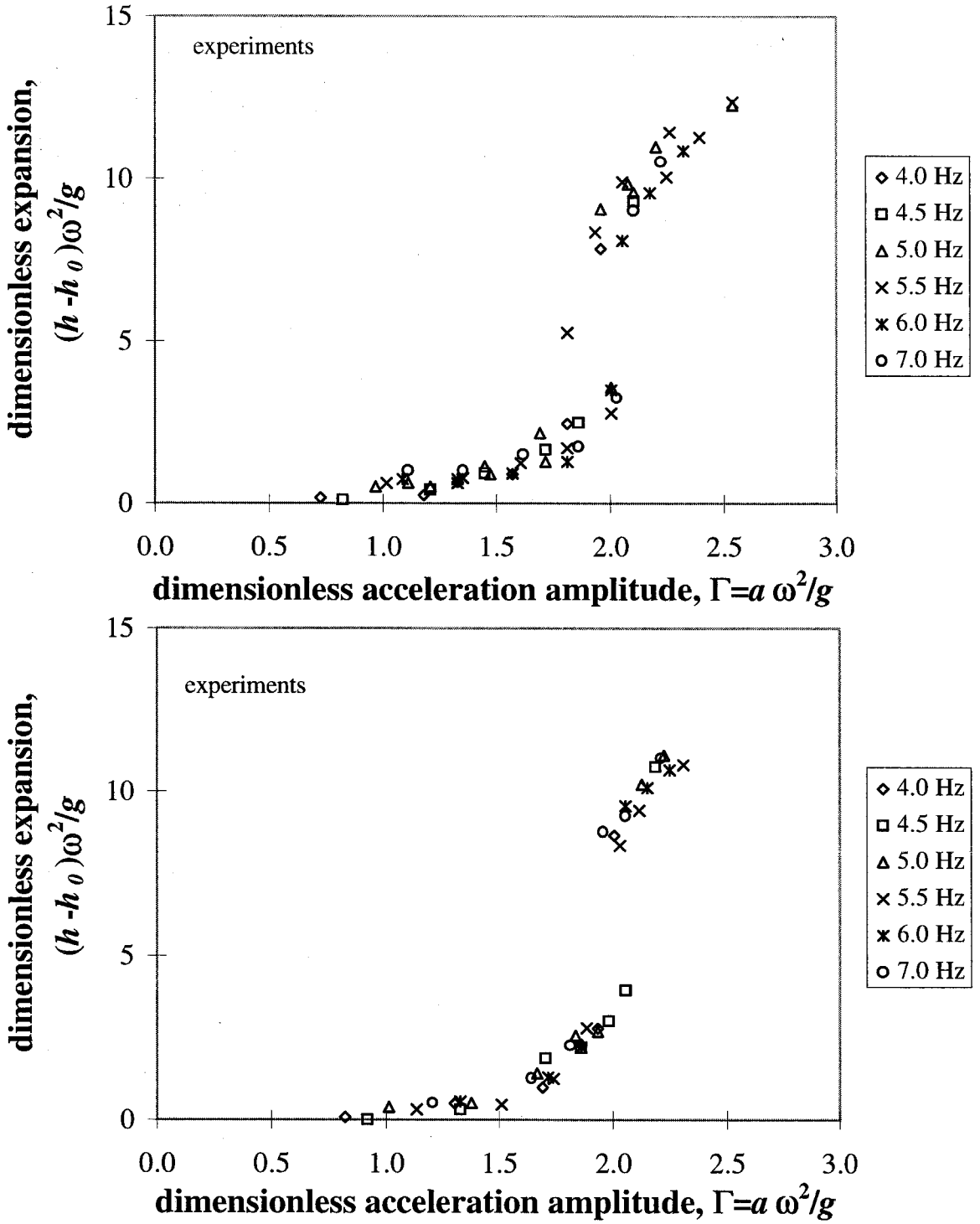

Figure 4.4: Dimensionless expansion, $(h - h_0)\omega^2/g$, plotted against dimensionless acceleration amplitude, $\Gamma = a\omega^2/g$, for experiments 2 and 3.

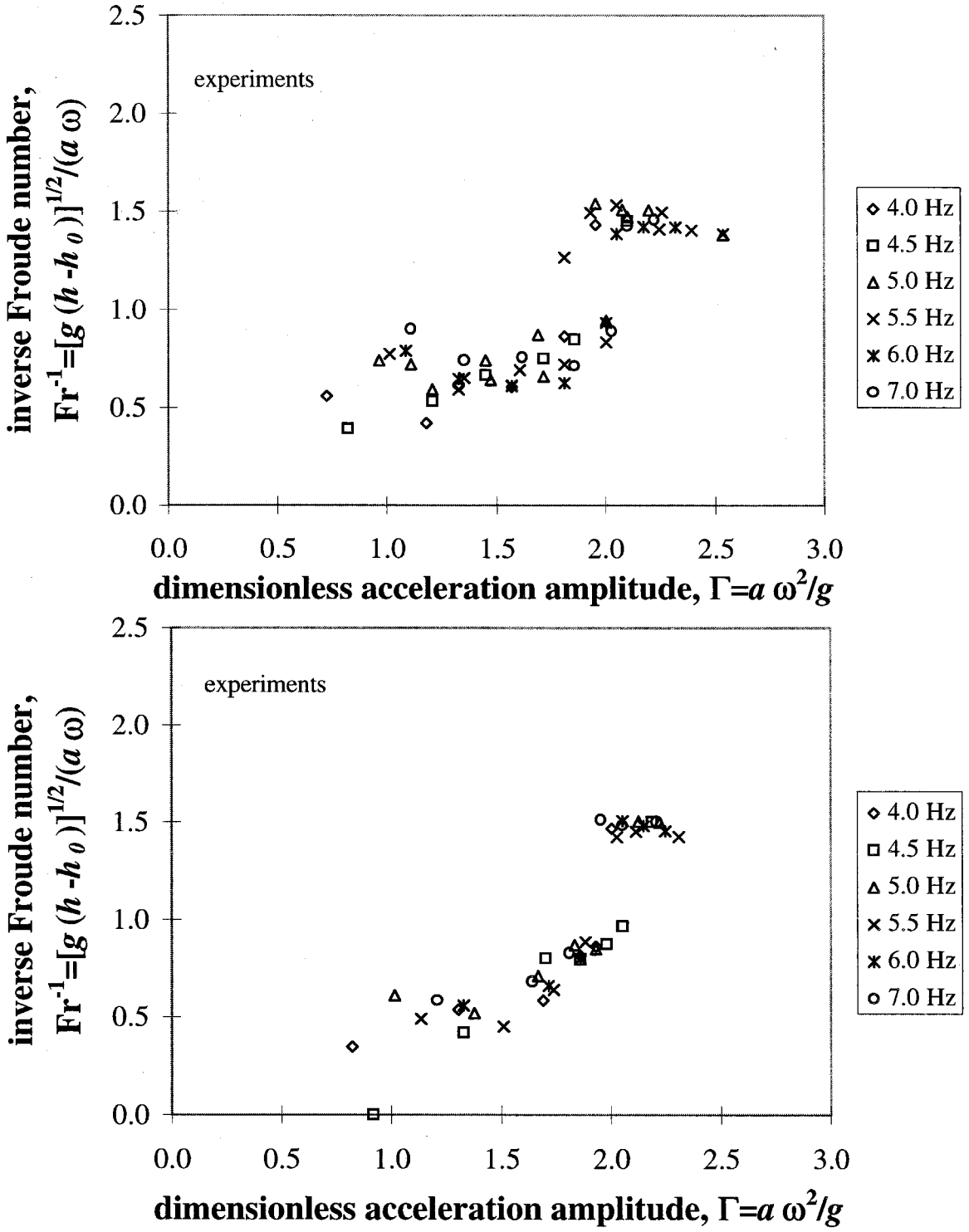

Figure 4.5: Inverse Froude number, $[g(h-h_0)]^{1/2}/a\omega$, plotted against the dimensionless acceleration amplitude, $\Gamma = a\omega^2/g$, for experiments 2 and 3.

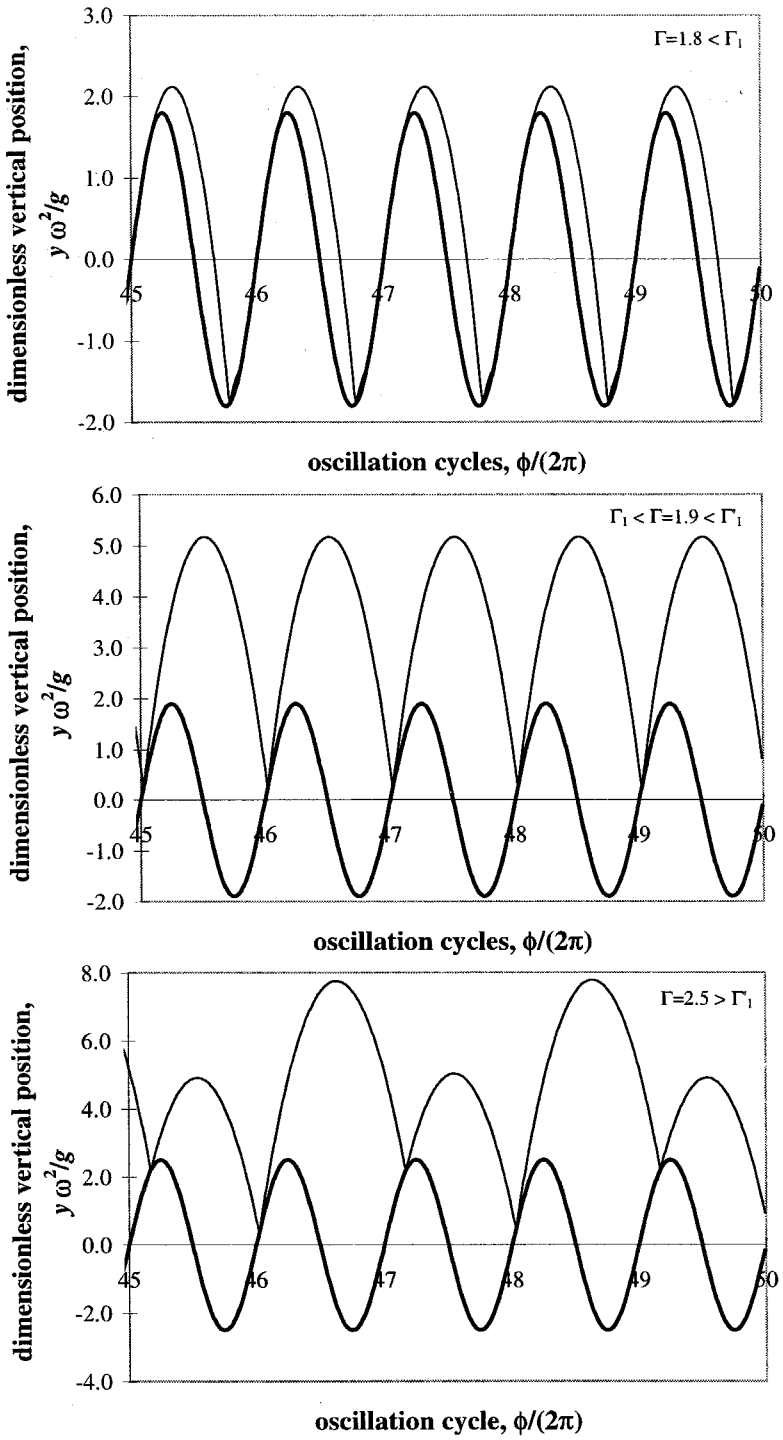

Figure 4.6: Particle and base trajectories as functions of oscillation phase angle. The coefficient of restitution for the calculations is $\epsilon = 0.25$ resulting in $\Gamma_1 = 1.89$ and $\Gamma_1' = 2.32$. The top figure shows the stable trajectories for $\Gamma = 1.8$, the middle figure is for $\Gamma = 1.9$, and the bottom is for $\Gamma = 2.5$. The dark line is the base trajectory and the lighter line is the particle trajectory.

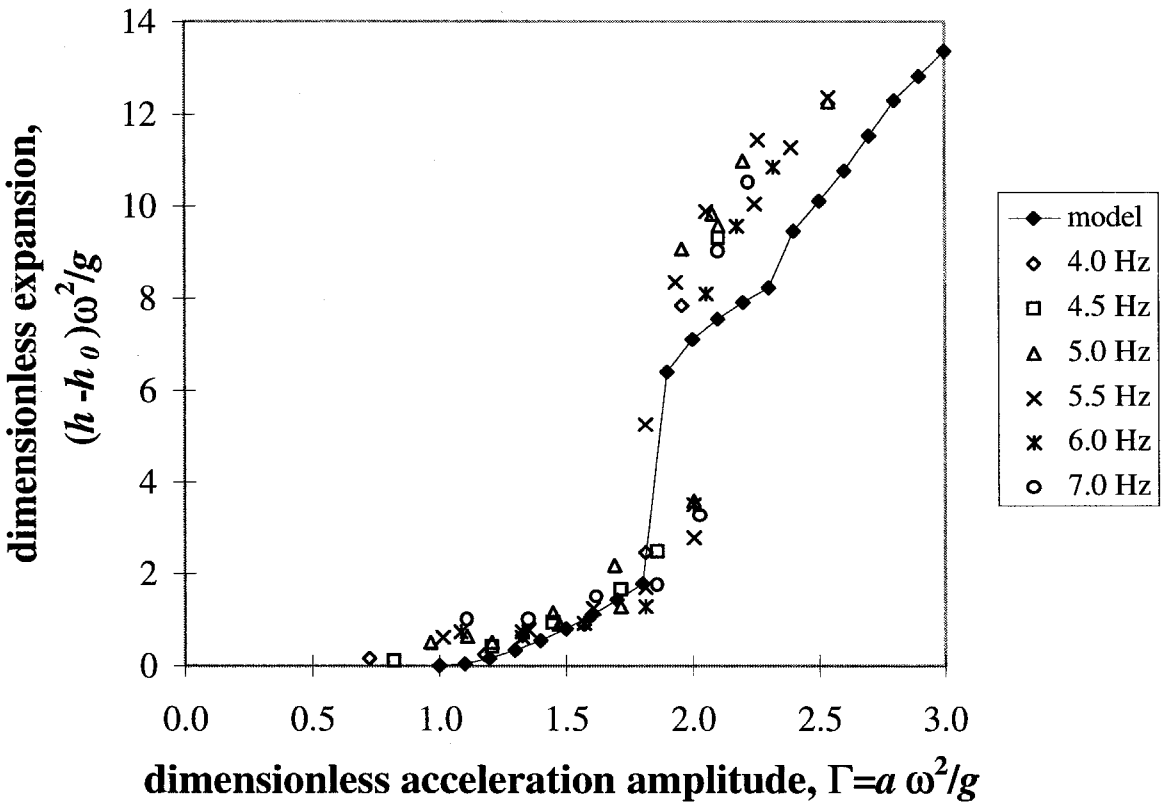

Figure 4.7: The dimensionless expansion, $(h - h_0)\omega^2/g$, plotted against the dimensionless acceleration amplitude, $\Gamma = a\omega^2/g$, for the data from experiment 2. The experimental data is compared with a numerical solution for a single particle bouncing on a sinusoidally oscillating base with $\epsilon = 0.25$.

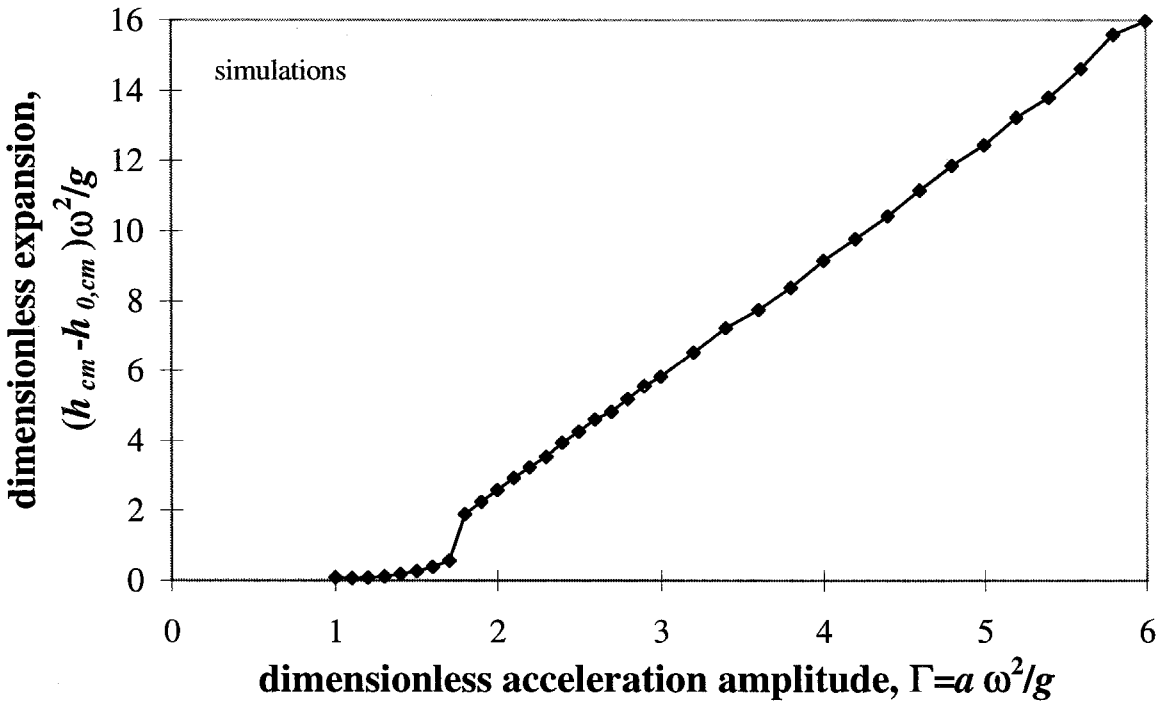

Figure 4.8: The average non-dimensional bed expansion, $\overline{(h_{cm} - h_{cm,0})}\omega^2/g$, plotted as a function of the oscillation acceleration amplitude, $\Gamma = a\omega^2/g$. The simulation parameters are given in table 4.1.

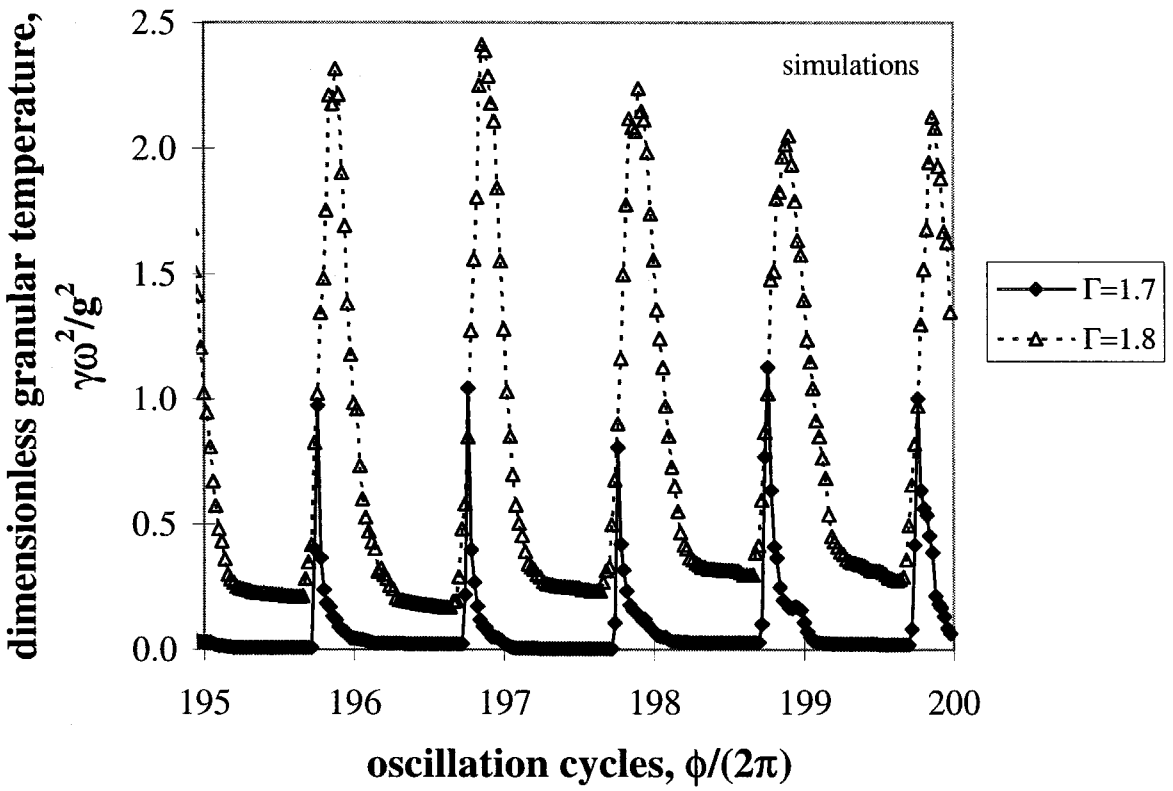

Figure 4.9: The dimensionless granular temperature per unit mass, $\gamma\omega^2/g^2$, plotted as a function of oscillation cycle for $\Gamma = 1.7$ and $\Gamma = 1.8$ at $f = 20$ Hz. The remainder of the simulation parameters are given in table 4.1.

Chapter 5 Side Wall Convection

5.1 Experiments

In deep beds, the inception value of Γ for side wall convection is $\Gamma \approx 1.2$, a value that is independent of particle and container size as well as oscillation frequency. As mentioned previously, the convection cell pattern is such that particles move down along the vertical walls of the container and up within the bulk returning to the free surface of the bed (refer to figure 3.1). By observing the motion of tracer particles, it was found that as particles moved down along the wall, they would enter the upward flow at various depths from the free surface. Note that these are the long term motions of the particles and not their instantaneous motion. The instantaneous motion is, in fact, up along the walls for a range of oscillation phase angles (discussed below); however, the long term motion is down at the boundaries.

Since measurements of the particle velocity were not made in these experiments, it was not possible to determine quantitatively how the convection velocity at the walls of the container varied with the vibration parameters. Qualitatively, however, the convection velocity increases with both increasing Γ at a fixed frequency and with decreasing frequency at a fixed Γ.

The effect of wall friction on the convection behavior was examined by using three different wall surfaces. When smooth glass walls were used, the convection velocity was essentially zero. Lucite walls produced weak, but observable, convection cells. Although these walls were smooth, static electricity effects between the walls and the particles were significant. Thus, the effective friction with the walls was greater than with the glass walls. The greatest convective motion was observed when sand paper was glued to the wall boundaries. For this last wall condition the particle motion at the walls could not be observed but the magnitude of the particle motion could be determined by examining the free surface of the bed. The faster the downward

motion at the walls, the greater the particle flux at the free surface.

By combining wall conditions, a vertical slice of the convection cell motion was observed. Using a narrow container with sand paper lined lateral walls and smooth glass front and rear walls, the structure of the convection cells was examined. Particles move downward along the sand paper walls in a boundary layer of approximately five to ten particle diameters thickness that extends from near the free surface to the base of the container. The thickness of the boundary layer does not vary significantly with the vibration parameters or with the container width for the containers used in the experiments.

The motion of the bed was also examined using the strobe lamp. The frequency of the strobe was tuned to approximately the forcing vibration frequency. Since the frequencies were not exactly equal, the state of the bed could be observed while the oscillation phase angle increased. This technique showed that the entire particle bed lifts off and re-collides with the base of the container once each oscillation cycle - an observation corroborated by the accelerometer output signal. Closer inspection revealed that the regions of the bed closest to the walls do not lift off the base as far as the regions at the center of the bed indicating that an effect at the wall boundaries is retarding the vertical movement of particles there.

A heap or mound also appears when $\Gamma > 1.2$ and is present until $\Gamma \approx 2.0$. The mound forms in the following manner. When Γ is just greater than one, the granular bed begins to deform near the wall boundaries and the disturbances slowly propagate toward the center of the container. The steady state behavior consists of a bed with a rounded free surface with the lowest points occurring at the walls and the highest point located in the center. Figure 3.2 shows a photo of a typical mound.

The stability of the formation was checked by perturbing the bed with a stirring rod. After the bed reached a steady state, the rod was immersed in the bed and stirred vigorously. The mound quickly reformed its original shape after the perturbations ceased.

An asymmetric heap observed by Evesque and Rajchenbach (1989) was not observed in the present experiments when care was taken to ensure that horizontal

vibrations were not present. When the experiments were first conducted, a peak similar to the one reported by Evesque and Rajchenbach was observed. The formation of the peak always appeared to one side of the container regardless of the initial conditions of the bed and despite perturbations with the stirring rod. In order to determine whether the container construction was affecting the results, the box was rotated 180°. The peak continued to appear to the same side of the container. Further experimentation showed that the location of the peak changed to the other side of the container when the oscillation frequency was below $f < 17$ Hz. Above 17 Hz the peak would reform to the other side. Thus, the peak location appeared to be dependent on the forcing frequency.

An additional accelerometer was mounted in a lateral orientation to the side of the container to determine whether horizontal vibrations were present in conjunction with the vertical vibrations. Indeed, significant horizontal accelerations, up to $1/3g$, were recorded occurring with a frequency equal to the forcing vertical vibrations. The source of the horizontal vibrations was traced to the shaker base construction. The Ling electromagnetic shaker has a trunnion style base that can rotate about a horizontal axis. When the container was mounted on the shaker such that the width (the longest dimension) of the box was perpendicular to the shaker's rotation axis, the asymmetric heap formation appeared. However, when the container was mounted parallel with the rotation axis, a symmetric rounded mound formed. A small asymmetric heap formed toward either the front or back wall of the container but its effect on the remaining bed behaviors was negligible. All of the remaining experiments were conducted in this configuration.

The depressions that form near the wall boundaries in the symmetric, rounded mounds are due to the downward motion of the particles at the walls. Particles leave the free surface at the wall as they move toward the base of the container. A depression forms since the particle bed has an angle of repose and particles do not fall into the depression until the local slope of the bed is greater than this angle. The critical angle is much less than the bed's static angle of repose because the oscillations affect the stability of the slope resulting in a lower effective angle of repose. As the

acceleration amplitude was increased, the slope of the mound at the walls decreased.

5.2 Simulations

In the simulations, side wall convection and mounding occur when $\Gamma > 1$. The qualitative appearance of both the convection cells and the mound is the same as that observed in the experiments. A snapshot from a simulations with a rounded mound is shown in figure 5.1. The long term particle velocities (refer to equations (3.1) and (3.2) in section 3.2) for the same particle bed are shown in figure 5.2.

The asymmetric mounds described by Evesque and Rajchenbach (1989) were never observed when horizontal oscillations were not included in the simulations. In order to check whether lateral vibrations were indeed the cause of the observed asymmetric peak, a simulation was performed that included both vertical and horizontal oscillations. The simulation employed a rectangular container that oscillated in the vertical and horizontal directions with acceleration amplitudes of $\Gamma_v = 1.5$ and $\Gamma_h = 0.3$, at the same frequency, $f = 20$ Hz. The remainder of the simulation parameters are given in table 5.1. A peak and circulation pattern formed similar to those found in the present experiments with horizontal vibrations. Figure 5.3 shows the steady state shape of the particle bed and the long term particle velocities. When the horizontal vibration was removed and only vertical vibration remained, the preference for the material to form a peak to one side of the container was eliminated. The remainder of the simulations utilize only vertical vibrations.

The simulation convection cell structure is similar to the experimentally observed structure. Particles move down along the vertical walls of the container in a narrow boundary layer and up within the bulk of the bed. Figure 5.4 shows the average particle displacements per oscillation cycle for a bed with $W/d = 50$, $h_0/d = 75$, $\Gamma = 1.6$ and $f = 20$ Hz. Note that two distinct convection cell centers, about which the particles move, are apparent.

In order to investigate the convection behavior quantitatively, three properties of the bed were measured based on the long term particle velocities. The three quantities

include the height of the convection cell center from the base, h, the width of the boundary layer, w, measured at height h, and the average number flux of particles, j_d, passing downward through width, w, at height h. Both w and h are determined by examining the vertical and horizontal particle velocities. The number flux of particles moving down in the boundary layer, j_d (with units of particles/m/cycle), is found by counting the number of particles that cross the plane extending from the wall boundary to the convection cell at height h each cycle. The definitions for w and h are illustrated in figure 5.4.

The parameters used in the baseline simulation for examining the convection cell behavior are given in table 5.2. The range of acceleration amplitudes, Γ, is restricted between 1.2 and 2.0. The lower bound is due to the very slow movement of particles at Γ near 1.0 and the upper bound is in order to avoid any $f/2$ wave effects. The experiments by Knight *et al.* (1996), with which many of the simulation results are compared, used discrete, sinusoidal taps as their forcing vibration signal. Since waves and kinks do not appear with this type of forcing, they were able to investigate convection behavior up to an acceleration of roughly $13g$. Although the shaking style and range of accelerations are different between the simulations and experiments, the results from the two are consistent. Note also that a high coefficient of friction, μ, of 1.0 is used in the simulations. This point is addressed in further detail below when discussing the effect of friction on the behavior of the convection cells. Fewer oscillation cycles are required for averaging when a high value of μ is used since the velocity fluctuations in the convection cells are much smaller than the mean velocities. The three measures, w, h, and j_d, were examined as functions of the oscillation acceleration amplitude, Γ, and frequency, f, container width, W, bed depth, h_0, coefficient of restitution, ϵ, and coefficient of friction, μ.

The vertical and horizontal velocity profiles corresponding to planes passing through the right convection cell center for the bed in figure 5.4 are shown in figure 5.5 and 5.6. Note that the aspect ratio of the bed, defined as the bed depth divided by the container width, h_0/W, is 1.5. The width, w, of the boundary layer and the convection cell height, h, are determined from these velocity profiles. The shape of the profiles is

also of interest. The vertical velocity profile shows that considerable shearing occurs in the downward flow of particles near the wall. The upward flow of particles in the interior of the bulk is more plug-like. Furthermore, the width of the boundary layer does not vary significantly with depth from the free surface. Knight *et al.* (1996) measured the vertical velocity profiles in experiments and found a similar qualitative shape as well as the w depth independence. They found that the vertical velocity profile was approximated equally well with a hyperbolic cosine or a first-order modified Bessel function. The solid and dashed lines in figure 5.5 are least squares fits to the functions

$$\frac{\dot{y}}{d} = \frac{\dot{y}_{c1}}{d} + \frac{B_1}{d}(1 - \cosh(\frac{x - \frac{W}{2}}{x_{c1}})) \tag{5.1}$$

and

$$\frac{\dot{y}}{d} = \frac{\dot{y}_{c2}}{d} + \frac{B_2}{d}(1 - I_0(\frac{x - \frac{W}{2}}{x_{c2}})) \tag{5.2}$$

where $\dot{y}_{c1}$, B_1, x_{c1}, $\dot{y}_{c2}$, B_2, and x_{c2} are adjustable parameters. The axial velocity is given by $\dot{y}_{c1}$ and $\dot{y}_{c2}$, the parameters B_1 and B_2 are the amplitude of the curvature term, and x_{c1} and x_{c2} are radial or horizontal width scales. Clearly the simulation velocity profile is fit well with these functional forms.

Three important observations are seen in the horizontal velocity profile (figure 5.6). First, particles enter the upward flow in the bulk at all depths below the convection cell center. Furthermore, the velocity at which the particles enter the upward flow is nearly independent of depth indicating that the flux of particles entering the upward flow is also independent of depth from the free surface (note that the density of particles crossing the vertical plane separating the downward and upward flowing remains nearly constant with increasing depth). Lastly, there is a small region extending from the free surface to the convection cell center where particles leave the upward flow and enter the downward flow. This last observation is a result of mass conservation of the particle flow.

The fact that the flux of particles entering the upward flowing region, j_e, is independent of depth,

$$j_e = \bar{j}_e \tag{5.3}$$

where $\bar{j_e}$ is a constant, implies that the downward flux of particles, j_d, increases linearly with height from the base (see figure 5.7) since

$$wj_d(y) = \int_0^y j_e d\xi = \bar{j_e} y \tag{5.4}$$

where y is measured from the base of the container and the bulk density of the bed is assumed to be constant. Note that the upward flux of particles (and centerline velocity) is proportional to the downward flux. Knight *et al.* (1996) measured the upward centerline particle velocity in their experiments and found that it increased exponentially with height from the base. They proposed a simple model in which the flux of particles scattered from the walls into the upward flow, $j_e(y)$, is directly proportional to the number of particles available to be scattered, $j_d(y)$. If the probability of scattering from the walls, p, is assumed to be independent of depth, the upward and downward flux of particles increase exponentially with height from the base,

$$j_u(y) \propto j_d(y) \propto e^{py} \tag{5.5}$$

The apparent discrepancy between the experiments and simulations, however, may be due to the different values of Γ examined. Knight *et al.* used values of Γ between 3.0 and 12.0 while the simulations examined $\Gamma < 2.0$. Note that the scattering probability p may decrease with decreasing Γ since the particle bed is in the air for a shorter duration of time. Furthermore, when py is small, the exponential function can be approximated by a linear function and the experimental and simulations become consistent.

The width of the downward flowing boundary layer, w, at the convection cell center height, h, is determined from the vertical velocity profile. The simulations indicate that w is independent of oscillation acceleration amplitude, Γ, and frequency, f, as well as the wall friction coefficient, μ_{pw}. The boundary layer width decreases with increasing coefficient of restitution, $\epsilon = \epsilon_{pp} = \epsilon_{pw}$, however. The width also varies proportionally with the container width in containers where the bed aspect

ratio, h_0/W, is greater than approximately 0.2. But remains nearly constant for $h_0/W < 0.2$. These observations are clearly seen in figure 5.8 which shows the results from simulations conducted with various container widths and bed depths (top figure). The bottom plot of figure 5.8 shows, for clarity, the variation of w with W for a bed with depth $h_0/d = 30$. Knight *et al.* (1996) found that the width of the boundary layer is proportional to container width in their experiments using beds with aspect ratios of order 2.0. This result is in agreement with the simulation results since Knight *et al.* performed their experiments with high aspect ratio beds. Note also that in the high aspect ratio beds, $h_0/d > 0.2$, the convection cells interact with each other (refer to figure 5.4) while in low aspect ratio beds, $h_0/W < 0.2$, the convection cells do not interact (figure 5.2). This suggests that the interaction between the convection cells may be the mechanism affecting the boundary layer width.

The height of the convection cell center from the base of the container, h, is found to vary linearly with the bed depth, h_0 as observed in figure 5.9. Simulations performed for various container widths, W, wall friction coefficients, μ_{pw}, and coefficients of restitution, $\epsilon = \epsilon_{pp} = \epsilon_{pw}$, indicate that the convection cell center height is independent of these parameters. The height does decrease, however, with increasing oscillation amplitude, a, and oscillation velocity amplitude, $a\omega$. The height, h, scales equally well with both a and $a\omega$ indicating that the oscillation frequency does not affect h significantly for the vibration parameters examined here. The height plotted against oscillation velocity amplitude is shown in figure 5.10. The decrease in h as $a\omega$ increases may be a consequence of mass conservation since the downward flux of particles, j_d, also increases with increasing oscillation amplitude and velocity (shown in figure 5.11), and the boundary layer width, w, remains constant.

The dependence of the particle flux, j_d, on the coefficient of wall friction, μ_{pw}, and coefficient of restitution, $\epsilon = \epsilon_{pp} = \epsilon_{pw}$, was also examined. Figure 5.12 shows that the flow of particles past the convection cell center each cycle, wj_d, increases with an increasing coefficient of wall friction, μ_{pw}. Note that the flow of particles approaches zero when $\mu_{pw} \approx 0.1$. Thus, the coefficient of wall friction is found to only affect the flux of particles in the convection cells and not the boundary layer width or

convection cell height. Additionally, when periodic boundaries are used $j_d = 0$ and no convection is observed.

The flux also varies with the coefficient of restitution, $\epsilon = \epsilon_{pp} = \epsilon_{pw}$ as shown in figure 5.13. The flux decreases with increasing ϵ and rapidly decreases when $\epsilon > 0.7$. A possible reason for this trend is discussed in the next section.

These trends suggest that particle/wall interactions as well as the vibration parameters are significant to the convection cell behavior. The precise mechanism that causes convection, however, has not yet been examined. As a result, the detailed motion of the bed over an oscillation cycle is studied. Since the particle/wall interactions appear to be fundamental to the convection mechanism, the forces acting on the walls due to the particle bed are examined.

The average total normal and shear forces acting on the particle bed due to the floor and vertical walls is plotted as a function of oscillation phase angle in figures 5.14 and 5.15 for a bed oscillating at $\Gamma = 1.6$ and $f = 20$ Hz. Figure 5.15 shows the same plots but for the range of phase angles where the bed is in flight. Forces acting on the walls due to particle bed (and, conversely, the forces acting on the particle bed due to the walls) are determined by summing particle/wall contact forces determined using the contact model described in section 2.2. The force profiles are consistent from cycle to cycle and the figure shows the forces averaged over 100 oscillation cycles. For $0 < \phi/(2\pi) < 0.20$, where ϕ is the oscillation phase angle in radians, the bed rests on the oscillating base as reflected in the forces acting on the container walls and base. As the acceleration of the base approaches $-1g$ the effective gravity acting on the particles decreases and the forces on the base and walls decrease proportionally with the effective gravity. When the particle bed leaves the floor the total vertical force on the floor is zero. The shear force acting on the vertical walls, however, is small but non-zero due to particle collisions. Measurements of the contact duration for collisions between particles and the walls indicate that nearly all of the contacts occur as binary collisions; particles are not "pressed" into the walls as has been suggested in previous studies (see Gallas *et al.* 1992 and Taguchi, 1992). Since the motion of the walls relative to the bed is down, particles contacting the walls are

retarded in their upward movement. When $\phi/(2\pi) = 0.54$ the bed begins to fall back toward the base and the motion of the walls is now upward relative to the bed. Thus, collisions with the walls act to reduce the downward movement of the particles. However, fewer collisions occur with the walls as the bed falls back toward the base than when the bed moves up relative to the base as illustrated in figure 5.16, which shows the collision rate with the walls, $\dot{N}_c$ (with units of collisions per second), as a function of phase angle, ϕ. As a result, the upward acting shear force on the bed is smaller than the downward acting shear force and a net downward acting shear force acts on the particle bed while it is in flight. When the bed re-collides with the base at $\phi/(2\pi) = 0.64$, a large normal and shear force peak occurs on the floor and walls. For the remainder of the cycle the bed rests on the floor of the container and the forces acting on the walls and floor are proportional to the effective gravity.

The reason fewer collisions occur with the walls as the bed flight progresses is because the bed dilates when it is sheared and particles move away from wall. Furthermore, the bed, while in flight, can dilate in the vertical direction since the floor boundary no longer restricts the movement of particles there. Thus, the shearing by the walls causes particles to move toward the centerline of the bed, which in turn dilates in the vertical direction to accommodate the incoming flux of particles. This particle motion is clearly seen when examining the instantaneous particle velocities in the bed at various phase angles of oscillation. Figure 5.17 shows the instantaneous particle velocities relative to the bed's center of mass (averaged over 20 oscillation cycles) at six oscillation phase angles. For $\phi/(2\pi) = 0.16$ the bed rests on the container base and moves with it. At $\phi/(2\pi) = 0.40$ the center of mass of the bed moves up relative to the base. Note that the particles near the container walls move down with respect to the center of mass of the bed due to interactions with the wall. Particle movement away from the walls is also evident. As the bed falls back toward the base at a phase angle of $\phi/(2\pi) = 0.60$, the particle flux away from the walls is easily observed. Furthermore, the velocity vectors at the top and bottom free surface of the bed, especially near the walls, show that the bed dilates in the vertical direction. Note that near the walls the separation distance from the particles and the base is

not as great as it is at the centerline. As a result, these regions near the walls collide with the base first as is shown at a phase angle of $\phi/(2\pi) = 0.72$. A consolidation wave is observed to propagate up through the bed as particles continue to collect on the base as is seen at phase angles of $\phi/(2\pi) = 0.74$ and $\phi/(2\pi) = 0.76$. The waves in the bed quickly dissipate and the bed moves with the base once again and the cycle is repeated.

5.3 Discussion

Side wall convection and heaping have been the most extensively studied vibrating bed behaviors. A number of experiments, simulations, and theoretical works have been performed in order to understand these phenomena better.

Zik and Stavans (1991) examined diffusion in vibrating beds and reported behavior similar to that reported in the present experiments. Clément *et al.* (1992) examined a single layer of monosize spherical glass beads constrained to move in two dimensions. They observed a large mound formation that forms as particles slip along dislocation zones. These effects are most likely the result of the strong tendency for particles of the same size in 2D to arrange themselves into a hexagonal packing structure. Rátkai (1976) examined beds in a container with fixed walls and a modulated vibrating base where the largest amplitude of vibration occurs in the center of the base and is zero at the walls. He reported the appearance of convection cells as well.

Simulations by Gallas *et al.* (1992) and Taguchi (1992) were not able to reproduce the rounded mounds, however; they used an unusual tangential interaction term in the simulations which may account for this discrepancy. The simulations by Lee (1994) did produce rounded mounds using a tangential interaction similar to that used in the present work. He found that increasing the inter-particle friction increased the slope of the mound but a sharp peak never formed.

This last point is a significant one. In all of the simulations and experiments performed here (not including those with horizontal vibrations), the mounds that appear consist of rounded, shallow peaks with the lowest points occurring next to

the wall boundaries. In experiments performed by Laroche *et al.* (1990) and Pak *et al.* (1995), sharp-peaked heaps appeared when $\Gamma > 1$, even when wall boundaries were not present. This discrepancy is most likely a result of the interstitial fluid effects on the particles. Laroche *et al.* and Pak *et al.* found that the sharp peaks only formed for small particles ($d < 1$ mm) in air. When large particles were used or when the experiments were performed in a vacuum, the sharp peaks disappeared. Both groups, however, observed mounds and convection cells similar to the ones described in the present experiments next to the container boundaries. To further support the idea that interstitial fluid effects produce the sharp peaks, the simulations performed here and elsewhere (see Lee, 1994, for example), which do not include interstitial fluid effects, produce only rounded mounds and never sharp peaks.

The asymmetric peak and convection cell observed by Evesque and Rajchenbach (1989) for $\Gamma > 1.2$ appears to be the result of vertical and horizontal vibrations as opposed to just vertical vibrations, which is consistent with the present experimental observations. The reason the coupled horizontal and vertical vibrations produce the asymmetric heap is straightforward. The mechanism is the same as that used for transporting material on vibrating conveyor belts (see for example, Evesque, 1992). Assuming that the base moves in a sinusoidal vertical and horizontal trajectory at the same frequency, the bed of material will move to the left or right depending on the flight time of the bed which, in turn, is a function of Γ. The assumption that the bed oscillates horizontally and vertically with the same frequency is made based on the accelerometer signals in the experiments. This matching of frequencies is a result of the vertical vibrations forcing the horizontal vibrations. At low vertical acceleration amplitudes the bed leaves the base once each oscillation cycle (assuming $\Gamma > 1$). When the bed leaves the base, it has a horizontal velocity due to the lateral velocity of the base at take-off. Furthermore, while the bed is in flight, the base moves horizontally as well as vertically. When the bed re-contacts the base, it can be in a different horizontal position, either to the left or right of its original position, depending on the acceleration level of the bed. The dependence on frequency in the present experiments may be a result of slippage with the base since at a given Γ the

velocity increases with decreasing frequency.

The experimental work by Knight *et al.* (1993, 1996) and Ehrichs *et al.* (1995) have, perhaps, the most quantitative experimental examination of the side wall convection phenomenon. Using magnetic resonance imaging (MRI) they examined the convection behavior in narrow cylinders (of order of 12-50d) filled with poppy seeds for $1.5 < \Gamma < 13.0$. Due to the constraints imposed by the MRI apparatus, they were not able to examine larger containers. Furthermore, since MRI requires some time to form an image, the applied vibration consisted of discontinuous, sinusoidal taps as opposed to the continuous oscillations used in the present experiments. They indicate that these taps produce convection patterns similar to those observed for continuous vibration. Note though that they do not report the appearance of other phenomena such as surface waves or kinks which may influence the convection cell behavior. The reason they do not see these other phenomena is most likely due to the style of shaking employed in their experiments. Nevertheless, the velocity profiles from the simulations compare well with their experimental results.

Previous studies have also used computer simulations to examine the convection phenomenon. Gallas *et al.* (1992), Taguchi (1992), Rosato and Lan (1994), Lee (1994), and Luding *et al.* (1994a) have all reported the appearance of convection cells for $\Gamma > 1$ in two-dimensional simulations of circular particles in containers subject to vertical, sinusoidal vibration. Care must be taken when interpreting the results since various boundary conditions were used in the simulations. For example, Gallas *et al.* (1992) used fixed vertical wall boundaries as opposed to wall boundaries that move in phase with the oscillating base. Surprisingly, none of these simulations were used to extract much quantitative information about the convection behavior. Most of the work has focused on examining the onset of the phenomenon and the effect of wall and interparticle friction. Nonetheless, several interesting results have been found. First, the strength of the convection behavior, measured by Taguchi (1992) as the sum of all the particle displacements over one oscillation cycle, increases with increasing Γ for a fixed frequency. Second, the convection strength decreases as the coefficient of wall friction decreases. Third, Rosato and Lan (1994) observed that the convection cells

remain close to the wall boundaries when very wide containers are used. All of these results are consistent with the observations made in the present experiments and simulations. One other interesting observation made in the simulations by Gallas *et al.* (1992) is that when the wall friction is zero, convection cells with particles moving up at the walls are sometimes observed. This behavior is never observed in the present simulations and may be a result of the unusual tangential particle interaction model used by Gallas *et al.*.

The convection behavior has also been observed in theoretical work by Goldshtein *et al.* (1995) and Savage (1988). Both works use a kinetic theory approach to determine the particle trajectories in vibrated beds. Several concerns about the assumptions used in both analyses are readily apparent. First, from the experimental and simulation work indicate that particles in the bed are in long duration contact with several neighboring particles during a large portion of the oscillation cycle. This clearly violates the kinetic theory assumption of binary, instantaneous contacts. Additionally, since particle velocities in the downward moving boundary layer vary significantly over a length of a few particle diameters, the continuum assumption in the kinetic theory approach is questionable. Although these kinetic theory approaches still provide interesting information and results, these issues must be addressed.

A number of hypotheses have been offered as to the cause of the side wall convection behavior. Rajchenbach (1991) suggests that heap formation causes convection. His argument is based on the idea that particles located deep in the bed have a greater confining pressure than particles in shallow regions and, as a result, tend to move less readily than particles in these shallow regions. Furthermore, particles with a given random kinetic energy (supplied by the vibrations) will have a tendency to migrate to regions that have less random energy. This argument has a number of difficulties. For example, it does not explain why particles should not always move toward the base of the container although the confining pressures there would be the greatest (assuming the bed is less than a few container diameters deep). Furthermore, in the present experiments when the bed was perturbed with a stirring rod such that one side of the container was considerably deeper than the other, the original, symmetric convection

cells and bed shape quickly reformed. According to Rajchenbach's hypothesis the perturbed formation should be stable.

Taguchi (1992) has also offered a mechanism to explain the appearance of the convection cells. His hypothesis is that during the part of the oscillation cycle in which the bed rests on the base of the container, the lateral wall boundaries, the base, and gravity induce a vertical and horizontal stress in the bed. When the bed is in flight, it can release this stored vertical strain energy by dilating in the vertical direction since the confining base no longer prevents particle movement. In the horizontal direction, however, the particles are still constrained by the walls and so the horizontal stress induces a horizontal flow of particles toward the center of the container. When the flowing particles collide at the center, their motion turns in the vertical direction. The flow cannot turn downward, however, due to the base and so particles move toward the free surface. The vacancy formed at the bottom of the bed, due to particle movement to the free surface is filled by horizontally neighboring particles. Although it would have been possible to examine this stress field in Taguchi's simulations, he did not do so. One problem with Taguchi's hypothesis is that it does not offer a mechanism that can explain the effect of wall friction on the convection strength. In fact, the mechanism is independent of wall friction and predicts convection even for frictionless walls contrary to what is observed in experiments (as in the present experiments using very smooth glass walls) and in simulations.

One other hypothesis that has been offered was first suggested by Gallas *et al.* (1992) and examined briefly in simulations by Lee (1994). Gallas *et al.*'s argument is as follows. When the bed first lifts off the base during an oscillation cycle, it is densely packed and exerts a strong pressure on the walls of the container which in turn results in a significant frictional force. Since the motion of the bed with respect to the walls is upward, the particles near the walls experience a downward acting drag force due to the boundaries. When the particle bed falls back to the container base and has an upward velocity relative to the walls, the bed packing is much looser and, as a result, the pressure on the walls is less. The lower pressure results in a smaller upward drag force acting on the particle bed near the walls. Thus, the bed experi-

ences a net downward acting drag force due to the walls. The force measurements from the present simulations indicate that this is indeed what is occurring during an oscillation cycle. Note though that the simulations indicate that particles are not "pressed" into the walls as suggested by Gallas *et al.* but instead are involved in binary collisions with the walls while in flight.

This asymmetric drag mechanism also explains the effect of increasing wall friction. If the wall friction is large, the velocity difference between particles at the walls and at the center of the bed will be larger than if the wall friction is small. At the limit of $\mu_{pw} = 0$, the particle velocity difference is zero and no convection occurs.

The decrease in the downward particle flow rate, wj_d, with increasing coefficient of restitution may be due to the fact that highly elastic particles will have a greater rebound velocity after a collision with the wall than if a lower coefficient were used. Thus, high ϵ particles will have a larger momentum away from the wall than low ϵ particles and will be less likely to remain in the immediate neighborhood of the wall boundaries. As a result, fewer collisions occur with the walls throughout the entire cycle of oscillation when high ϵ particles are used and the convection cell flow rate is reduced.

The asymmetric drag mechanism may also explain the effect of the bed aspect ratio on the boundary layer width. When the aspect ratio is large, $h_0/W > 0.2$, particles moving away from the walls toward the center of the container have a large effective "ambient" pressure into which to move. Since convection cells interact in high aspect ratio beds, particles moving away from the walls collide in the center of the bed. This, in effect, increases the ambient pressure into which the particles move away from the walls. Thus, the narrower the container, the greater the convection cell interaction, and the greater the effective ambient pressure. The result is that particles are forced to turn in the vertical direction after a short distance from the wall and, consequently, the boundary layer width is reduced.

Three different mechanisms can produce mounds and convection cells in beds subject to vertical accelerations greater than $1g$. When horizontal oscillations and interstitial fluid effects are negligible, an asymmetric drag mechanism causes the

convection cell behavior. The rounded mounds that appear are the direct result of particle movement at the wall boundaries of the container. Measurements from the simulated bed correlate well with the experimental and simulation results of others. In addition, the present simulations were used to investigate the side wall convection behavior in more detail than has been done previously.

Tables and Figures

Γ_v	1.5
Γ_h	0.3
f	20 Hz
W/d	100
h_0/d	10
N	1000
ϵ_{pp}	0.80
$k_{n,pp}$	$5.289 * 10^3$ N/m
ν_{pp}	$8.337 * 10^{-3}$ N/(m/s)
$k_{s,pp}$	$5.289 * 10^3$ N/m
μ_{pp}	1.0
lateral boundaries	walls
$k_{n,pw}$	$1.058 * 10^4$ N/m
ν_{pw}	$1.667 * 10^{-2}$ N/(m/s)
$k_{s,pw}$	$1.058 * 10^4$ N/m
μ_{pw}	1.0
d	0.9 - 1.1 mm
ρ	2500 kg/m^3
Δt	$3.504 * 10^{-6}$ sec

Table 5.1: The simulation parameters used to examine the asymmetric heap observed when the container is subject to vertical and horizontal oscillations.

W/d	50
h_0/d	20
N	1000
ϵ_{pp}	0.80
$k_{n,pp}$	$5.289 * 10^3$ N/m
ν_{pp}	$8.337 * 10^{-3}$ N/(m/s)
$k_{s,pp}$	$5.289 * 10^3$ N/m
μ_{pp}	1.0
lateral boundaries	walls
$k_{n,pw}$	$1.058 * 10^4$ N/m
ν_{pw}	$1.667 * 10^{-2}$ N/(m/s)
$k_{s,pw}$	$1.058 * 10^3$ N/m
μ_{pw}	1.0
d	0.9 - 1.1 mm
ρ	2500 kg/m^3
Δt	$3.504 * 10^{-6}$ sec

Table 5.2: The simulation parameters used to examine the side wall convection behavior.

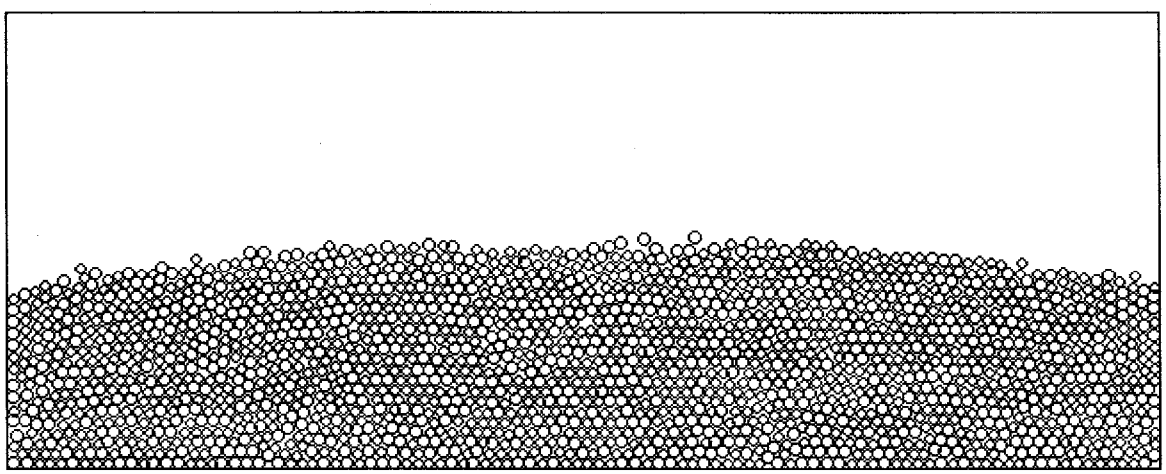

Figure 5.1: Simulation showing a particle bed after 821 oscillation cycles (approximately 42 seconds) at $\Gamma = 1.5$ and $f = 20$ Hz. The container width is $W/d = 100$ and the bed height is $h_0/d = 20$. A rounded mound is clearly observed on the free surface of the bed. The remainder of the simulation parameters are given in table 5.2.

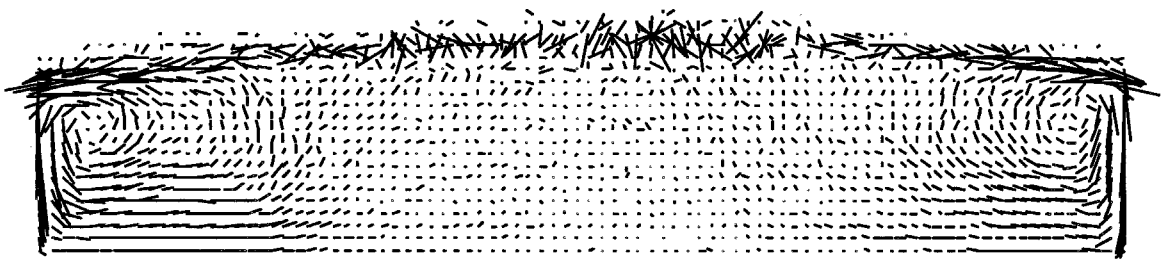

Figure 5.2: The average displacement per cycle vectors (long term velocities) for particles in the bed shown in figure 5.1. The direction of the convection cells is down along the vertical walls and up in the interior of the bulk. The velocity vectors are averaged over 800 oscillation cycles. Note that the velocity vectors have been scaled and so appear to extend beyond the container walls.

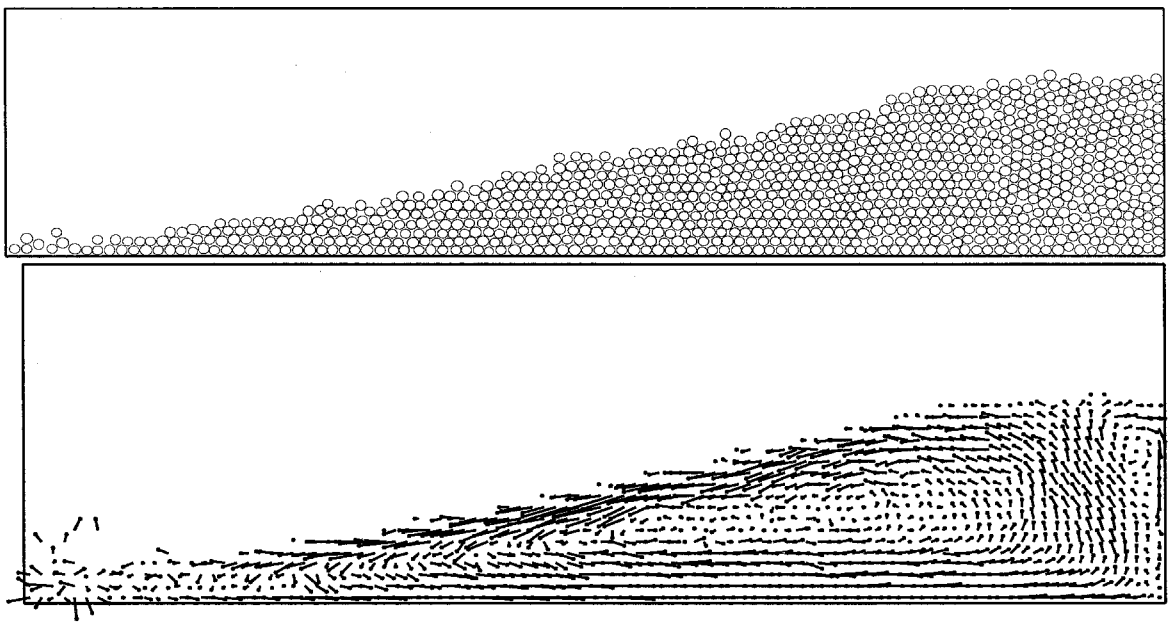

Figure 5.3: Top: A particle bed subject to vertical and horizontal oscillations. Bottom: The long term particle velocity vectors for the same bed. The method for determining the particle velocities is described in the text. The figures show the bed after 100 oscillation cycles and the velocity vectors averaged over 50 cycles. The solid circles at the end of the vectors are the vector arrowheads. The simulation parameters are given in table 5.1. Note that the velocity vectors have been scaled and so appear to extend beyond the container walls.

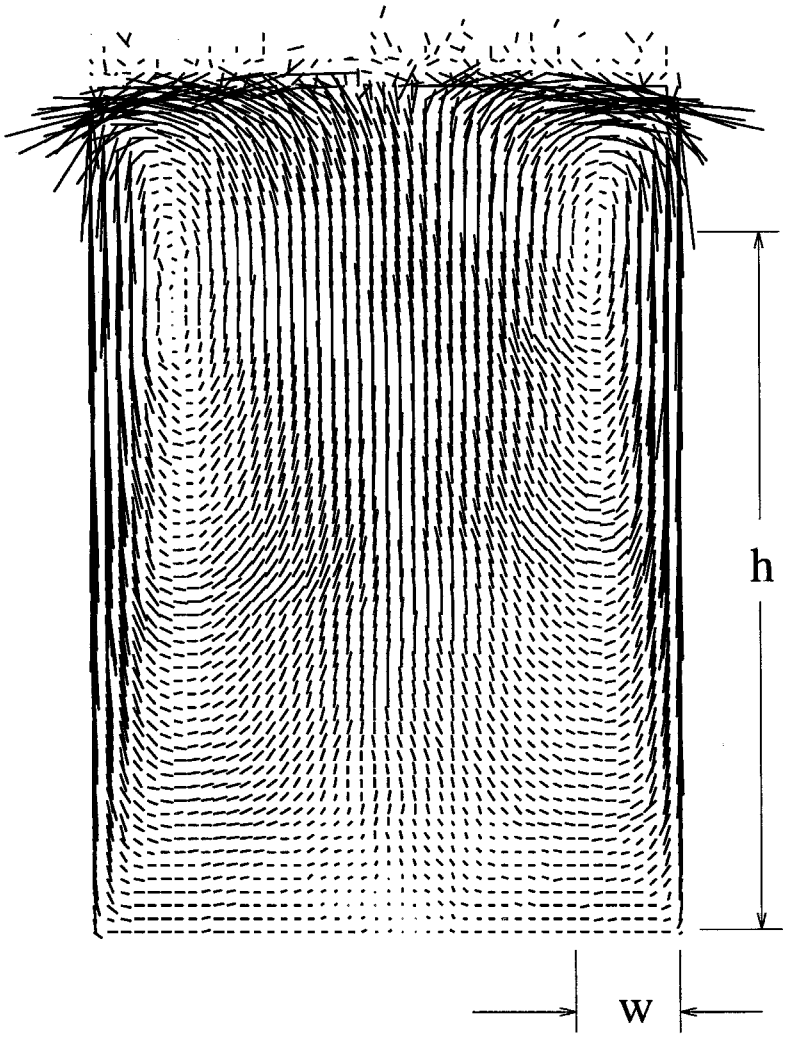

Figure 5.4: The average displacement per cycle vectors (long term velocities) for particles in a bed with $W/d = 50$, $h_0/d = 75$ ($N = 3750$), $\Gamma = 1.6$, and $f = 20$ Hz. The velocity vectors are averaged over 130 oscillation cycles. The remainder of the simulation parameters are given in table 5.2. The direction of the convection cells is down along the vertical walls and up in the interior of the bulk. Note that the velocity vectors have been scaled and so appear to extend beyond the container walls. The definitions for the boundary layer width, w, and convection cell height, h, are also illustrated for the right convection cell.

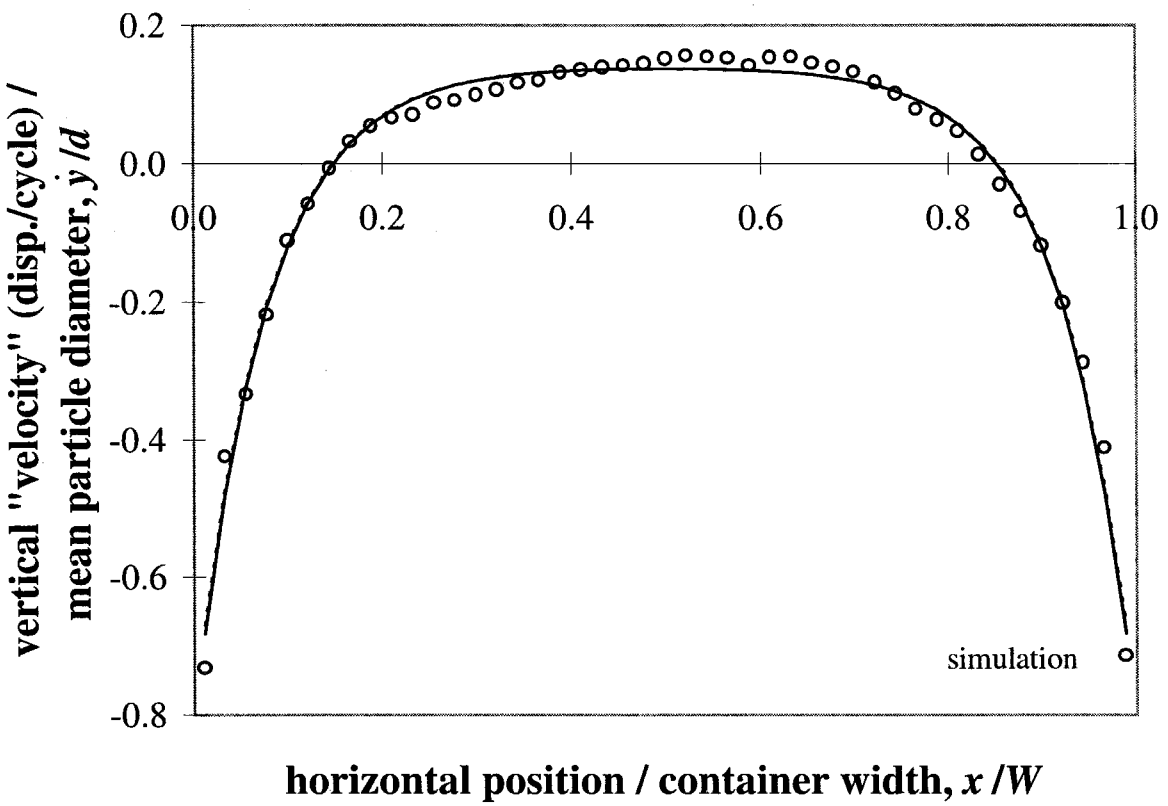

Figure 5.5: The vertical velocity profile measured at the plane that passes through the center of the right convection cell for the bed in figure 5.4. The solid and dashed lines are least squares fits to the functions $\dot{y}/d = \dot{y}_{c1}/d - B_1/d * (1 - \cosh(\frac{(x-x_0)/d}{x_{c1}/d}))$ and $\dot{y}/d = \dot{y}_{c2}/d - B_2/d * (1 - I_0(\frac{(x-x_0)/d}{x_{c2}/d}))$, respectively where x_0 is the center line position of the container. The two curve fits lie on top of one another and are indistinguishable. The adjustable parameters are: $\dot{y}_{c1}/d = 0.14$, $B_1/d = 0.0030$, $x_{c1}/d = 3.86$, $\dot{y}_{c2}/d = 0.14$, $B_2/d = 0.0055$, and $x_{c2}/d = 3.56$.

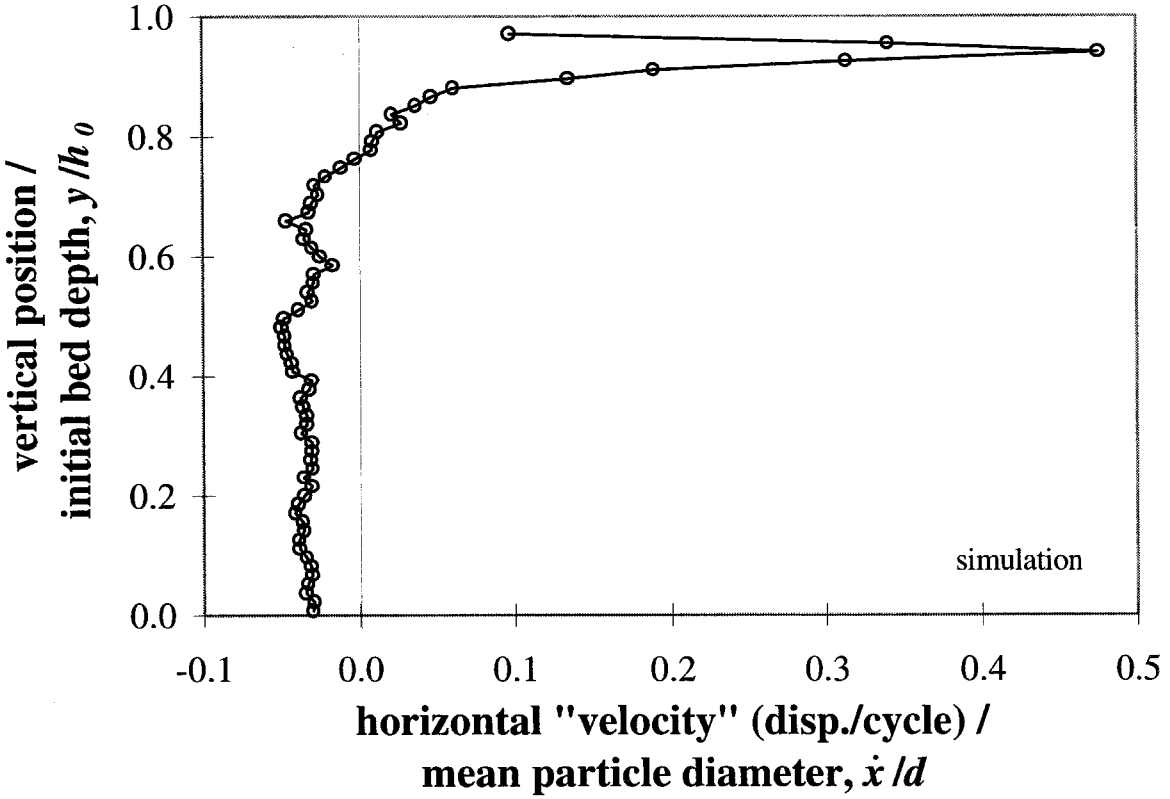

Figure 5.6: The horizontal velocity profile measured at the plane that passes through the center of the right convection cell in figure 5.4.

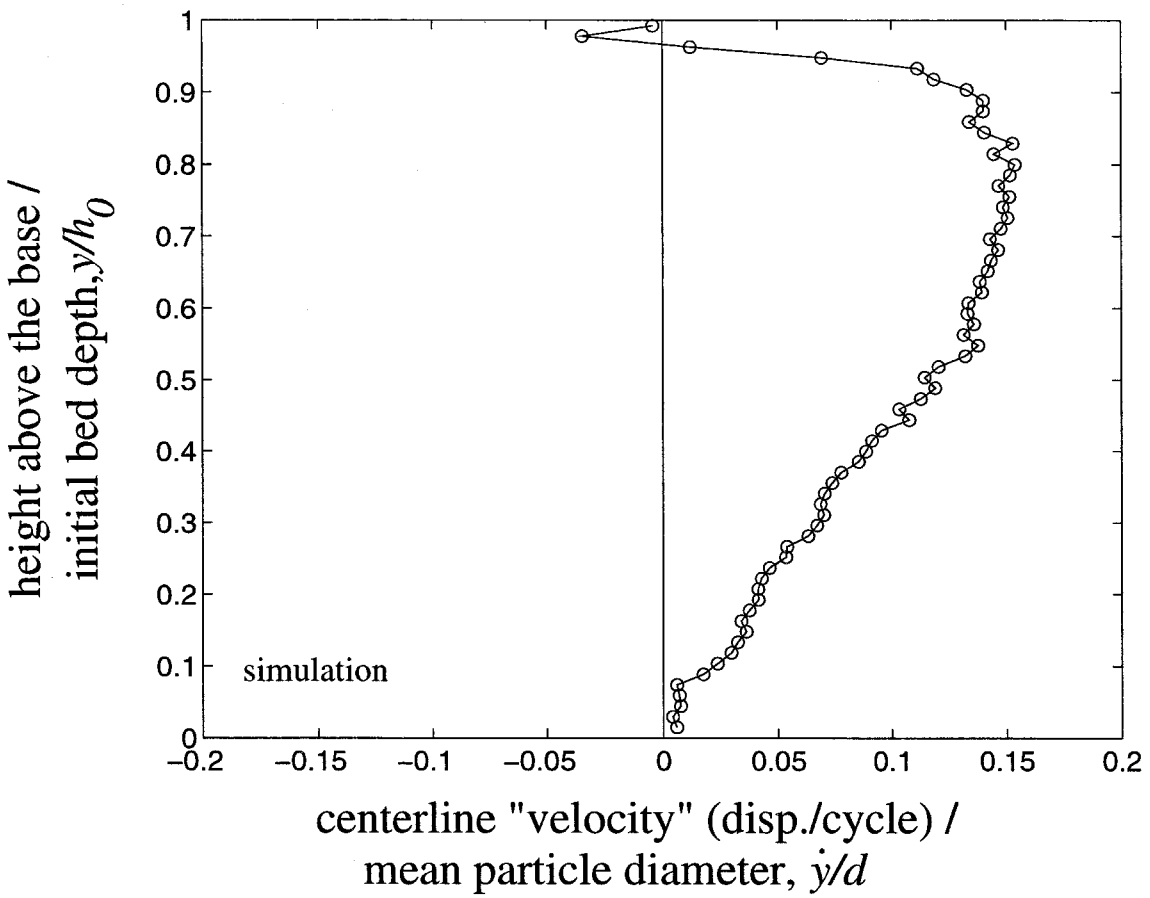

Figure 5.7: The vertical velocity measured at the plane that passes through the centerline of the container ($x = W/2$), $\dot{y}/d$, plotted as a function of dimensionless height from the container base, y/h_0, for the bed in figure 5.4.

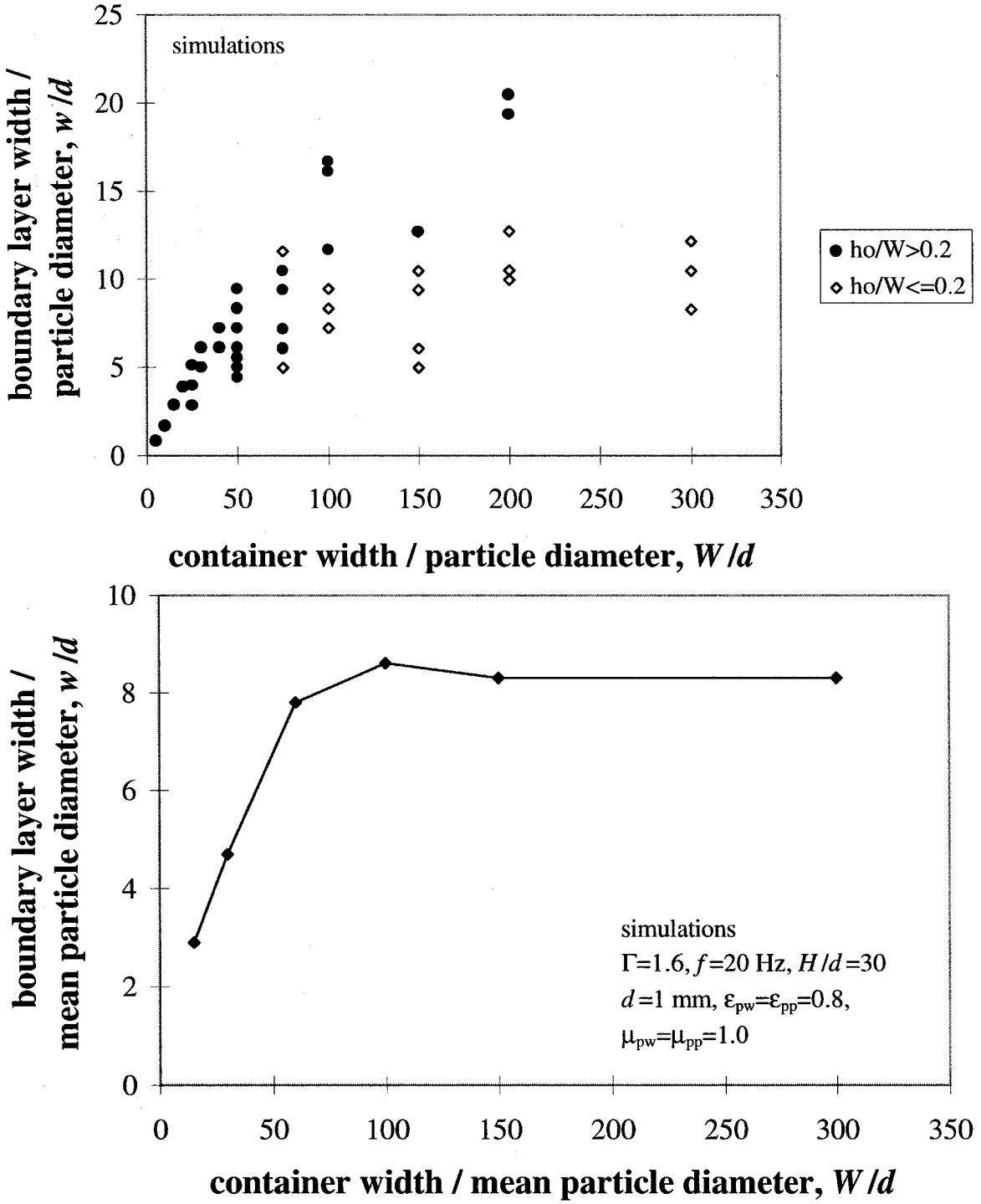

Figure 5.8: Top: The boundary layer width divided by the particle diameter, w/d, plotted against the dimensionless container width, W/d, for various container widths and bed depths. Bottom: The boundary layer width divided by the particle diameter, w/d, plotted against the dimensionless container width, W/d, for a bed with $h_0/d = 30$. The data points are the average for the two convection cells in each simulation.

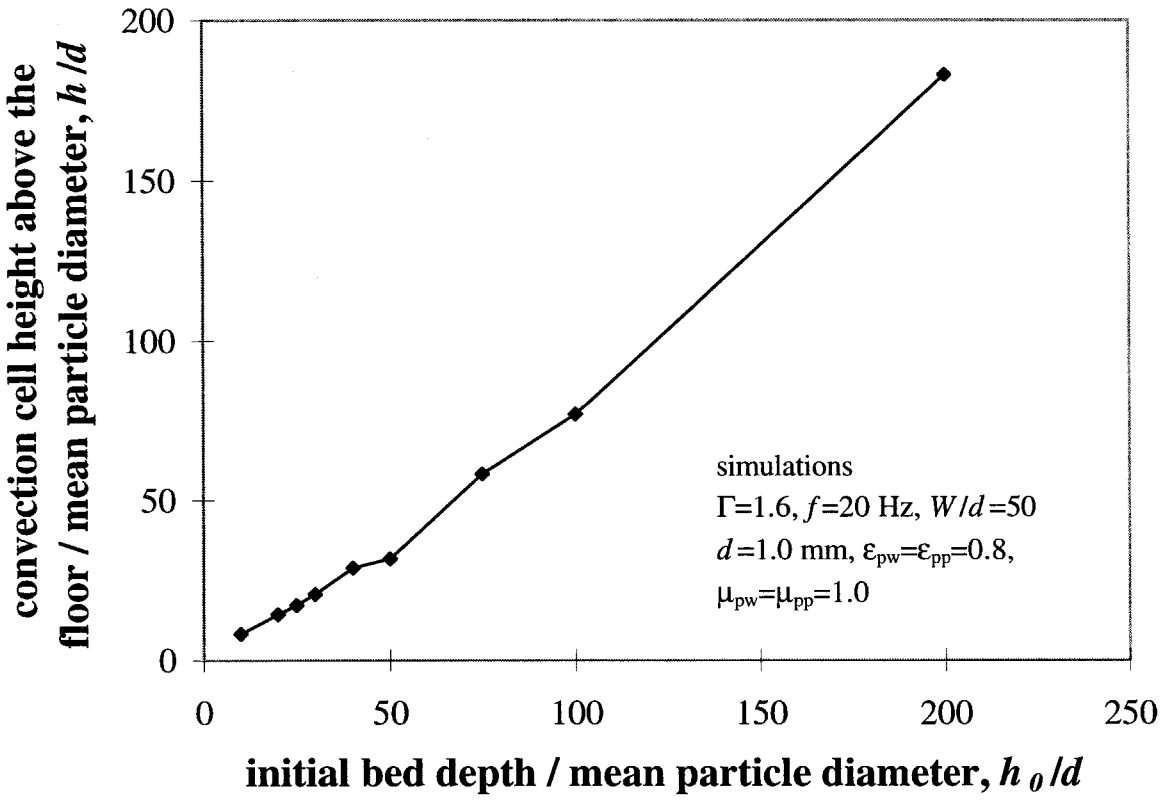

Figure 5.9: The height of the convection cell center, h, as a function of the bed depth, h_0 for a container of width, $W/d = 50$. The data points are the average for the two convection cells in each simulation.

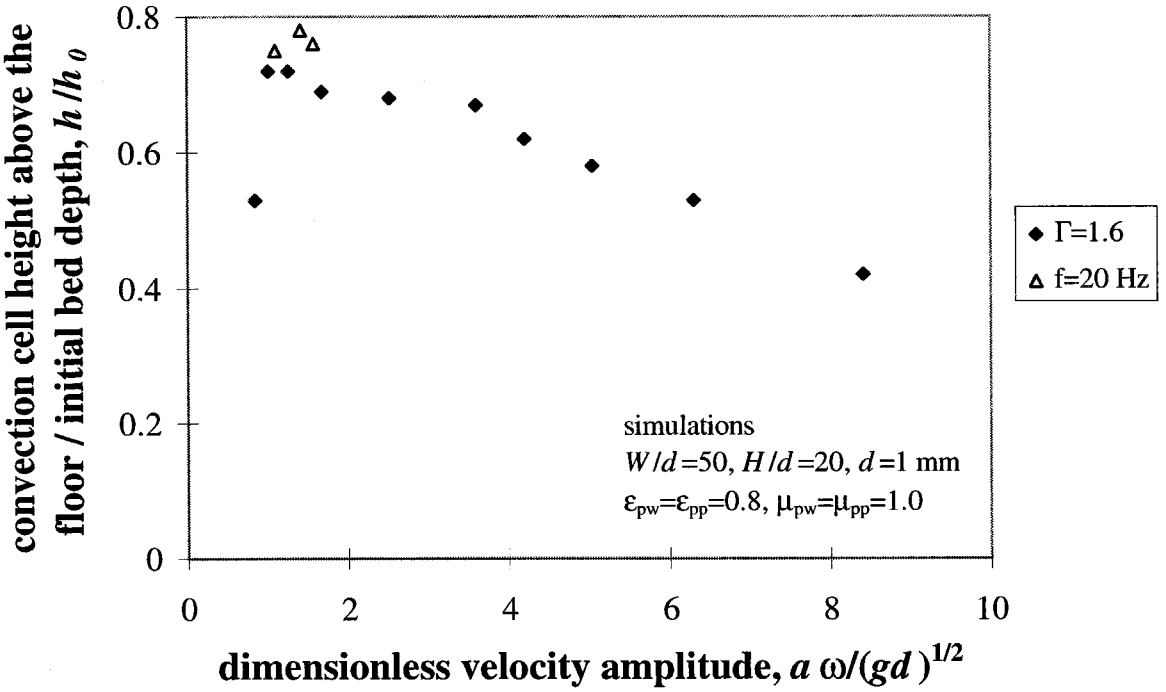

Figure 5.10: The height of the convection cell center, h/d, as a function of the oscillation velocity amplitude, $a\omega/(gd)^{\frac{1}{2}}$. The data points are the average for the two convection cells in each simulation.

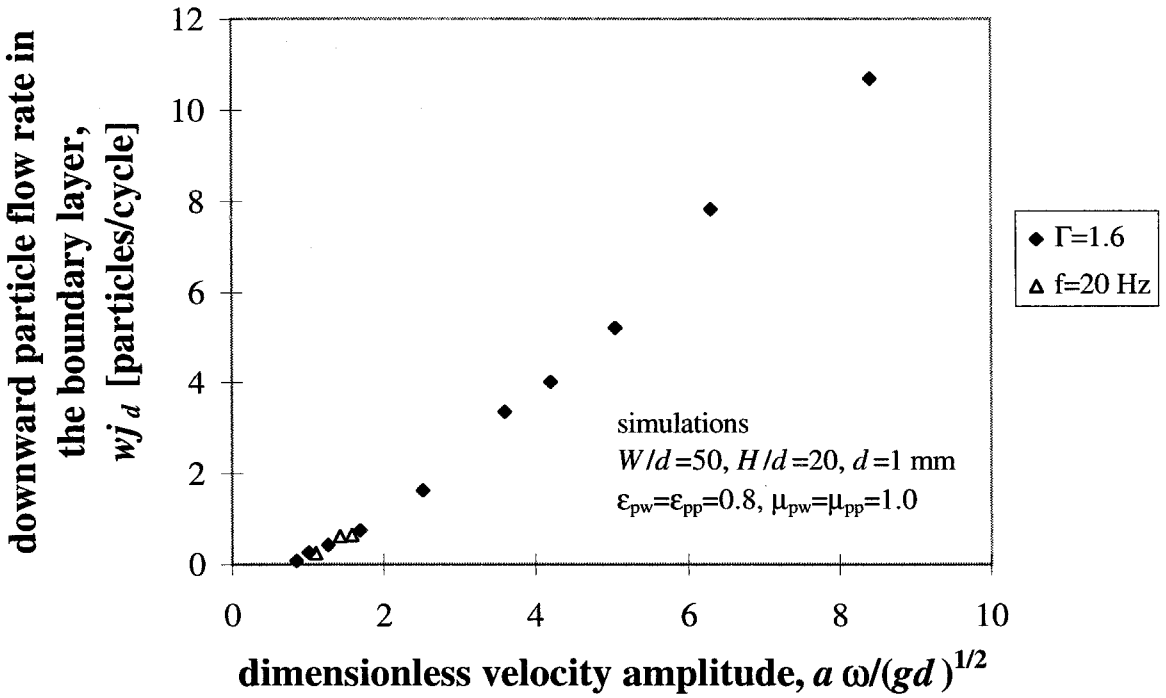

Figure 5.11: The number of particles that flow downward past the convection cell center each oscillation cycle, wj_d, as a function of the dimensionless oscillation velocity amplitude, $a\omega/(gd)^{\frac{1}{2}}$. The data points are the average for the two convection cells in each simulation. The remainder of the simulation parameters are given in table 5.2.

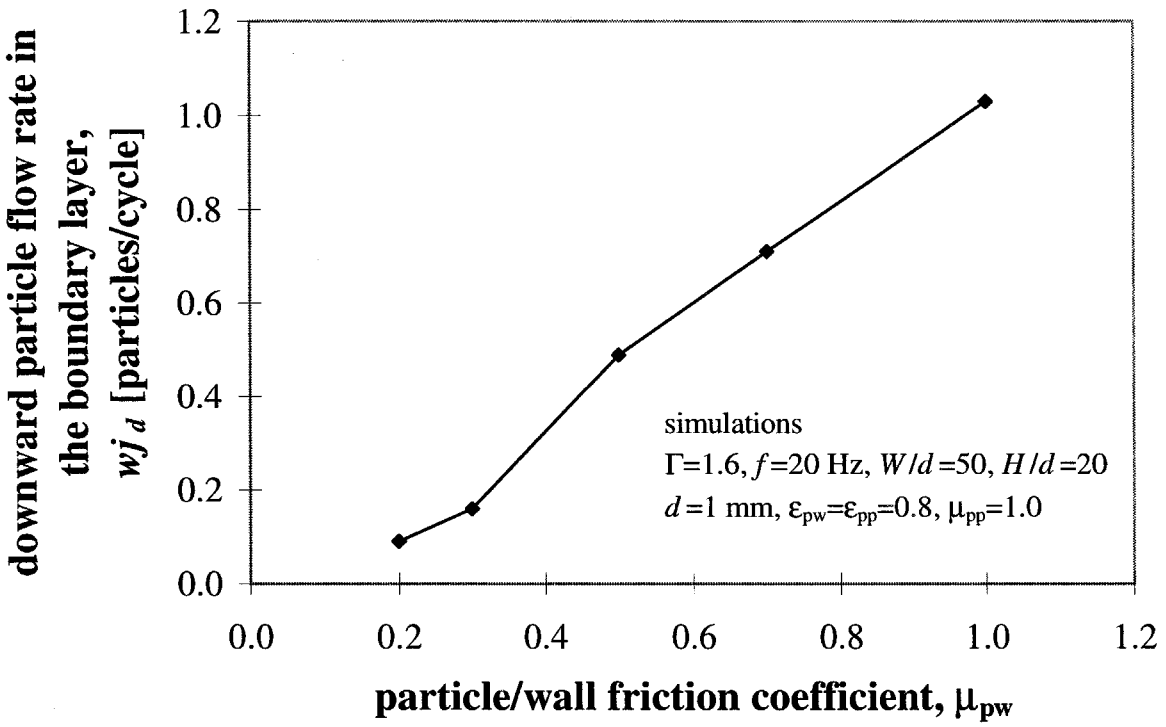

Figure 5.12: The number of particles that flow downward past the convection cell center each oscillation cycle, wj_d, as a function of the particle/wall coefficient of friction, μ_{pw}. The data points are the average for the two convection cells in each simulation. The remainder of the simulation parameters are given in table 5.2.

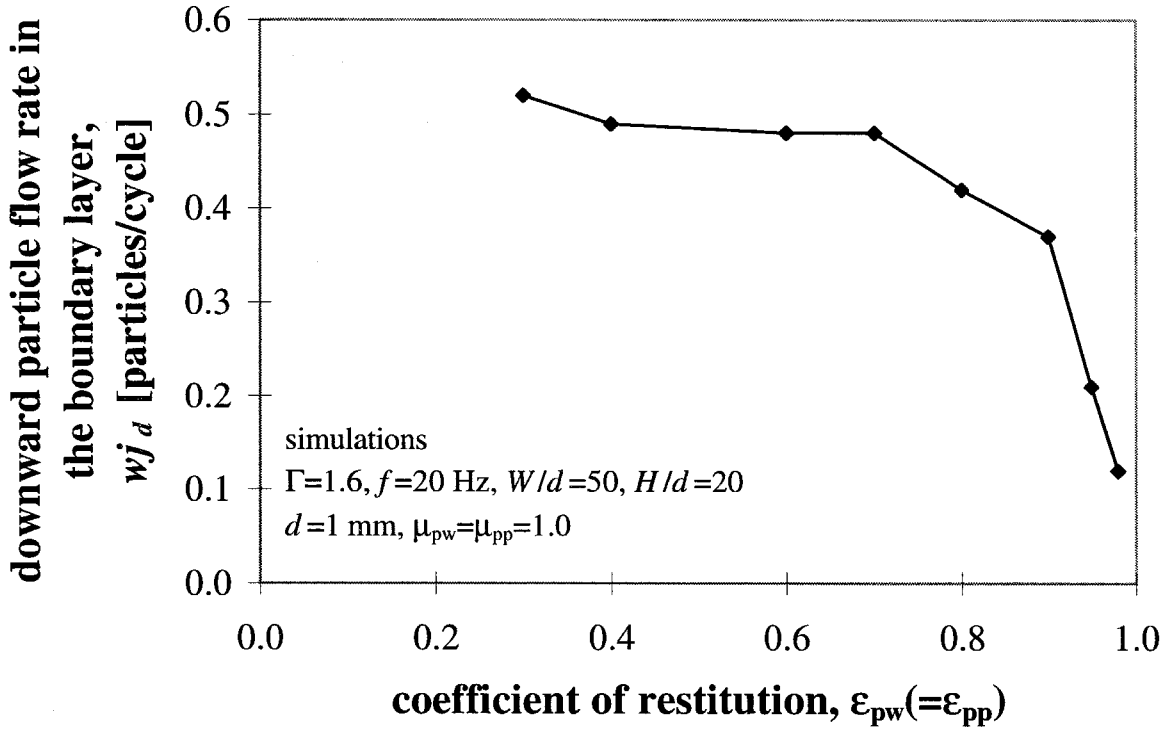

Figure 5.13: The number of particles that flow downward past the convection cell center each oscillation cycle, wj_d, as a function of the coefficient of restitution $\epsilon = \epsilon_{pw} = \epsilon_{pp}$. The data points are the average for the two convection cells in each simulation. The remainder of the simulation parameters are given in table 5.2.

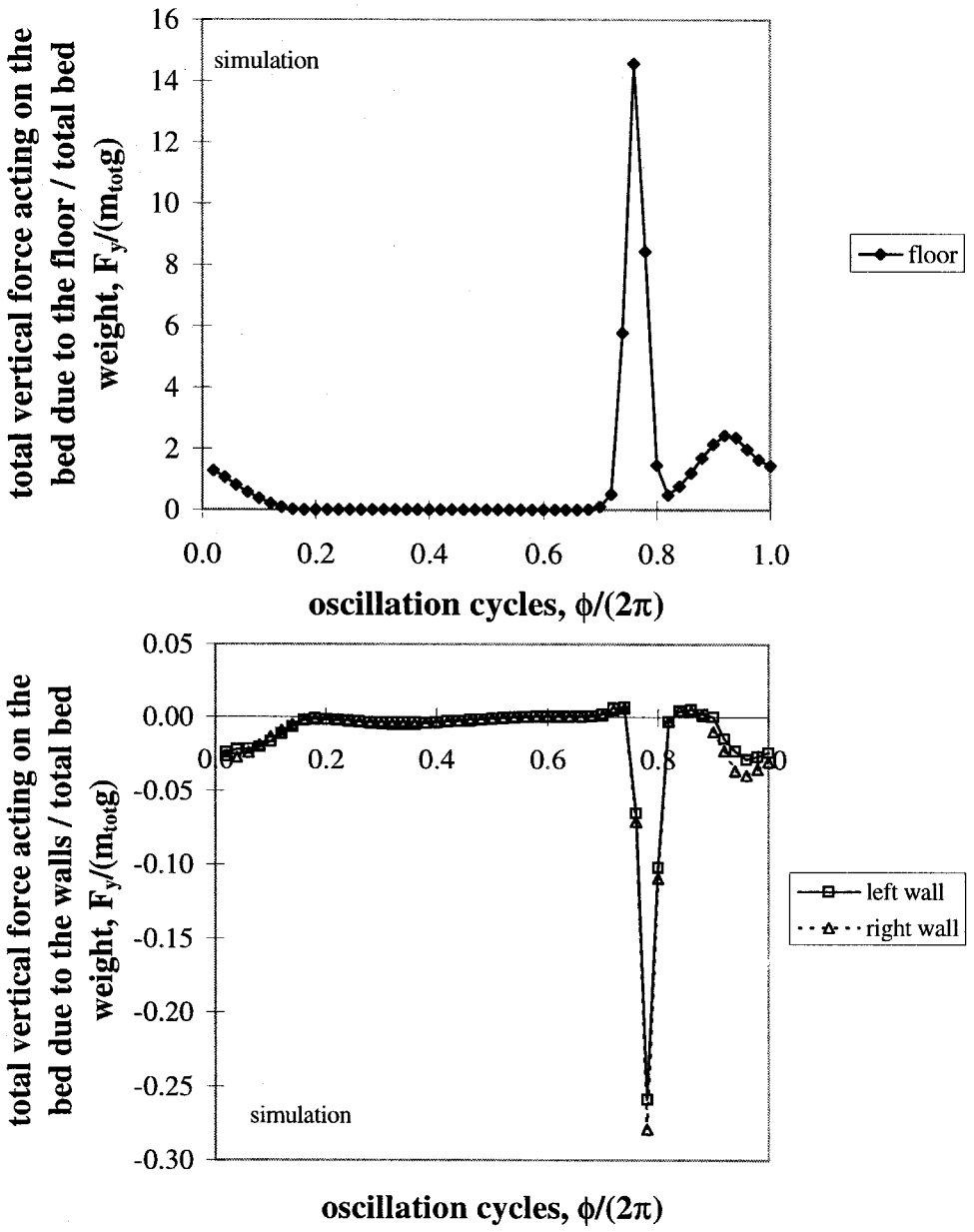

Figure 5.14: The total vertical force acting on the particle bed due to the (a) floor and the (b) walls divided by the total weight of the particle bed, $m_{tot}g$, as a function of the oscillation cycle, $\phi/(2\pi)$. The simulation force data was averaged over 100 oscillation cycles at an acceleration amplitude of $\Gamma = 1.6$ and a frequency of $f = 20$ Hz. The remainder of the simulation parameters are given in table 5.2.

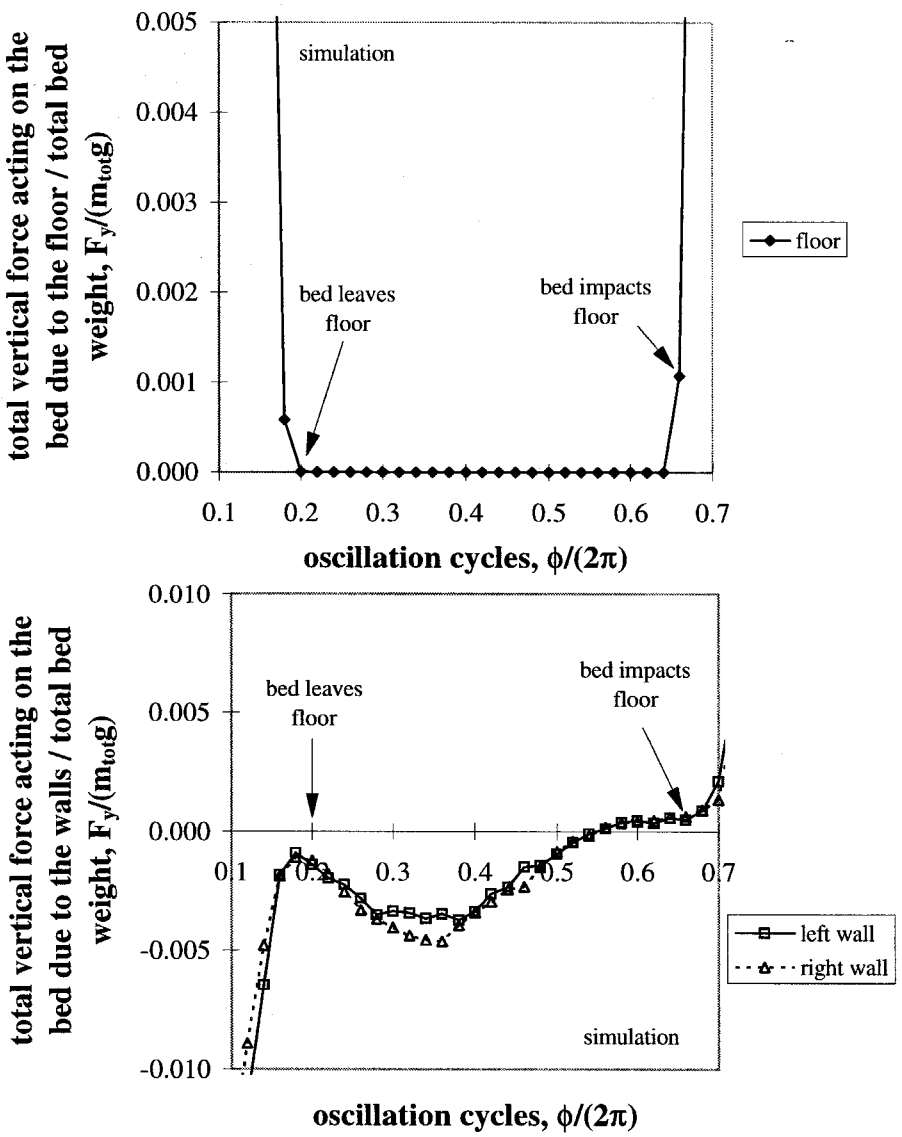

Figure 5.15: Enlarged portions of the plots in figure 5.14. The total vertical forces acting on the particle bed due to the (a) floor and the (b) walls divided by the total weight of the particle bed, $m_{tot}g$, as a function of the oscillation cycle, $\phi/(2\pi)$. The arrows indicate when the bed leaves and re-collides with the floor.

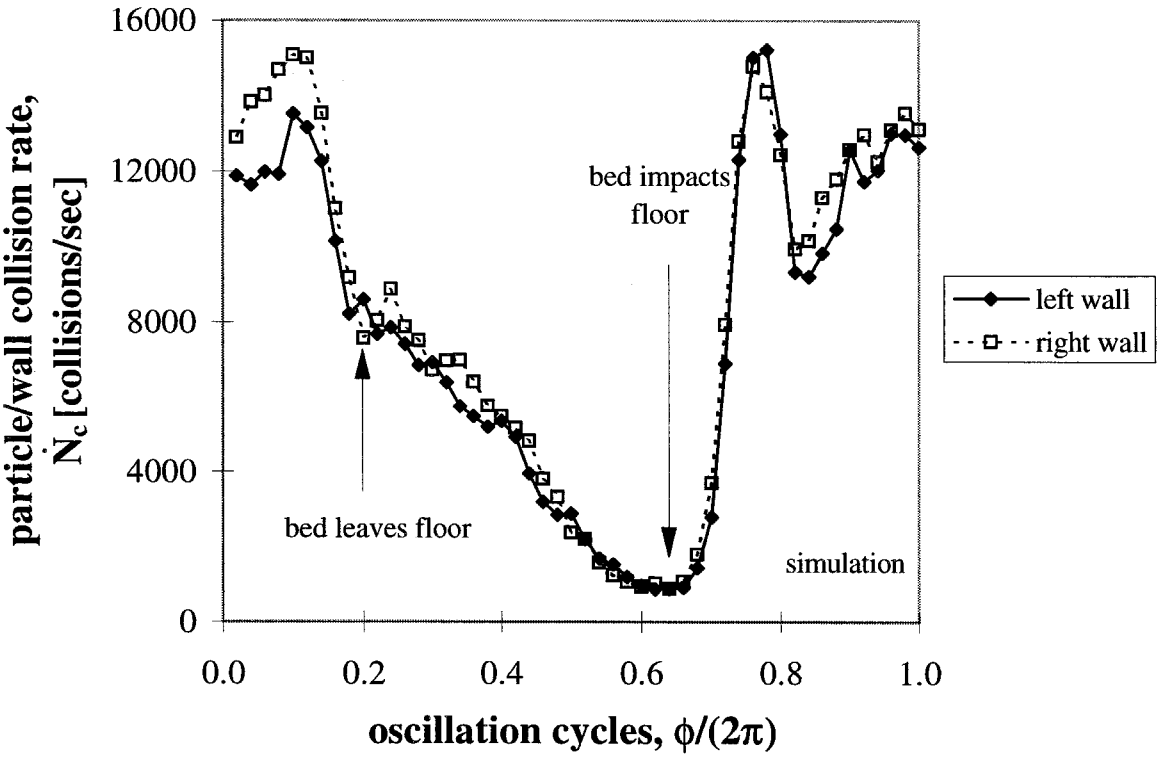

Figure 5.16: The particle collision rate with the walls, $\dot{N}_c$ (with units of collisions per second), as a function of the oscillation cycle, $\phi/(2\pi)$, for the bed described in figure 5.14. The arrows indicate when the bed leaves the floor. The collision rate was averaged over 100 oscillation cycles.

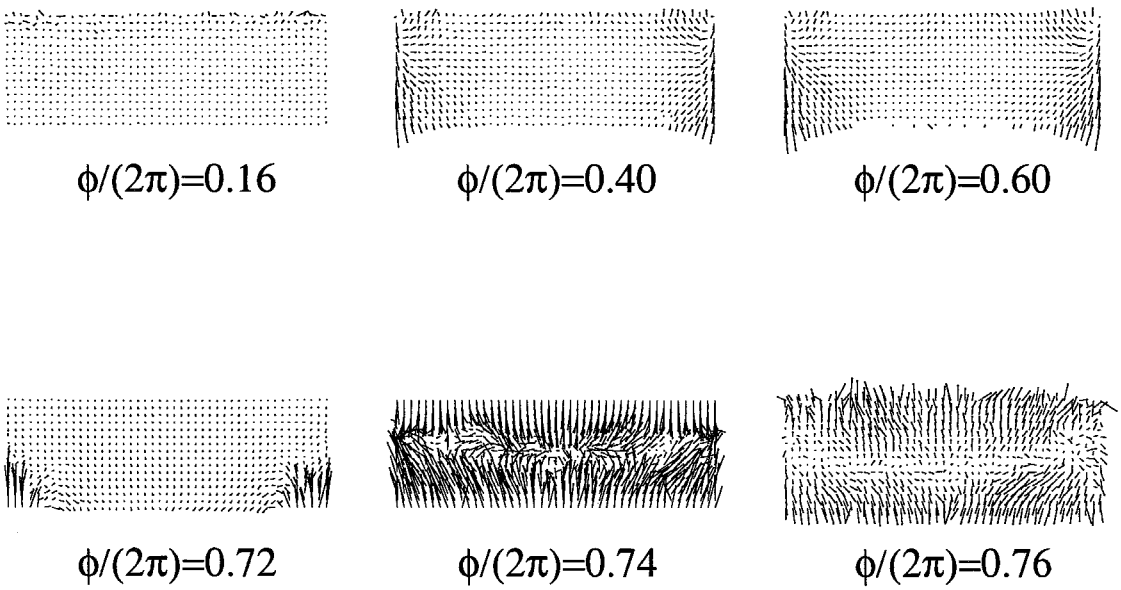

Figure 5.17: The averaged instantaneous particle velocities relative to the bed's center of mass at various oscillation phase angles for the bed described in figure 5.14. The velocity vectors are averaged over 20 oscillation cycles. Note that the vectors for $\phi/(2\pi) \leq 0.60$ have a scale five times that of the vectors for $\phi/(2\pi) > 0.60$ for clarity.

Chapter 6 Standing Surface Waves

6.1 Experiments

Surface waves appear for two separate regions of Γ. The first set occurs when $2.2 < \Gamma < 4.2$ when $h_0/d = 10$ while the second set appears for $5.8 < \Gamma$ to at least $\Gamma = 7.0$ for the same value of h_0/d. Recall that the range at which the waves appear shifts to smaller Γ with increasing h_0/d as discussed in section 3.1. The mound observed when Γ is just greater than one is no longer observed although the convection cells are still present at the walls when the lucite or sand paper walls were used. The smooth glass walls were employed for the remainder of the experiments to eliminate the effects of the side wall convection.

The wave motion on the free surface was difficult to discern under normal lighting conditions, especially for waves with small amplitude. However, when a strobe lamp, tuned a frequency nearly equal to the wave formation frequency, was used to illuminate the bed the waves could easily be observed.

The two sets of waves are referred to as $f/2$ and $f/4$ waves based on the wave formation frequency. The $f/2$ waves appear at the lower values of Γ and form at one-half the forcing oscillation frequency. At the higher range of Γ are the $f/4$ waves which appear at one-quarter the forcing frequency. The reason for the change in the wave formation frequency is that between wave regimes, the flight motion of the bed undergoes a period doubling bifurcation. This behavior is explored further in the next chapter.

Measurements of the the bed's flight time show that for both sets of waves there exists a single flight time. The $f/2$ waves have a flight time that is less than the oscillation period of the forcing vibrations while the $f/4$ waves have a flight time greater than the oscillation period. Consequently, the bed flight motion repeats every oscillation cycle for $f/2$ waves and every two oscillation cycles for the $f/4$ waves.

Figures 6.1 and 6.2 show illustrations of the wave motion for both $f/2$ and $f/4$ waves. Note that wave anti-nodes always appeared at the boundaries of the container.

At low oscillation amplitudes and velocities, for example at $\Gamma = 3.3$ and $f = 20$ Hz corresponding to $a/d = 1.6$ and $a\omega/\sqrt{gd} = 2.3$, rounded, nearly sinusoidal waves are observed (refer to figure 3.3). These rounded waves are only observed for the $f/2$ waves in the present experiments. At higher vibration amplitudes and vibration velocities, for example at $\Gamma = 6.2$ and $f = 20$ Hz corresponding to $a/d = 3.0$ and $a\omega/\sqrt{gd} = 4.3$, sharp, cusped shaped waves are seen (refer to figure 3.4). These wave shapes are observed with the $f/4$ waves at all frequencies.

Due to the nearly two-dimensional container shape, there was typically no variation in the wave shape along the short axis of the container. Occasionally more complicated wave patterns were observed for the $f/2$ waves. These included "sloshing" waves where the wave sloshes from the front wall of the container to the rear wall, and cnoidal waves in which the wave peaks along the long axis of the container alternated between the front and rear walls. These wave patterns appear more readily in containers that have cross sectional dimensions on the order of several wavelengths. Melo *et al.* (1994, 1995) and Metcalf *et al.* (1996) examined these wave patterns in more detail and reported patterns, when viewed from above, consisting of stripes, squares, pentagons, and hexagons. Both groups also found that the appearance of these patterns depends on both the oscillation frequency and acceleration amplitude. These waves patterns were not investigated in the present work but it is interesting to note that at high accelerations and low frequencies, for example when $\Gamma = 7.0$ and $f = 20$ Hz, the $f/4$ wave peaks begin to sway from side to side, alternately leaning towards and away from one another.

Particles are in a fluidized state at the free surface of the bed. For the round-shaped waves the fluidized layer was typically only a few particle diameters deep. A greater depth was fluidized when cusp-shaped waves are present. Additionally, particles are ejected from the peaks of the cusp-shaped waves resulting in a significant amount of particle mixing at the bed's free surface.

In contrast to the top free surface, the bottom surface of the bed remains relatively

flat with small regions of curvature occurring near the wall boundaries. The least clearance between the base and the particle bed is at the walls. The bottom surface has a more irregular shape for the cusp-shaped waves. Unlike the round-shaped waves, cusp-shaped waves influence the motion of particles within the entire bed. When a wave peak forms, the particles below it move up with the peak leaving caverns or pockets with large radii of curvature along the bottom surface of the bed. Clément *et al.* (1996) also reported this observation noting that the depth of these pockets decreases with increasing oscillation frequency.

Measurements of the wave amplitude and wavelength were made for both sets of waves for varying vibration parameters. All of the measurements were made using the 1.3 mm diameter glass spheres in the 13.5 by 1.6 cm container with $h_0/d = 18$. A grid scale was taped to the outside, rear wall of the container in order to make vertical and horizontal scalar measurements. The strobe lamp, operating at close to the wave formation frequency, was used to illuminate the bed from behind while a video camera recorded the wave motion over many oscillation cycles. Recordings of the waves were made for oscillation frequencies between 15 and 40 Hz in 5 Hz increments and acceleration amplitudes between $2.6 \leq \Gamma \leq 4.6$ and $6.0 \leq \Gamma \leq 7.8$ in increments of $\Gamma = 0.2$. The wave amplitude, η, is defined as twice the maximum distance between a wave peak and a neighboring wave trough while the wavelength, λ, is the distance between neighboring wave peaks. Determination of the peak and trough locations was made visually. Determining the lateral location of wave peaks was easier for the cusp-shaped waves than for the round-shaped waves since the round wave amplitude gradient was small. Five amplitude and wavelength measurements were made at each set of vibration parameters with several oscillation cycles passing between each measurement.

The amplitude data divided by the particle diameter is shown in figures 6.3 and 6.4 as a function of Γ. Typical error bars are shown only for the data collected at 30 Hz. Note that the wave amplitude increases with increasing Γ and decreasing f. Additionally, the data for the $f/2$ waves at $f = 15$ and 20 Hz shows a maximum at $\Gamma \approx 3.6$ and $\Gamma \approx 4.0$, respectively. As shown in figure 6.5, the wave amplitude for

both the $f/2$ and $f/4$ waves is proportional to the oscillation amplitude, a.

The wave amplitude is also plotted in terms of a Froude number based on the vibration velocity amplitude, $a\omega$, and the measured wave amplitude, η,

$$Fr = \frac{a\omega}{\sqrt{g\eta}} \tag{6.1}$$

where g is the gravitational acceleration. The Froude number can be interpreted as a measure of the maximum kinetic energy of the waves, $(a\omega)^2$, to the maximum potential energy of the waves, $g\eta$. The wave amplitude data plotted in this form as a function of Γ collapses to a single curve for both the $f/2$ and $f/4$ waves as shown in figures 6.6 and 6.7. The Froude number for the $f/2$ waves increases from $Fr \approx 1$ at $\Gamma = 2.6$ to $Fr \approx 1.5$ for $\Gamma = 4.6$ while the Froude number for the $f/4$ is approximately 1.3 for all Γ.

The wavelength data divided by the particle diameter is shown in figures 6.8 and 6.9 as a function of Γ. Again, only the scatter bars for $f = 30$ Hz are shown. The data indicates that for a given frequency, the wavelength changes little as a function of Γ. The data for the $f/4$ waves at $f = 20$ Hz, however, shows an increasing trend with Γ.

In order to facilitate comparison with the measurements of Melo *et al.* (1995), Metcalf *et al.* (1996), and Clément *et al.* (1996), the wavelength data is also plotted as a function of the inverse oscillation frequency squared, $1/f^2$ and is shown in figures 6.10 and 6.11. The results of Melo *et al.*, Metcalf *et al.*, and Clément *et al.* indicate that the dispersion relation relation for both sets of waves at low frequency is similar to that for gravity waves in deep inviscid fluids, $\lambda \propto g_{\text{eff}}/f^2$, where g_{eff} is an effective gravity term. The data for the $f/2$ waves does not clearly exhibit this trend and is scattered instead. The $f/4$ waves follow the linear trend more closely. Note that the data corresponding to $f = 20$ Hz ($1/f^2 = 0.0025s^{-2}$) also shows the increasing wavelength trend with increasing Γ. Figure 6.12 shows the data for $\Gamma = 6.8$ for the $f/4$ waves with a least squares fit to the equation, $\lambda/d = \lambda_0/d + (g_{\text{eff}}/d)/f^2$. The minimum wavelength, corresponding to the wavelength occurring at infinite fre-

quency, is $\lambda_0/d = 20.6$ and the effective gravity for the fit is $g_{\text{eff}} = 19.85$ m/s^2, roughly $2g$.

6.2 Simulations

The $f/2$ and $f/4$ waves also appear in the simulations for values of Γ similar to the experimental values (refer to section 3.2). The range of Γ over which the waves are observed increases with decreasing inter-particle friction, μ_{pp}. For example, when $\mu_{pp} = 1.0$, a bed with $h_0/d = 20$ exhibits $f/2$ waves for $1.8 < \Gamma < 3.6$. However, for frictionless particles, $\mu_{pp} = 0$, the $f/2$ waves appear for $1.4 < \Gamma < 3.6$. A similar trend is observed for the $f/4$ waves. Note that for $\Gamma_1' < \Gamma < \Gamma_1^*$, poorly formed $f/2$ and $f/4$ waves appear intermittently.

Measurements of the wavelengths were made with the simulation for $\Gamma = 1.6 \rightarrow 3.6$ in steps of $\Gamma = 0.2$ at $f = 15$ Hz, and for frequencies of $f = 8$, 9, 10, 11, 12, and 15 Hz at $\Gamma = 3.0$. The remainder of the simulation parameters are given in table 6.1. Note that the coefficient of restitution for particle collisions, ϵ_{pp}, is 0.5. The low value of ϵ_{pp} was used to reduce the amount of saltation occurring at the free surface of the bed.

The wave amplitudes were not measured in the simulation due to difficulties determining the peak amplitudes. Qualitatively, the trends were the same as those observed in the experiments. The wave amplitudes increased with increasing Γ at a fixed frequency and for decreasing f at a fixed Γ. Both round- and cusp-shaped waves were observed for the $f/2$ waves (as shown in figure 6.13) while only cusp-shaped waves appeared for $f/4$ waves.

The wavelength plotted as a function of the acceleration amplitude, Γ, is shown in figure 6.14 for $f = 15$ Hz. The data indicates that the wavelength is independent of Γ. In figure 6.15, the wavelength is plotted against the square of the inverse oscillation frequency, $1/f^2$, for $\Gamma = 3.0$. The solid line in the figure is a least squares fit to the equation $\lambda/d = \lambda_0/d + (g_{\text{eff}}/d)/f^2$. The value of the minimum wavelength, λ_0/d, is 19.3 and the effective gravity is $g_{\text{eff}} = 4.7$ m/s^2. It is interesting to note that the

wavelength values in the simulation are quantized. Since the wavelength is determined by dividing the container width by the number of wave peaks, the wavelengths will be equal to W/n where n is a positive integer.

6.3 Discussion

Fauve *et al.* (1989) were the first to point out the similarities between the standing waves observed in granular beds and the those observed in vertically, vibrated fluids. The latter waves, called Faraday instability waves, were first reported by Faraday (1831) and have been examined in a number of works (see, for example, Miles and Henderson, 1990). Both types of waves form as a result of the coupling between the base oscillations and the particle motion. The two relevant time scales in the formation of the waves are the forcing oscillation period and the free fall time of the particles. This resonance condition selects the wavelength and amplitude of the waves since the particles must recover from one wave to form a neighboring wave.

The Froude number scaling for the wave amplitude is not unexpected since the Froude number can be interpreted as a measure of the maximum kinetic energy of the waves, $(a\omega)^2$, to their maximum potential energy, $g\eta$. The significance of a Froude number greater than one suggests that some of the kinetic energy supplied by the oscillating base is not being completely converted into potential energy in the waves. The horizontal particle velocities and inelastic particle collisions may account for this energy deficit.

Clément *et al.* (1996) also measured wave amplitudes in their experiments using a two-dimensional layer (the container cross sectional dimensions were of order $100d$ by d) of 1.5 mm diameter aluminum spheres operating in the $f/2$ wave regime ($3.0 < \Gamma < 4.2$ for $h_0/d \leq 16$; the range of frequencies is not clear). They found that the wave amplitude varies linearly with vibration amplitude ($\eta \propto a$) which is consistent with the present data for the $f/2$ wave amplitudes. If the Froude number (refer to equation (6.1)) varies linearly with Γ, the wave amplitude will be proportional to the oscillation amplitude and inversely proportional to Γ ($\eta \propto a/\Gamma$). Thus, for a fixed Γ,

η is proportional to a. The experimental $f/2$ wave amplitude data plotted in terms of a Froude number against Γ is shown in figure 6.6. The trend can be certainly be considered linear for $3.0 < \Gamma < 4.6$.

The experiments (for the $f/4$ waves) and simulations (for the $f/2$ waves) show that the wavelength of the surface waves has a weak dependence on the oscillation acceleration amplitude, Γ, and varies proportionally with the square of the inverse oscillation frequency, $1/f^2$. The experimental data for the $f/2$ waves does not show this trend and instead is roughly constant with $1/f^2$. The reason for this trend is not clear.

The experimental data for the $f/4$ waves and simulation data for the $f/2$ waves, however, show that λ increases linearly with $1/f^2$. A high frequency minimum wavelength of $\lambda_0/d \approx 20$ is also observed for both the experiments and the simulations. The experimental work by Melo *et al.* (1995), Metcalf *et al.* (1996), and Clément *et al.* (1996) have all indicated a similar dispersion relationship. The comparison with fluids is often made since the wavelength for gravity waves in a deep fluid is also proportional to $1/f^2$. Note that the effective gravity for the scaling at $\Gamma = 6.8$ is approximately $2g$ while the simulations at $\Gamma = 3.0$ give $g_{\text{eff}} \approx 0.5g$. The experiments by Melo *et al.* and Metcalf *et al.* give a value of $g_{\text{eff}} \approx 0.3g$ for a Γ of 3.0 and 3.5. Clément *et al.* report that $g_{\text{eff}} \approx 0.1g$ for $3.3 < \Gamma < 4.2$. Note that in determining the dispersion relation for the fluid case, the wave amplitude is assumed to be much smaller than a wavelength. In the present experiments, the $f/4$ wavelength data follows a similar dispersion relationship yet the wave amplitude is on the same order as the wavelength.

Just as viscosity has an effect on the onset of the Faraday instability waves in fluids, the inter-particle friction, μ_{pp}, affects the onset of the waves in granular materials. The critical Γ at which the waves appear in fluids decreases as the fluid viscosity decreases (refer to Bechhoefer *et al.*, 1995). A similar effect is observed in the simulations with inter-particle friction. When μ_{pp} is decreased, the critical onset Γ for both the $f/2$ and $f/4$ waves decreases suggesting that inter-particle friction in granular materials contributes to the effective viscosity of a granular fluid.

These results for the $f/2$ and $f/4$ waves imply that vibrating granular beds have many similarities with a fluid. Parametrically forced surface waves are observed for both vibrating granular materials and fluids. The amplitude of the granular waves scale with a Froude number based on the oscillation velocity amplitude while the dispersion relation for the granular waves can be approximated by a relation based on that for gravity waves in a deep fluid layer. Additionally, inter-particle friction contributes to the effective viscosity of granular materials.

Tables and Figures

W/d	200
h_0/d	15
N	3000
ϵ_{pp}	0.50
$k_{n,pp}$	$3.602 * 10^3$ N/m
ν_{pp}	$2.092 * 10^{-2}$ N/(m/s)
$k_{s,pp}$	0.0 N/m
μ_{pp}	0.0
lateral boundaries	periodic
ϵ_{pw}	0.50
$k_{n,pw}$	$7.203 * 10^3$ N/m
ν_{pw}	$4.184 * 10^{-2}$ N/(m/s)
$k_{s,pw}$	0.0 N/m
μ_{pw}	0.0
d	0.9 - 1.1 mm
ρ	2500 kg/m^3
Δt	$4.337 * 10^{-6}$ sec

Table 6.1: The simulation parameters used to examine the surface wave behavior.

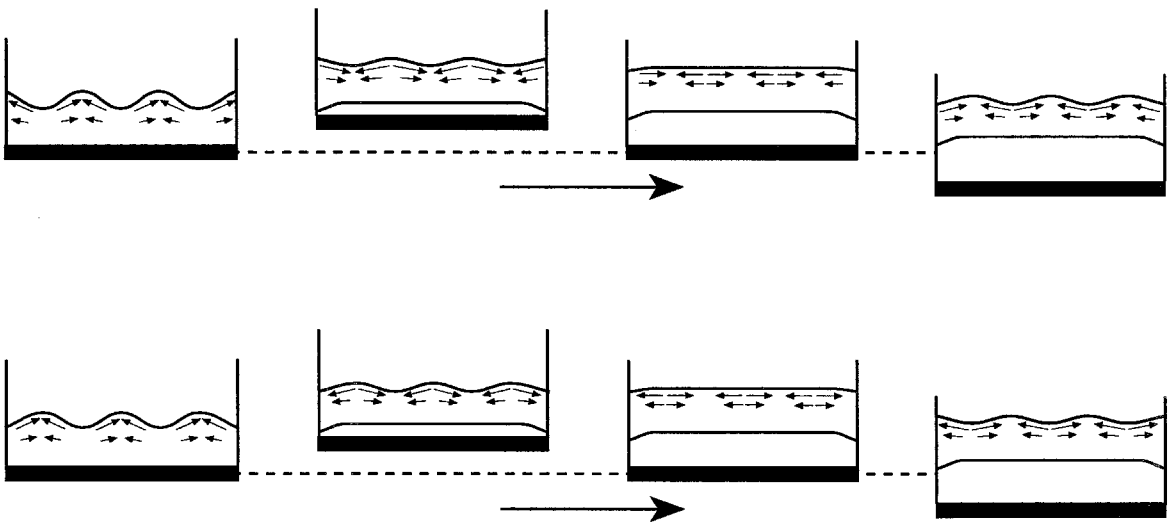

Figure 6.1: An illustration showing the motion of the particles for $f/2$ waves over two oscillation cycles.

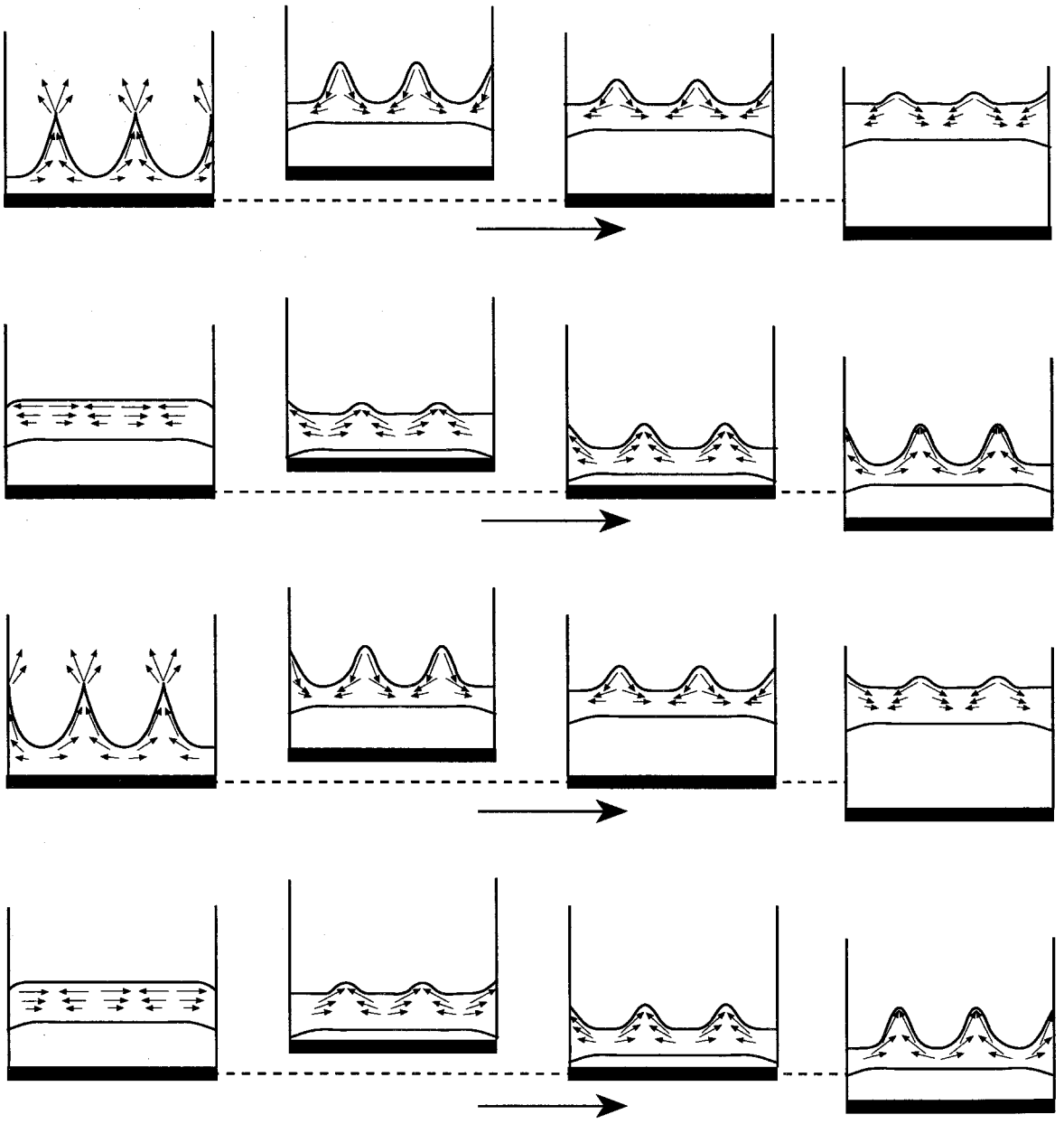

Figure 6.2: An illustration showing the motion of the particles for $f/4$ waves over four oscillation cycles.

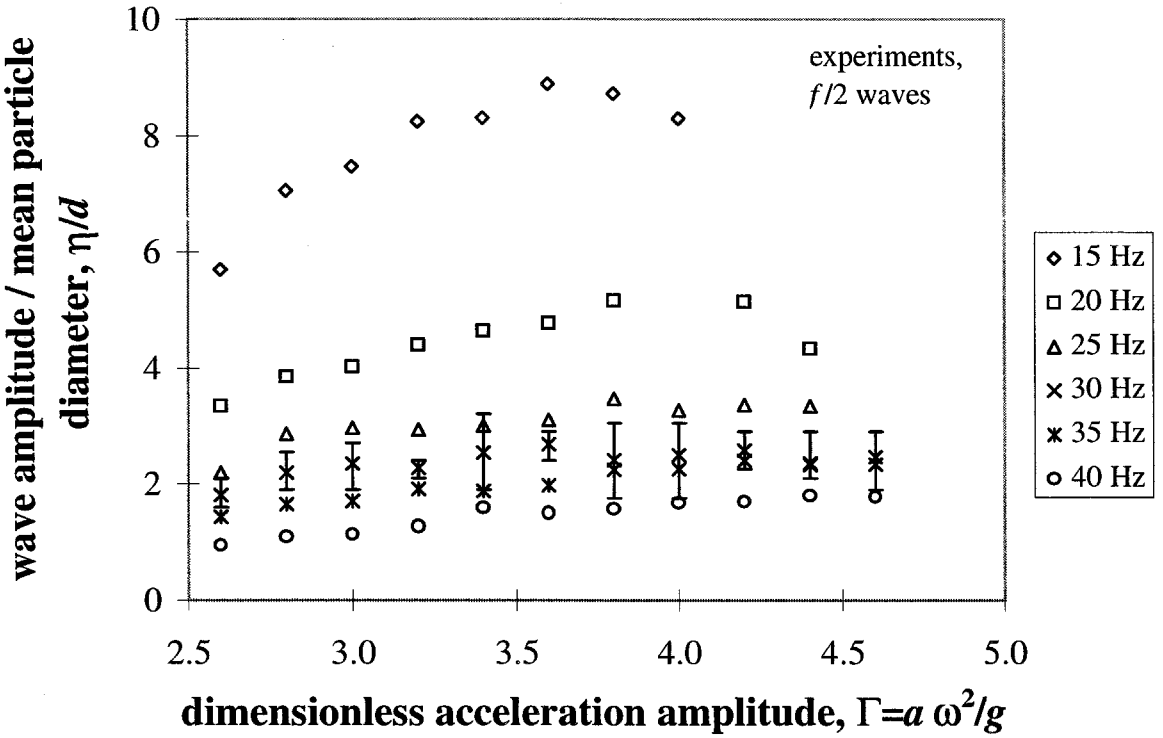

Figure 6.3: The wave amplitude, η, divided by the particle diameter, d, for the $f/2$ waves plotted against the dimensionless acceleration amplitude, Γ. Typical scatter bars are shown only for the data collected at 30 Hz.

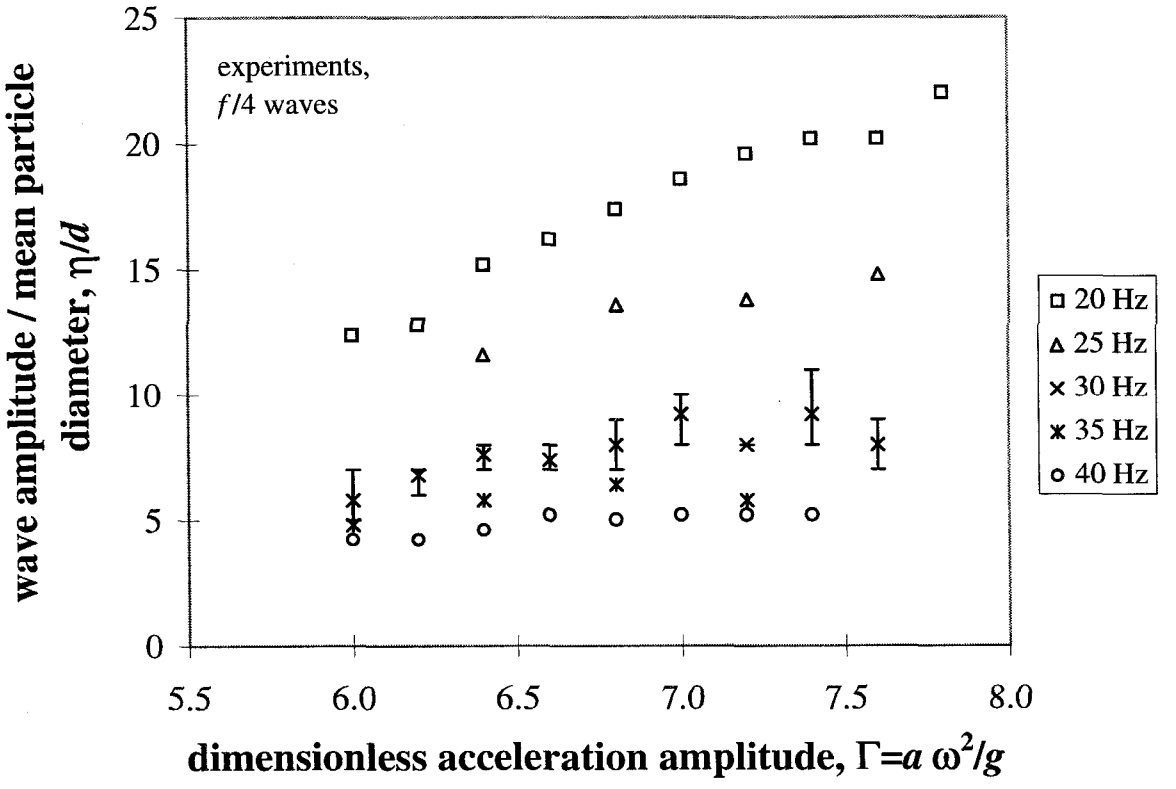

Figure 6.4: The wave amplitude, η, divided by the particle diameter, d, for the $f/4$ waves plotted against the dimensionless acceleration amplitude, Γ. Typical scatter bars are shown only for the data collected at 30 Hz.

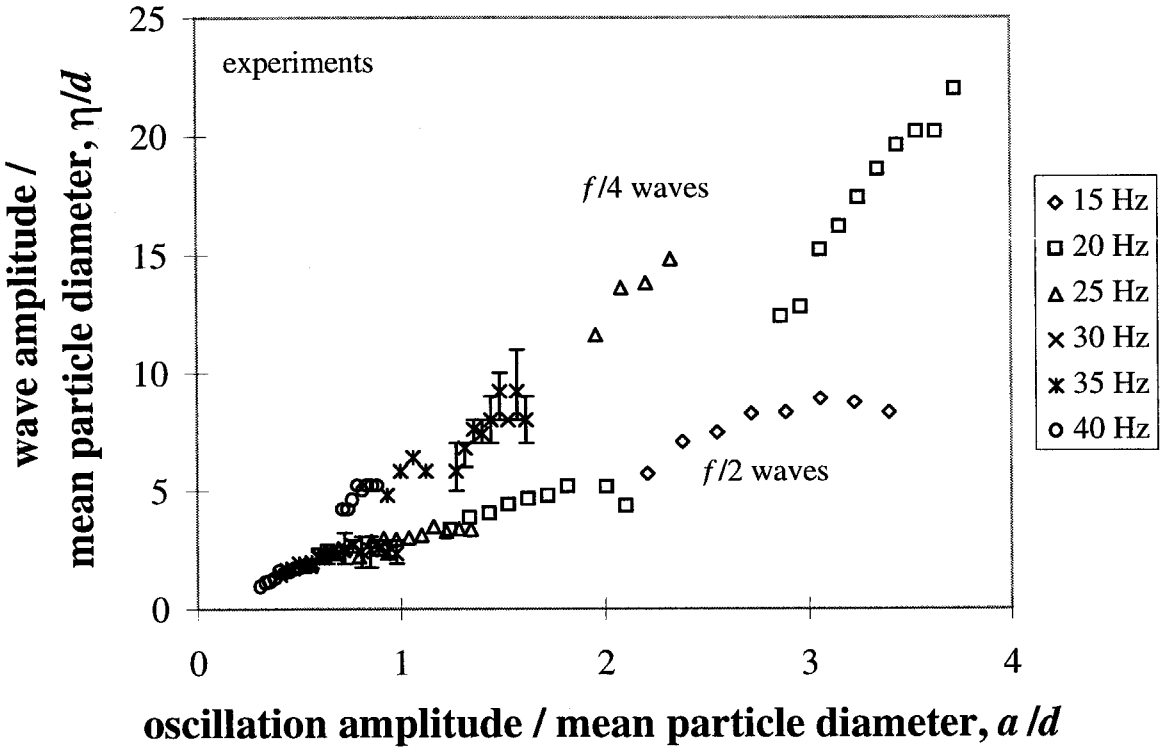

Figure 6.5: The wave amplitude divided by the mean particle diameter, η/d, plotted as a function of the oscillation amplitude divided by the mean particle diameter, a/d, for the $f/2$ and $f/4$ waves. Typical scatter bars are shown only for the data collected at 30 Hz.

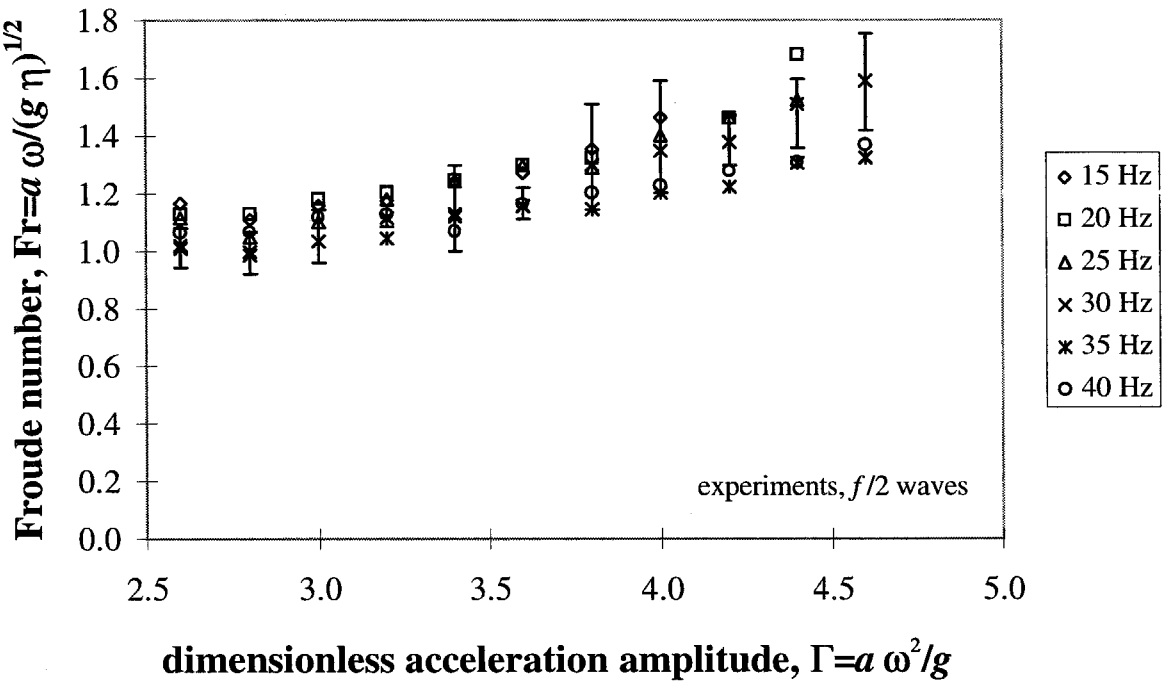

Figure 6.6: The Froude number, $Fr = a\omega/(g\eta)^{\frac{1}{2}}$, based on the oscillation velocity amplitude and measured wave amplitude for the $f/2$ waves plotted against the dimensionless acceleration amplitude, Γ.

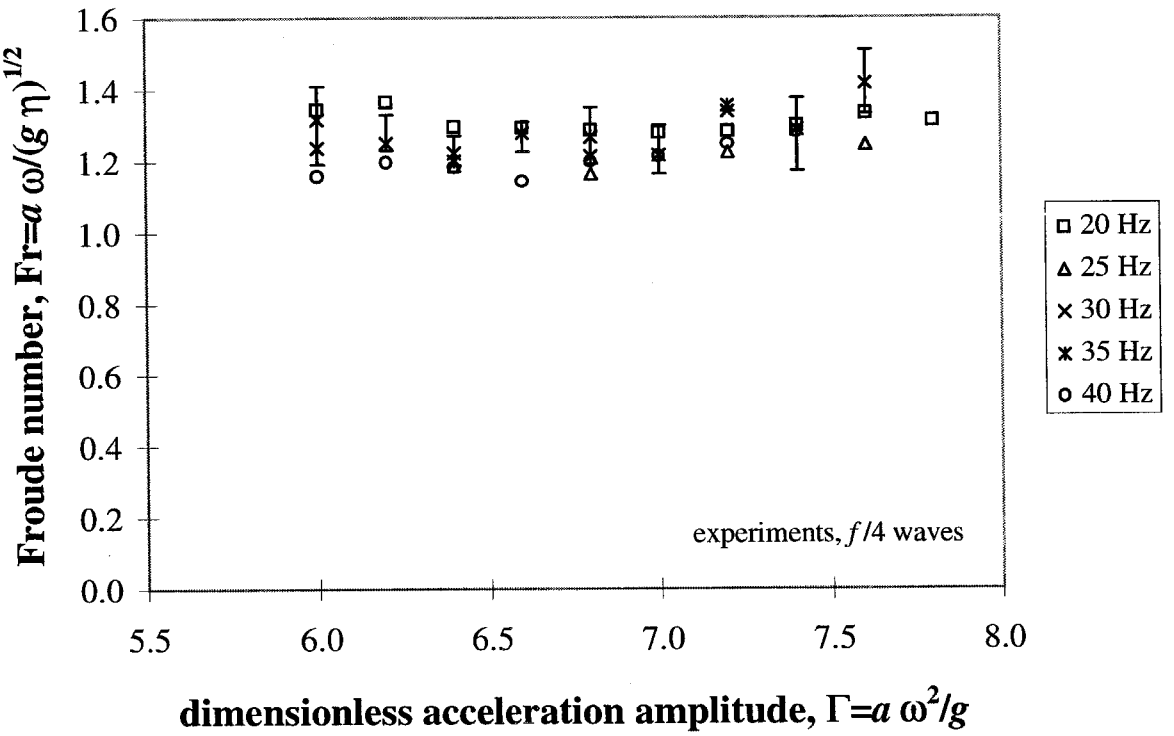

Figure 6.7: The Froude number, $Fr = a\omega/(g\eta)^{\frac{1}{2}}$, based on the oscillation velocity amplitude and measured wave amplitude for the $f/4$ waves plotted against the dimensionless acceleration amplitude, Γ.

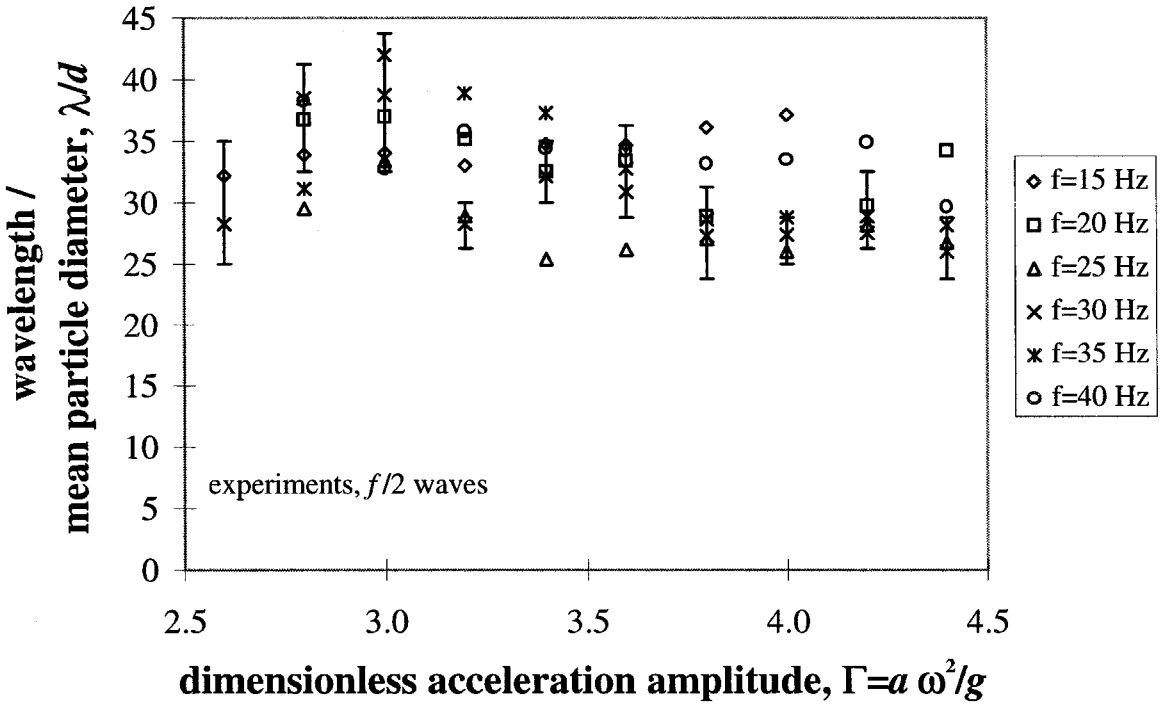

Figure 6.8: The wavelength, λ, divided by the particle diameter, d, for the $f/2$ waves plotted against the dimensionless acceleration amplitude, Γ. Typical scatter bars are shown only for the data collected at 30 Hz.

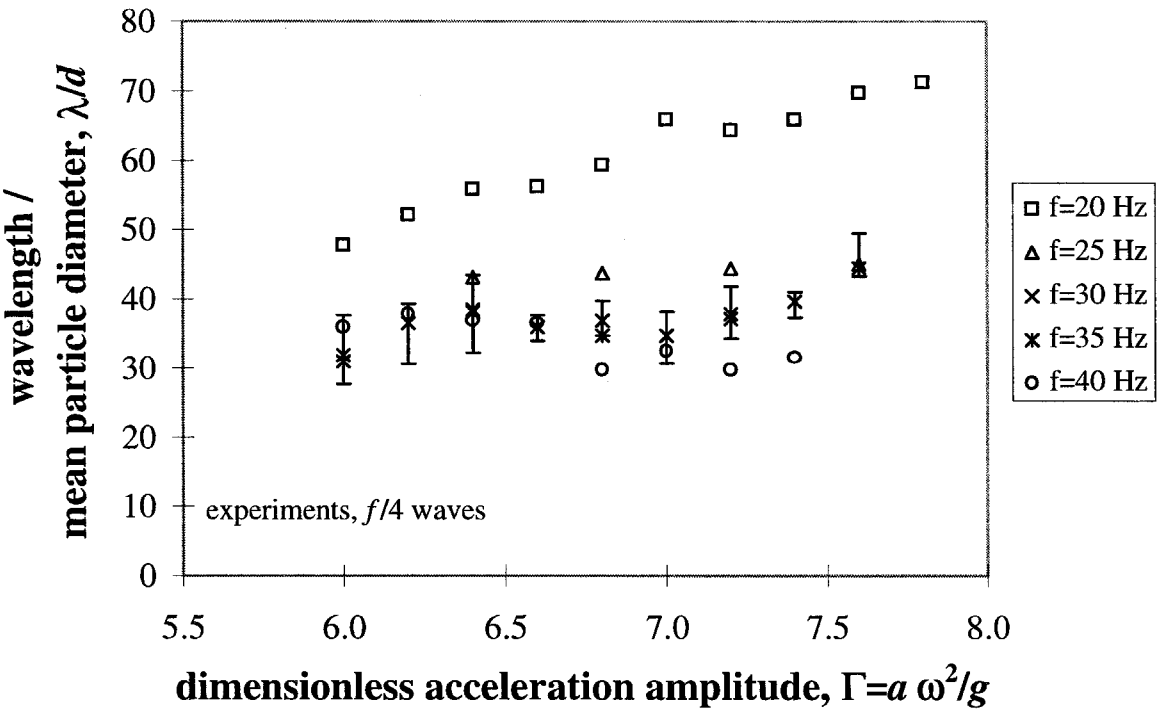

Figure 6.9: The wavelength, λ, divided by the particle diameter, d, for the $f/4$ waves plotted against the dimensionless acceleration amplitude, Γ. Typical scatter bars are shown only for the data collected at 30 Hz.

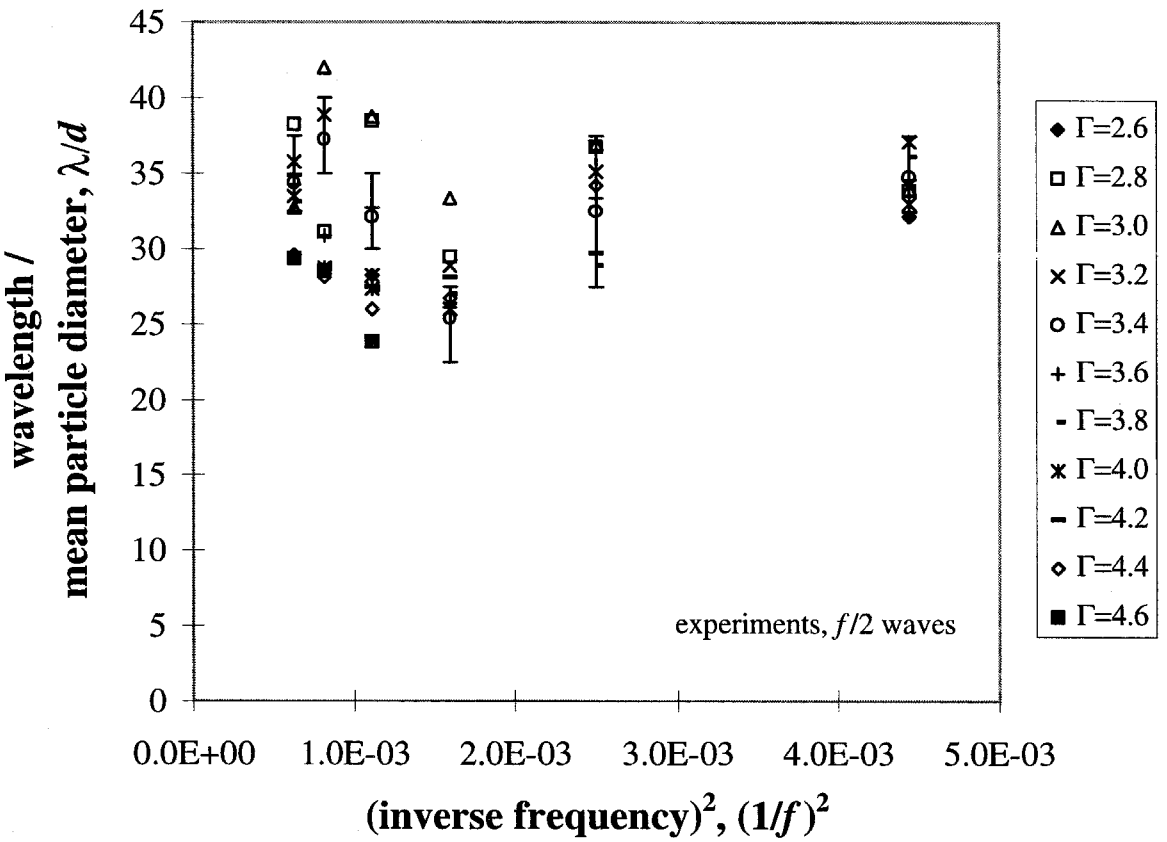

Figure 6.10: The dimensionless wavelength, λ/d, plotted against the inverse frequency squared, $(1/f)^2$ for the $f/2$ waves. Scatter bars are shown only for the $\Gamma = 3.2$ data.

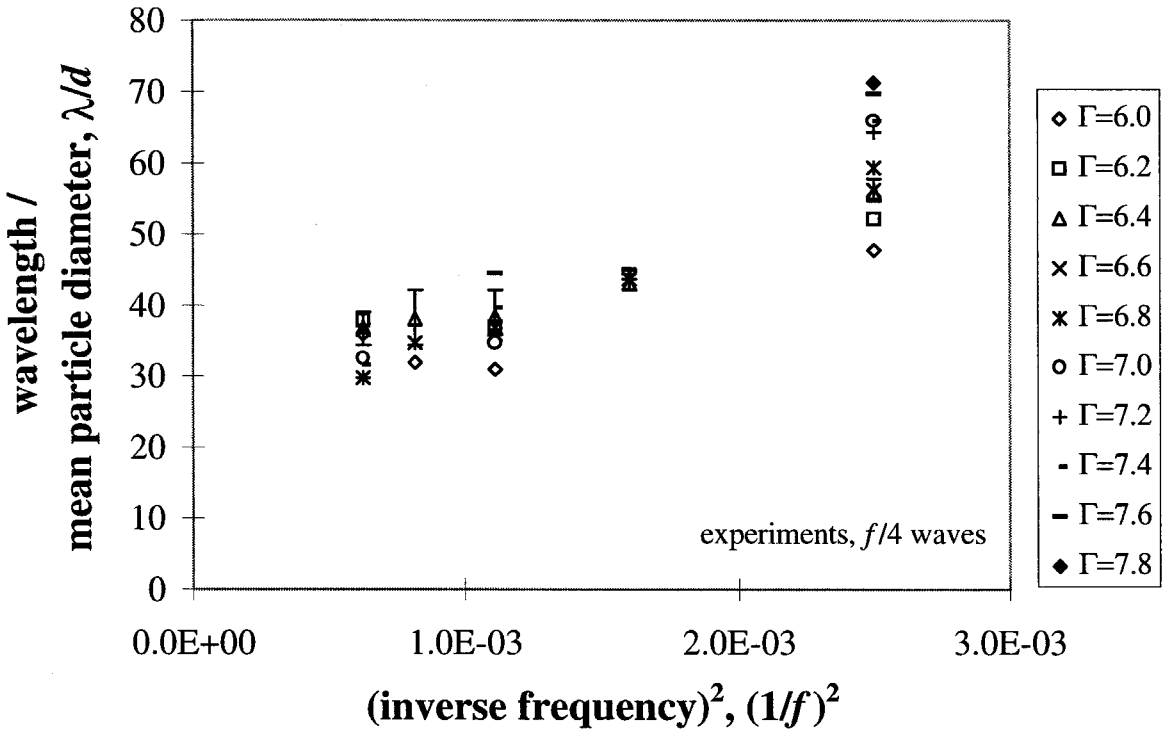

Figure 6.11: The dimensionless wavelength, λ/d, plotted against the inverse frequency squared, $(1/f)^2$ for the $f/4$ waves. Scatter bars are shown only for the $\Gamma = 6.0$ data.

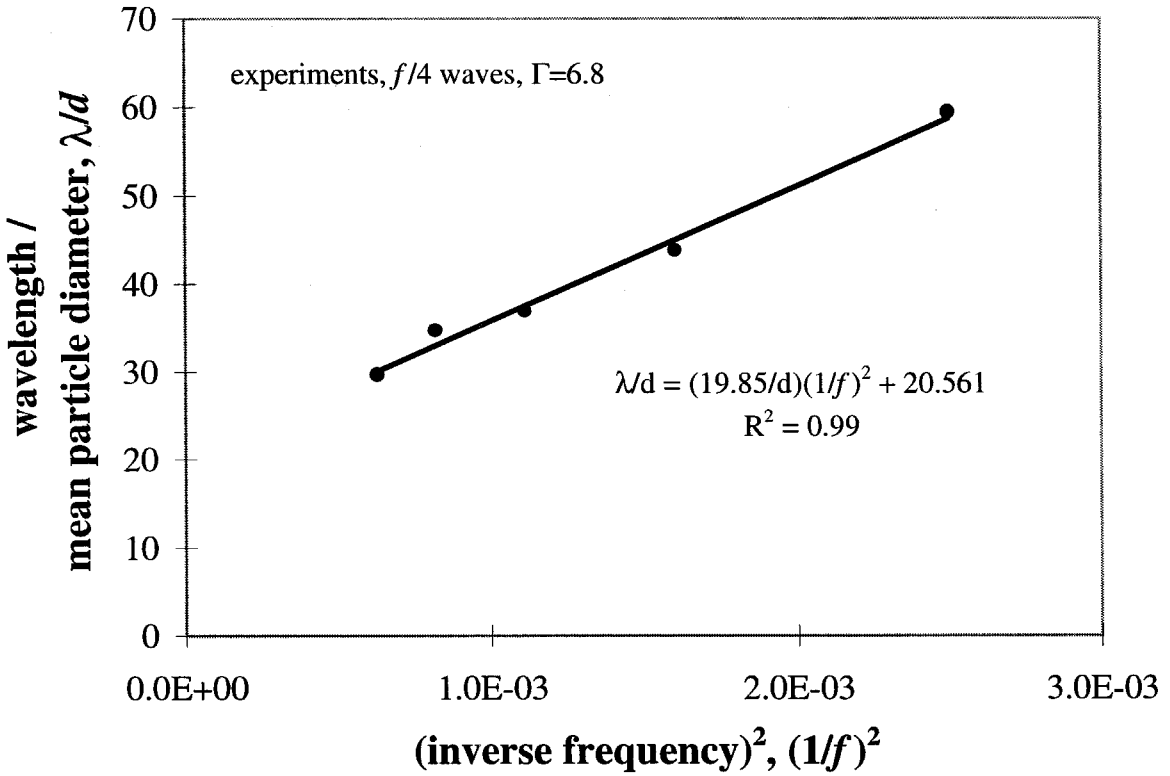

Figure 6.12: The dimensionless wavelength, λ/d, plotted against the inverse radian frequency squared, $(1/\omega)^2$ for the $f/4$ waves at $\Gamma = 6.8$. The solid line is a least squares fit to the equation, $\lambda/d = \lambda_0/d + (g_{\text{eff}}/d)/f^2$ with $\lambda_0/d = 20.56$ and $g_{\text{eff}} = 19.85$ m/s^2.

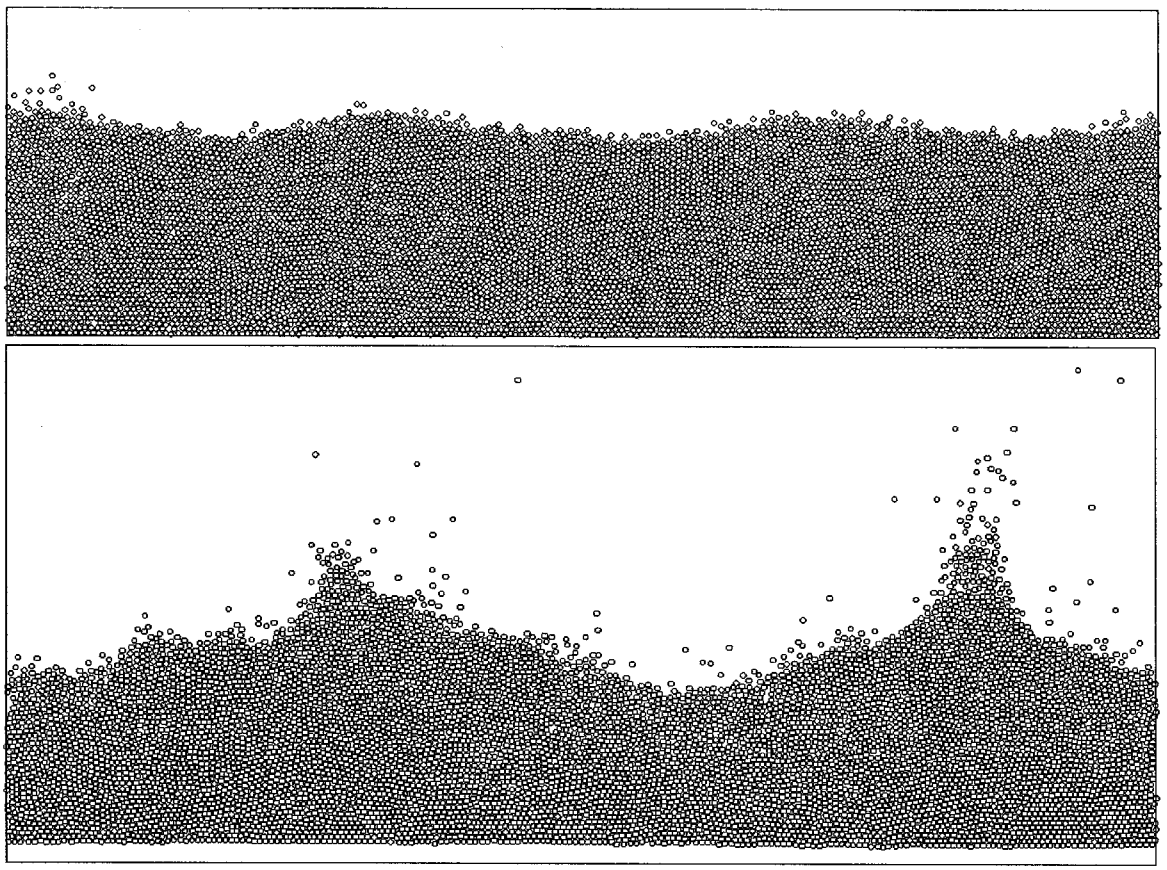

Figure 6.13: Simulations showing $f/2$ round-shaped waves (top) and cusp-shaped waves (bottom) for a container oscillating at $\Gamma = 2.0$ and $f = 25$ Hz (top) and $f = 10$ Hz (bottom). The simulation uses a container with $W/d = 200$ and $h_0/d = 40$ ($N = 8000$). The remainder of the simulation parameters are given in table 5.2.

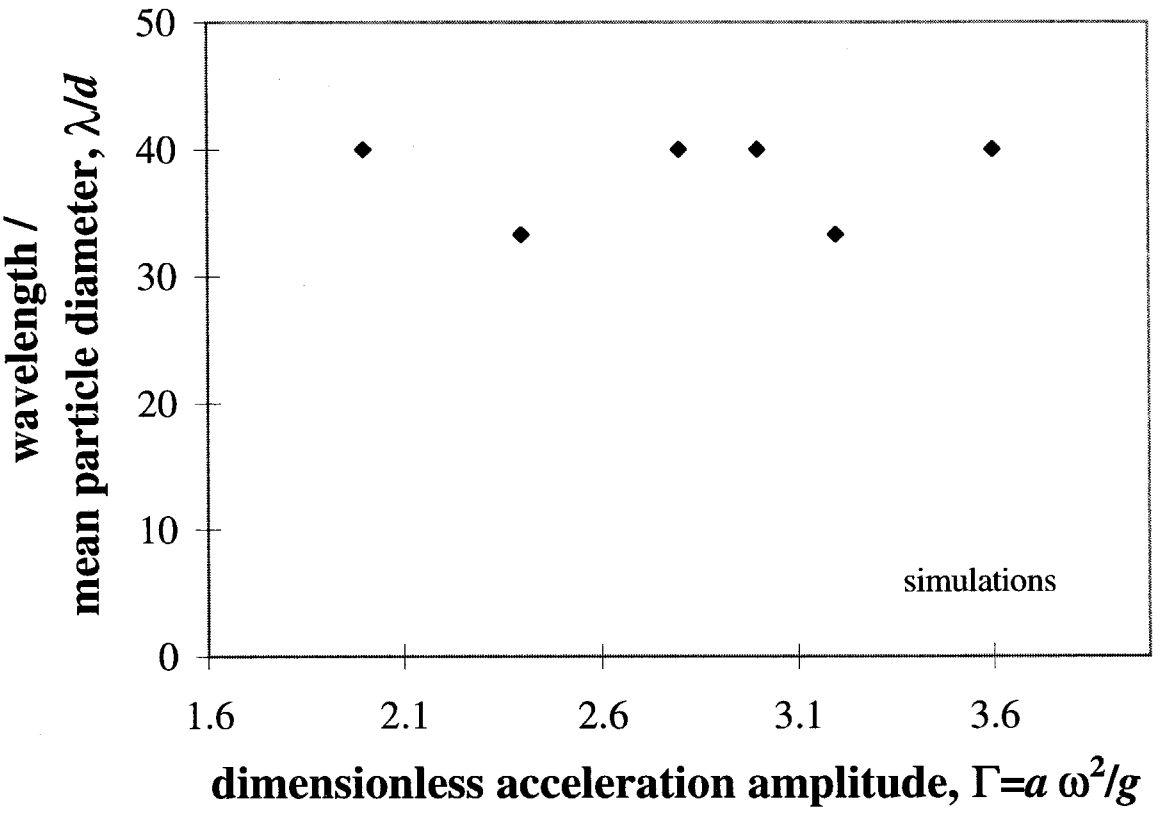

Figure 6.14: The dimensionless wavelength, λ/d, plotted against the dimensionless acceleration amplitude, Γ, for $f = 15$ Hz. The remainder of the simulation parameters are given in table 6.1.

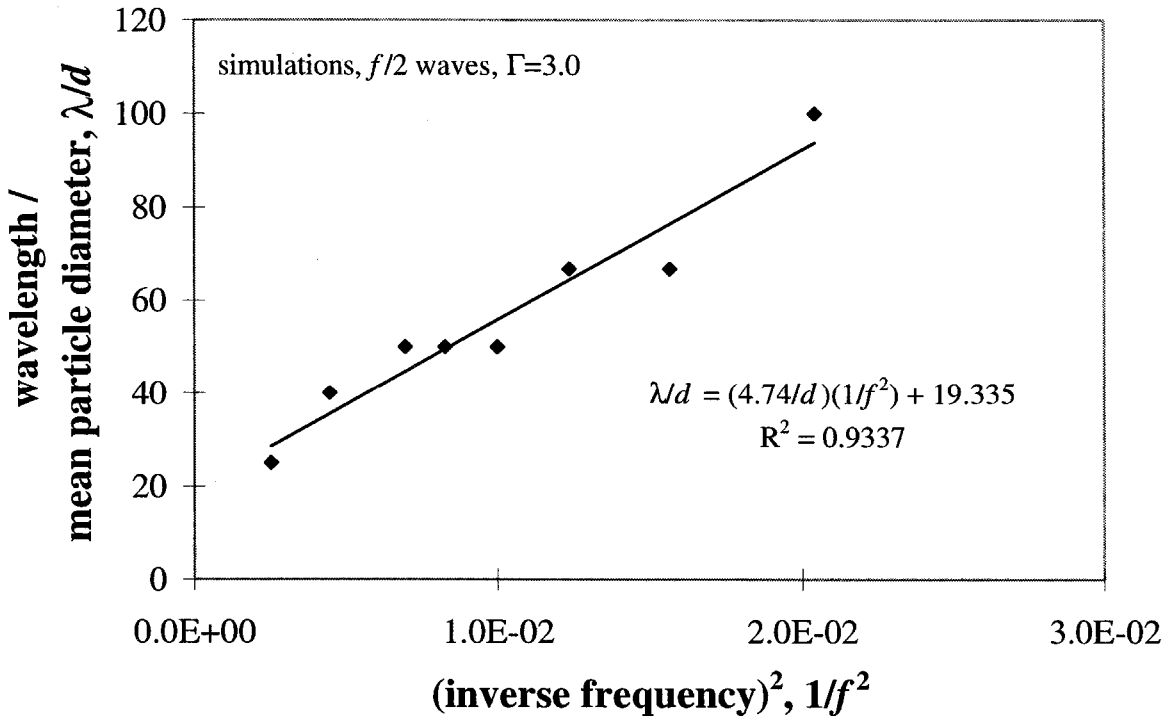

Figure 6.15: The dimensionless wavelength, λ/d, plotted against the square of the inverse frequency, $1/f^2$, for $\Gamma = 3.0$. The solid line is the equation $\lambda/d = \lambda_0/d + (g_{\text{eff}}/d)/f^2$ where $\lambda_0 = 19.3$ and $g_{\text{eff}} = 4.7$ m/s^2. The remainder of the simulation parameters are given in table 6.1.

Chapter 7 Kinks and Kink Convection

7.1 Experiments

When the flight time of the bed is greater than an oscillation cycle, another interesting phenomenon, referred to as a "kink", can form in the particle bed. Kinks are the regions of the particle bed located between two sections of the bed that oscillate out-of-phase with one another. A photograph of a bed with three kinks is shown in figure 3.5 and the motion of the bed is illustrated in figure 7.1. Note that kinks are never observed at wall boundaries.

The experimental measurements of the bed flight time (interpreted from the accelerometer signal and from observations) indicate that kinks only appear after the flight time of the bed undergoes a period doubling bifurcation. This bifurcation occurs after a critical Γ, Γ_1', which decreases with increasing bed depth. For example, when $h_0/d = 10$, the experimental value for Γ_1' is 4.2 but $\Gamma_1' = 3.0$ for $h_0/d = 40$.

Another interesting observation regarding the kink behavior is that different numbers of kinks can exist for the same particle bed and vibration parameters. Furthermore, kinks can be added or removed from the bed by perturbing the bed sufficiently. A simple experiment was conducted where a bed exhibiting two kinks was stirred with a mixing rod (for example, $\Gamma = 6.5$, $h_0/d = 18$, and $f = 20$ Hz). After the perturbation ceased, only one kink remained. Further agitation with the mixing rod produced three kinks. Subsequent experimentation found that for a given bed depth and container size, there is a maximum number of kinks that can be appear in the bed. This observation corresponds with the observations by Douady *et al.* (1989) that there exists a minimum distance between kinks, l, that is a function of both the bed depth, h_0, and the vibration acceleration amplitude, Γ. Thus, the number of kinks for a given bed depth, container width, and vibration parameters is not necessarily unique.

Measurements of this minimum distance were made using the 1.3 mm particles in the 13.5 by 1.6 cm container for acceleration amplitudes, Γ, between 4.0 and 7.0 and bed depths, h_0/d, between 5.5 and 46.1. The experiments were conducted in the following manner. The bed starts with a given number of kinks and the acceleration amplitude is slowly decreased while the frequency is held constant. The Γ at which a kink suddenly disappears is recorded. The distance between the kinks just prior to the transition is the critical kink separation distance. Note that the measurements are insensitive to frequency for $15 < f < 40$ Hz. The measured transitions were sudden and repeatable and the results are shown in figure 7.2 for $f = 30$ Hz where the vertical axis is the particle bed depth, h_0/d divided by the measured minimum node separation distance, l/d, and the horizontal axis is the acceleration amplitude, Γ. The ratio, h_0/l, clearly increases with increasing Γ indicating that for a given container width and Γ, the maximum number of kinks decreases with increasing h_0/d. Similarly, the maximum number of kinks decreases for a fixed h_0/d as Γ decreases. The plot also indicates that h_0/l approaches zero when $\Gamma \approx 4.0$, the approximate value at which kinks first appear. Douady *et al.* (1989) made similar measurements using 0.63-0.80 mm diameter glass spheres and found that the ratio h_0/l varied linearly with Γ where $h_0/l = 0.16(\Gamma - 4.2)$. A linear fit to the current data gives a slope of 0.27.

Bracketing each kink is a pair of counter-rotating convection cells. The motion of particles, when averaged over several oscillation periods, is such that particles move down at a kink and up on either side of it. An illustration of the long term particle motion is shown in figure 3.6 for a bed with three kinks. The rotational speed of the convection cells increases with increasing Γ and as the number of kinks increases. When kinks are located near wall boundaries, particles move up at the walls (note that kinks are never observed at the walls) implying that the kink convection is stronger than the side wall convection.

7.2 Theory

In order for kinks to form, a period doubling bifurcation in the bed flight dynamics must occur. This effect is illustrated in a simple model consisting of two totally inelastic balls separated by some horizontal distance and constrained to move vertically on a sinusoidally oscillating base. This model is very similar to the one used to investigate the sudden bed expansion observed in shallow beds in section 4.2. The only differences with the present model are that two balls are considered and each ball is assumed to be completely inelastic. Modeling the bed (or sections of the bed) as a completely inelastic particle is a valid assumption since the large number of collisions that occur between particles during a collision with the base quickly dissipates all of the kinetic energy in the bed though individual collisions between particles are nearly elastic.

For a totally inelastic particle, the mapping equations 4.6 and 4.7 reduce to

$$-\frac{1}{2}(\phi_n - \phi_{n-1})^2 + \dot{P}^+_{n-1}(\phi_n - \phi_{n-1}) + \Gamma \sin\phi_{n-1} - \Gamma \sin\phi_n = 0 \tag{7.1}$$

$$\dot{P}^+_n = \Gamma \cos\phi_n \tag{7.2}$$

Since the collision is completely inelastic, the balls assume the velocity and position of the base after a collision until the acceleration of the base is less than $-g$,

$$-\Gamma \sin\phi_n < -1 \tag{7.3}$$

The bifurcation analysis performed in section 4.2 indicates that saddle node bifurcations occur at

$$\Gamma_m = m\pi \tag{7.4}$$

and change of stability bifurcations occur at

$$\Gamma'_m = \sqrt{m^2\pi^2 + 4} \tag{7.5}$$

where m is a positive integer.

For $\Gamma < \Gamma_1$ ($\Gamma < \pi$), only a single trajectory is possible with a flight time, Δt, less than an oscillation period, T. The motion of the ball repeats every cycle. Thus the stable motion for the two balls is identical and synchronous. In the upper left corner of figure 7.3 the trajectory for the balls when $\Gamma = 2.0$ is shown. The corresponding flight time can be determined from figure 7.4 which shows Δt as a function of Γ.

When $\Gamma_1 < \Gamma < \Gamma_1'$ ($3.1 < \Gamma < 3.7$), two trajectories appear with flight time $\Delta t = T$. The two are 180^o out-of-phase but only one of the trajectories is stable. The stable motion of the balls for $\Gamma = 3.4$ is shown in the upper right of figure 7.3 and the flight time is indicated in figure 7.4.

For $\Gamma_1' < \Gamma < \Gamma_2$ ($3.7 < \Gamma < 6.3$), the ball has a single trajectory but with two flight times, $\Delta t_1 > T$ and $\Delta t_2 < T$, the sum of which is less than two oscillation periods, $\Delta t_1 + \Delta t_2 < 2T$. Thus, the ball motions can be out-of-phase. Furthermore, each trajectory repeats every two oscillation cycles as is shown at the bottom right of figure 7.3 for $\Gamma = 4.0$ (refer to figure 7.4 for the flight times). The two possible particle trajectories are indicated in the figure.

Another interesting trajectory occurs when $\Gamma_1^* = 4.6$. For $\Gamma_1^* < \Gamma < \Gamma_2'$, the ball has a single flight time (figure 7.4). As Γ increases from Γ_1' to Γ_1^*, the first flight time Δt_1 increases and the second flight time, Δt_2 decreases until at Γ_1^*, only a single flight time remains with $\Delta t < 2T$. The ball motions still repeat every two oscillation cycles as seen at the bottom left of figure 7.3. Note that other period doubling bifurcations occur at higher values of Γ.

7.3 Simulations

Kinks and their associated convection cells are also observed in the simulations. A snapshot from a simulation with two kinks is shown in figure 7.5 with the long term convective motion shown in figure 7.6.

The convection cells form as a result of the out-of-phase motion of the bed (possible only after the period doubling bifurcation) and the dilation of the particle bed during

flight. When a section of the particle bed collides with the oscillating base, particles in that region consolidate and, in effect, become "solidified." The particles that are still in flight avalanche over these solid-like regions of material. This effect is clearly seen by examining the average instantaneous particle velocity vectors for various stages of the kink evolution. The method for determining the averaged instantaneous velocity vectors was described previously when discussing side wall convection. Figure 7.7 shows the averaged instantaneous particle velocities relative to the base at a phase angle of zero radians for a bed exhibiting two kinks. The solidified region of particles is clearly seen in the center of the figure as the region with small magnitude velocity vectors. Particles avalanching down and away from the solidified region are also apparent. A similar velocity field is observed for the same phase angle during the next cycle except the in-flight and solidified regions of the particle bed are switched. Particles still avalanche toward the base at the kinks but the horizontal velocity component is opposite that for the previous cycle. The average particle motion over several oscillation cycles produces the pairs of counter-rotating convection cells that bracket each kink.

These convection cells appear whenever kinks occur, even when $\mu = 0.0$ - counter to the case for side wall convection. Additionally, the two convection mechanisms compete when wall boundaries are included in the simulations. At the walls, the side wall convection behavior forces particles to move down at the walls while, if a kink is present near the wall (recall that kinks never appear at wall boundaries), the kink convection results in upward particle movement at the walls. In all of the simulations observed here, the kink convection mechanism is stronger than the side wall convection mechanism and as a result, particles move up at the walls when kinks are near wall boundaries. However, when kinks are far from the walls, the side wall mechanism dominates and particles move down at the walls.

7.4 Discussion

The observation that Γ_1' and Γ_1^* decrease with increasing h_0/d is different than what is reported by Douady *et al.* (1989). They found that the critical values increase with increasing h_0/d and attribute this behavior to the effects of the interstitial fluid. The reason for this discrepancy is not clear. Indeed, drag on the particle bed will cause the critical values of Γ to increase. One effect that may also be an important factor is the vertical dilation of the bed but this was not studied in the present work.

Douady *et al.* (1989) proposed a mechanism that explains the trend for the minimum kink separation distance as well as the observed convection cells. Their hypothesis emphasizes the differences in the packing structure of the bed and is best explained using the series of illustrations shown in figure 7.8. Recall that kinks appear because sections of the bed oscillate out-of-phase with each other. When a region of the bed comes into contact with the container base, the particles in that region consolidate and "solidify." The particles in the dilated, fluid-like regions avalanche down the slopes of the solidified region toward the base and also become solidified. The minimum separation distance, l, is the width achieved by the solidified region before it leaves the container base. The convection cell behavior is also produced. Particles avalanching down the solidified region's slopes have a downward motion away from the solidified region. However, during the next oscillation cycle, the solidified and fluid-like regions are switched and so particles have a downward motion toward the formerly solidified region. Since mass must be conserved, particles at the center of the fluidized regions are forced upwards. This particle motion, when observed over several oscillation cycles, produces a pair of counter-rotating convection cells where particles move down at the kinks. The simulations indicate that this effect is indeed occurring.

Tables and Figures

Γ	6.0
f	25 Hz
W/d	200
h_0/d	40
N	8000
ϵ_{pp}	0.70
$k_{n,pp}$	$4.701 * 10^3$ N/m
ν_{pp}	$1.251 * 10^{-2}$ N/(m/s)
$k_{s,pp}$	0.0 N/m
μ_{pp}	0.0
lateral boundaries	periodic
ϵ_{pw}	0.70
$k_{n,pw}$	$9.402 * 10^3$ N/m
ν_{pw}	$2.502 * 10^{-2}$ N/(m/s)
$k_{s,pw}$	0.0 N/m
μ_{pw}	0.0
d	0.9 - 1.1 mm
ρ	2500 kg/m^3
Δt	$4.337 * 10^{-6}$ sec

Table 7.1: The simulation parameters used for the simulation shown in figure 7.5.

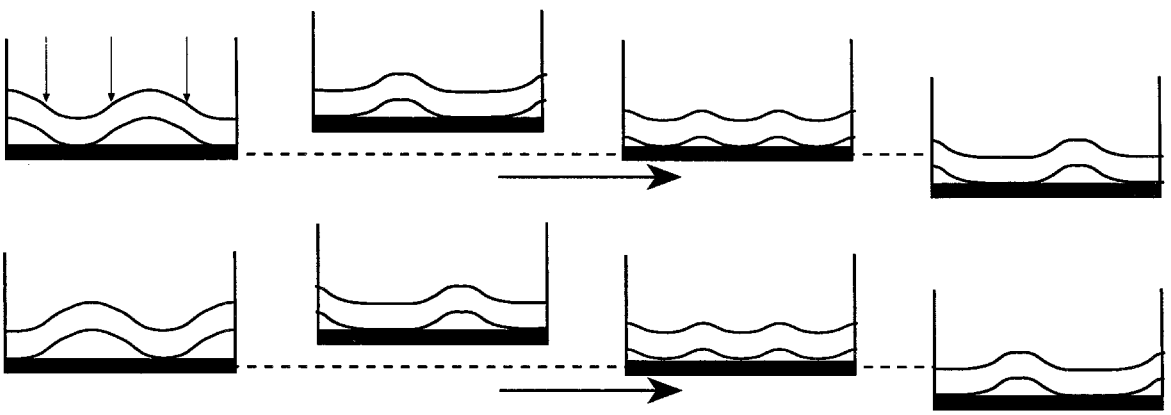

Figure 7.1: A series of illustrations of the bed motion with three kinks (indicated by arrows) over two oscillation cycles.

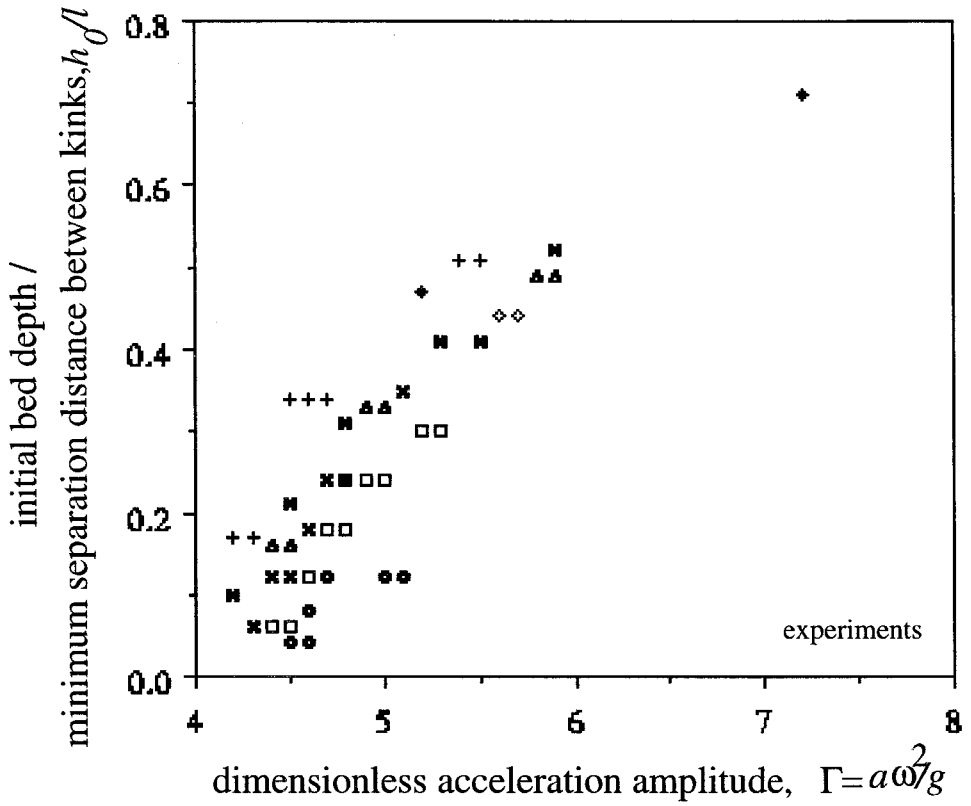

Figure 7.2: The particle bed depth, h_0, divided by the minimum distance between kinks, l, as a function of the dimensionless acceleration amplitude, $\Gamma = a\omega^2/g$. The measurements were taken when $f = 30$ Hz in the 13.5 by 1.6 cm container. Legend: $\diamond = h_0/d = 5.5$, $\square = h_0/d = 6.3$, $\times = h_0/d = 8.3$, $* = h_0/d = 14.5$, $\triangle = h_0/d = 17.2$, $+ = h_0/d = 23.8$, $\bullet = h_0/d = 33.3$, $\circ = h_0/d = 46.1$.

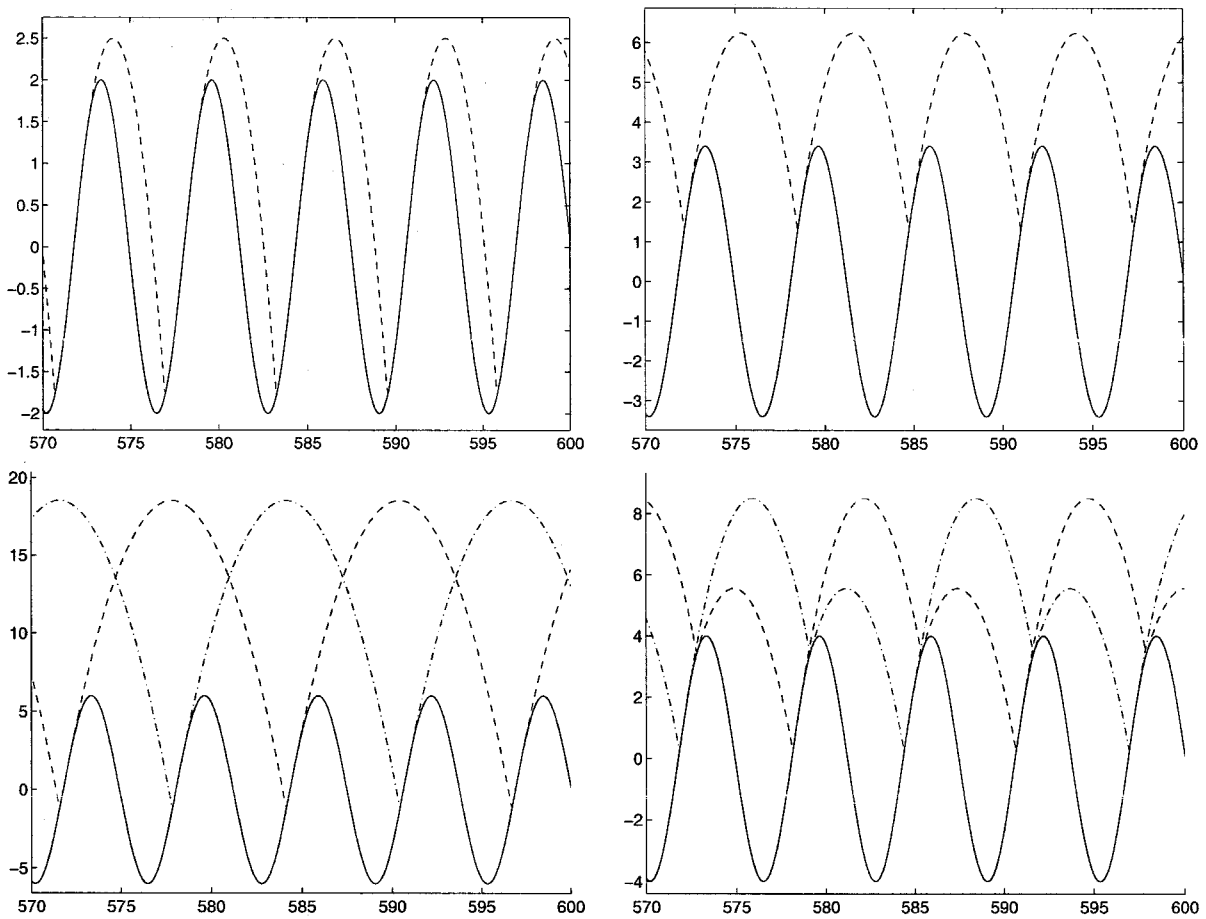

Figure 7.3: Trajectories for a completely inelastic ball ($\epsilon = 0$) on a sinusoidally oscillating base as a function of dimensionless time, $\phi = \omega t$. Clockwise from the upper left: $\Gamma = 2.0$, $\Gamma = 3.4$, $\Gamma = 4.0$, and $\Gamma = 6.0$. The solid line is the floor trajectory and the dashed lines are the particle trajectories.

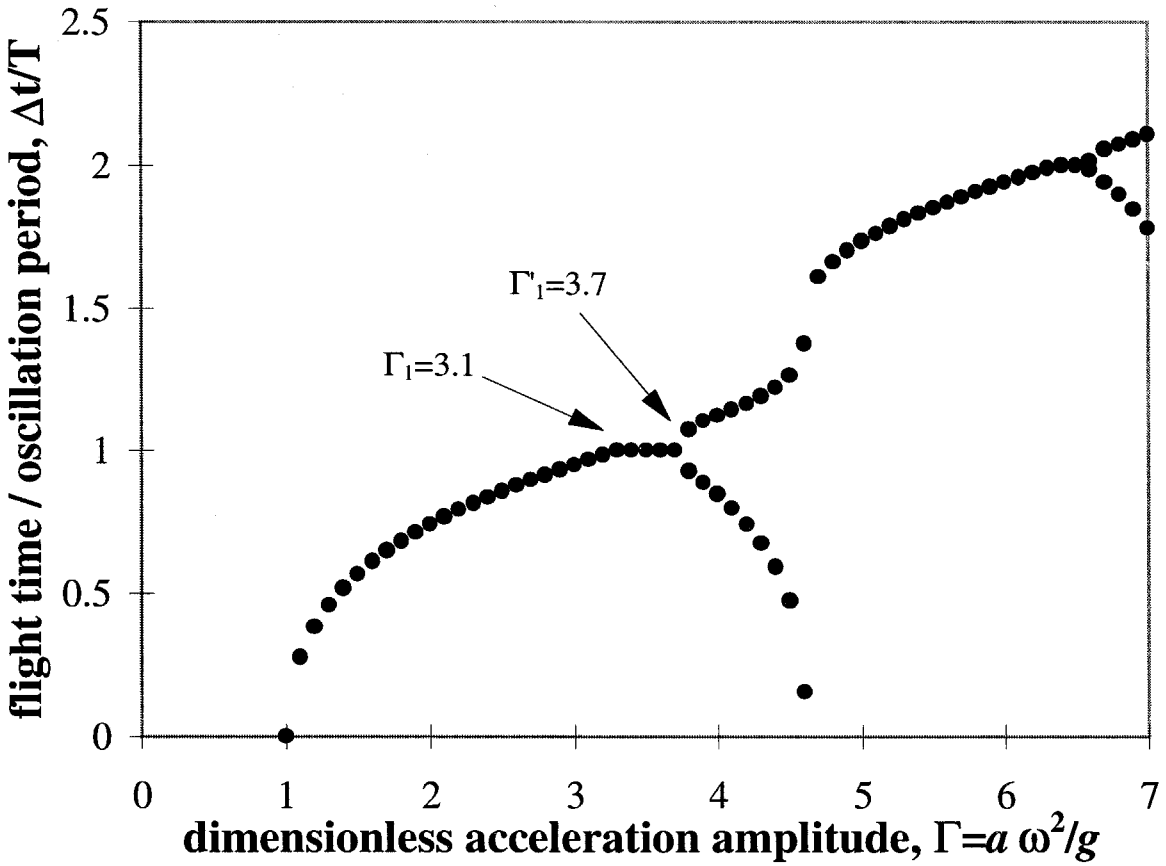

Figure 7.4: Flight time, Δt, plotted against acceleration amplitude, Γ, for a completely inelastic ball on a sinusoidally oscillating table.

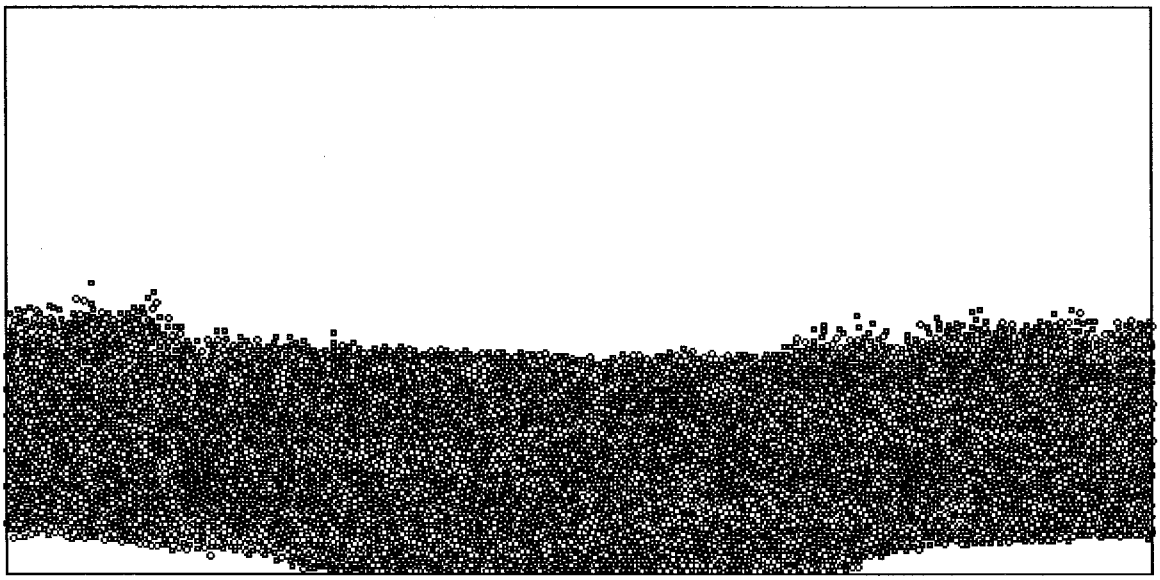

Figure 7.5: A particle bed with two kinks for $\Gamma = 6.0$ and $f = 25$ Hz. The remainder of the simulation parameters are given in table 7.1.

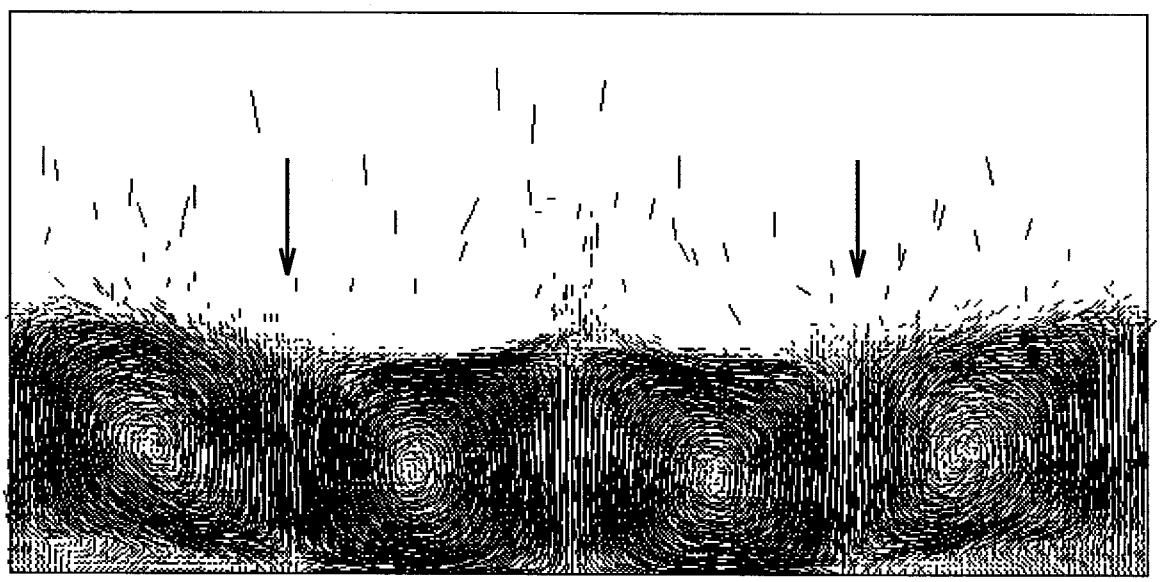

Figure 7.6: The long term particle velocity vectors for the bed in figure 7.5. Particles move down at the kinks which are indicated with arrows. The velocity vectors are averaged over eight samples.

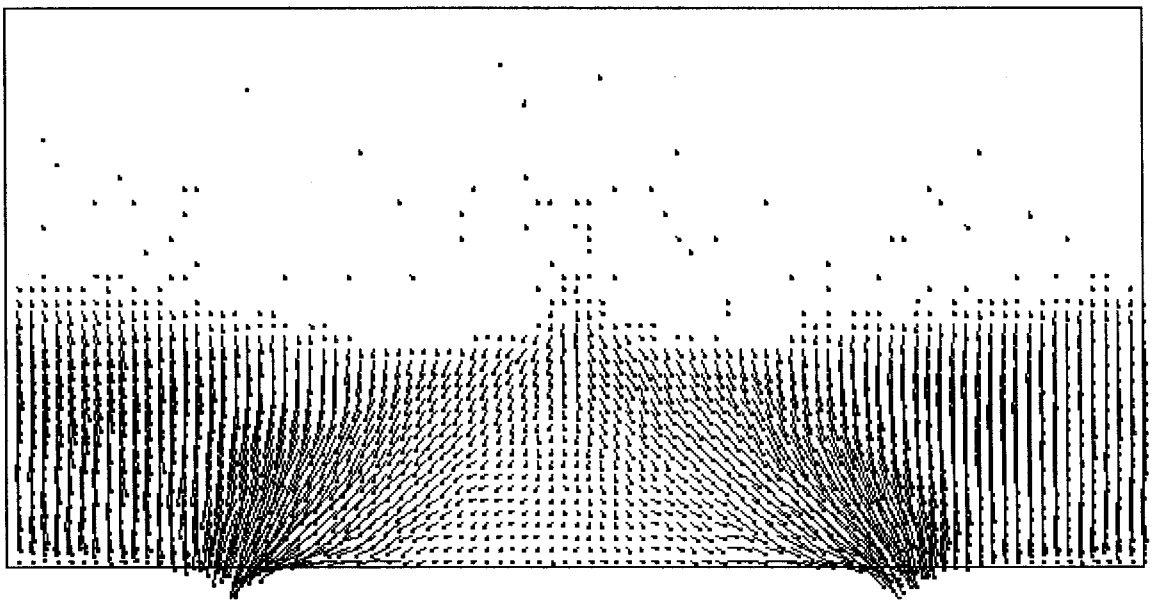

Figure 7.7: The average instantaneous particle velocities for the bed in figure 7.5 at a phase angle of zero degrees. The velocity vectors represent the average value of eight samples.

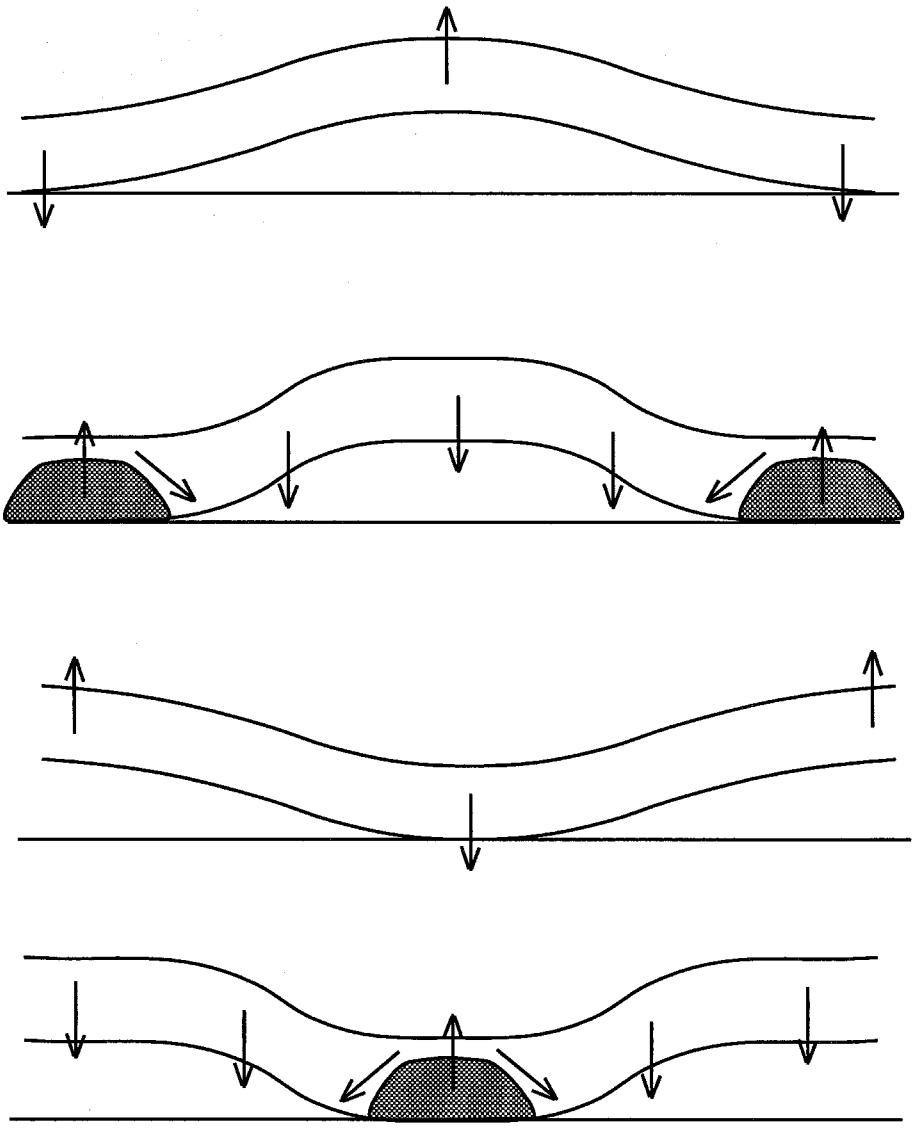

Figure 7.8: Illustrations showing the mechanism proposed by Douady *et al.* (1989) to explain the minimum kink separation distance and the convection cells associated with kinks.

Chapter 8 Vibrating Hopper Flows

8.1 Experiments

The experimental apparatus for examining vibrating hopper flows is similar to that described in section 2.1.2 for studying the vibrated, deep bed behaviors. A two-dimensional wedge hopper was mounted on the Ling electromagnetic shaker that provided vertical, sinusoidal vibrations. The acceleration level and frequency of the oscillations could be controlled independently and were monitored with an accelerometer mounted on the base plate of the shaker. The front and rear hopper walls were lined with smooth window glass and the lateral inclined boundaries consisted of lucite with a milled surface. The distance between the front and back walls of the hopper, W_{fb}, was 1.27 cm (approximately $10d$) deep and had an exit width, W_e, of 4.0 mm (approximately $3.1d$) with walls angled 45^0 outward from the vertical centerline of the hopper.

The hopper was filled with approximately 200 gms of 1.3 mm diameter glass spheres giving an average free surface height above the exit plane, h_0, of $24We$. For the non-vibrating hopper the total time of discharge for the material was 21.8 seconds resulting in an average mass discharge rate of $\dot{D}_0 = 9.2$ gm/sec. The discharge time was determined by recording the time it took for the hopper to completely discharge after the exit was first opened. The discharge rate is constant during most of the discharge period except for a short initial transient period when the hopper exit is first opened and a final transient when the head of material is less than roughly W_e (see, for example, Nedderman *et al.*, 1982). The initial and final transient effects did not significantly affect the average discharge rate.

During discharge without vibration, the free surface of the material formed a V-shaped valley. Particles avalanched continuously down the sloped surfaces toward the centerline of the hopper. Next to the inclined walls, two stagnant flow regions

were observed characteristic of funnel-flow conditions. As material discharged from the hopper, the stagnant flow regions became smaller until all of the material in the hopper flowed.

When the exit was closed and the hopper subjected to vertical oscillations, a circulation pattern formed similar to the one described in chapter 5 but opposite in direction. A boundary layer of particles moved up to the free surface along the inclined walls of the container and down at the centerline of the hopper as shown in figure 8.1. A small region near the exit of the hopper always remained stagnant, however. When the hopper exit was opened, the convection cells were no longer apparent and mass-flow behavior resulted instead of the funnel flow behavior observed for the static hopper. Using a strobe lamp, $f/2$ surface waves were observed on the free surface of the bed when the dimensionless acceleration amplitude, Γ, was greater than 2.5 up to $\Gamma = 4.0$, the maximum Γ examined in these experiments. The waves continued to form as the material discharged until the bed height in container was approximately $5W_e$ above the exit plane.

The mean discharge rate from the vibrating hopper was also measured. The discharge rate divided by the static hopper discharge rate is plotted in figure 8.2 as a function of the dimensionless oscillation velocity amplitude, $a\omega/\sqrt{gd}$. For dimensionless velocity amplitudes less than approximately 0.40, the discharge rate from the hopper is greater than that for a non-vibrating hopper. For example, at $a\omega/\sqrt{gd} = 0.3$, $\dot{D}/\dot{D}_0 \approx 1.05$. As the velocity amplitude of the oscillations increases, however, the discharge rate decreases. When $a\omega/\sqrt{gd} > 0.7$, the vibrating hopper discharge rate is less than the static hopper discharge rate and at $a\omega/\sqrt{gd} = 2.8$, $\dot{D}/\dot{D}_0 \approx 0.75$.

8.2 Simulations

The soft particle method described in section 2.2 was also used to investigate the vibrating hopper experiment. The baseline simulated hopper consisted of two walls angled outward from the centerline of the hopper at 45^0 with an exit width of $10d$. The remainder of the simulation parameters are given in table 8.1.

Simulations were first run for a vibrating hopper with a closed exit. Convection cell patterns similar to those observed in the experiments were produced. Figure 8.3 shows the long term particle velocities for a bed oscillating at $\Gamma = 2.0$ and $f = 5$ Hz (the remainder of the simulation parameters for this simulation are given in table 8.2). The convective motion of particles is clearly seen with particles moving up at the walls and down in the center of the hopper. The convective motion is weaker at higher frequencies and smaller Γ similar to the trends observed in chapter 5. On the free surface of the bed $f/2$ waves are also observed.

The discharge rate from the hopper was also examined for varying vibration parameters. In order to examine the discharge rate from the simulated hopper over long periods of time while keeping the number of particles in the simulation small, particles discharged from the hopper were recycled back into the top of the hopper. When particles were greater than an exit width, W_e, below the hopper exit plane, their vertical position was changed such that they were placed just above the free surface of the bed. The particle velocities were also set to zero in order to reduce the impact magnitude with the bed. Since the free surface of the bed was approximately $6.5W_e$ above the exit plane, the refilling procedure had little effect on the particle behavior near the hopper exit. As a check, the discharge rate for a simulation where particles are not recycled was compared with the discharge results compared with a refilled hopper and the results were similar. The discharge rate results for the simulated hopper using the parameters in table 8.1 are shown in figure 8.2. Note that the discharge rate for the simulated hopper is non-dimensionalized by the discharge rate for a simulated non-vibrating hopper. The simulation discharge rate also decreases with increasing vibration velocity amplitude but the small increase at low vibration velocities is not observed.

The instantaneous discharge rate was also examined using the simulations. Figure 8.4 shows the instantaneous discharge rate, $\dot{d}$, non-dimensionalized by the mean discharge rate for a non-vibrating hopper, $\dot{D}_0$, as a function of the dimensionless oscillation phase angle, $\phi/(2\pi)$, where ϕ is the phase angle in radians. The instantaneous discharge rate was determined by counting the number of particles that pass the exit

plane of the hopper over a specified period of time. The data suggests that the discharge rate from the hopper varies with the effective gravity acting on the bed. Thus, when the hopper walls are accelerating upwards, the effective gravity acting on the bed is greater than g and the discharge rate increases. When the bed is decelerating and the effective gravity is less than g, the discharge rate decreases. Note, though, that when the bed is in-flight and the effective gravity is zero (the bed is in free fall), the particles continue to discharge from the hopper.

8.3 Discussion

The side wall convection up at inclined walls can be explained using the asymmetric drag argument proposed in section 5.2. When the bed leaves the floor in the inclined wall container, few particle collisions occur with the walls since the walls slope away from the bed (refer to the top of figure 8.5). Thus, the downward acting shear force on the bed is nearly zero. While the bed is in flight, it dilates since it is no longer constrained by the container walls. As a result of the dilation, when the bed falls back to the container base it contacts the inclined walls of the container prior to impacting the base (the bottom of figure 8.5). These collisions result in an upward acting shear force on the bed since the walls of the container are moving up relative to the bed. Thus, the net shear force acting on the bed due to the container walls is in the positive vertical direction over an oscillation cycle and the upward moving boundary layer at the walls is produced. This convection behavior at inclined walls has also been observed in experiments by Takahashi *et al.* (1968) and Knight *et al.* (1993).

The decrease in the discharge rate from hopper may be attributed, in part, to the effective gravity acting on the bed over an oscillation cycle (refer to Suzuki *et al.*, 1968). The instantaneous discharge rate from the hopper, $\dot{d}$, is given by

$$\dot{d} \propto \rho_b \sqrt{g_{\text{eff}}} D_h^{5/2} \tag{8.1}$$

where ρ_b is the bulk density of the granular material, g_{eff} the effective gravity acting

on the bed, and D_h the hydraulic diameter of the exit orifice (refer to Nedderman *et al.*, 1982). The effective gravity varies over an oscillation cycle since the bed rests on the accelerating hopper walls, is in free flight, and impacts the hopper walls at different times in the oscillation cycle. The values for the effective gravity are given by,

$$g_{\text{eff}} = \begin{cases} g(1-\Gamma\sin(\omega t)) & 0 \le t < t_0 & \text{the bed rests on the hopper walls} \\ 0 & t_0 \le t < t_1 & \text{the bed is in flight} \\ d\dot{y}_p/dt & t_1 \le t < t_1 + \Delta t & \text{the bed impacts the hopper walls} \\ g(1-\Gamma\sin(\omega t)) & t_1 + \Delta t \le t < T & \text{the bed rests on the hopper walls} \end{cases} \tag{8.2}$$

where t_0 is the time at which the bed starts to free fall, $d\dot{y}_p/dt$ the acceleration of the bed during impact with the hopper walls, t_1 the time at which the bed first contacts the hopper walls, Δt the impact duration, and T the oscillation period. The mean acceleration of the bed during impact is given by,

$$\overline{d\dot{y}_p/dt} = \frac{\dot{y}_p(t_1+\Delta t) - \dot{y}_p(t_1)}{\Delta t} \tag{8.3}$$

where $\dot{y}_p(t_1+\Delta t) = a\omega\cos(\omega(t_1+\Delta t))$ and $\dot{y}_p(t_1) = -g(t_1-t_0) + a\omega\cos(\omega t_0)$. Note that if $\Gamma \le 1$, the bed does not leave the hopper walls and

$$g_{\text{eff}} = g(1-\Gamma\sin(\omega t)) \tag{8.4}$$

over the entire oscillation period. Additionally, it is also assumed that particles do not re-enter the hopper exit during free fall.

If the time of impact is assumed to be small such that, $t_1 + \Delta t \approx t_1$, the mean discharge rate over an oscillation cycle, $\dot{D}$, non-dimensionalized by the mean discharge rate for a non-vibrating hopper, $\dot{D}_0$, for $\Gamma > 1$ is given by

$$\frac{\dot{D}}{\dot{D}_0} = \frac{1}{2\pi}\left(\int_0^{\phi_0}\sqrt{1-\Gamma\sin\phi}d\phi + \sqrt{\Gamma\cos\phi_1 - \Gamma\cos\phi_0 + \phi_1 - \phi_0}\sqrt{\Delta\phi} + \int_{\phi_1}^{2\pi}\sqrt{1-\Gamma\sin\phi}d\phi\right) \tag{8.5}$$

where $\phi = \omega t$. The phase angles at which the bed leaves the hopper walls, ϕ_0, and re-contacts the walls after free-falling, ϕ_1, are functions of Γ and can be determined from equations (7.1), (7.2), and (7.3). If $\Gamma \leq 1$,

$$\frac{\dot{D}}{\dot{D}_0} = \frac{1}{2\pi}\left(\int_0^{2\pi}\sqrt{1-\Gamma\sin(\phi)}d\phi\right) \tag{8.6}$$

Suzuki *et al.* (1968) also derived equations (8.5) and (8.6) but included an empirically derived expression for the bulk density of the bed as a function of Γ (ρ_b is assumed constant in the present analysis). Suzuki *et al.* also assumed that the dimensionless impact time, $\Delta\phi$, remains constant for all operating conditions. Thus, the mean discharge rate given by equation 8.5 depends only on Γ. Figure 8.6 shows the experimental and simulation data for $\dot{D}/\dot{D}_0$ as a function of Γ for the frequencies examined here. The solid line is equation (8.5) and (8.6) using a value of $\Delta\phi$ determined from the experimental data for $\Gamma = 2$ and $f = 20$ Hz. As is evident in the plot, the experimental data clearly does not collapse to a single curve when plotted against Γ as suggested by the model. Several problems with the model may account for this discrepancy. First, the model assumes that no particles discharge from the hopper while the bed is off the hopper walls. The simulation results clearly show that this is not the case (refer to figure 8.4). Particles continuously discharge from the hopper even at high Γ. Second, the dimensionless impact time, $\Delta\phi$ is assumed to be a constant and small compared to the flight time of the bed. However, at high frequencies the impact time may comprise a significant portion of oscillation period. Lastly, the model presented here does not include the effects of changes in the bulk density of the material as a function of the oscillation parameters. The simulations suggest that when the bed is in flight, the bed dilates and as a result, the bulk density

decreases. Hence the discharge rate will also decrease. Despite these deficiencies, the model does a reasonable job of predicting the discharge rate trend for the range of Γ and frequencies examined here.

The effect causing the slight increase in the discharge rate at low velocity amplitudes is unclear. One possible mechanism that may account for this trend is the decrease in the effective viscosity of the granular material as a result of the oscillations. The vibration causes particles to oscillate in their local neighborhoods - continuously forming and breaking contacts with surrounding particles resulting in more fluid material. Indeed, the experimental measurements by Zik *et al.* (1992) show that the mobility of a particle in a vibrating bed is much greater when $\Gamma > 1$ than for $\Gamma < 1$. It should be noted though that Zik *et al.* also indicate that the mobility decreases with increasing frequency. Thus, for a fixed Γ, the mobility decreases with decreasing velocity amplitude since $a\omega = g\Gamma/\omega$. However, as the velocity amplitude decreases, the maximum height that the bed reaches above the hopper exit also decreases and the effective gravity mechanism becomes less significant. Hence, the two mechanisms may compete at low velocity amplitudes.

Tables and Figures

f	20 Hz
W_e/d	10
θ_w	45^0
h_0/W_e	6.5
N	5000
ϵ_{pp}	0.80
$k_{n,pp}$	$5.289 * 10^3$ N/m
ν_{pp}	$8.337 * 10^{-2}$ N/(m/s)
$k_{s,pp}$	$5.289 * 10^3$ N/m
μ_{pp}	0.577
ϵ_{pw}	0.90
$k_{n,pw}$	$1.181 * 10^4$ N/m
ν_{pw}	$8.334 * 10^{-3}$ N/(m/s)
$k_{s,pw}$	$1.181 * 10^4$ N/m
μ_{pw}	0.577
d	0.8 - 1.2 mm
ρ	2500 kg/m^3
Δt	$3.310 * 10^{-6}$ sec

Table 8.1: The simulation parameters used to examine the vertically vibrating hopper.

Γ	2.0
f	5 Hz
W_e/d	25.0
θ_w	25^o
N	513
ϵ_{pp}	0.90
$k_{n,pp}$	$5.904 * 10^3$ N/m
ν_{pp}	$4.167 * 10^{-2}$ N/(m/s)
$k_{s,pp}$	$5.904 * 10^3$ N/m
μ_{pp}	0.5
ϵ_{pw}	0.90
$k_{n,pw}$	$1.181 * 10^4$ N/m
ν_{pw}	$8.334 * 10^{-3}$ N/(m/s)
$k_{s,pw}$	$1.181 * 10^4$ N/m
μ_{pw}	1.0
d	0.8 - 1.2 mm
ρ	2500 kg/m^3
Δt	$3.310 * 10^{-6}$ sec

Table 8.2: The simulation parameters used to examine the closed vertically vibrating hopper.

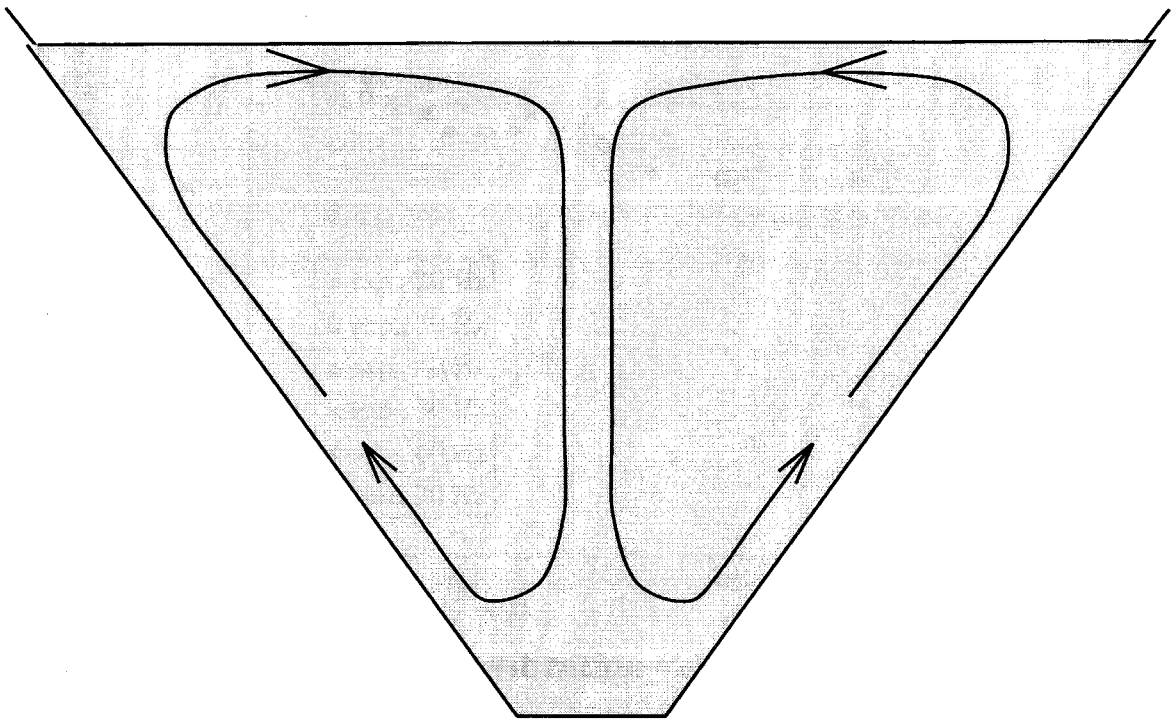

Figure 8.1: An illustration of the side wall convection cells in a vertically vibrating wedge-shaped hopper.

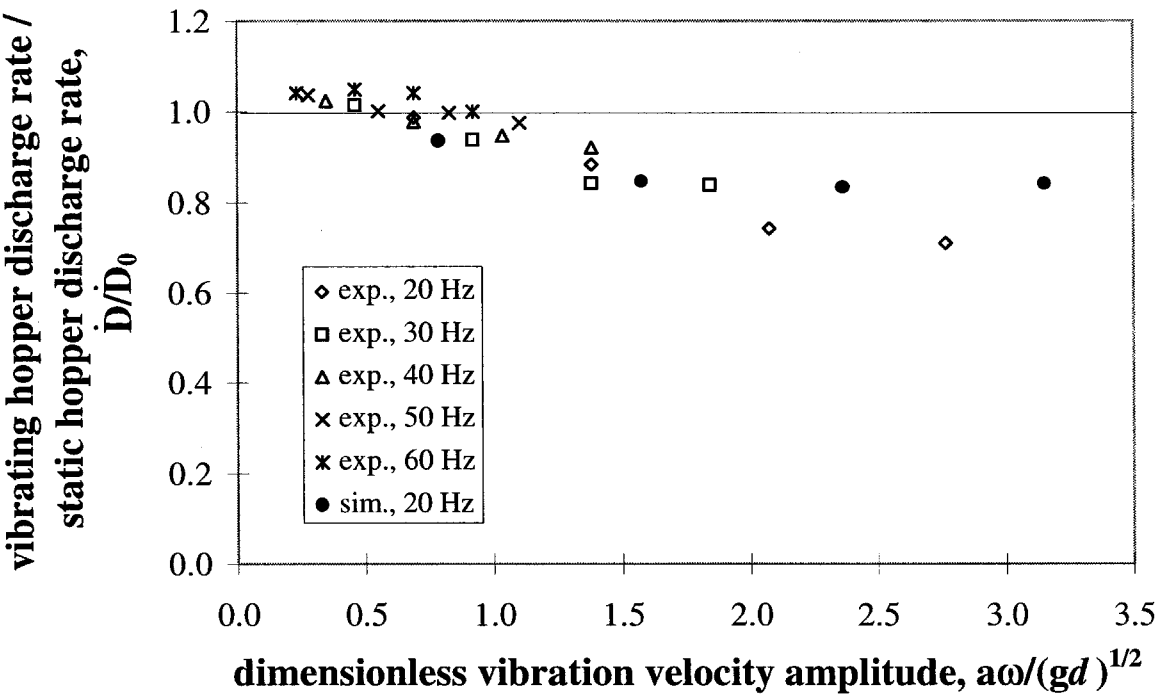

Figure 8.2: The discharge rate from the hopper non-dimensionalized by the discharge rate for a non-vibrating hopper, $\dot{D}/\dot{D}_0$, plotted against the dimensionless oscillation velocity amplitude, $a\omega/(gd)^{\frac{1}{2}}$.

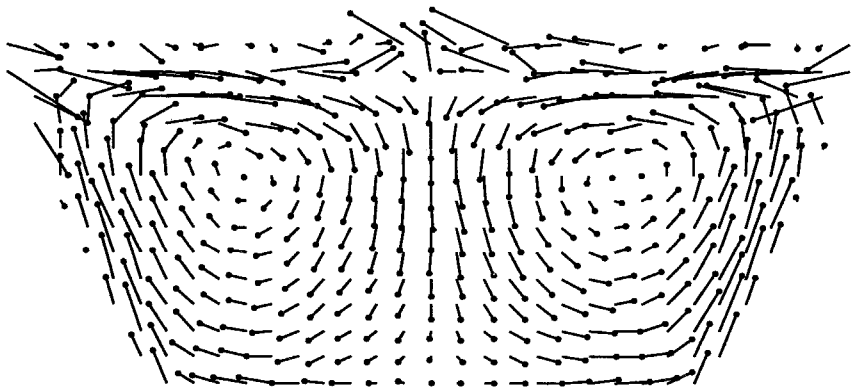

Figure 8.3: The long term velocity vectors for a wedge-hopper with a closed exit. Particles move up along the walls and down in the center of the container. The velocity vectors were averaged over 20 cycles and the circles at the end of the vectors indicate the vector arrowheads. The remainder of the simulation parameters are given in table 8.2.

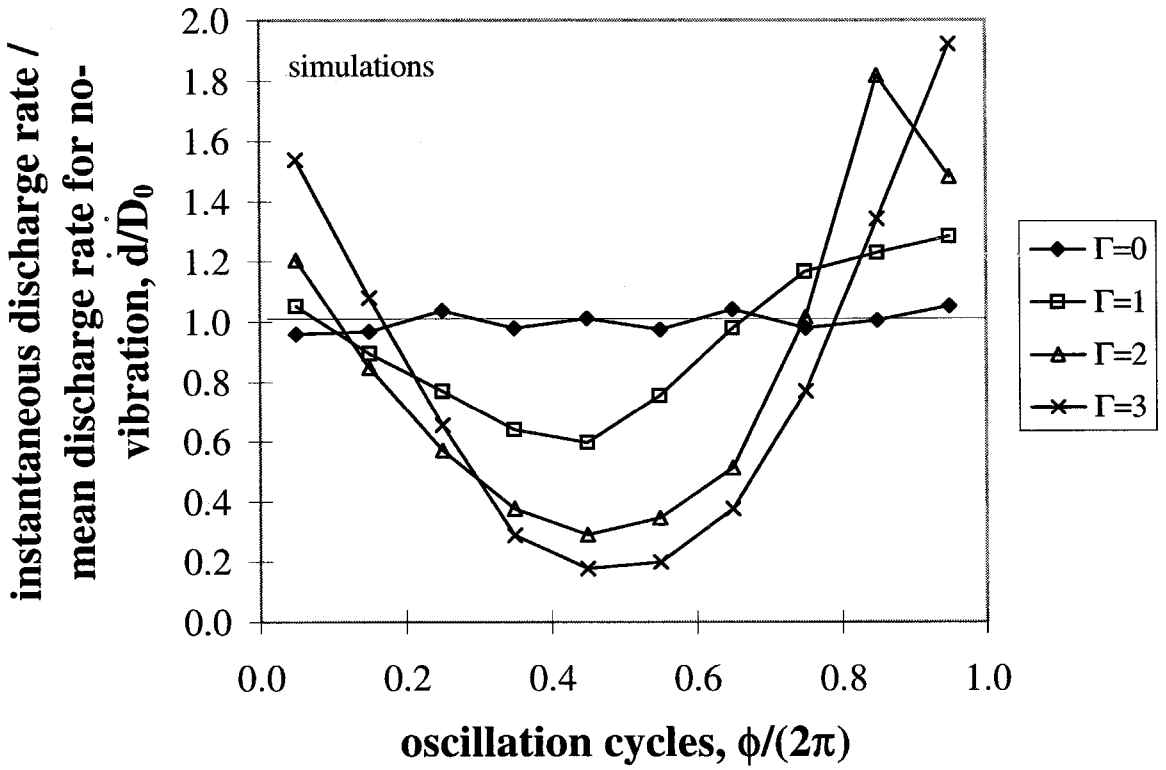

Figure 8.4: The instantaneous discharge rate, $\dot{d}$, non-dimensionalized by the mean discharge rate for a non-vibrating hopper, $\dot{D}_0$, as a function of the dimensionless oscillation phase angle, $\phi/(2\pi)$, for a simulated hopper. The hopper is oscillating at $f = 20$ Hz and the remainder of the simulation parameters are given in table 8.1.

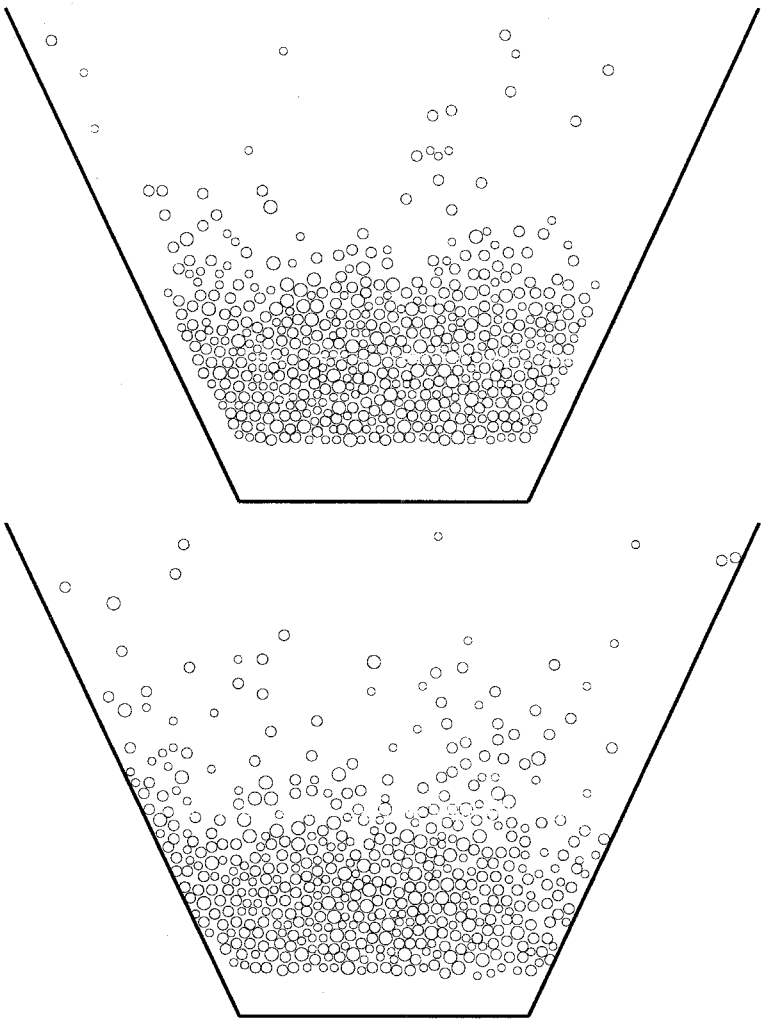

Figure 8.5: The particle bed in figure 8.3 at a phase angle of $\phi/(2\pi) = 0.30$ (top) and $\phi/(2\pi) = 0.80$ (bottom). The simulation parameters are given in the caption to table8.2.

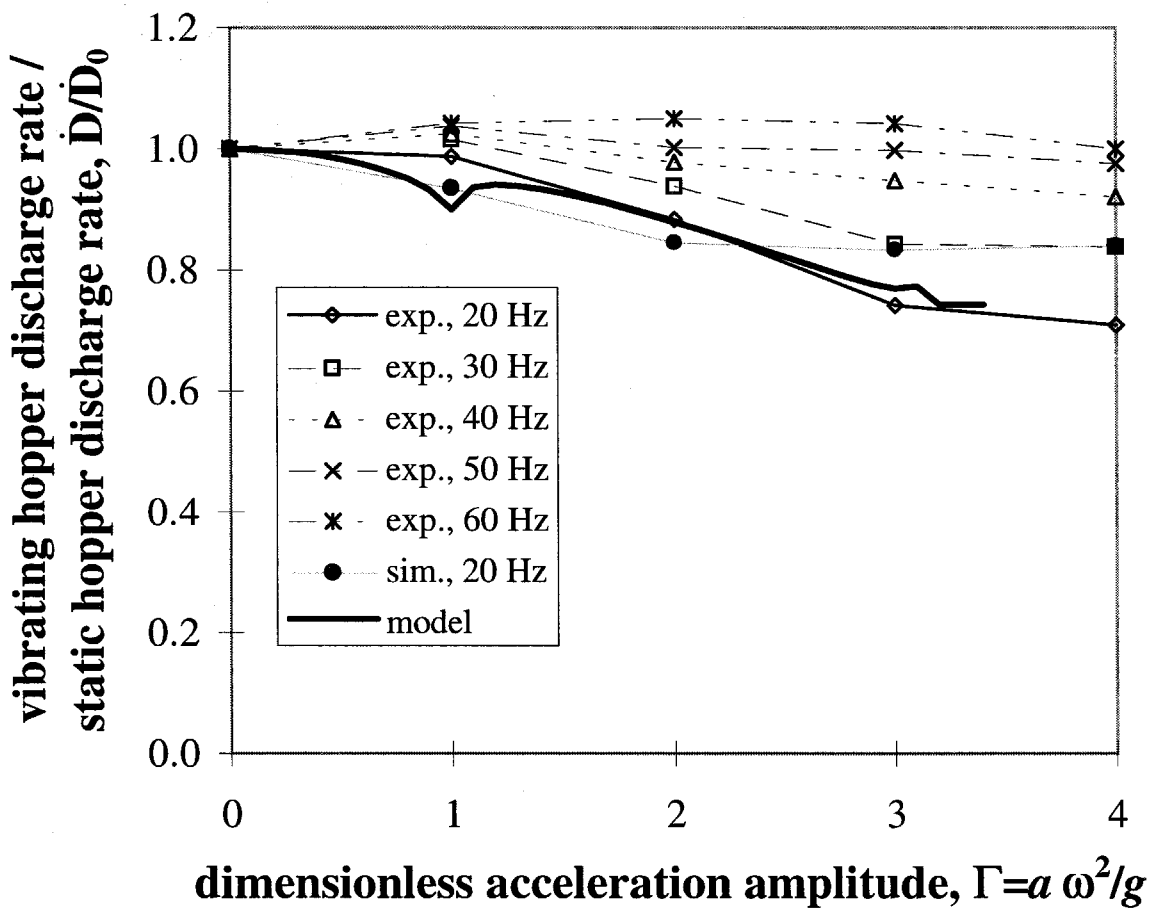

Figure 8.6: The mean discharge rate from a vibrating hopper, $\dot{D}$, non-dimensionalized by the discharge rate for a non-vibrating hopper, $\dot{D}_0$, as a function of the dimensionless acceleration amplitude, $\Gamma = a\omega^2/g$. The solid line is equation 8.5 and 8.6 with the independent constant, $\Delta\phi$, chosen from the experimental data for $\Gamma = 2.0$ and $f = 20$ Hz.

Chapter 9 Summary and Conclusions

9.1 Summary of the Current Work

The results of the experiments and simulations with granular beds subject to vertical, sinusoidal oscillations are summarized. Shallow and deep beds have significantly different behavior. In experiments using 1 mm and 3 mm glass spheres, the critical bed depth differentiating the two regimes was found to be approximately six particle layers when the acceleration amplitude of the oscillations is approximately $2g$. Discrete element simulations indicate that the transition between the two states depends upon the dissipation of random kinetic energy in the bed. When the energy is dissipated prior to the next oscillation cycle, deep bed behavior results and the particles in the bed move as a single, coherent mass. However, if the random kinetic energy is non-zero at the start of the next oscillation cycle, the bed remains in a fluidized, shallow bed state.

Shallow beds are characterized by particle fluidization in which particles have random motions and do not interact significantly. Four bed states, differing in the degree of coherency in the particle motions, were observed similar to those described by Thomas *et al.* (1989). The appearance of the various states in the experiments depends primarily upon the dimensionless bed depth, h_0/d, where h_0 is the bed depth and d a particle diameter, and on the acceleration amplitude of the oscillations, $\Gamma = a\omega^2/g$, where a is the oscillation amplitude, ω the oscillation frequency, and g the acceleration due to gravity.

In the shallowest beds, particles bounce around randomly and the structure of the bed changes very little during an oscillation cycle (the Newtonian-I state.) For slightly deeper beds, particles continue to bounce around randomly during most of an oscillation cycle, however; a dense band of particles forms near the base of the container once each cycle (the Newtonian-II state.) In the third state, referred to

as the coherent-expanded state, the particles move as a coherent mass, however; the mass expands and contracts considerably during an oscillation cycle. The last state, known as the coherent-condensed or deep bed state occurs when $h_0/d \approx 6$ for glass spheres. In this state, the particle bed moves as a coherent, completely inelastic body. The transitions between all but the last two states are gradual. The transition from the coherent-expanded state to the deep bed behavior is sudden and repeatable.

The transition from the deep bed state to the coherent-expanded state is characterized by a sudden expansion of the bed. For a fixed bed depth, this transition occurs at a critical oscillation acceleration amplitude of approximately $\Gamma = 1.9$ for glass spheres. Furthermore, the inverse Froude number based on the oscillation velocity amplitude and the bed expansion can be used to quantify the expansion of the bed in both the sub-critical and super-critical regimes. The expansion is a result of the elasticity of the bed. A simple model consisting of a partially elastic ball bouncing on a sinusoidally oscillating table exhibits a similar sudden expansion (defined as the maximum height between the ball and the base) at a critical acceleration amplitude. The sudden expansion occurs due to a period doubling bifurcation in the flight dynamics of the bed (or ball). Simulations indicate that increasing the rate of energy dissipation in the bed, for example by increasing the friction coefficient or decreasing the coefficient of restitution, causes the critical acceleration amplitude to increase.

The behavior of deep beds ($h_0/d > 6$) is significantly different and is characterized by the coherent motion of the particles which move together like a single, plastic mass. In the deep bed regime, a number of interesting behaviors are observed depending primarily upon the acceleration amplitude, Γ. The depth of the bed is also an important parameter since the Γ at which the various phenomena appear decreases with increasing h_0/d. These phenomena include side wall convection, mounds, surface waves, kinks, and the convection cells associated with kinks.

The side wall convection behavior appears for $\Gamma > 1$ and consists of particles moving down along the vertical walls of the container, subducting back into the bulk of the bed at various depths from the free surface, and returning to the free surface in an upward flow within the bulk. The width of the downward boundary layer is inde-

pendent of depth and is on the order of ten particle diameters, when the bed aspect ratio (defined as the bed depth, h_0, over the container width, W) is less than 0.2. For this range of aspect ratios the convection cells at opposite walls of the container do not interact. However, when $h_0/W > 0.2$, the convection cells interact and the boundary layer thickness is proportional to the container width. The height of the convection cell center above the base, h, varies linearly with the depth of the bed, h_0. The ratio, h/h_0, decreases with increasing acceleration velocity amplitude; an effect that is due to mass conservation. The downward particle flux in the boundary layer, j_d, also increases with increasing oscillation velocity amplitude. Computer simulations indicate that increasing the particle/wall friction increases j_d, while increasing the coefficient of restitution decreases the downward flux in the boundary layer.

The mechanism causing the side wall convection behavior involves particle interaction with the boundaries and the dilation of the particle bed during flight. When the bed first leaves the base, it is densely packed and collisions occur with the walls of the container. Since the walls are moving down relative to the bed, particles that contact the wall are retarded in their upward movement compared to the remainder of the bed. In addition to affecting the particle vertical velocities, the shearing at the walls causes the particles to move away from the walls toward the center of the bed. This action, coupled with the fact that the bed is free to dilate in the vertical direction, means that fewer collisions occur between the particles and the walls as the flight time of the bed progresses. Thus, as the bed falls back toward the base, fewer collisions occur with the walls, which are now moving up relative to the bed. As a result, over an oscillation cycle a net downward shear force acts on the bed creating the downward boundary layer observed at the vertical walls. This same mechanism is also able to explain the upward movement of particles at inclined walls such as in a vibrating wedge-shaped hopper.

Rounded, symmetric mounds form as a result of the convective motion at the walls. Particles at the boundaries move down along the walls leaving the free surface of the bed. The depression that remains is not immediately filled by the neighboring particles since beds of granular materials have an angle of repose. The slope of this

mound is much less than the static angle of repose due to the de-stabilizing effects of the forcing oscillations.

At least two other mechanisms have been shown to form mounds and convection cells. Interstitial fluid effects, important when small particles are used, produce sharp peaked mounds and convection cells far from the influence of wall boundaries (Pak *et al.*, 1995). Additionally, horizontal vibrations coupled with vertical vibration can form asymmetric mounds and convection cells as a result of a vibrating conveyor mechanism (Evesque, 1995). These behaviors emphasize the sensitivity of the bed behavior to external oscillations and fluid effects.

Parametrically forced standing surface waves are another phenomenon observed in deep beds subject to vertical oscillations. Two regimes of waves appear depending on the acceleration amplitude of the vibrations. The range of the acceleration amplitude at which the waves appear increases with decreasing inter-particle friction which plays a role similar to that of viscosity in fluids. The first set of waves, known as $f/2$ waves form at a frequency that is one-half the forcing oscillation frequency. The second set of waves form at one-quarter the forcing frequency and are referred to as $f/4$ waves. The Froude number for the waves, based on the velocity amplitude of the oscillations and the wave amplitude, is nearly constant regardless of oscillation frequency or acceleration amplitude. Furthermore, the wavelength of the standing waves scales with the inverse oscillation frequency squared, the same as that for gravity driven surface waves.

For acceleration amplitudes beyond a critical value, kinks appear in the particle bed. Kinks are the regions of the bed between two sections that oscillate out-of-phase with each other. The simple model used to examine the sudden expansion in the shallow beds, consisting of a single inelastic ball on an oscillating base, can be used to describe the kink behavior. One key difference for modeling the kink motion, however, is that the bed is considered to be completely inelastic. Using this approach, period doubling bifurcations are observed to occur in the flight dynamics. When the first such bifurcation appears, the kinks can appear.

The number of kinks that may appear for a given operating condition is not nec-

essarily unique. Experiments indicate that the number of possible kinks is limited by a minimum kink separation distance which is inversely proportional to the oscillation acceleration amplitude and proportional to the depth of the bed. The physical mechanism limiting the number of kinks also explains the pairs of counter-rotating convective cells that bracket each kink. The mechanism consists of solid-like regions of material forming during impact with the oscillating base and the remaining fluid-like particles avalanching over them. The resulting motion averaged over several oscillation cycles produces the convection cell motion.

Many of the same phenomena observed in vertically vibrating boxes are also observed in vertically vibrated wedge-shaped hoppers. Side wall convection cells appear along the inclined walls of the container with particles moving up along the walls and down in the center of the bed - a direction opposite that for vertical walls. Surface waves are also observed on the free surface of the bed, even as the material in the hopper is discharging. The discharge from the hopper is also significantly affected by the external vibrations. At low oscillation velocities, the mass discharge rate from the hopper increases slightly, while at high oscillation velocities the discharge rate decreases significantly. The cause of the discharge rate dependence on the oscillation velocity is not entirely clear. At low velocity amplitudes the effective viscosity of the bed may be reduced resulting in the increased discharge rate. The decrease in the discharge rate at higher oscillation velocities is due, at least partially, to the change in the effective gravity acting on the particle bed. Examination of the discharge velocity as a function of oscillation phase angle indicates that the flow from the hopper decreases when the effective gravity acting on the bed decreases, but does not go to zero as is expected when the effective gravity is zero.

9.2 Broader Issues

These experiments and simulations illustrate some of the important issues regarding the behavior of flowing granular materials in general. First, the boundary conditions can play a significant role in the behavior of beds of particles. Not only do parti-

cle/wall properties such as friction or coefficient of restitution affect the response of a flowing material as is seen with the downward particle flux associated with side wall convection cell, but the style of the input of energy at the boundaries also is important. The coordinated movement of the particle bed as a result of the vertical, sinusoidal movement of the base gives rise to periodic bed motions such as standing surface waves and kinks. It is not clear that these behaviors would appear if this boundary were modeled as an input of random kinetic energy. Thus, an accurate representation of the boundary conditions is important when modeling a system of granular material.

A second important issue concerns the interaction of particles in a flowing granular material. The phenomena observed in the present experiments indicate that the fluid- and solid-like nature of a granular material as well as the interactions between the two are important to the behavior of the bed. For example, the convection cells associated with kinks are caused by such a fluid/solid interaction. Additionally, the observed surface waves show many fluid-like properties while the mounding behavior can form a stable slope, a solid-like property. This fluid/solid interaction is also evident in the transition between the deep bed and shallow bed states. Current modeling techniques such as the kinetic theory or soil plasticity methods do not address these fluid/solid interactions.

The work performed here also reflects some of the limitations of current experimental techniques and demonstrates the value of computer simulations. For example, all of the observations in the present work have been limited to observing the behavior of particles at boundaries. As is evident with the side wall convection behavior, what occurs at the boundaries may not be representative of what is occurring within the bulk of the material. Additionally, measurements of properties such as inter-particle forces or particle-particle contact duration may provide useful information but are not readily obtainable using current experimental techniques. Computer simulations, however, can provide such information. Furthermore, the trends observed in the experiments are reproducible in simulations suggesting that simulations can also be used qualitatively as a valuable predictive tool.

References

Bachmann, D., 1940, *Verfahrenstechnik Z.V.D.I. Beiheft*, No. 2, pg. 43. (cited by Thomas *et al.*, 1989.)

Bagnold, R.A., 1954, "Experiments on a gravity-free dispersion of large solid spheres in a Newtonian fluid under shear," *Proc. Roy. Soc.*, Vol. 225, pp. 49–63.

Baxter, G.W. and Behringer, R.P., 1991, "Cellular automata models for the flow of granular materials," *Physica D*, Vol. 51, pp. 465–471.

Bechhoefer, J., Ego, V., Manneville, S., and Johnson, B., 1995, "An experimental study of the onset of parametrically pumped surface waves in viscous fluids," *J. Fluid Mech.*, Vol. 288, pp. 325-350.

Ben-Naim, E., Knight, J.B., and Nowak, E.R., 1996, "Slow relaxation in granular compaction," preprint.

Brennen, C.E., Ghosh, S., and Wassgren, C.R., 1996, "Vertical oscillation of a bed of granular material," *J. of Appl. Mech.*, Vol. 63, No. 1, pp. 156–161.

Campbell, C.S., 1982, *Shear flows of granular materials*, Ph.D. Thesis, California Institute of Technology.

Campbell, C.S., 1986, "Computer simulation of rapid granular flows," *Proc. 10th US National Congress of Appl. Mech.*, pp. 327–338.

Campbell, C.S., 1996, "Computer simulation of powder flows," in *Powder Technology Handbook*, to be published.

Chladni, E.F.F., 1787, "Entdeckungen ueber die Theorie des Klangen."

Chlenov, V.A. and Mikhailov, N.V., 1965, "Some properties of a vibrating fluidized bed," *J. of Eng. Phys.*, Vol. 9, pp. 137–139.

Clément, E., Duran, J., and Rajchenbach, J., 1992, "Experimental study of heaping in a two-dimensional sandpile," *Phys. Rev. Lett.*, Vol. 69, No. 8, pp. 1189–1192.

Clément, E., Vanel, L., Rajchenbach, J., and Duran, J., 1996, "Pattern formation in a vibrated 2D granular layer," preprint.

Cundall, P.A. and Strack, O.D.L., 1979, "A discrete numerical model for granular assemblies," *Geotechnique*, Vol. 29, No. 1, pp. 47–65.

Cundall, P.A., 1988, "Formulation of a three-dimensional distinct element model - Part I. A scheme to detect and represent contacts in a system composed of many polyhedral blocks," *Int. J. Rock Mech. Min. Sci. and Geomech. Abstr.*, Vol. 25, No. 3, pp. 107–116.

Douady, S., Fauve, S., and Laroche, C., 1989, "Subharmonic instabilities and defects in a granular layer under vertical vibrations," *Europhys. Lett.*, Vol. 8, No. 7, pp. 621–627.

Ehrichs, E., Jaeger, H., Karczmar, G., Knight, J.B., and Kuperman, V., 1995, "Granular convection observed by magnetic resonance imaging," *Science*, Vol. 267, No. 5204, pp. 1632–1634.

Ennis, B.J., Green, J., and Davies, R., 1994, "The legacy of neglect in the U.S.," *Chem. Eng. Prog.*, Vol. 90, No. 4, pp. 32–43.

Evesque, P. and Rajchenbach, J., 1989, "Instability in a sand heap," *Phys. Rev. Lett.*, Vol. 69, No. 1, pp. 44–46.

Evesque, P., 1990, "Comment on: Convective flow of granular masses under vertical vibrations," *J. Phys. France*, Vol. 51, No. 8, pp. 697–699.

Evesque, P., 1992, "Shaking dry powders and grains," *Contemp. Phys.*, Vol. 33, No. 4, pp. 245–261.

Evesque, P. and Meftah, W., 1993, "Mean flow of a vertically vibrated hourglass," *Int. J. of Mod. Phys.*, Vol. 7, Nos. 9 and 10, pp. 1799–1805.

Faraday, M., 1831, "On a peculiar class of acoustical figures and on certain forms assumed by groups of particles upon vibrating elastic surfaces," *Phil. Trans. R. Soc. London*, Vol. 52, pp. 299–340.

Fauve, S., Douady, S., and Laroche, C., 1989, "Collective behaviors of granular masses under vertical vibration", *J. Phys. France*, Vol. 50, No. 3, pp. 187–191.

FEMA Web Page, 1996, http://www.fema.gov/fema/landsli.html

Foerster, S.F., Louge, M.Y., Chang, H., and Allia, K., 1994, "Measurements of the collision properties of small spheres," *Phys. Fluids*, Vol. 6, No. 3, pp. 1108–1115.

Gallas, J., Herrmann, H., and Sokolowski, S., 1992, "Convection cells in vibrating granular media," *Phys. Rev. Lett.*, Vol. 69, No. 9, pp. 1371–1374.

Goldshtein, A., Shapiro, M., Moldavsky, L., Fichman, M., 1995, "Mechanics of collisional motion of granular materials. Part 2. Wave propagation through vibrofluidized granular layers," *J. Fluid Mech.*, Vol. 287, pp. 349–382.

Goldsmith, W., 1960, *Impact: The theory and physical behavior of colliding solids.*

Gutman, R.G., 1976, "Vibrated beds of powders. Part I: A theoretical model for the vibrated bed," *Trans. Inst. Chem. Engrs.*, Vol. 54, pp. 174–183.

Haff, P.K., 1983, "Grain flow as a fluid-mechanical phenomenon," *J. Fluid Mech.*, Vol. 134, pp. 401–430.

Holmes, P., 1982, "The dynamics of repeated impacts with a sinusoidally vibrating table," *J. of Sound and Vibration*, Vol. 84, No. 2, pp. 173–189.

Hopkins, M.A. and Shen, H.H., 1992, "A Monte-Carlo solution for rapidly shearing granular flows based on the kinetic-theory dense gases," *J. Fluid Mech.*, Vol. 244, pp. 477-491.

Jaeger, H. and Nagel, S., 1992, "Physics of the granular state", *Science*, Vol. 255, No. 5051, pp. 1523–1531.

Jenkins, J.T. and Savage, S.B., 1983, "A theory for rapid flow of identical, smooth, nearly elastic spherical particles," *J. Fluid Mech.*, Vol. 130, pp. 187–202.

Knight, J.B., Jaeger, H.M., Nagel, S.R., 1993, "Vibration-induced size separation in granular media: the convection connection," *Phys. Rev. Lett.*, Vol. 70, No. 24, pp. 3728–3731.

Knight, J.B., Ehrichs, E.E., Kuperman, V.Y., Flint, J.K., Jaeger, H.M., and Nagel, S.R., 1996, "An experimental study of granular convection," submitted to *Phys. Rev. E.*

Kroll, W., 1954, "Fliessersheinungen an Haufwerken in schwingenden Gefässen," *Chemie Ing. Techn.*, Vol. 27, No. 1, pp. 33–38.

Lan, Y. and Rosato, A.D., 1995. "Macroscopic behavior of vibrating beds of smooth inelastic spheres", *Phys. Fluids*, Vol. 7, No. 8, pp. 1818–1831.

Langston, P.A., Tüzün, U., and Heyes, D.M., 1994, "Continuous potential discrete particle simulations of stress and velocity fields in hoppers: transition from fluid to granular flow," *Chem. Eng. Science*, Vol. 49, No. 8, pp. 1259–1275.

Laroche, C., Douady, S., and Fauve, S., 1990a, "Convective flow of granular masses under vertical vibrations," *J. Phys. France*, Vol. 50, No. 7, pp. 699-706.

Laroche, C., Douady, S., and Fauve, S., 1990b, "Reply to Comment on: Convective flow of granular masses under vertical vibrations," *J. Phys. France*, Vol. 51, No. 8, pg. 700.

Lee, J., 1994, "Heap formation in two-dimensional granular media," J. Phys. A, Vol. 27, pp. L257–L262.

Luck, J.M. and Mehta, A., 1993, "Bouncing ball with a finite restitution: chattering, locking, and chaos," *Phys. Rev. E*, Vol., 48, No. 5, pp. 3988–3997.

Luding, S., Clément, E., Blumen, A., Rajchenbach, J., and Duran, J., 1994a, "Onset of convection in molecular dynamics simulations of grains," *Phys. Rev. E*, Vol. 50, No. 3, pp. R1762–R1765.

Luding, S., Herrmann, H.J., and Blumen, A., 1994b, "Simulations of two-dimensional arrays of beads under external vibrations: scaling behavior," *Phys. Rev. E*, Vol. 50, No. 4, pp. 3100–3108.

Maw, N, Barber, J.R., and Fawcett, J.N., 1976, "The oblique impact of elastic spheres," *Wear*, Vol. 38, No. 1, pp. 101–114.

Mehta, A. and Luck, J., 1990, "Novel temporal behavior of a nonlinear dynamical system: The completely inelastic bouncing ball," *Phys. Rev. Lett.*, Vol. 65, No. 4, pp. 393–396.

Melo, F., Umbanhowar, P., and Swinney, H., 1994, "Transition to parametric wave patterns in a vertically oscillated granular layer," *Phys. Rev. Lett.*, Vol. 72, No. 1, pp. 172–175.

Melo, F., Umbanhowar, P., and Swinney, H., 1995, "Hexagons, kinks, and disorder in oscillated granular layers," *Phys. Rev. Lett.*, Vol. 75, No. 21, pp. 3838–3841.

Mindlin, R.D., 1949, "Compliance of elastic bodies in contact," *J. Appl. Mech.*, Vol. 71, No. 3, pp. 259–268.

Metcalf, T.H., Knight, J.B., and Jaeger, H.M., 1996, "Standing wave patterns in shallow beds of vibrated granular material," preprint.

Miles, J. and Henderson, D., 1990, "Parametrically forced surface waves," *Ann.*

Rev. Fluid Mech., Vol. 22, pp. 143–165.

Mindlin, R.D. and Deresiewicz, H., 1953, "Elastic spheres in contact under varying oblique forces," *J. Appl. Mech.*, Vol. 20, pp. 327–344.

Nedderman, R.M., 1982, "The theoretical prediction of stress distributions in hoppers," *Trans. IChemE*, Vol. 60, pp. 259–275.

Nedderman, R.M., Tüzün, U., Savage, S.B., and Houlsby, G.T., 1982, "The flow of granular materials-I. Discharge rates from hoppers," *Chemical Engineering Science*, Vol. 37, No. 11, pp. 1597–1609.

Nedderman, R.M., 1992, *Statics and Kinematics of Granular Materials*, Cambridge University Press.

Nield, D.A. and Bejan, A., 1992, *Convection in Porous Media*, Springer, NY.

Nguyen, T.V., Brennen, C.E., and Sabersky, R.H., 1980, "Funnel flow in hoppers," *J. of Appl. Mech.*, Vol. 47, No. 4, pp. 729–735.

Pak, H. and Behringer, R., 1993, "Surface waves in vertically vibrated granular materials," *Phys. Rev. Lett.*, Vol. 71, No. 12, pp. 1832–1835.

Pak, H., Van Doorn, E., and Behringer, R., 1995, "Effects of ambient gases on granular materials under vertical vibration," *Phys. Rev. Lett.*, Vol. 74, No. 23, pp. 4643–4646.

Potapov, A.V. and Campbell, C.S., 1996, "Computer simulation of hopper flow," submitted to *Physics of Fluids A*.

Press, W.H., Teukolsky, S.A, Vetterling, W.T., and Flannery, B.P., 1992, *Numerical Recipes in C*, Cambridge University Press.

Rajchenbach, J., 1991, "Dilatant process for convective motion in a sand heap," *Europhys. Lett.*, Vol. 16, No. 2, pg. 149–152.

Rátkai, G., 1976, "Particle flow and mixing in vertically vibrated beds," *Powder Tech.*, Vol. 15, pp. 187–192.

Reynolds, O., 1885, "On the dilatancy of media composed of rigid particles in contact," *Phil. Mag.*, Vol. 20.

Richman, M.W. and Martin, R.E., 1992, "Unconfined granular materials thermalized by fluctuating horizontal surfaces," *Proceedings of the 9th Converence on*

Engineering Mechanics, edited by L.D. Lutes and J.N. Niezwecki (ASCE, New York), pp. 900–903.

Rosato, A. and Lan, Y., 1994, "Granular dynamics modeling of vibration-induced convection of rough inelastic spheres," *Proceedings of the First International Particle Technology Forum*, Denver, CO., pp. 446–453.

Rosato, A., Prinz, F., Standburg, K.J., and Swendsen, R., 1986, "Monte Carlo simulation of particulate matter segregation," *Powder Tech.*, Vol. 49, pp. 59–69.

Sadd, M.H., Tai, Q-M., and Shukla, A., 1993, "Contact law effects on wave propagation in particulate materials using distinct element modeling," *Int. J. Non-Linear Mechanics*, Vol. 28, No. 2, pp. 251–265.

Savage, S.B., 1984, "The mechanics of rapid granular flows," *Advances in Applied Mechancis*, Vol. 24, pp. 289–366.

Savage, S.B., 1988, "Streaming motions in a bed of vibrationally fluidized dry granular material," *J. Fluid Mech.*, Vol. 194, pp. 457–478.

Sondergaard, R., Chaney, K., and Brennen, C.E., 1990, "Measurements of solid spheres bouncing off flat plates," *J. Appl. Mech.*, Vol. 57, pp. 694–699.

Suzuki, A., Takahashi, H., and Tanaka, T., 1968, "Behavior of a particle bed in the field of vibration. II. Flow of particles through slits in the bottom of a vibrating vessel," *Powder Tech.*, Vol. 2, pp. 72–77.

Takahashi, H., Suzuki, A., and Tanaka, T., 1968, "Behavior of a particle bed in the field of vibration. I. Analysis of particle motion in a vibrating vessel," *Powder Tech.*, Vol. 2, pp. 65–71.

Taguchi, Y-h., 1992, "New Origin of convective motion: elastically induced convection in granular materials," *Phys. Rev. Lett.*, Vol. 69, No. 9, pp. 1367–1370.

Tanaka, T., Kajiwara, Y., and Inada, T., 1988, "Flow dynamics of granular materials in a hopper," *Trans. of ISIJ*, Vol. 28, pp. 907–915.

Thomas, B., Mason, M.O., Liu, Y.A., and Squires, A.M., 1989, "Identifying states in shallow vibrated beds," *Powder Tech.*, Vol. 57, pp. 267–280.

Ting, J.M., Khwaja, M., Meachum, L.R., and Rowell, J.D., 1993, "An ellipse-based discrete element model for granular-materials," *Int. J. for Num. and Anal.*

Meth. in Geomech., Vol. 17, No. 9, pp. 603–623.

Tüzün, U., Houlsby, G.T., Nedderman, R.M., and Savage, S.B., 1982, "The flow of granular materials-II. Velocity distributions in slow flow," *Chemical Engineering Science*, Vol. 37, No. 12, pp. 1691–1709.

Walton, O.R., 1992, "Numerical simulation of inclined chute flows of monodisperse, inelastic, frictional spheres," *Advances in Micromechanics of Granular Materials*, H.H. Shen *et al.*, eds., Elsevier Science Publishers, B.V.

Walton, O.R., 1993, "Numerical simulation of inelastic, frictional particle-particle interactions," *Particulate Two-Phase Flow*, Ed. M.C. Roco, Butterworth-Heinemann, pp. 884–911.

Wassgren, C.R., Brennen, C.E., and Hunt, M.L., 1995, "Granular flow in a vertically vibrating hopper," *Proceedings of the 10th ASCE Engineering Mechanics Specialty Conference*, Boulder, CO.

Wassgren, C.R., Brennen, C.E., and Hunt, M.L., 1996a, "Vertical vibration of a deep bed of granular material in a container," to appear in *J. Appl. Mech.*

Wassgren, C.R., Brennen, C.E., and Hunt, M.L., 1996b, "Vertical side wall convection in deep beds of granular material subjected to vertical, sinusoidal oscillations," *Proceedings of the 5th World Congress of Chemical Engineering*, San Diego, CA.

Werner, B.T., 1987, *A physical model of wind-blown sand transport* Ph.D. Thesis, California Institute of Technology.

Zik, O. and Stavans, J., 1991, "Self-diffusion in granular flows," *Europhys. Lett.*, Vol. 16, No. 3, pp. 255-258.

Zik, O., Stavans, J., and Rabin, Y., 1992, "Mobility of a sphere in vibrated granular media," *Europhys. Lett.*, Vol. 17, No. 4, pp. 315–319.

Appendix I: Remarks on the Effect of the Interstitial Fluid

When $\Gamma > 1$, the particle bed lifts off the base of the container. As a result, the interstitial fluid (usually air) percolates through the particle bed from the atmosphere to fill the gap between the bed and base. Conversely, when the bed falls back toward the base, the interstitial fluid in the gap is forced back through the particle bed into the atmosphere. The motion of the fluid relative to the particles in the bed may affect the observed deep bed phenomena. In order to quantify this effect, a simple analysis is performed below comparing the pressure gradient acting on particles due to the percolation of the interstitial fluid through the bed to the pressure gradient in the bed due to the weight of the particles.

The pressure gradient due to the fluid effects can be estimated from Darcy's Law, which in 1D, is given by

$$(dp/dy)_f = \frac{\mu_f}{\kappa} v \tag{9.1}$$

where $(dp/dy)_f$ is the pressure gradient in the bed, μ_f the viscosity of the interstitial fluid, κ the permeability of the bed, and v the velocity of the fluid relative to the bed. For the present analysis, the permeability of the bed, κ, is assumed to follow the Ergun relation (refer to Nield and Bejan, 1992)

$$\kappa = \frac{d^2 \Phi^3}{150(1-\Phi)^2} \tag{9.2}$$

where d is the particle diameter and Φ is the bed porosity ($\Phi = 1 - \nu$ where ν is the solid fraction of particles in the bed). Additionally, a representative velocity in the system is the velocity amplitude of the oscillations, $v = a\omega$, where a is the oscillation amplitude and ω is the oscillation radian frequency ($\omega = 2\pi f$ where f is the cyclic oscillation frequency).

The pressure gradient in the bed due to the weight of the particles is simply the

hydrostatic pressure given by

$$(dp/dy)_h = \rho_b g_{eff} \tag{9.3}$$

where ρ_b is the bulk density in the bed ($\rho_b = (1-\phi)\rho_p$ where ρ_p is the density of an individual particle) and g_{eff} is the effective gravity acting on the bed. For the vibrating bed this can be estimated as the oscillation acceleration amplitude, $a\omega^2$.

Taking the ratio of the two pressure gradients and simplifying gives

$$\frac{(dp/dy)_f}{(dp/dy)_h} = \frac{150\mu_f(1-\Phi)}{\rho_p d^2 \Phi^3 \omega} \tag{9.4}$$

For a bed of glass spheres ($\rho_p = 2500$ kg/m^3) in a random packed arrangement ($\Phi \approx 0.4$) in dry air ($\mu_f = 1.80 * 10^{-5}$ N·s/m), the ratio becomes

$$\frac{(dp/dy)_f}{(dp/dy)_h} = \frac{1.0 * 10^{-5}}{d^2 \omega} \tag{9.5}$$

For frequencies between 10 and 20 Hz this ratio is one when d is approximately 0.3 mm. In all of the experiments performed here, the particles have diameters on the order of 1 mm diameter, well above this critical diameter. Thus, interstitial fluid effects are not expected to significantly affect the particle bed behavior for these parameters. A more detailed analysis of the effects of the interstitial fluid on the bed behavior can be found in Pak *et al.* (1995).

Appendix II: Remarks on the Choice of Particle/Particle Simulation Interaction Parameters

The particle/particle interaction parameters used in the simulations include the

- coefficient of restitution, ϵ_{pp},
- sliding friction coefficient, μ_{pp},
- normal spring constant, $k_{n,pp}$,
- tangential spring constant, $k_{s,pp}$.
- normal dashpot coefficient, ν_{pp},

The procedure for determining these parameters is described in chapter 2, section "Simulation Parameters." The effect of varying these parameters on the simulation results is discussed here.

Most of the simulations use the same value for the parameters: $\epsilon_{pp} = 0.8$, $\mu = 1.0$, $k_{n,pp} = k_{s,pp} = 5.289 * 10^3$ N/m, and $\nu_{pp} = 8.337 * 10^{-3}$ N/(m/s) as indicated in the tables at the end of each chapter. Overall, the deep bed phenomena did not differ significantly in a qualitative sense over the entire range of ϵ_{pp} and μ_{pp} investigated.

The sensitivity of the behaviors on the normal and tangential spring stiffnesses, $k_{n,pp}$ and $k_{s,pp}$, and the normal dashpot coefficient, ν_{pp}, was not examined in the present work. The value of $k_{n,pp}$ was chosen such that the typical overlap in a particle/particle collision is less than 1% of the smallest particle radius in the system. The results are expected to be insensitive to the spring stiffness as long as $k_{n,pp}$ is sufficiently large so that dense assemblies of particles overlap less than 1% of the particle radius . When the overlap is greater than 1%, the excluded volume (or area in 2D) is large enough to affect the measured values of the transport properties (see, for example, Campbell, 1986). The ratio of the tangential spring stiffness to the normal spring stiffness, $k_{s,pp}/k_{n,pp}$, should be between 2/3 and 1 according to the analytical results of Mindlin (1949). In the present work $k_{s,pp}/k_{n,pp} = 1$ for all of the simulations. Cundall and Strack (1979) determined that this ratio is significant when particles are in

constant contact and the friction coefficient is large. For the simulations performed here the particles are not in constant contact during a considerable portion of the oscillation period and consequently it was expected that this ratio would not significantly affect the simulation results. Lastly, the normal dashpot coefficient, ν_{pp}, was not varied independently in the present simulations since it is an explicit function of $k_{n,pp}$ and ϵ_{pp}.

The effect of changing the particle/particle sliding friction coefficient, μ_{pp}, and the coefficient of restitution, ϵ_{pp}, on the observed deep bed behaviors was examined qualitatively and found not to be fundamental to the deep bed phenomena.

The side wall convection behavior appeared for $\mu_{pp} = 0.0$ as well as for $\mu_{pp} = 1.0$ as long as frictional walls were used in the simulation. The effect of μ_{pp} on the side wall boundary layer characteristics was not studied quantitatively, however. Since the side wall convection behavior appears to be caused by frictional particle/wall interactions, the sensitivity of the side wall convection phenomenon on the particle/wall sliding friction coefficient, μ_{pw}, was examined. The particle flow rate in the boundary layer along the wall, wj_d, decreases with decreasing μ_{pw}, and is zero when $\mu_{pw} = 0$. Additionally, wj_d decreases for coefficients of restitution, ϵ_{pw} and ϵ_{pp}, greater than approximately 0.8. In the many of the simulation used to investigate the side wall convection behavior, $\mu_{pw} = 1.0$ and $\epsilon_{pp} = \epsilon_{pw} = 0.8$. The high value of μ_{pw} was chosen because it gives a high flow rate in the boundary layer. Consequently, fewer oscillation cycles are required over which to average in order to determine the mean motion of the particles. The value of ϵ_{pp} was chosen since it is a representative value of ϵ_{pp} for glass spheres.

The surface waves appeared throughout the studied range of $0.0 \leq \mu_{pp} \leq 1.0$. Two qualitative changes were noticeable in the wave behavior. First, the waves appeared over a wider range of Γ when μ_{pp} was decreased and, second, the degree of saltation on the free surface of the bed increased as μ_{pp} decreased. The effects on the wave amplitude and wavelength were not examined. The qualitative effect of the coefficient of restitution, ϵ_{pp}, over the range from $0.3 < \epsilon_{pp} < 0.98$ was also examined. The waves appeared over the studied range of ϵ_{pp} but the degree of saltation of particles at the

free surface of the bed increased with increasing ϵ_{pp}. The benchmark simulation for studying the wavelength of the surface waves in the simulations used $\mu_{pp} = 0.0$ and $\epsilon_{pp} = 0.5$. The value for μ_{pp} was chosen in order to reduce the number of simulation parameters and ϵ_{pp} was chosen to decrease the degree of saltation on the free surface of the bed and allow for easy determination of the surface wave peaks.

Kinks and kink convection also appeared over the studied ranges of $0.0 \leq \mu_{pp} \leq 1.0$ and $0.3 \leq \epsilon_{pp} \leq 0.98$. As with the surface waves, decreasing μ_{pp} or increasing ϵ_{pp} resulted in an increase in the degree of saltation of particles.

In summary, the particle/particle interaction properties such as μ_{pp} and ϵ_{pp} do not appear to be fundamental to the formation of the deep bed phenomena investigated here. The detailed appearance of the behaviors, such as the degree of saltation at the free surface of the bed, however, is affected and increases with decreasing energy dissipation in the particle contacts. A more quantitative investigation of these particle interaction parameters is needed to determine what value of these parameters is most appropriate for simulating real materials. The vibrating bed simulation, however, may not be the best environment to determine the appropriate parameters since the phenomena appear to be robust to changes in μ_{pp} and ϵ_{pp}.

Appendix III: Simulation Code

Following is the C code for a soft particle simulation of a vertically oscillating container. The code was written by the author.

```
/*
        Program:  bench.c

        This is a 2D soft-particle discrete element simulation.
        The simulation is set upsimulating a
        two-dimensional box with vertical walls subjected to
        vertical sinusoidal vibrations.  WALL BOUNDARIES AND FRICTION.
*/

# include <stdio.h>
# include <stdlib.h>
# include <math.h>
# include <time.h>
# include <malloc.h>

# define PI (3.14159265)

/* gravity acceleration */
# define g (9.81)

/* ratio of overlap to the smallest particle radius at which a warning
  is printed. */
# define MAX_OVERLAP (0.03)

/* maximum number of contacts per particle */
# define CONTACT_MAX (8)

/* function to tell the sign of a variable */
# define sgn(x) ((x)>=0.0  ?  1.0  :  -1.0)

/* input data file name */
# define filename_in ("bench.in")

/*
  the data structure for all particles in the simulation:
  num:  the particle identifying number (between 1 and N where N is the
      total number of particles
  cellx, celly:  the cell in which the particle is located
  contact[]:  the numbers of the particles that are currently in
          contact with this particle
  x, y, thetaz:  the translational and rotational positions of the particle
  xdot, ydot, thetazdot:  the trans. and rot. velocities of the particle
  Fx, Fy, Tz:  the forces and torques acting on the particle
  r, m, I:  the particle's radius, mass, and moment of inertia
  deltas[]:  the tangential displacement for each particle in contact with
          this particle
  *prev, *next:  pointers to the previous and next particles in the
            the cell in which the current particle is located
```

```
*/
struct state
{
 short int num, cellx, celly, contact[CONTACT_MAX+1];
 double x, y, thetaz, xdot, ydot, thetazdot,
      Fx, Fy, Tz, r, m, I, deltas[CONTACT_MAX+1];
 struct state *prev, *next;
} *particle;


/* the structure for the cell pointers */
struct element
{
 struct state *next;
} **cell;

/*
  Define global variables.
  N:  total number of particles
  x_wall_flag:  the flag that tells whether wall boundaries (1) or
          periodic boundaries (0) are being used
  cellmax_x, cellmax_y:  the total number of cells in the environment
  wall_num:  the total number of wall boundaries
  Gamma:  the oscillation acceleration amplitude
  a:  the oscillation amplitude
  w:  the oscillation radian frequency
  gx, gy:  the gravity acceleration components
  deltat:  the simulation time step
  t:  the time
  tmax:  the time at which the simulation will end
  x_width, y_width:  the rectangular container dimensions
  k_pn, nu_pn:  the particle/particle normal contact spring constant and
          dashpot coefficient
  k_ps, mu_p:  the particle/particle tangential contact spring constant
          and coefficient of friction
  k_wn, nu_wn:  the particle/wall normal contact spring constant and
          dashpot coefficient
  k_ws, mu_w:  the particle/wall tangential contact spring constant
          and coefficient of friction
  cellsize:  the length of the square cell
  dmax:  the maximum particle diameter
  rmin:  the minimum particle radius
  deltat_samp_recordstate:  the time between successive recordings of the
                  particle states
  t_samp_recordstates:  the time at which the next recording of the particle
                  states will be made
*/
```

```
int N, x_wall_flag, cellmax_x, cellmax_y, wall_num;
double Gamma, a, w, gx, gy, deltat, t, tmax, x_width, y_width,
      k_pn, nu_pn, k_ps, mu_p,
      k_wn, nu_wn, k_ws, mu_w,
      cellsize, dmax, dbar, rmin,
      deltat_samp_recordstates, t_samp_recordstates;

/* ***** */

void main (int argc, char **argv)
{
  void read_data(FILE *outfile);
  void calculate_forces(void);
  void integrate_eqns(void);
  void record_states(FILE *outfile);
  FILE *outfile;
  extern int N;
  extern double t, tmax, w,
       t_samprecordstates, deltat_samp_recordstates;

  /* make sure enough arguments are given in the command line */
  if (argc < 2)
    {
     printf("Command line error.\n");
     printf("Format:  bench state.out\n");
     exit(1);
    }

  /* Open the output data files */
  if ((outfile = fopen(argv[1], "wb")) == NULL)
    {
     printf("Cannot open outfile.\n");
     exit(1);
    }

  /* goto the subroutine that reads in the input data. */
  read_data(outfile);

  /* start the simulation. */
  t = 0.0;
  record_states(outfile);
  do
    {
     /*
            goto the subroutine that determines the forces acting on each
            of the particles
     */
     calculate_forces();
```

```
    /* record the particle states */
    if (t >= t_samp_recordstates)
            {
             printf("states:  cycles = %.3f (%.1f percent completed)\n",
                        w*t/(2.0*PI), 100.0*t/tmax);
             t_samp_recordstates += deltat_samp_recordstates;
             record_states(outfile);
            }

    /* goto the subroutine to integrate the equations of motion */
    integrate_eqns();

   } while (t<tmax);

 calculate_forces();
 record_states(outfile);
 printf("cycles = %.3f (%.1f percent completed)\n",
     w*t/(2.0*PI), 100.0*t/tmax);
 fprintf(outfile,"#\n");

 /* close the output file */
 fclose(outfile);
}

/* ***** */

void calculate_forces(void)
/*
  This routine initializes the particle forces with the gravity force and
  then determines which particles could be in contact.  It calls other
  routines to actually do the calculations for the forces.
*/

{
 void x_wall_forces(int i, int j);
 void y_wall_forces(int i, int j);
 void particle_forces(int i, int j, double pj_dx);
 int i, j, cellx, celly, x, y;
 struct state *particlej;
 extern int N, cellmax_x, cellmax_y, x_wall_flag;
 extern double gx, gy;
 extern struct state *particle;
 extern struct element **cell;

  /* initialize particle forces with gravity force */
 for (i=1; i<=N; i++)
   {
```

```
  particle[i].Fx = gx*particle[i].m;
  particle[i].Fy = gy*particle[i].m;
  particle[i].Tz = 0.0;
 }

/* check for collisions with the bottom wall */
celly = particle[N+1].celly;
for (y=celly; y<=celly+1; y++)
 {
  for (x=1; x<=cellmax_x-1; x++)
        {
         if ((particlej = cell[x][y].next) != NULL)
          {
           do
                {
                 y_wall_forces(particlej->num, N+1);
                } while((particlej=particlej->next) != NULL);
          }
        }
 }

/* check for collisions with the top wall */
celly = particle[N+2].celly;
for (y=celly-1; y<=celly; y++)
 {
  for (x=1; x<=cellmax_x-1; x++)
        {
         if ((particlej = cell[x][y].next) != NULL)
          {
           do
                {
                 y_wall_forces(particlej->num, N+2);
                } while((particlej=particlej->next) != NULL);
          }
        }
 }

if (x_wall_flag == 1)  /* wall boundaries */
 {
  /* check for collisions with the left wall */
  cellx = particle[N+3].cellx;
  for (x=cellx; x<=cellx+1; x++)
        {
         for (y=particle[N+1].celly; y<=particle[N+2].celly; y++)
          {
           if ((particlej = cell[x][y].next) != NULL)
                {
                 do
```

```
                        {
                         x_wall_forces(particlej->num, N+3);
                        } while((particlej=particlej->next) != NULL);
                      }
                  }
              }

    /* check for collisions with the right wall */
    cellx = particle[N+4].cellx;
    for (x=cellx-1; x<=cellx; x++)
            {
             for (y=particle[N+1].celly; y<=particle[N+2].celly; y++)
              {
               if ((particlej = cell[x][y].next) != NULL)
                      {
                       do
                        {
                         x_wall_forces(particlej->num, N+4);
                        } while((particlej=particlej->next) != NULL);
                      }
              }
            }
   }

/* check for interparticle collisions */
for (i=1; i<=N-1; i++)
  {
    cellx = particle[i].cellx;
    celly = particle[i].celly;

    /*
            check for collisions with cells around and including current
            cell
    */
    for (x=cellx-1; x<=cellx+1; x++)
            {
             for (y=celly-1; y<=celly+1; y++)
              {
               if ((particlej = cell[x][y].next) != NULL)
                      {
                       do
                        {
                         if (particlej->num > i)
                                particle_forces(particle[i].num, particlej->num, 0.0);
                        } while((particlej=particlej->next) != NULL);
                      }
              }
            }
```

```
   if (x_wall_flag == 0)  /* periodic boundaries */
          {
           if (cellx==1)
            {
             for (y=celly-1; y<=celly+1; y++)
                    {
                     if ((particlej = cell[cellmax_x-1][y].next) != NULL)
                      {
                       do
                              {
                               if (particlej->num > i)
                                 particle_forces(particle[i].num,particlej->num,
                                                        -x_width);
                              } while((particlej=particlej->next) != NULL);
                      }
                    }
            }

           if (cellx==cellmax_x-1)
            {
             for (y=celly-1; y<=celly+1; y++)
                    {
                     if ((particlej = cell[1][y].next) != NULL)
                      {
                       do
                              {
                               if (particlej->num > i)
                                 particle_forces(particle[i].num,particlej->num,
                                                        x_width);
                              } while((particlej=particlej->next) != NULL);
                      }
                    }
            }
          }
   }
}

/* ***** */

void x_wall_forces(int i, int j)
/*
  This routine first determines if a particle is in contact with either the
  left or right vertical wall boundaries and if so, calculates
  the forces acting on the particle.
*/
{
 int k, q;
```

```
double dx,          /* the particle separation in the x-direction */
      overlap,      /* amount of particle overlap */
      nx, sy,       /* direction vector components */
      fnmag, fsmag,  /* normal and tangential forces */
      dxdot, dydot,  /* relative velocities in the x and y directions */
      ndot, sdot;    /* relative velocities in the n and s directions */
extern double rmin, k_wn, nu_wn, k_ws, mu_w, deltat;
extern struct state *particle;

/* determine the amount of overlap between particles */
dx = particle[j].x-particle[i].x;
overlap = particle[i].r - fabs(dx);

if (overlap >= 0.0) /* is there contact? */
  {
    if (overlap/rmin > MAX_OVERLAP)  /* is there too much overlap? */
          {
           printf("WARNING: t=%.3e sec\t%d/W%d", t, i, j);
           printf("\toverlap/rmin=%.3e\n", overlap/rmin);
          }

    /* determine the direction vectors for the contact */
    nx = sgn(dx);
    sy = nx;

    /* determine the relative contact velocities */
    dxdot = particle[j].xdot - particle[i].xdot;
    dydot = particle[j].ydot - particle[i].ydot;
    ndot = dxdot*nx;
    sdot = dydot*sy - particle[i].r*particle[i].thetazdot;

    /* determine the normal force */
    fnmag = -k_wn*overlap + nu_wn*ndot;
    particle[i].Fx += fnmag*nx;

    /*
          determine if the contact between these two particles is a
          continuing contact or if it is a new contact
    */
    /* go through the contact list */
    k = 1;
    while ((particle[i].contact[k] != j) &&
           (k <= CONTACT_MAX))
          k++;
    if (k <= CONTACT_MAX)  /* this is an old contact */
          q = k;
    else  /* this is a new contact */
          {
```

```
            k = 1;
            while (particle[i].contact[k] != 0)
              k++;
            q = k;
            particle[i].contact[q] = j;
            particle[i].deltas[q] = 0.0;
           }

    /* update the tangential spring extension for this contact */
    particle[i].deltas[q] += sdot*deltat;

    /*
            check to see if there is slip between these particles, if so
            adjust the spring extension appropriately
    */
    if (mu_w*fabs(fnmag) < fabs(k_ws*particle[i].deltas[q]))
           particle[i].deltas[q] = sgn(k_ws*particle[i].deltas[q])*
                                          mu_w*fabs(fnmag)/k_ws;

    /* determine the force in the tangential direction */
    fsmag = k_ws*particle[i].deltas[q];
    particle[i].Fy += fsmag*sy;
    particle[i].Tz += particle[i].r*fsmag;
   }
  else
   {
    /*
            remove reference to particle j in particle[i].deltas since
            particle i and particle j are not in contact
    */
    for (k=1; k<=CONTACT_MAX; k++)
           if (particle[i].contact[k] == j)
             particle[i].contact[k] = 0;
   }
}

/* ***** */

void y_wall_forces(int i, int j)
/*
  This routine first determines if a particle is in contact with either
  the horizontal top or bottom wall boundaries and if so, calculates
  the forces acting on the particle.
*/
{
 int k, q;
 double dy,          /* the particle separation in the y-direction */
      overlap,      /* amount of particle overlap */
```

```
    ny, sx,      /* direction vector components */
    fnmag, fsmag,  /* normal and tangential forces */
    dxdot, dydot,  /* relative velocities in the x and y directions */
    ndot, sdot;   /* relative velocities in the n and s directions */
extern double rmin, k_wn, nu_wn, k_ws, mu_w, deltat;
extern struct state *particle;

/* determine the amount of overlap between particles */
dy = particle[j].y-particle[i].y;
overlap = particle[i].r - fabs(dy);

if (overlap >= 0.0)    /* is there contact? */
 {
  if (overlap/rmin > MAX_OVERLAP)  /* is there too much overlap? */
        {
         printf("WARNING: t=%.3e sec\t%d/W%d", t, i, j);
         printf("\toverlap/rmin=%.3e\n", overlap/rmin);
        }

  /* determine the direction vectors for the contact */
  ny = sgn(dy);
  sx = -ny;

  /* determine the relative contact velocities */
  dxdot = particle[j].xdot - particle[i].xdot;
  dydot = particle[j].ydot - particle[i].ydot;
  ndot = dydot*ny;
  sdot = dxdot*sx - particle[i].r*particle[i].thetazdot;

  /* determine the normal force */
  fnmag = -k_wn*overlap + nu_wn*ndot;
  particle[i].Fy += fnmag*ny;

  /*
        determine if the contact between these two particles is a
        continuing contact or if it is a new contact
  */
  /* go through the contact list */
  k = 1;
  while ((particle[i].contact[k] != j) &&
          (k <= CONTACT_MAX))
        k++;
  if (k <= CONTACT_MAX)  /* this is an old contact */
        q = k;
  else  /* this is a new contact */
        {
         k = 1;
         while (particle[i].contact[k] != 0)
```

```
            k++;
           q = k;
           particle[i].contact[q] = j;
           particle[i].deltas[q] = 0.0;
          }

    /* update the tangential spring extension for this contact */
    particle[i].deltas[q] += sdot*deltat;

    /*
          check to see if there is slip between these particles, if so
          adjust the spring extension appropriately
    */
    if (mu_w*fabs(fnmag) < fabs(k_ws*particle[i].deltas[q]))
          particle[i].deltas[q] = sgn(k_ws*particle[i].deltas[q])*
                                        mu_w*fabs(fnmag)/k_ws;

    /* determine the force in the tangential direction */
    fsmag = k_ws*particle[i].deltas[q];
    particle[i].Fx += fsmag*sx;
    particle[i].Tz += particle[i].r*fsmag;
   }
 else
   {
    /*
          remove reference to particle j in particle[i].deltas since
          particle i and particle j are not in contact
    */
    for (k=1; k<=CONTACT_MAX; k++)
          if (particle[i].contact[k] == j)
          particle[i].contact[k] = 0;
   }
}

/* ***** */

void particle_forces(int i, int j, double pj_dx)
/*
  This routine first determines if two particles are in contact
  and if so, calculates the forces acting on them.
*/
{
 int k; q;
 double dx, dy,      /* the particle separation in the x and y directions */
       dij,         /* the distance between the particle centers */
       overlap,     /* amount of particle overlap */
       nx, ny,      /* the direction vectors in the norm. direction */
       sx, sy,      /* the direction vectors in the tang. direction */
```

```
    fnmag, fsmag,  /* normal and tangential forces */
    dxdot, dydot,  /* relative velocities in the x and y directions */
    ndot, sdot;    /* relative velocities in the n and s directions */
extern double rmin, k_pn, nu_pn, k_ps, mu_p, deltat;
extern struct state *particle;

/* determine the amount of overlap between particles */
dx = (particle[j].x+pj_dx) - particle[i].x;
dy = particle[j].y - particle[i].y;
dij = sqrt(dx*dx+dy*dy);
overlap = (particle[j].r+particle[i].r) - dij;

/* Contact forces. */
if (overlap >= 0.0)  /* is there contact? */
  {
   if (overlap/rmin > MAX_OVERLAP)  /* is there too much overlap? */
          {
           printf("WARNING: t=%.3e sec\t%d/%d", t, i, j);
           printf("\toverlap/rmin=%.3e\n", overlap/rmin);
          }

   /* determine the direction vectors for the contact */
   nx = dx/dij;
   ny = dy/dij;
   sx = -ny;
   sy = nx;

   /* determine the relative contact velocities */
   dxdot = particle[j].xdot-particle[i].xdot;
   dydot = particle[j].ydot-particle[i].ydot;
   ndot = dxdot*nx + dydot*ny;
   sdot = dxdot*sx + dydot*sy -
          particle[j].r*particle[j].thetazdot -
           particle[i].r*particle[i].thetazdot;

   /* determine the normal force */
   fnmag = -k_pn*overlap + nu_pn*ndot;
   particle[i].Fx += fnmag*nx;
   particle[i].Fy += fnmag*ny;
   particle[j].Fx -= fnmag*nx;
   particle[j].Fy -= fnmag*ny;

   /*
          determine if the contact between these two particles is a
          continuing contact or if it is a new contact
   */
   /* go through the contact list */
   k = 1;
```

```
    while ((particle[i].contact[k] != j) &&
              (k <= CONTACT_MAX))
           k++;
    if (k <= CONTACT_MAX) /* this is an old contact */
           q = k;
    else  /* this is a new contact */
           {
            k = 1;
            while (particle[i].contact[k] != 0)
             k++;
            q = k;
            particle[i].contact[q] = j;
            particle[i].deltas[q] = 0.0;
           }

    /* update the tangential spring extension for this contact */
    particle[i].deltas[q] += sdot*deltat;

    /*
           check to see if there is slip between these particles, if so
           adjust the spring extension appropriately
    */
    if (mu_p*fabs(fnmag) < fabs(k_ps*particle[i].deltas[q]))
      particle[i].deltas[q] = sgn(k_ps*particle[i].deltas[q])*
                                          mu_p*fabs(fnmag)/k_ps;

    /* determine the force in the tangential direction */
    fsmag = k_ps*particle[i].deltas[q];
    particle[i].Fx += fsmag*sx;
    particle[i].Fy += fsmag*sy;
    particle[i].Tz += particle[i].r*fsmag;
    particle[j].Fx -= fsmag*sx;
    particle[j].Fy -= fsmag*sy;
    particle[j].Tz += particle[j].r*fsmag;
   }
  else
   {
    /*
           remove reference to particle j in particle[i].deltas since
           particle i and particle j are not in contact
    */
    for (k=1; k<=CONTACT_MAX; k++)
           if (particle[i].contact[k] == j)
            particle[i].contact[k] = 0;
   }
}

/* ***** */
```

```
void integrate_eqns(void)
/*
  This routine integrates the equations of motion for the particles and the
  moving boundaries.
*/
{
 void remove_from_cell(int x, int y, int i);
 void add_to_cell(int x, int y, int i);
 int i, cellx, celly;
 extern int N, wall_num, x_wall_flag;
 extern double t, deltat, a, w, x_width, y_width, cellsize;
 extern struct state *particle;
 extern struct element **cell;

 /* update time */
 t += deltat;

 /* update wall boundary positions and velocities */
 for (i=N+1; i<=N+wall_num; i++)
  particle[i].ydot = a*w*cos(w*t);
 particle[N+1].y = a*sin(w*t);
 particle[N+2].y = particle[N+1].y+y_width;

 /* update particle positions and velocities */
 for (i=1; i<=N; i++)
  {
   /* this is a "leap frog" integration scheme */
   particle[i].xdot += (particle[i].Fx/particle[i].m)*deltat;
   particle[i].ydot += (particle[i].Fy/particle[i].m)*deltat;
   particle[i].thetazdot += (particle[i].Tz/particle[i].I)*deltat;
   particle[i].x += particle[i].xdot*deltat;
   particle[i].y += particle[i].ydot*deltat;
   particle[i].thetaz += particle[i].thetazdot*deltat;

   /* keep rotational position between 0 and 2*PI */
   if (particle[i].thetaz > 2.0*PI)
        particle[i].thetaz = particle[i].thetaz -
                    2.0*PI* (int) ((particle[i].thetaz)/(2.0*PI));

   /*
        if using periodic boundaries, check to see if the particle has
        wrapped around in the horizontal direction
   */
   if (x_wall_flag == 0)
        {
         if (particle[i].x < 0.0)
          particle[i].x += x_width;
```

```
            if (particle[i].x > x_width)
              particle[i].x -= x_width;
           }

    /* check to see if the particle has changed cells */
    cellx = (int) (particle[i].x/cellsize)+1;
    celly = (int) ((particle[i].y-particle[N+1].y)/cellsize)+1;
    if ((particle[i].cellx != cellx) || (particle[i].celly != celly))
           {
            remove_from_cell(particle[i].cellx,particle[i].celly,i);
            add_to_cell(cellx,celly,i);
           }
   }

}

/* ***** */

void read_data(FILE *outfile)
/*
  This routine reads in the input data file and calls a routine to
  initialize the simulation.
*/
{
  void initialize_states(void);

  int i, j;              /* temporary integers */
  double cycles,         /* total number of oscillation cycles to perform */
       f,              /* cyclic frequency [Hz] */
       theta_g,        /* the gravity vector angle from the vertical */
       r,              /* temporary radius */
       e_wn, e_pn,     /* particle/particle and particle/wall
                                  coefficient of restitution */
       ddev,           /* the deviation from the mean diameter */
       dmin,           /* the minimum particle diameter */
       rho_m,          /* the particle mass density */
       overlap=0.01,   /* the expected maximum ratio of the overlap to
                                  the mean particle radius for a collision with */
       xd_r=1000.0,    /* a relative impact velocity equal to
                                 (xd_r)*(mean particle radius)*(1 sec) */
       tau_tp, tau_rp, /* the translational and rotational periods
                                  for a particle in contact with six other
                                  fixed particle contacts */
       rbar,           /* the mean particle radius */
            mbar,          /* the mean particle mass */
            Ibar,          /* the mean particle moment of inertia*/
            alpha,         /* temporary variable */
            samps_per_cycle;  /* the number of samples to record per cycle */
```

```
FILE *infile;          /* input file pointer */

extern int N, x_wall_flag, wall_num, cellmax_x, cellmax_y;
extern double Gamma, x_width, y_width,
          k_pn, nu_pn, k_ps, mu_p,
          k_wn, nu_wn, k_ws, mu_w,
          dbar, dmax, deltat, a, w, gx, gy, tmax,
          t_samp_recordstates, deltat_samp_recordstates,
          cellsize;
extern struct state *particle;
extern struct element **cell;

/* set up the pointer for the input data file */
if ((infile = fopen(filename_in,"rb")) == NULL)
  {
   printf("Error opening input file.\n");
   exit(1);
  }

/* read in the input file data */
fscanf(infile, "%lg", &Gamma);
fscanf(infile, "%lg %lg %lg",
          &cycles, &f, &samps_per_cycle);
fscanf(infile, "%lg %lg %lg %d",
          &x_width, &y_width, &theta_g, &x_wall_flag);
fscanf(infile, "%d", &N);
fscanf(infile, "%lg %lg %lg",
          &e_pn, &k_ps, &mu_p);
fscanf(infile, "%lg %lg %lg",
          &e_wn, &k_ws, &mu_w);
fscanf(infile, "%lg %lg %lg", &dbar, &ddev, &rho_m);
fclose(infile);

wall_num = 4;  /* the number of wall boundaries */
/* make room for *particle */
printf("%d bytes required for *particle.\n",
          (N+wall_num+1) * sizeof(struct state));
if ( (particle = (struct state *)
    calloc(N+wall_num+1, sizeof(struct state))) == NULL )
  {
   printf("Not enough storage for *particle.\n");
   fclose(outfile);
   exit(1);
  }

/*
   randomly choose the particle radii and then determine the
   particle mass and moment of inertia, note that mass and moment of
```

```
  inertia are based on that of a sphere
*/
srand((unsigned) time(NULL));  /* initialize the random number generator */
for (i=1; i<=N; i++)
 {
  particle[i].r = 0.5*dbar*
        (1.0+2.0*ddev*(0.5-(double) rand()/(double) RAND_MAX));
  particle[i].m = rho_m*4.0/3.0*PI*
        particle[i].r*particle[i].r*particle[i].r;
  particle[i].I = 2.0/5.0*particle[i].m*particle[i].r*particle[i].r;
  particle[i].num = i;
 }
rbar = 0.5*dbar;
mbar = rho_m*4.0/3.0*PI*rbar*rbar*rbar;
Ibar = 2.0/5.0*mbar*rbar*rbar;
dmax = dbar*(1.0+ddev);
dmin = dbar*(1.0-ddev);
rmin = 0.5*dbar;

/* determine particle/particle spring constants and dashpot coefficient */
alpha = PI/log(e_pn);
k_pn = (0.5*mbar)*(xd_r/overlap*exp(-atan(alpha)/alpha))*
  (xd_r/overlap*exp(-atan(alpha)/alpha));
nu_pn = sqrt(4.0*(0.5*mbar)*k_pn/(1.0+alpha*alpha));
k_ps = k_ps*k_pn;

/* determine particle/wall spring constants and dashpot coefficients */
alpha = PI/log(e_wn);
k_wn = (mbar)*(xd_r/overlap*exp(-atan(alpha)/alpha))*
  (xd_r/overlap*exp(-atan(alpha)/alpha));
nu_wn = sqrt(4.0*(mbar)*k_wn/(1.0+alpha*alpha));
k_ws = k_ws*k_wn;

/* determine the simulation time step */
/*
  translational period for a particle in contact with six other (fixed)
  particles with no damping
*/
tau_tp = 2.0*PI*sqrt(mbar/(3.0*(k_pn+k_ps)));

/*
  translational period for a particle in contact with six other (fixed)
  particles with no damping
*/
tau_rp = 2.0*PI*sqrt(Ibar/(6.0*k_ps*rbar*rbar));

/* choose the smallest period and make the simulation time step
  one-tenth that period*/
```

```
if (tau_tp < tau_rp)
  deltat = tau_tp/10.0;
else
  deltat = tau_rp/10.0;

/*
   determine the oscillation radian frequency and amplitude from the
   the cyclic frequency, f, and the acceleration amplitude, Gamma
*/
w = 2.0*PI*f;
a = g*Gamma/(w*w);

/* determine the gravity acceleration components */
gx = g*sin(theta_g*PI/180.0);
gy = -g*cos(theta_g*PI/180.0);

/*
   determine the maximum time for the simulation based on the specified
   number of cycles, cycles, and the cyclic frequency, f
*/
tmax = cycles/f;

/* determine the container widths */
x_width *= dbar;
y_width *= dbar;

/*
   determine the next time a recording of the output states will be
   made and the time between successive recordings
*/
t_samp_recordstates = 0.0;
deltat_samp_recordstates = (2.0*PI/w)/samps_per_cycle;

/*
   make room for the cell list pointers, note that the cellsize is
   just larger than the maximum particle diameter, dmax
*/
cellmax_x = (int) (x_width/dmax)+1;
cellsize = x_width/(double) (cellmax_x-1);
cellmax_y = (int) (y_width/cellsize)+1;
printf("%d bytes required for **cell.\n",
          (cellmax_x+1) * sizeof(struct element *) *
          (cellmax_y+1) * sizeof(struct element));
if ((cell = (struct element **)
    calloc(cellmax_x+1,sizeof(struct element *)))==NULL)
  {
   printf("Can't assign cell row pointers.\n");
   exit(1);
```

```
 }
for (i=0; i<=cellmax_x; i++)
 {
  if ((cell[i] = (struct element *)
          calloc(cellmax_y+1, sizeof(struct element)))==NULL)
         {
          printf("Not enough storage for cell columns.\n");
          exit(1);
         }
 }

/* initialize cell list */
for (j=0; j<=cellmax_y; j++)
 for (i=0; i<=cellmax_x; i++)
  cell[i][j].next = NULL;

/*
  call the routine to determine the initial conditions for the
  simulation
*/
initialize_states();

/* print the input data to the screen */
printf("\nGamma=%.2f\n", Gamma);
printf("cycles=%.2f  f=%.2f Hz  samps_per_cycle=%.2e  theta_g=%.3e deg\n",
          cycles, f, samps_per_cycle, theta_g);
printf("tau_tp=%.3e s  tau_rp=%.3e s  deltat=%.3e s\n",
          tau_tp, tau_rp, deltat);
printf("x_width=%.3e m   x_width/dbar=%.3e\n", x_width, x_width/dbar);
printf("y_width=%.3e m   y_width/dbar=%.3e\n", y_width, y_width/dbar);
printf("theta_g=%.3e deg  x_wall_flag=%d\n",
          theta_g*180.0/PI, x_wall_flag);
printf("N=%d\n", N);
printf("k_pn=%.3e N/m  nu_pn=%.3e N/(m/s)  e_pn=%.3f\n",
          k_pn, nu_pn, e_pn);
printf("k_ps=%.3e N/m  mu_p=%.3f\n",
          k_ps, mu_p);
printf("k_wn=%.3e N/m  nu_wn=%.3e N/(m/s)  e_wn=%.3f\n",
          k_wn, nu_wn, e_wn);
printf("k_ws=%.3e N/m  mu_w=%.3f\n",
          k_ws, mu_w);
printf("dbar=%.3e m   ddev=%.3e          rho_m=%.3e kg/m^3\n\n",
          dbar, ddev, rho_m);

/* print the input data to the output file */
fprintf(outfile,"%e\n", Gamma);
fprintf(outfile,"%e %e %e %e\n",
          cycles, f, samps_per_cycle, theta_g);
```

```
 fprintf(outfile,"%e %e %e\n",
            tau_tp, tau_rp, deltat);
 fprintf(outfile,"%e %e %e %d\n",
            x_width, y_width, theta_g, x_wall_flag);
 fprintf(outfile,"%d\n", N);
 fprintf(outfile,"%e %e %f %e %f\n",
            k_pn, nu_pn, e_pn, k_ps, mu_p);
 fprintf(outfile,"%e %e %f %e %f\n",
            k_wn, nu_wn, e_wn, k_ws, mu_w);
 fprintf(outfile,"%e %f %e\n", dbar, ddev, rho_m);
 for (i=1; i<=N; i++)
   fprintf(outfile,"%e %e\n", particle[i].r, particle[i].m);
}

/* ***** */

void initialize_states(void)
/*
  This routine determines the initial conditions for the simulations.
  The wall conditions are initialized and then the particles conditions
  are assigned.  Note that particles are placed in the container at
  prescribed positions (in a grid) but with random initial velocities.
*/
{
 void add_to_cell(int x, int y, int i);

 int i, xcounter, n, cellx, celly;
 double deltan;
 extern int N;
 extern double x_width, y_width, cellsize, dmax, dbar;
 extern struct state *particle;
 extern struct element **cell;

 /* initialize wall states */
 for (i=N+1; i<=N+wall_num; i++)
   {
    particle[i].x = 0.0;
    particle[i].y = 0.0;
    particle[i].thetaz = 0.0;
    particle[i].xdot = 0.0;
    particle[i].ydot = 0.0;
    particle[i].thetazdot = 0.0;
    particle[i].r = 0.0;
    particle[i].num = i;
   }
 particle[N+1].y = 0.0;
 particle[N+2].y = y_width;
 particle[N+3].x = 0.0;
```

```
particle[N+4].x = x_width;

/* put the walls in the proper cells */
for (i=N+1; i<=N+2; i++)
  {
    particle[i].cellx = 0;
    particle[i].celly = (int) ((particle[i].y-particle[N+1].y)/
                                                cellsize)+1;
  }
for (i=N+3; i<=N+4; i++)
  {
    particle[i].cellx = (int) (particle[i].x/cellsize)+1;
    particle[i].celly = 0;
  }

/* initialize particle states */
srand((unsigned) time(NULL));
n = (int) (x_width/(1.05*dmax));
deltan = x_width/(double) (n);
xcounter = 1;

for (i=1; i<=N; i++)
  {
    particle[i].x = deltan*(xcounter-0.5);
    particle[i].y = deltan*((double) ((int) ((i-1)/n)+1));
    particle[i].thetaz = 0.0;
    particle[i].xdot = 50.0*dbar*
          (0.5-(double) rand()/(double)RAND_MAX);
    particle[i].ydot = 50.0*dbar*
          (0.5-(double) rand()/(double)RAND_MAX);
    particle[i].thetazdot = 0.0;

    /* put the particles in the proper cells */
    cellx = (int) (particle[i].x/cellsize)+1;
    celly = (int) ((particle[i].y-particle[N+1].y)/cellsize)+1;
    add_to_cell(cellx,celly,i);

    xcounter++;
    if (xcounter > n)
          xcounter = 1;
  }
}

/* ***** */

void remove_from_cell(int x, int y, int i)
/*
  This routine removes a particle from a cell.
```

```
*/
{
 extern struct state *particle;
 extern struct element **cell;

 if (particle[i].prev == NULL)
   cell[x][y].next = particle[i].next;
 else
   (particle[i].prev)->next = particle[i].next;
 if (particle[i].next != NULL)
   (particle[i].next)->prev = particle[i].prev;
}

/* ***** */

void add_to_cell(int x, int y, int i)
/*
  This routine adds a particle to a cell.
*/
{
 extern struct state *particle;
 extern struct element **cell;

 if (cell[x][y].next != NULL)
   (cell[x][y].next)->prev = &(particle[i]);
 particle[i].next = cell[x][y].next;
 particle[i].prev = NULL;
 cell[x][y].next = &(particle[i]);
 particle[i].cellx = x;
 particle[i].celly = y;
}

/* ***** */

void record_states(FILE *outfile)
/*
  This routine prints the particle state data to the output file.
*/
{
 int i;
 extern int N;
 extern double t;
 extern struct state *particle;

 fprintf(outfile,"* %.5e\n", t);
 for (i=1; i<=N; i++)
   {
    fprintf(outfile,"%.5e %.5e %.5e %.5e %.5e %.5e\n",
```

```
            particle[i].x, particle[i].y, particle[i].thetaz,
                  particle[i].xdot, particle[i].ydot,
                  particle[i].thetazdot);
      }
}
```